U.PORTO
FEUP FACULDADE DE ENGENHARIA UNIVERSIDADE DO PORTO

lepabe
Laboratory for Process Engineering, Environment, Biotechnology and Energy

CHEMICAL ENGINEERING DEPARTMENT

ELECTROCHEMICAL TECHNOLOGIES FOR RENEWABLE ENERGY STORAGE

Tiago Martinho Rodrigues Lagarteira

Dissertation presented to obtain the degree of

DOCTOR IN CHEMICAL AND BIOLOGICAL ENGINEERING

by the

UNIVERSITY OF PORTO

2022

ALiCE ASSOCIATE LABORATORY IN CHEMICAL ENGINEERING

U.PORTO
FEUP FACULDADE DE ENGENHARIA UNIVERSIDADE DO PORTO

lepabe
Laboratory for Process Engineering, Environment, Biotechnology and Energy

GOVERNO DA REPÚBLICA PORTUGUESA

UNIÃO EUROPEIA
FEDER

ACKNOWLEDGMENTS

This thesis was financially supported by: i) BI-DSC under the Specific Program "Ideas" of the European Research Council for research and technological development as part of an Advanced Grant Agreement No.321315 from European Commission through the Seventh Framework Program, ii) EU FP7/2007-2013 for Fuel Cell and Hydrogen Joint Technology Initiative under Grant No. 621237 (INSIDE) and to the Erasmus program of University of Porto, iii) PEMFC-SUDOE - nº SOE1/P1/E0293 funded by FEDER funds through COMPETE2020 - Programa Operacional Competitividade e Internacionalização (POCI) and Programa Operacional Regional do Norte (NORTE2020) and by national funds (PIDDAC) through FCT/MCTES, iv) "SunStorage -Harvesting and storage of solar energy", with reference POCI-01-0145-FEDER-016387 funded by European Regional Development Fund (ERDF), through Operational Programme for Competitiveness and Internationalisation (COMPETE 2020- Programme for Competitiveness and Internationalization (OPCI), and by national funds, through FCT.

The finantial support from projects is a very important part of my PhD, but the most important one was the group people, including Prof. Adélio Mendes, that surrounded me since the very first day until today. I owe a special thank to the many labmates I had, not only at FEUP but also from the places I was lucky to be hosted at for short research stays. I will always remember you. The huge number of hours that we shared during these years allowed me to learn and adopt other perspectives from our fruitfull interactions.

I would like also to thank the people that enabled me to visit their instititutions and opened doors for further research collaborations. In this case, a special thanks to my very first supervisor, during my Master Thesis in Germany, Dr. Rémi Costa. It was with Rémi that I left my confort zone in my first working environment and managed to become his friend for life. Another special relationship is with Prof. Ultich Stimming: I was a religious reader of his works in the field of electrochemistry and had the chance

to meet him, start discussing science and then start a research collaboration. But the most important is the friendship that we are growing everyday.

Still from my working environment, a special thanks to Dr. Paula Dias. Our relationship came a bit later than expected from my perspective, but today she is sharing with me the most challenging time in my career, namely on the 112CO2 project and in growing a startup company together.

But nothing of this would be possible without my family (including personal friends) my brother Zé, my sister Bia and my parents, Martinho and Célia. To my parents, I will be always grateful to you because you were the ones always backing me even when I was not on the right path. You always believed that I could do much better and you were and still are a criticial push for me to become a better Engineer but manily a better person.

Finally, the most important ones, my son João and my wife Cláudia. It is for us as a family that I am doing all of this and give you both the best possible from me. It is because of Cláudia that today I am an Engineer because, when I first met her, I was already thinking on giving up on my graduation and I was already working in a textile company and then on civil construction. Because of this and much more, I would like to dedicate this work to you…

PREFACE

The present work was developed at the Laboratory for Process Engineering, Environment, Biotechnology and Energy (LEPABE) facilities, in the Chemical Engineering Department of the Faculty of Engineering - University of Porto (FEUP), between 2018 and 2022.

The findings of this work are published in five peer-reviewed scientific articles.

This thesis is divided into seven chapters: starting with a brief introduction; followed by five chapters describing the experimental work and results; and a final chapter with the general conclusions and perspectives for future work.

CONTENTS

Abstract XV
Sumário XVII
List of abbreviations and symbols XIX

CHAPTER 1

INTRODUCTION 1
1.1 Motivation 6
1.2 Electrochemistry 8
1.2.1 Thermodynamics 8
1.2.2 Electrolytic *vs* galvanic cells 11
1.2.3 Efficiency 13
1.2.4 Polarization losses 14
1.2.5 Electrochemical characterization methods 18
1.3 Hydrogen Energy Storage 21
1.3.1 Fuel Cells 23
1.3.2 Proton Exchange Membrane Fuel Cells 25
1.3.3 PEMFC components 27
1.3.4 Proton Exchange Membrane Electrolyzers 30
1.4 Redox Flow Batteries 33
1.6 Objectives and outline of this work 37
References 39

CHAPTER 2

HIGHLY ACTIVE SCREEN-PRINTED IR-Ti_4O_7 ANODES FOR PROTON EXCHANGE MEMBRANE ELECTROLYZERS
Abstract 49

2.1 Introduction 50
2.2 Experimental 51
2.2.1 CCM fabrication 51
2.2.1.1 Screen printing of the anode 51
2.2.1.2 Wet spray of the cathode 53
2.2.1.2 Membrane swelling treatment 53
2.2.2 Catalyst loading calculation through thermal gravimetric analysis 54
2.2.3 Surface morphology analysis with atomic force microscopy 54
2.2.4 Single cell measurements 55
2.3 Results and discussion 56
2.3.1 The role of the screen printing solvents 56
2.3.2 Catalyst loading calculation 60
2.3.3 Electrical surface conductivity 61
2.3.4 Electrolysis measurements 64
2.5 Conclusions 67
References 69

CHAPTER 3

AIR BLEEDING STRATEGIES TO INCREASE THE EFFICIENCY OF PROTON EXCHANGE MEMBRANE FUEL CELL STATIONARY APPLICATIONS FUELLED WITH CO PPM-LEVELS

Abstract 77
3.1 Introduction 78
3.2 Experimental 80
3.3 Results and discussion 83
3.3.1 Electrochemical performance with pure hydrogen 83
3.3.2 Internal air bleeding 84

3.3.3 External air bleeding 90
3.3.4 Stability upon implementation of bleeding strategies 92
3.4 Conclusions 94
References 96

CHAPTER 4

THE ROLE OF PT LOADING ON REDUCED GRAPHENE OXIDE SUPPORT IN THE POLYOL SYNTHESIS OF CATALYSTS FOR OXYGEN REDUCTION REACTION

Abstract 104
4.1 Introduction 105
4.2 Experimental 106
4.2.1 Modified polyol synthesis 106
4.2.2 Physicochemical characterization 107
4.2.3 Electrochemical characterization 108
4.3 Results and discussion 109
4.3.1 Suitability of the polyol method 109
4.3.2 Influence of the carbon support 110
4.3.3 Influence of the Pt loading in rGO 117
4.3.4 Hybrid support to avoid rGO stacking 119
4.3.5 Stability upon accelerated degradation 120
4.4 Conclusions 121
References 123

CHAPTER 5

OXYGEN REDUCTION STABILITY OF GRAPHENE-SUPPORTED ELECTROCATALYST AND DEGRADATION MECHANISMS

Abstract 131
5.1 Introduction 133
5.2 Experimental 135
5.2.1 Materials 135
5.2.2 Electrochemical measurements 136
5.2.3 Accelerated stress tests 136
5.2.4 Physical measurements 137
5.3 Results and discussion 138
5.3.1 Morphological and electrochemical measurements at BoL 138
5.3.2 Triangular wave cycling at high potentials (AST1) 143
5.3.3 Open circuit potential holding (AST2) 149
5.3.4 Triangular wave cycling at low potentials (AST3) 151
5.4 Conclusions 154
References 156

CHAPTER 6

***IN-SITU* MEASUREMENT OF VANADIUM CROSSOVER FOR THE VANADIUM REDOX FLOW BATTERY**

Abstract 168
6.1 Introduction 169
6.2 Experimental 172
6.2.1 Materials and cell components 172
6.2.2 Experimental set-up 172
6.2.3 Crossover measurement 173

6.2.4 Crossover diagnosis after aging 174
6.2.5 Determination of vanadium concentration 175
6.3 Results and discussion 175
6.3.1 Optimization of parameters 175
6.3.2 Electrochemical method *vs ex-situ* vanadium quantification 177
6.3.3 Vanadium crossover on different membranes 178
6.3.4 Vanadium crossover after battery cycling 179
6.3.5 Crossover of all ionic vanadium states 181
6.4 Conclusions 183
References 185
Supplementary information 190

CHAPTER 7

GENERAL CONCLUSIONS AND OUTLOOK 195

ABSTRACT

The transition away from the current carbon-based economy is necessary to avoid irreversible global warming. Renewables sources are expected to play the major role in terms of energy generation, creating the need for efficient energy storage and conversion technologies. Renewable energy is known to be intermittent and seasonal while the production of energy needs to be balanced with the demand. There are different strategies to make energy dispatchable, namely using a mix of energy sources and implementing energy storage technologies. Among these technologies, electrolysers and namely the polymer electrolyte membrane (PEM) electrolysers can be used to convert floatable electricity into green hydrogen; to retrieve the energy stored in hydrogen back to electricity two technologies may be used, PEM fuel cells and hydrogen turbines.

The membrane-electrode assembly (MEA) is the most important component of any PEM electrolyser cell or stack. It is composed of a proton exchange membrane, electrocatalysts/ionomer and porous transport layers. Precious metals, such as platinum and iridium, are the choice for the electrocatalysts and they make up an important contribution for the overall system cost. Therefore, the loading of these metals but also their utilization to ensure high performance and stability must be met.

Low cost and easy scalable techniques such as screen printing and wet spray were developed to fabricate high performance MEAs for PEM electrolysers. Due to the slow kinetics of the oxygen evolution reaction, typical iridium loadings at the anode are 1-3 mg cm^{-2}. The present work describes an improved anode, with an iridium loading of 0.4 mg cm^{-2}, displaying a superior performance compared to a commercial MEA (50 % more current density per gram of iridium @ 1.7 V and 40 °C). The textural form (dissolved, colloid or precipitate) of the ionomer dispersed over the catalytic layer depends on the dielectric constant of the solvent used in the ink. Cyclohexanol was found to maximize the number of iridium active sites by ensuring a better coverage of ionomer without electronically insulating the iridium particles.

The present work also addresses the stability of PEM fuel cells when the hydrogen feed contains small amounts of carbon monoxide. It was studied the role of co-feeding small amounts of oxygen (1 - 3 %) or forcing the permeation of oxygen from the cathode

side (crossover) to minimize the negative impacts caused by the carbon monoxide (concentrations of 5 - 30 ppm) which in these conditions is mostly oxidized to carbon dioxide, that is far less harmful to the catalyst. For increasing the stability of platinum-based electrocatalysts at the cathode, platinum supported on graphene samples were prepared using the polyol method. The catalytic activity was assessed using electrochemical methods including accelerated stress tests in a rotating disk electrode. The optimum gravimetric loading of Pt on graphene was found to be 30 %, since for this concentration the Pt particles displayed the best compromise between particle size and crystallinity.

Finally, this work also addresses the development of a new electrochemical method for obtaining *in-situ* the membrane crossover in vanadium redox flow batteries. This method was inspired in an equivalent method developed for obtaining the membrane crossover in PEMFC. Using this technique new in the field of redox flow batteries, the crossover of the four vanadium oxidized species was measured for proton exchange membranes with different thickness and for an anion exchange membrane.

All the knowledge obtained in the different works of this thesis allowed to recently start working in a new field, electrochemical reduction of carbon dioxide. This a led to a new discovering that was filled in a patent, where we use semiconductor materials to tune the selectivity towards desired products in gas-phase electrolysers with higher efficiency.

SUMÁRIO

A transição de uma economia baseada no carbono é necessária para evitar o aquecimento global irreversível. Fontes renováveis deverão ter um papel crucial em termos de geração de energia, criando a necessidade de tecnologias de armazenamento e conversão de energia eficientes. A energia renovável é conhecida por ser intermitente e sazonal enquanto a sua geração necessita ser balançada com a demanda. Existe diferentes estratégias tornar a energia despachável, nomeadamente a utilização de combinações de fontes de energia e da implementação de tecnologias de armazenamento. Entre tais tecnologias, os eletrolisadores e mais especificamente eletrolisadores de membrana de permuta protónica (PEM) podem converter o excesso de eletricidade renovável em hidrogénio verde; para reconverter a energia armazenada sob a forma de hidrogénio em eletricidade, duas tecnologias podem ser utilizadas, pilhas de combustível de membrana de permuta protónica (PEM) ou turbinas de hidrogénio.

O conjunto membrana-elétrodos é o componente central do eletrolisador PEM. Este é composto por uma membrana de permuta protónica, eletrocatalisadores/ionómero e camadas difusionais porosas. Metais preciosos, tais como platina e irídio, são tipicamente usados como eletrocatalisadores e são uma contribuição importante do custo total destes sistemas. Assim sendo, uma baixa carga e alta taxa de utilização têm de ser garantidas para garantir um alto desempenho em termos de eficiência e de estabilidade.

Técnicas de baixo custo e facilmente escaláveis, tais como impressão à tela e deposição por spray, foram desenvolvidas para fabricar conjuntos membrana-elétrodos para eletrolisadores PEM. Considerando a cinética lenta da reação de evolução de oxigénio, as cargas de irídio variam tipicamente entre 1-3 mg cm^{-2}. Este trabalho descreve ânodos com 0.4 mg cm^{-2} de carga de irídio que demostram desempenho superior à referência comercial (50 % maior densidade de corrente por grama de irídio a 1.7 V e 40 °C). A conformação (dissolvido, coloide ou precipitado) do ionómero disperso na camada catalítica depende da constante dielétrica do solvente usado na tinta. Ciclohexanol maximizou o número de sítios ativos de irídio, garantindo melhor cobertura do ionómero sem isolar eletronicamente as partículas de irídio.

Este trabalho aborda também a estabilidade de pilhas de combustível com alimentações de hidrogénio contando pequenas quantidades de monóxido de carbono. Foi estudado a introdução de pequenas quantidades de oxigénio (1 - 3 %) ou promovendo a permeação de oxigénio a partir do cátodo (crossover) para minimizar os impactos negativos causados pelo monóxido de carbono (concentrações entre 5 – 30 ppm) que nestas condições é oxidado a dióxido de carbono, que é muito menos prejudicial para o eletrocatalisador. Para aumentar a estabilidade de eletrocatalisadores de platina no cátodo, foram sintetizadas amostras de platina suportada em grafeno através do método poliol. A atividade catalítica dos mesmos foi estudada incluindo testes de degradação acelerada em elétrodo rotativo. A carga gravimétrica ótima de platina em grafeno foi de 30 %, demonstrando o melhor compromisso entre o tamanho e a cristinalidade das partículas de platina.

Finalmente, este trabalho também inclui o desenvolvimento de um novo método de determinação *in-situ* de permeação de espécies de vanádio através da membrana para baterias de escoamento. Este foi inspirado num método equivalente usado para determinação de permeação de hidrogénio da membrana de pilhas de combustível. Usando esta técnica nova para baterias de escoamento, a permeação das quatro espécies oxidadas de vanádio foi medida em membranas de permuta protónica de diferentes espessuras e também numa membrana de permuta aniónica.

O conhecimento adquirido no desenvolvimento dos diferentes trabalhos desta tese permitiu começar a trabalhar numa nova área, redução eletroquímica de dióxido de carbono. Isto levou à submissão de uma patente, onde utilizamos semiconductores para controlar a seletividade em relação a produtos desejados em eletrolisadores em fase gasosa com maior eficiência.

LIST OF ABBREVIATIONS AND SYMBOLS

Variables	Definition	Units
A	active area	cm^2
a_i	activities of species	
b	cell thickness	m
C	capacitance	F
D_i	diffusion coefficient of the reactant species i	$cm^2 \cdot s^{-1}$
E (or U)	electrode potential	V
$E_{Ag/AgCl}$	potential of the Ag/AgCl reference electrode	V
E^o	standard reversible electrochemical potential	V
E_{onset}	onset potential	V
E_{redox}	redox potential	V
E_{RHE}	potential of the reversible hydrogen electrode	V
F	Faraday constant (F = 96 485,3(40) $C \cdot mol^{-1}$)	$C\ mol^{-1}$
ΔG^o	Gibbs free energy of a reaction	$J\ mol^{-1}$
ΔH^o	Enthalpy of a reaction	$J\ mol^{-1}$
I (or J)	electric current	A
i (or j)	current density	$A\ cm^{-2}$
n	number of electrons exchanged in a reaction	
P	electric power	W
q	elementary charge (q = 1.6021(76)×10^{-19} C)	C
R	ideal gas constant (R = 8.3144(72) $J \cdot K^{-1} \cdot mol^{-1}$)	$J\ K^{-1}\ mol^{-1}$
R_{Bulk}	bulk charge transport resistance	Ω
R_{CT}	charge transfer resistance	Ω
R_{Series}	series resistance	Ω
ΔS	standard entropy for the overall cell reaction	$J\ mol^{-1}\ K^{-1}$
T	temperature	K
t	time	s
ΔV	potential difference	V
V_{oc}	open-circuit voltage	V
Z	impedance	Ω
Z'	real part of impedance	Ω

Z''	imaginary part of impedance	Ω

Greek symbols	Definition	Units
ε_0	vacuum permittivity (ε_0 = 8.8541(88)×10^{-12} C·V^{-1}·m^{-1})	C V^{-1} m^{-1}
ε_r	dielectric constant	
ε	efficiency	%
ε_F	faradaic efficiency	%
η_{ct}	charge transfer overpotential	V
η_{ohm}	ohmic losses	V
η_{mt}	mass transport losses	V
λ	wavelength	nm
μ_i	mobility of species *i*	m^2 V^{-1} s^{-1}
ν	frequency	Hz
υ_i	stoichiometric coefficients	

Subscripts	Definition
d	decomposition
i	species in reaction
n	electrons
0	ambient conditions

Superscripts	Definition
in	input
º	standard conditions
out	output
z	number of electrons

Abbreviations	Definition
AEM	anion exchange membrane
AES	atomic emission spectroscopy
AFM	atomic force microscopy

ALD	atomic layer deposition
BP	bipolar plate
BPM	bipolar membrane
CC	current collector
CCM	catalyst coated membrane
CE	counter electrode
CPE	constant phase element
CV	cyclic voltammetry
CVD	chemical vapor deposition
e^-	electrons
ECSA	electrochemical surface area
EIS	electrochemical impedance spectroscopy
$ERCO_2$	electrochemical reduction of carbon dioxide
GC	glassy carbon
GDE	gas diffusion electrode
GDL	gas diffusion layer
HER	hydrogen evolution reaction
HOR	hydrogen oxidation reaction
LSV	linear sweep voltammetry
ICP	inductively coupled plasma
I-V	current-voltage characteristics
MEA	membrane electrodes assembly
MS	mass spectrometry
NHE	normal hydrogen electrode
OER	oxygen evolution reaction
ORR	oxygen reduction reaction
PAFC	phosphoric acid fuel cell
PEM	proton exchange membrane
PEMFC	proton exchange membrane fuel cell
PEMWE	proton exchange membrane water electrolyser
RDE	rotating disk electrode
RE	reference electrode
RFB	redox flow battery
RHE	reversible hydrogen electrode

SEM	scanning electron microscopy
SHE	standard hydrogen electrode
SOFC	solid oxide fuel cell
SPE	solid polymer electrolyte
TEM	transmission electron microscopy
WE	working electrode
XPS	X-ray photoelectron spectroscopy
XRD	X-ray diffraction

CHAPTER 1

INTRODUCTION

1

INTRODUCTION

The global energy sector is undergoing a dynamic and unprecedented transition which is mandatory to ensure the future of Humanity beyond the next two centuries. Emerging concerns on climate change, geo-political issues and energy safety are underpinning developments and industrial strategies to enable the widespread adoption of renewables and related technologies. The main goal is to replace fossil energy and decarbonize the energy sector. Since 2014, more renewable electricity was added to the grid annually than that from fossil fuels and nuclear combined (Figure 1.1). Wind and solar power generation now dominate the global market for new electricity generation capacity, as they have become the cheapest sources of electricity in many markets. A record level of 260 gigawatts (GW) of renewables-based generation capacity was added globally in 2020, more than four times the capacity added from other sources [1]. This a promising trajectory for rapid decarbonisation of the power sector.

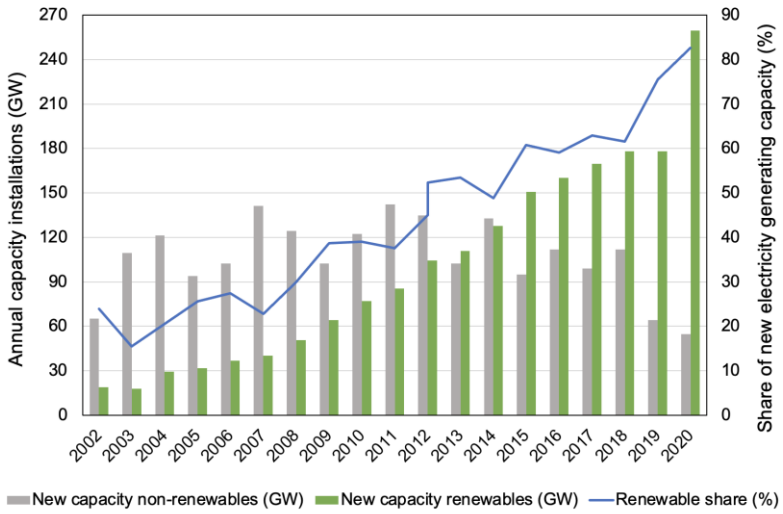


Figure 1.1 - Worldwide energy capacity installations in GW and share of renewables between 2002 to 2020 (adapted from [1]).

Unlike fossil fuels, renewable sources like wind or solar have the disadvantage of not being capable to generate power upon immediate demand. Moreover, electricity grids typically do not withstand peak power loads and surplus renewable electricity is then wasted. The solution is to use systems that can store energy during off-peak periods or release energy during high-demand periods. Energy storage systems can also help to provide power quality improvement, frequency and voltage regulation, power variations and ancillary services [2]. Today, several types of energy storage technologies are under development, and they showcase different advantages depending on power and capacity requirements. These technologies can be classified as mechanical, electrochemical, chemical and thermal storage systems. From Figure 1.2, it becomes clear that the form of energy determines the type of the storage device that is suitable for a certain application, response time and system size.

Among the energy storage technologies, batteries are considered especially suited to be used in off-grid systems to control frequency, power fluctuations and stability [3]. Among the different types of batteries, they can store energy from the power system and transfer it back to the power system when necessary. Another important direct use of renewables is to produce green hydrogen through water electrolysis. Green hydrogen has many advantages over other forms of energy storage, especially to be used in transportation, industrial and residential applications. Despite the lower round-trip efficiency compared to typical batteries, hydrogen is a clean and more versatile energy vector since it can be transported over long distances or stored in a wide portfolio of other molecules. In addition to the ability of being used to generate clean electricity using fuel cells or turbines, hydrogen is also a valuable feedstock for the production steel, ammonia or petrochemicals [4].

Like batteries, hydrogen fuel cells and electrolysers are also electrochemical devices and share many similarities in terms of stack design or materials. Nevertheless, there are special needs in key components of the cell/stack due to the use of different redox chemistries, physical state of redox species and operation conditions [5]–[7]. The two technologies are often seen as competitors. However, differences in terms of power density, capacity and efficiency will make them the best choice to be used depending on

the application. More recently, other forms of storing electricity in electrochemical systems have been developed [8]. Coupled with water electrolysis, the electrochemical reduction of carbon dioxide allows to store electricity in the form of valuable chemicals/fuels while consuming and using the green-house effect gas. The idea is to use renewable electricity to produce desirable products like methane, methanol, ethylene, formic acid, among others (Power-to-X concept) [9]. The technology is still in early stage of development, but it expected to become an important technology to harvest more renewable energy while consuming carbon dioxide, thus becoming a technology with negative carbon balance.

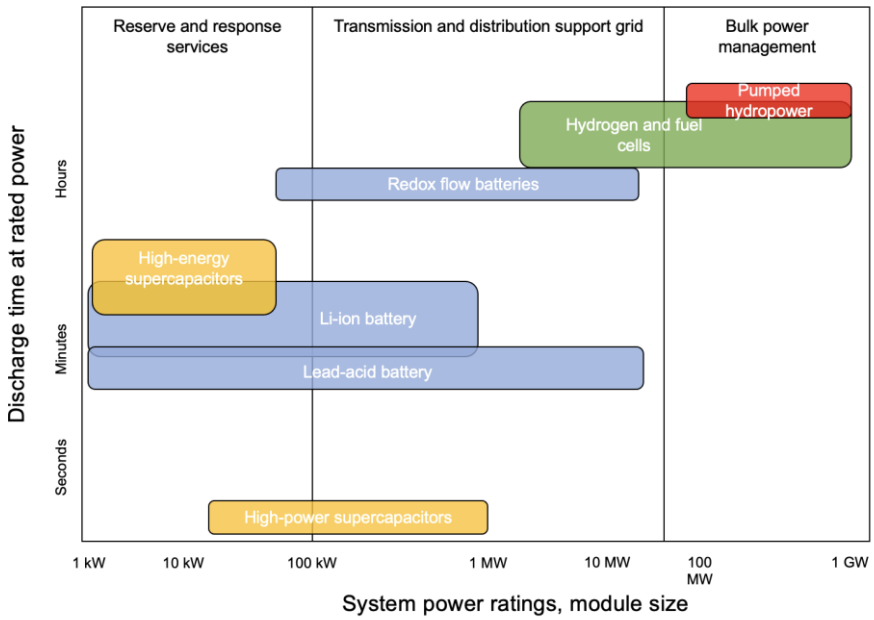


Figure 1.2 - Classification of different types of energy storage in terms of response time, application and system size (adapted from [10]).

Electrochemical energy storage has been attracting tremendous interest and countless investments at the megawatt scale, but much is still to be done. Fundamental aspects are critical like improvements in electrocatalysis, development of new materials and advancements in failure diagnosis tools. But, at the system level, there are other

challenges that require enormous efforts in terms of up-scaling, coupling with auxiliary systems, and integration with already existing storage systems. It is then important to prioritize fabrication techniques and materials that are sustainable and can be used in large scale. The increasing adoption of renewable power sources will completely change the energy market. Mass production of batteries, fuel cells and electrolysers will be needed to immediately replace systems that burn coal or natural gas to produce electricity. The transition towards a decarbonized economy is mandatory and urgent, but it must be done smoothly. Irreversible global warming needs to be avoided but, at the same time, deterioration of human life quality caused by a sudden decrease of available energy or unbearable costs needs to be mitigated. Thus, cooperation between academia and industry is the key to generate valuable *know-how* that will bring new and cleaner energy technologies, while meeting people's needs in terms of economic and social impacts.

1.1. MOTIVATION

The most important challenge of the present and future generations is the development and quick implementation of a sustainable global energy strategy. World population is expected to increase, requiring more industrialization and more energy consumption. Furthermore, most of our current energy needs rely on fossil fuels, which generate enormous CO_2 emissions that are leading us to a global emergency. Thus, the exploitation of new and promising technologies based on alternative and clean energy sources becomes imperative.

At the National and European level, ambitious strategies are being pursued by Portugal and the European Union [11], [12]. Portugal's energy and climate policies to meet carbon neutrality are primarily based on a broad electrification of energy demand and a fast expansion of renewable electricity generation, along with increased energy efficiency. There is a strong focus on reducing energy import dependency and maintaining affordable access to energy. In the longer-term, Portugal will consider hydrogen as the central piece to achieve carbon neutrality.

Renewable electricity (from solar and wind) can be used directly or to produce green hydrogen that can be later used to generate electricity on demand in fuel cells or

hydrogen turbines. Green hydrogen is a high valuable chemical feedstock, and it will play a major role to decarbonize conventional chemical processes like the synthesis of ammonia or methanol. The Portuguese hydrogen strategy aims to mobilise 7 to 9 billion € of investments, of which 85 % from the private sector, by 2030 that would fund the effort to ramp up hydrogen solutions.



Figure 1.3 – The Portuguese and Dutch Governments agreed on a bilateral cooperation in 2020 for the deployment of green hydrogen production, storage and distribution (copyrights: Miguel A. Lopes-Lusa).

Following to the Next Generation EU Recovery Plan that was launched to help repairing immediate economic and social damage caused by the coronavirus pandemic, Portugal has decided to use these extraordinary funds to invest in cutting-edge energy technologies and become one of the front-runners in the European decarbonization strategy. It means that now is the time to develop new *know-how*, intellectual property and businesses in key technologies that are expected to play decisive role in future economies and societies worldwide. Cooperation between industry and universities/research institutes will be decisive because the demand for qualified human resources is already growing exponentially. The EU, and Portugal in particular, need to catch up with the USA and China to keep in their borders highly qualified Europeans and their *know-how*.

1.2. ELECTROCHEMISTRY

The field of electrochemistry, despite its long history with more than 500 years, is becoming increasingly more important in the last decades. The replacement of fossil fuels by renewable energy sources coupled with massive electrification of the energy sector is already generating a big demand for the industrialization of electrochemical systems (batteries, fuel cells and electrolysers). From its definition, electrochemistry is the field of science that concerns to the relationship between electrical potential and chemical reactions. In any electrochemical process, electrons are involved and moved between electrodes through an electron-conducting phase, separated by an ion-conducting and electron-insulating electrolyte. When a chemical reaction is driven by a difference of electrical potential, it is called electrochemical reaction. The electrons (and ions) involved in electrochemical reactions are not transferred through regular molecules like in chemical reactions, but through the phase boundaries between electronic and ionic conduction phases that compose the electrical circuit. Electrochemical reactions are a heterogeneous phenomenon, and they take place at the electrode-electrolyte interface. The interfacial potential is the driving force for charge transfer, and it affects the electrode reaction. The cell potential results from the sum of the interfacial potentials between cathode and anode and it is a fundamental parameter in any electrochemical process or device. The application of an external voltage or the release of chemical energy can trigger changes in oxidation state of atoms, molecules or ions through reduction-oxidation (redox) reactions. Typically, oxidation and reduction take place simultaneously in two electrically-insulated electrodes; oxidation corresponds to the reaction that releases electrons, while reduction is the reaction that consumes electrons.

1.2.1. THERMODYNAMICS

In an electrochemical cell, the maximum electrical work corresponds to the maximum useful work obtained from the overall reaction. The electrical work is related to the maximum cell voltage where the two half reactions are occurring. The reversible (or zero-current) voltage (***E***) is obtained only if the overall reaction velocity is infinitely slow. The cell potential is associated to the change in Gibbs free energy and its theoretical value can be determined through thermodynamics. When reactants and

products are in their standard states at the temperature of the reaction *i.e.*, gases are at 1 atm of absolute pressure and the soluble species at a mean activity of 1, then the free energy corresponds to its standard value ΔG^0 and then the relationship with the standard potential E^0 can be established by Equation 1.1:

$$\Delta G^0 = -nF\,E^0 \tag{1.1}$$

where n is the number of electrons trasnferred in the reaction and F is the Faraday constant (96 485 C mol^{-1}). The standard Gibbs free energy ΔG^0 for a wide list of chemical reactions is available in typical thermodynamic tables. They can also be calculated from the Gibbs-Helmholtz (Equation 1.2) equation using the standard enthalpies ΔH^0 and entropies of formation ΔS^0 for reactants and products involved in the overall reaction at 298 K:

$$\Delta G^0 = \Delta H^0 - T\Delta S^0 \tag{1.2}$$

where T is the absolute temperature and $T\Delta S^0$ corresponds to the heat exchanged in the reaction. The change in Gibbs free energy in the electrode where the reaction is occurring is given by Equation 1.3:

$$\Delta G = \Delta G^0 + RT \cdot \ln(K) = \Delta G^0 + RT \cdot \ln\left(\frac{\prod a_{P_i}^{v_i}}{\prod a_{R_i}^{v_i}}\right) \tag{1.3}$$

where K is the equilibrium constant of the electrode reaction, a is the activity of each redox specie, T is the absolute temperature and R is the universal constant for gases (8.314 J K^{-1} mol^{-1}). Combining Equations 1.1 and 1.3, the Nernst equation (Equation 1.4) is obtained:

$$E = E^0 + \frac{RT_{\text{cell}}}{nF} \cdot \ln\left(\frac{\prod a_{P_i}^{v_i}}{\prod a_{R_i}^{v_i}}\right) \tag{1.4}$$

This relationship allows to calculate the redox potential of a reaction (half-cell or full cell reaction) for different temperatures from its standard potential, number of electrons exchanged in the redox reaction, and chemical activities (often approximated by concentrations or partial pressures) of the redox species. One common example is the dependence of the energy required to split water with temperature at ambient pressure is shown in Figure 1.4. But this dependence is not linear due to the latent heat needed to vaporize water at 100 ºC. At higher temperatures, water is supplied in the form of vapor thus, only sensible heat is exchanged with the exterior. Moreover, the demand for electrical energy is also reduced with temperature, which paired by faster kinetics can make electrolysis operation more efficient.

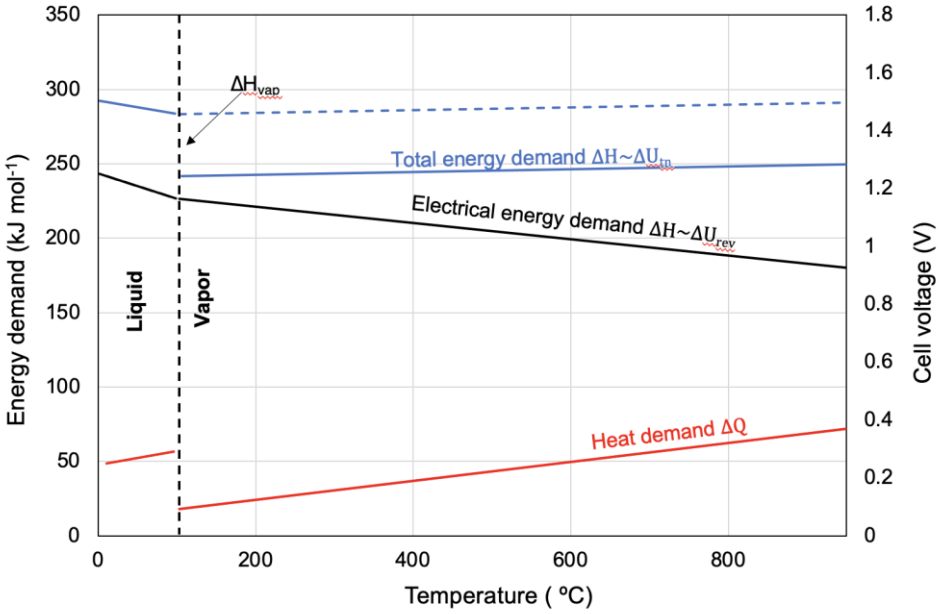


Figure 1.4 - Total (ΔH), thermal ($T\Delta S^0$) and electrical (ΔG) energy demand of an ideal electrolysis process as function of the temperature at ambient pressure.

From the first law of thermodynamics, the overall energy demand, ΔH, of the reaction can be partially supplied by heat, $T\Delta S^0$, and electrical energy, ΔG. The thermoneutral cell voltage, E_{tn}, is given by Equation 1.5 and it refers to the minimum voltage needed to drive electrolysis in an ideal device with heat integration, meaning that the overall energy demand (including heat) is supplied electrically.

$$E_{\mathrm{tn}} = -\frac{\Delta H}{nF} \tag{1.5}$$

The thermoneutral cell potential is approximately 1.48 V (286 kJ mol^{-1}) when water is in liquid state, thus accounting for the latent heat needed to form steam. But the thermoneutral potential is reduced to 1.26 - 1.29 V (243 - 249 kJ mol^{-1}) if water is already in the form of vapor, between 100 - 1000 °C at ambient pressure (Figure 1.4).

1.2.2. ELECTROLYTIC *VS* GALVANIC CELLS

The electrochemical decomposition of a substance through the passage of an external current is called electrolysis, and it corresponds to the conversion of electrical into chemical energy. To operate an electrolytic cell, the potential difference between the two electrodes, or cell voltage (E_{cell}), must exceed the equilibrium or reversible potential E_{r} to work at relevant current densities.

Electrochemical cells in which the electrode reactions take place spontaneously, generating an electric current, are called galvanic cells. Typical examples of galvanic cells that can convert chemical energy into electrical energy include fuel cells or first-generation batteries. If the external resistance between electrodes is increased, the flow of electrical current becomes very small, and the observed cell potential difference becomes the rest potential. Under equilibrium conditions, this corresponds to the reversible cell potential, E_{r}, which can be calculated from the free energy of the overall reaction, and from Nernst equation as a function of the temperature and pressure.

In a galvanic cell, $E_{\mathrm{cell}} < E_{\mathrm{r}}$, and the inequality in Equation 1.6 is maintained for any value of electrical current.

$$\Delta G_{\mathrm{r}} + nFE < 0 \tag{1.6}$$

When the current flow is changed to the reverse direction, an electrolytic process will occur and the potential required to drive the cell needs to be higher than the reversible potential, $E_{\text{cell}} > E_{\text{r}}$, thus ensuring that the inequality in Equation 1.7 is satisfied.

$$\Delta G_{\text{f}} + nFE > 0 \tag{1.7}$$

Regardless of the type of electrochemical cell (electrolytic or galvanic), the electrode at which the negative charge is consumed is called the cathode. Similarly, at the anode of any electrochemical cell negative charge is generated and positive charge is consumed (Figure 1.5).

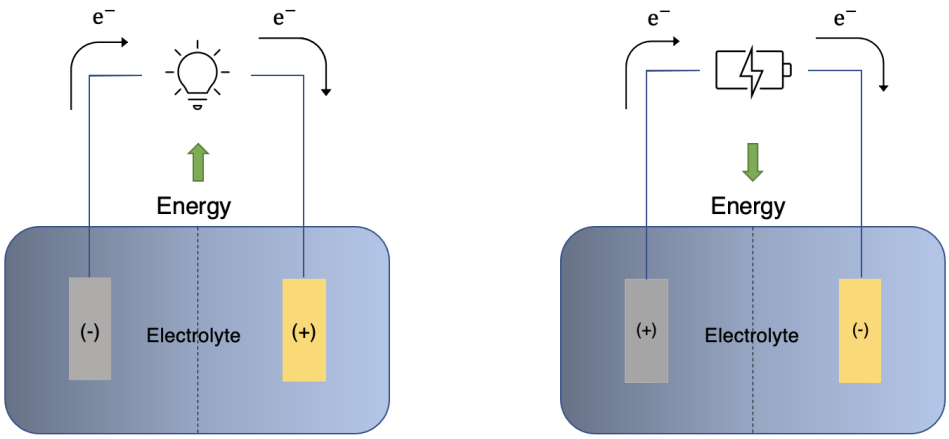


Figure 1.5 - Schematic of two possible configurations of an electrochemical cell: galvanic (left) and electrolytic (right).

Considering the case of water electrolysis, the overall reaction is split in two half-cell reactions that take place at the surface of electrodes, separated by the electrolyte. Each specie has its own intrinsic redox potential, and they are a measure of the tendency of chemical species to exchange (acquire or lose) electrons with an electrode. Redox potential is never an absolute quantification but a difference between two electrodes, in which one of them can just be used as a reference. Among other reference electrodes, the standard hydrogen electrode (SHE) is the reference from which all standard redox potentials are determined, assigned with an arbitrary half-cell potential of 0 V. In

practice, the reversible hydrogen electrode (RHE) is more convenient since it does not depend on the pH in which electrochemical reactions are taking place.

1.2.3. EFFICIENCY

The performance of any electrochemical device (battery, fuel cell or electrolyser) can be evaluated through its electrical efficiency. There are diverse ways to express efficiency depending on the way the system is assessed and compared. In the case of batteries, the current (or faradaic) efficiency is the ratio between the discharge and charge capacities (Equation 1.8). It describes "how efficient" is the electron transfer, accounting side reactions and crossover of unreacted species that typically reduce the battery capacity and imbalance of electrolytes in contact with the two electrodes.

$$\varepsilon_{\mathrm{F}} = \frac{Q_d}{Q_c} = \frac{\int_{t_d}^{t_c} I_d \, dt}{\int_0^{t_c} I_c \, dt} \tag{1.8}$$

The potential (often written as voltage) efficiency is calculated through the ratio between average potential during charge and discharge of the battery, as described in Equation 1.9. In this case, polarization losses are also accounted, because the voltaic efficiency decreases for higher current densities, which are responsible for higher ohmic losses.

$$\varepsilon_{\mathrm{V}} = \frac{\bar{E}_d}{\bar{E}_c} = \frac{\int_{t_d}^{t_c} E_d \, dt}{\int_0^{t_c} E_c \, dt} \tag{1.9}$$

The energy efficiency is calculated from Equation 1.10 and it comes from the product of voltaic and faradaic efficiencies. It is typically related to the overall performance of the battery:

$$\varepsilon_{\mathrm{E}} = \varepsilon_{\mathrm{F}}\varepsilon_{\mathrm{V}} = \frac{\int_{t_d}^{t_c} P_d \, dt}{\int_0^{t_c} P_c \, dt} = \frac{\int_{t_d}^{t_c} E_d \, I_d dt}{\int_0^{t_c} E_c \, I_c dt} \tag{1.10}$$

In the case of water electrolysers, the efficiency can be defined as the useful energy from conversion into chemical energy ($W_{\mathrm{H_2}}$) divided by the required energy for that same conversion W_{el} [6]. These terms, expressed in Equation 1.11, are a function of the hydrogen production rate or a function of the current, potential and time-on-stream:

$$\varepsilon = \frac{W_{\mathrm{H_2}}}{W_{\mathrm{el}}} = \frac{\dot{F}_{\mathrm{H_2}} H}{\Delta G + T\Delta S} = \frac{\dot{F}_{\mathrm{H_2}} H}{\Delta G} = \frac{\dot{F}_{\mathrm{H_2}} H}{nFE} \tag{1.11}$$

where $\dot{F}_{\mathrm{H_2}}$ is the molar rate of produced hydrogen, H is the heating value for hydrogen and E is the working potential. In the case of hydrogen fuel cells, efficiency is defined as a ratio between the electricity produced and hydrogen consumed [13], accordingly to Equation 1.12.

$$\varepsilon = \frac{W_{\mathrm{el}}}{W_{\mathrm{H_2}}} = \frac{\Delta G}{\Delta H} = \frac{nFE}{\dot{F}_{\mathrm{H_2}} H} \tag{1.12}$$

Commonly, instead of hydrogen's higher heating value (HHV), δH_{HHV} – 286 kJ mol^{-1}, the lower heating value (LHV) is used (δH_{LHV} = 241kJ mol^{-1}). The difference between the higher and lower heating value corresponds to the heat of water condensation produced in a fuel cell or to the vaporization of water that is fed to an electrolyser. Because water can be present as liquid or as vapor, both values are correct; however, the type of heating value used to calculate the efficiency must be specified.

1.2.4. POLARIZATION LOSSES

The cell potential required to drive the reaction forward is higher than the theoretical potential as there are potential losses involved in the system, often called as polarization losses, η. In an electrolyser, the cell voltage, E, is the sum of the thermoneutral voltage E_{tn} and the losses caused by ohmic resistance E_{ohm}, charge transfer (or activation) overpotentials E_{act} and mass transport limitations E_{mt}:

$$E_{\mathrm{electrolyser}} = E_{\mathrm{tn}} + E_{\mathrm{ohm}} + E_{\mathrm{act}} + E_{\mathrm{mt}} \tag{1.13}$$

Evidently, in a fuel cell, the resulting voltage comes from the subtraction of the different polarization losses from the thermoneutral voltage (Equation 1.14). During operation, the flow of current causes a deviation from the open circuit potential (OCP) that corresponds to the electrical work done or required to drive the electrochemical process.

$$E_{\mathrm{fuel\ cell}} = E_{\mathrm{tn}} - E_{\mathrm{ohm}} - E_{\mathrm{act}} - E_{\mathrm{mt}} \tag{1.14}$$

In practice, polarization losses relate to several factors like electrode morphology and size, type of membrane, electrolyte composition, cell design, temperature, pressure,

among others. Since electrochemical reactions take place at the interface between electrode and electrolyte, polarization losses are associated to the following steps:

- Diffusion (or mass transport) of reactants from the bulk electrolyte to the interface with the electrode;
- Adsorption of reactants at the electrode surface;
- Electron transfer at the electrode surface;
- Desorption of the products from the electrode surface;
- Diffusion of products from the electrode to the bulk electrolyte.

The kinetic losses, due to limited velocities of electrochemical reactions, represent an important contribution for the deviation of the equilibrium potential and are called activation (or charge transfer) overpotential. It corresponds to the potential difference needed to overcome the activation energy of the cell reactions to start generating a net flow of current. The reaction mechanism can also lead to a barrier for subsequent electron transfer caused by the accumulation of electrons at the electrode surface. For each redox reaction at the electrode, the current density, i, is given by a simplified form of Butler-Volmer equation:

$$i = i_0 \left[\exp\left(\frac{\alpha_a F \eta_{act}}{RT}\right) - \exp\left(-\frac{\alpha_c F \eta_{act}}{RT}\right) \right] \quad (1.15)$$

with i_0 the exchange current density, α_a and α_c the transfer coefficients for the anodic and cathodic reactions, respectively. From Faraday's law, that states that the amount of consumed/produced redox species is proportional to the charge flowing in the cell, slower exchange current density causes slow reaction kinetics. Equation 1.15 is valid when charge transfer dominates de reaction (at low current and low overpotential). The charge transfer coefficient dictates when the electrode reaction is favoured in the anodic or cathodic direction at a certain applied potential. At high activation overpotential, η_{act}, typically above 100 mV, both positive or negative, one of the two terms in the Equation 1.15 is negligible and the equation is simplified:

$$i = i_0 \, exp\left(-\frac{\alpha_a F \eta_{act}}{RT}\right) \quad (1.16)$$

For convenience it is possible to rearrange Equation 1.16 in another form:

$$\eta_{\text{act}} = \beta \log\left(\frac{i}{i_0}\right) \tag{1.17}$$

The exponential relation between current and activation overpotential is called Tafel equation. The term is the Tafel slope, which shows how the overpotential changes in function of the logarithm of the current density expressed in volts (Figure 1.6).

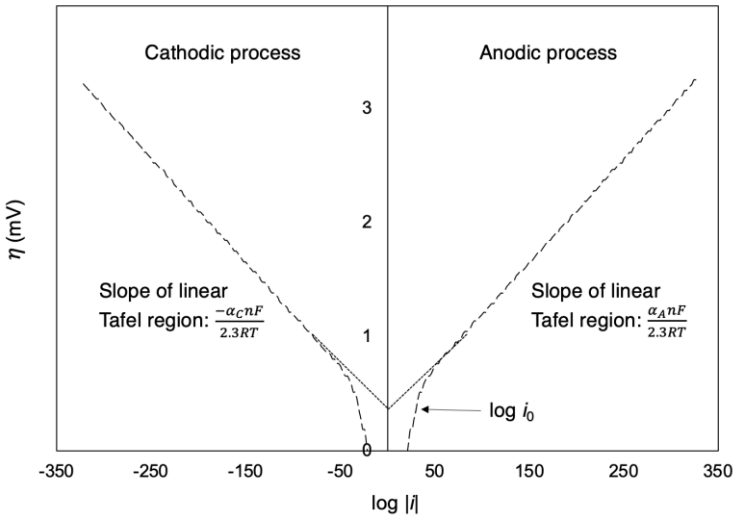


Figure 1.6 - General example of a Tafel plot.

Mass diffusion limitations are another important type of polarization losses. They are caused by gradient concentration of reactants and products between the electrode surface and bulk electrolyte. At high current densities, with the active sites "working" at maximum velocity, diffusion rates become dominant and reactant depletion at the active sites lead to logarithmic losses for increasing current densities. Mass transport in an electrochemical cell is described by Nernst-Planck equation [14], which accounts for three possible contributions: diffusion, migration and convection. In practice, for diffusion-controlled processes the concentration of reactants decreases for higher currents:

$$i = \frac{nFD}{\delta}(c_b - c_i) \tag{1.18}$$

At high current density, the reactants are converted at the electrode surface, dropping the concentration at the interface, c_i, to zero. Such current density reaches then its maximum and can be calculated by simplifying Equation 1.18:

$$i_{lim} = \frac{nFD}{\delta} c_b \tag{1.19}$$

D is the diffusion coefficient of the reagents, c_b is the bulk concentration of the reagents and δ is the diffusion layer thickness. The concentration of the reactant as a function of the current density, i, can be obtained:

$$c = \frac{i_{\text{lim}} - i}{i_{\text{lim}}} c_b \tag{1.20}$$

When migration of ionic species can be considered negligible, the resulting mass transport overpotential, η_{mt}, can be obtained from:

$$\eta_{\text{mt}} = E - E^0 = \frac{RT}{nF} \ln\left(\frac{c_i}{c_b}\right) \tag{1.21}$$

Combining the two equations, η_{mt} can be also obtained as a function of the current density, i:

$$\eta_{\text{mt}} = \frac{RT}{nF} \ln\left(1 - \frac{i}{i_{\text{lim}}}\right) \tag{1.22}$$

The last type of polarization losses that play an important role in the performance of an electrochemical cell are ohmic losses caused by the membrane and electrical contacts. They are caused by the conduction of electrical charges (electrons and ions), causing a linear loss of efficiency as a function of the current density. In this case ohmic overpotential is also expressed in volts and is calculated from Ohm's law:

$$\eta_{\text{ohm}} = i(R_{\text{electrodes}} + R_{\text{plates}} + R_{\text{electrolyte}} + R_{\text{membrane}}) \tag{1.23}$$

The resistance assigned to both membrane and electrolyte, $R_{\text{electrolyte/membrane}}$, is expressed in ohms and can be calculated from Equation 1.24 [15]:

$$R_{\text{electrolyte/membrane}} = \frac{L_{\text{electrolyte/membrane}}}{\kappa_{\text{electrolyte/membrane}} \cdot A_{\text{electrode}}} \tag{1.24}$$

where L is the length between the two electrodes or membrane thickness, A is the active area of the electrodes and κ is the specific conductivity of membrane or supporting electrolyte.

1.2.5. ELECTROCHEMICAL CHARACTERIZATION METHODS

Electrochemical methods are of upmost importance to operate or to develop electrochemical technologies from the cell to stack level. The most used ones include cyclic/linear voltammetry, chronoamperometry and chronopotentiometry. These can be carried out in different set-ups, like single cell or stack - two electrodes configuration - or through half-cell connected to external reference electrodes like rotating disk electrode (RDE) or rotating ring disk electrode - three electrodes configuration. Depending on the type of electrochemical technology (battery *vs* fuel cell/electrolyser), the most relevant type of measurement to showcase their performance is different.

Charge/discharge cycling provides information about a battery in terms of power density, efficiency and capacity. Typically, the potential is recorded as a function of time at constant current density. In fact, Figure 1.7 consists of several chronopotentiometries at symmetric values of current density depending on if the battery is charging or discharging.

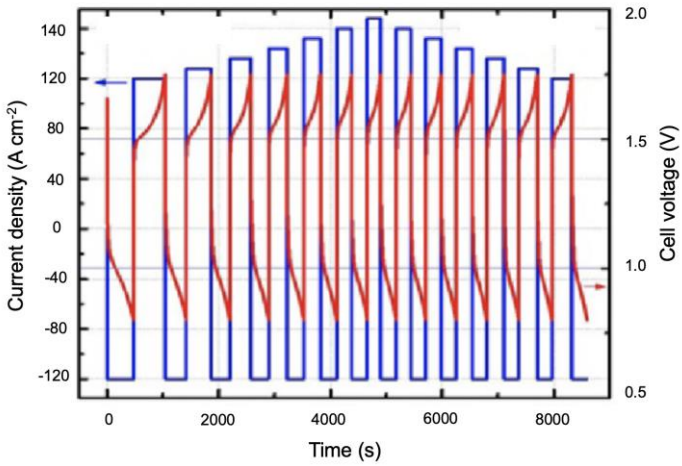


Figure 1.7 - Typical profile of charge/discharge battery cycling. Current density is defined for both charge and discharged and the voltage is recorded over time.

In the case of an electrolyser or fuel cell, the most important electrochemical measurement to express their performance is the polarization curve (also known as *i-V*

curve), which is shown for the two systems in Figure 1.8. In this case, the cell potential is plotted against the current density and the shape of the curve depends on the magnitude of each type of overpotential that was discussed in Section 1.2.4.

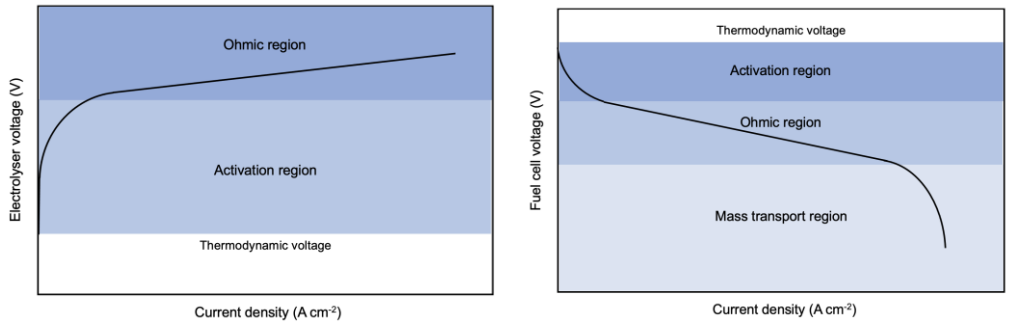


Figure 1.8 – Typical shape of polarization curve of an electrolyser (left) and a fuel cell (right). The voltage is plotted as function of the current density with the respective type of voltage losses.

Electrochemical impedance spectroscopy is a technique of major importance for the study of materials and electrochemical processes and one example of a spectrum recorded from a fuel cell is shown in Figure 1.9. Impedance, represented by the symbol *Z*, is a measure of the opposition to electrical flow. It is measured in ohms. In principle, each property or external parameter that has an influence on the electrical conductivity of an electrochemical system can be studied by measurement of the impedance. The measured data can provide information for a pure phase, such as electrical conductivity, dielectric constant, or mobility of equilibrium concentration of charge carriers. In addition, parameters related to interfacial properties of a system can be studied: heterogeneous electron-transfer constants between ion and electron conductors, or capacity of the electrical double layer. Very relevant for fitting equivalent circuits to experimental data, the constant phase element (CPE) is a capacitive element with a frequency-independent negative phase between current and voltage which interpolates between a capacitor and a resistor.

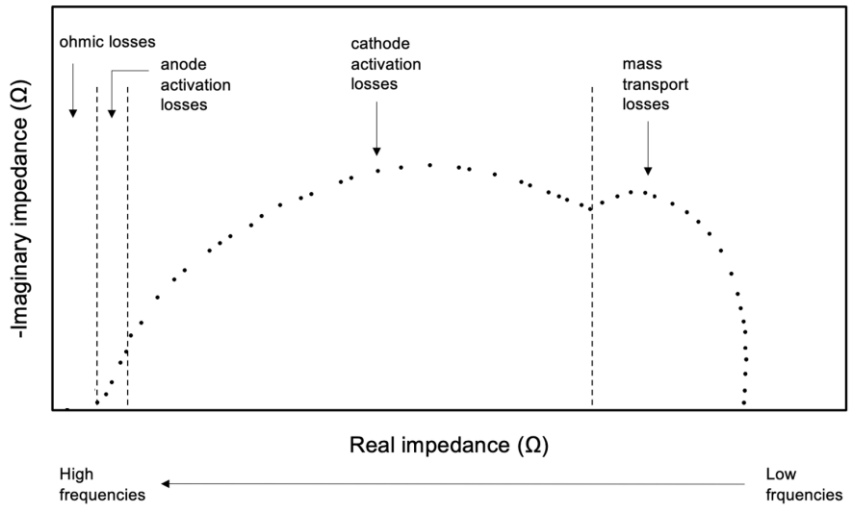


Figure 1.9 – Typical impedance spectrum (Nyquist plot) of a fuel cell recorded at constant current density with a small AC perturbation. Different types of polarization losses are identified as a function of the frequency.

Electrochemical studies using three-electrodes configurations (*i.e.* RDE) are crucial to develop and pre-screen components for electrochemical technologies, like electrocatalyst, electrodes, electrolytes and redox chemistries. The three most important reasons are:

- ability to precisely control mass diffusion because it is important to exclude this contribution when measuring electrochemical surface area (ECSA) and kinetic parameters of an electrocatalyst (Figure 1.10);
- the use of a reference electrode allows to carry out half-cell measurements, thus avoiding interference from a second electrode;
- use of very low quantities of material which allows to screen several formulations before up-scaling synthesis methods.

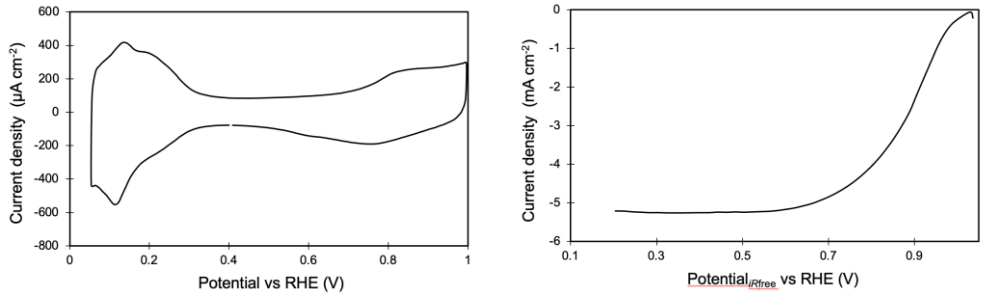


Figure 1.10 - RDE electrochemical measurements: cyclic voltammetry (left) and linear sweep voltammetry (right).

1.3. HYDROGEN ENERGY STORAGE

Hydrogen like electricity, is a carbon-free energy carrier. These two energy carriers are expected to become the future of a sustainable energy system. Renewable energy resources are unevenly distributed over the world. There is then the need for an energy carrier that can be cost-efficiently transported and stored to deliver renewable energy from good remote resource areas, at the right time and place to the energy demand. Next to this systemic role, hydrogen is emerging to decarbonize the energy use in hard to abate sectors in industry, mobility, electricity balancing and heating. Green hydrogen, produced by water electrolysis systems with the surplus electricity from renewables, is expected to replace fossil electricity generation currently used to compensate load fluctuations in electrical grids and to serve as a valuable chemical stock in industries of steel, ammonia, petrochemistry, etc. Figure 1.11 showcases the evolution of fuels used in the energy sector since the Industrial Revolution in which coal was the main source of energy that was then being replaced by liquid fuels. Today, to achieve full decarbonization, natural gas is seen as a less-pollutant transition fuel that will be also being replaced by hydrogen.

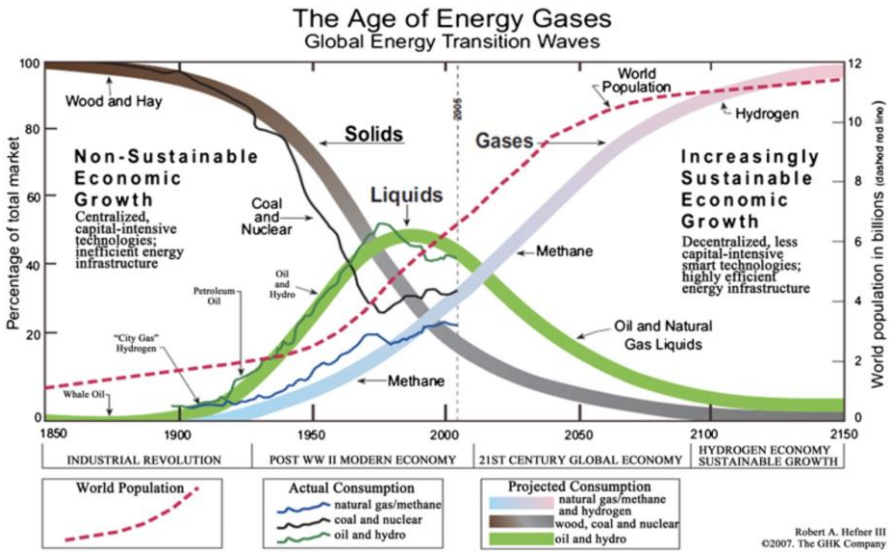


Figure 1.11 - World's primary energy generation sources and global population in the past two Centuries (extracted from [16]).

Hydrogen distribution and storage infrastructures are still very scarce. Initially, hydrogen will be blended with natural gas in current gas distribution systems to serve as an initial market of the first hydrogen production plants. In the future, adaptions to the gas infrastructure will be done without major changes while both production and demand constantly increase with the phasing-out of fossil fuels. Nowadays, hydrogen is already shipped and commercialised in any place in the world. This trend will dramatically increase in the coming decades and many other hydrogen carriers will be developed depending on the application. There are many forms of storing and transporting hydrogen such as pressurized hydrogen, liquid hydrogen carriers (methanol, ammonia, etc.) or in the form of metal hydrides. Figure 1.12 displays a simplified scheme on the future energy scenario when hydrogen gets massively adopted. Apart from continuing being used as a chemical feedstock, hydrogen can also be used in combustion or turbines to produce heat, electricity, or mechanical power. Anyway, electrochemical conversion of hydrogen into electricity and heat will be done mostly in fuel cells, which are expected to become mainstream in applications for industrial, residential and transport sectors.

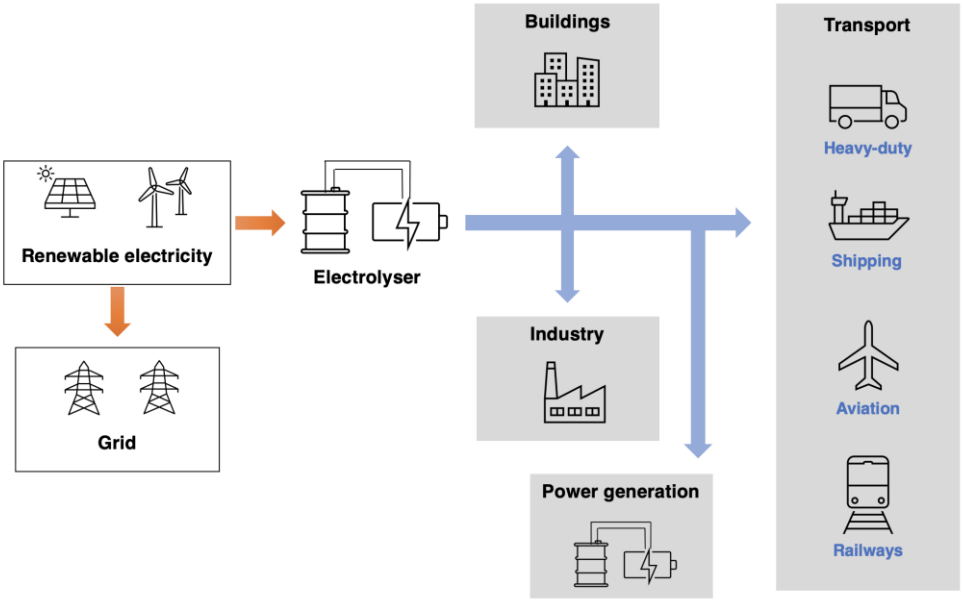


Figure 1.12 - Schematic of the future hydrogen economy scenario.

1.3.1. FUEL CELLS

Early in the 20th century, the conversion of chemical energy into electrical energy became more important due to widespread electrification of industrial and residential sectors. Electrical energy conversion systems were firstly introduced as small, decentralized power generators but they soon start being upscaled to megawatt-range powerplants. But increasing environmental concerns with the use of fossil fuels, used to produce electricity and heat or to fuel the transport sector, have led to the increasing interest on fuel cells. They can help decreasing greenhouse emissions due to higher electrical efficiency compared to combustion engines [17]. When fed with pure hydrogen, water is the only product (apart from electricity and some heat) thus fuel cells can be zero-emissions power generators. The increasing adoption of renewable sources to produce electricity requires energy storage solutions to balance electricity grids since solar or wind technologies are non-dispatchable energy sources. The combination of production of green hydrogen with fuel cells is one of the most promising solutions to compensate the grid during off-peak periods. There are different types of fuel cells that share many similarities but also many differences as show in Table 1.1.

Table 1.1 - Types of fuel cell technologies and main differences in terms of components, operation and application.

	PEMFC	AFC	PAFC	MCFC	SOFC
Electrolyte	Polymer membrane	Potassium hydroxide	Phosphoric acid	Molten mixture	Ceramic membrane
Catalyst	Platinum	Nickel	Platinum	Nickel	Perovskites
Temperature	50 – 90 ºC	50 – 90 ºC	160 -220 ºC	*ca.* 650 ºC	800 - 1000 ºC
Applications	Portable, transport and small-scale stationary	Portable and small-scale stationary	Stationary	Stationary	Stationary

Fuel cells are typically classified by the electrolyte that they use. A second classification can be done based on the operation temperature of each fuel cell. High-temperature fuel cells (800 - 1000 ºC), also known as solid oxide fuel cells (SOFC), are being developed to be used in stationary applications. But the possible use of abundant and low-cost materials that have good ionic conductivity (electrolyte) and high electrochemical activity/stability (electrodes) at high temperature make them attractive for centralized applications if coupled with processes that produce heat in abundance. Low-temperature fuel cells are expected to play an important role both on stationary and mobile applications. Phosphoric acid fuel cells (PAFC) typically operate between 160 - 220 ºC and are especially suited to be used in stationary applications due to their higher CO tolerance and easier water management [18]. But proton exchange membrane fuel cells (PEMFCs) will be the choice for the transport sector due to the lower operation temperature, high power density and ability to withstand cold-starts. Direct methanol fuel cells (DMFCs) are also an interesting alternative to PEMFCs due to the higher volumetric energy density of methanol (liquid at atmospheric conditions) compared to hydrogen. However, the reaction kinetics of methanol oxidation is slower than hydrogen oxidation, requiring development of better electrocatalysts. Methanol crossover through the membrane also needs to be decreased without using very thick membranes that generate more ohmic losses related to ion-conduction between the electrodes.

1.3.2. PROTON EXCHANGE MEMBRANE FUEL CELLS

PEM fuel cells are electrochemical systems that are manufactured as a stack of identical repeating cells comprising a membrane electrodes assembly (MEA) and gas diffusion layers (GDLs), all compressed by bipolar plates (BPs) used to feed reactants, remove products, and harvest electrical current. The proton exchange membrane requires hydration to transport protons, thus PEMFCs typically operate between 80 - 100 ºC at pressures slightly above ambient pressure at the electrodes [19]. As shown in Figure 1.13, power generation results from the combination of a fuel (hydrogen) and an oxidant (oxygen) which are electrochemically oxidised and reduced, respectively in two compartments between an electronic insulating separator (membrane).

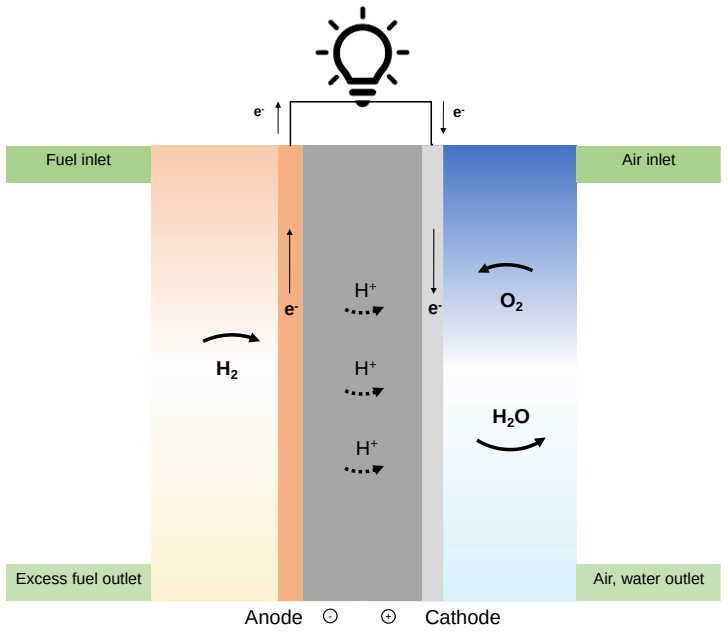


Figure 1.13 - Basic operation principles of a PEM fuel cell including the main reactants and products as well as flow paths of protons and electrons.

Unlike common batteries, PEMFCs are systems with power decoupled from capacity allowing higher gravimetric power density and fast refuelling time, making them especially suited for heavy-weight transportation like trucks, buses, ships, trains or airplanes [20]. The only persisting technical barrier for the widespread

commercialization of PEMFCs for transport applications is the insufficient durability of up-to-date cathodic electrocatalysts, namely from carbon nanoparticles used as support [21]. Due to their unmatched catalytic activity for the hydrogen oxidation reaction (HOR) and oxygen reduction reaction (ORR), platinum-based catalysts are used in both cathode and anode. Much has been done in recent years to dramatically reduce the precious metal loadings while ensuring high performances, namely by dispersing them in high surface area supports with highly electronic conductivity [22].

Electrochemical reactions take place at the thin layers of electrocatalyst particles surrounded by ionomer that compose a typical electrode. Their combination with the membrane (and GDLs) consists in the core component of the fuel cell, the MEA. PEMFC catalysts are based on Pt (in the form of nanoparticles dispersed on carbon black supports), contributing to the current high system cost. Apart from the support, carbon is the main component of bipolar plates and GDLs. High electron and heat conductivities coupled with high mechanical and chemical resistances are important properties that need to be ensured in these cell components. Hydrophobic behaviour is another property typically needed from GDLs. Their porosity and surface chemistry enhances water removal from the active sites, which could cause flooding effects that affect fuel cell performance operating at high current densities [23].

The current targets set by the US DOE for electrocatalysts in automotive PEMFCs aim for a total PGM loading of 0.125 mg cm^{-2}. With such loading, MEAs can deliver stack power densities of 8.0 $kW g^{-1}_{Pt}$ [24]. It means a total of 8 g of precious metal per vehicle, which is similar to the loading used in exhausts of internal combustion engines. System integration requires MEAs that produce at least 0.6 V at 1.5 - 2 A cm^{-2} owing to radiator size and related cooling constraints. But under automotive conditions, electrocatalysts must survive hundreds of thousands of load cycles and tens of thousands of start-up and shut-down events over the 5000-hour lifetime of the stack [24]. Serious degradation is associated with the tendency for the cathode to reach potentials above the onset of oxidation of carbon in contact with Pt, during even the short times when hydrogen/air waves move through the flow fields during start-up or shut-down [25]. Some of the countermeasures being developed are using more stable graphitized carbon, using

catalyst supports that will not electrochemically corrode, and adding oxygen evolution catalysts to the mix to clamp the potentials at the start of water oxidation [26], [27].

1.3.3. PEMFC COMPONENTS

The combination of electrodes and membrane is the core component of the PEM fuel cell, the MEA. A catalyst coated membrane (CCM) consists in a 3-layer MEA in which the electrodes are deposited on the two sides of the membrane. It is also possible to deposit the electrode in the GDL - gas diffusion electrode (GDE). In the case of using GDEs, they are typically hot-pressed against the membrane to reduce interfacial contact resistances. Figure 1.14 also includes the other components needed to assemble a single cell like sealing gaskets, graphite plates with flow field channel, current collectors and end plates. In a fuel cell system, several single cells are assembled and electrically connected in series.

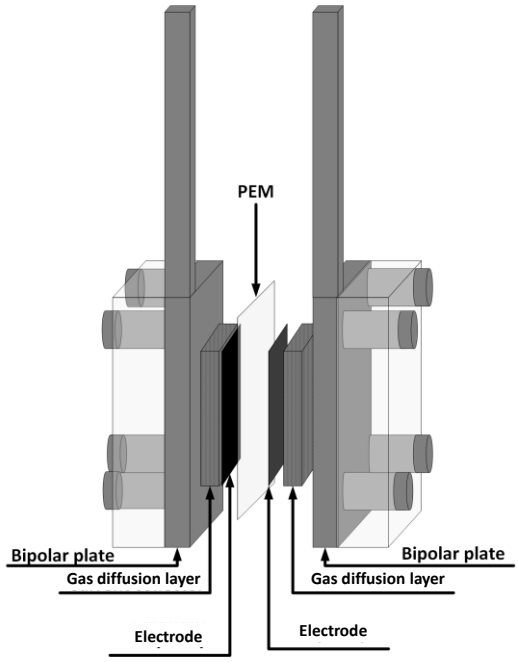


Figure 1.14 - Typical components of a PEMFC.

State-of-the-art proton exchange membranes are made of perfluorosulfonic acid (PFSA), and these have been produced by Dupont, Gore, Dow and 3M, among others. PFSA membranes gather most of the important properties needed to work as a thin solid electrolyte for PEM devices: they display high protonic conductivity, and high mechanical and electrochemical stability [30].

The polymer has three distinct regions in its molecular structure:

- Polytetrafluoroethylene (PTFE) acting as a backbone structure (hydrophobic region);
- Ether-linked side chains of varying length and flexibility that connect the PTFE backbone to the acidic functional groups;
- Sulphonic acid groups (hydrophilic region).

A schematic of the PFSA molecular structure is presented in Figure 1.15.

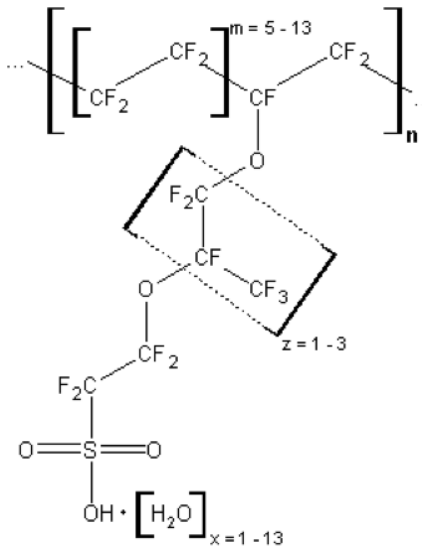


Figure 1.15 - Molecular structure of PFSA.

Upon hydration of the membrane, protons from the sulfonic acid group become mobile as hydronium ions, allowing their movement between the sulfonic acid sites (vehicular mechanism). In parallel, proton conduction through PFSA membranes can also take place by proton hoping (or Grotthuss mechanism) [28]. Mobility of protons under good

humidification conditions translates to a very low voltage drop due to ohmic resistance, approximately 20 mV at 1 A cm^{-2} [29]. PFSA membranes of several thicknesses are available in the market, and they can be chosen depending on the type of application. Thinner membranes display lower ohmic drop but they have a poorer mechanical stability and higher gas crossover than thicker ones.

The development of electrocatalysts and their deposition method are the main current challenges to fabricate high performance MEAs. In general, electrodes are very thin and porous layers of small particles often called as catalyst layers. The ideal catalyst layer should provide high catalyst utilization, high durability, high electronic conductivity and enhanced mass transport capability [30]. The use of precious metals as catalysts brings the need to decrease their loading without harming the electrochemical performance. Great advances have been done in the past years in the development of novel catalytic structures and deposition techniques to maximize the number of triple phase boundaries [31]. Figure 1.16 illustrates the triple-phase boundary concept in which a catalytic particle is only electrochemically active if three conditions are ensured: open diffusion pathways, electrical conduction and ionic conduction. To extend ionic conduction away from the membrane, an ionomer is dispersed through the catalyst layer. This is a solubilized form of the membrane that extends proton conduction paths into the porous structure of the electrode, connecting ionically more electrocatalyst sites to the membrane.

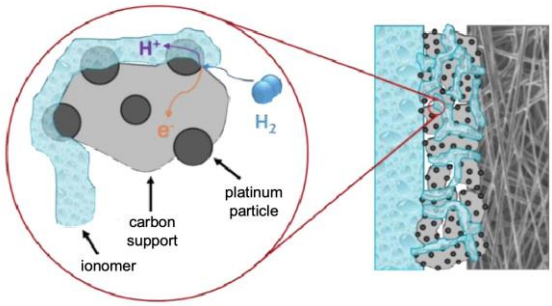


Figure 1.16 - Illustration of the triple phase boundary system including the carbon support, platinum particles and ionomer and their location in a MEA cross-section (adapted from [32]).

Bipolar plates and gas diffusion layers are the other important components. Generally, graphite is used to produce the bipolar plates as this material is lightweight, electronic conductive, and displays minimal corrosion in the fuel cell environment. Graphite plates can become an expensive component because they are difficult to machine. An alternative to graphite is to use stainless steel; titanium has also been used due to its unmatched corrosion resistance [33]. Carbon is also the main component of typical GDLs. Different structures using carbon fibers are available in the market like cloth, felt and paper. Different surface properties are also possible that impact on the hydrophobic behaviour, electronic conductivity and mass transport of reactants/products [5].

1.3.4. PROTON EXCHANGE MEMBRANE ELECTROLYSERS

Intermittency and fluctuation of renewable energy sources remain major issues for an efficient utilization, while the power flow and utility frequency of the grid need to be steadily regulated and balanced. Hydrogen can be produced through water electrolysis using the surplus from renewables when available and stored as a carbon neutral energy carrier. Among other types, PEM electrolysis is a promising technology for coupling renewables with hydrogen due to ability to operate with dynamic loads thanks to fast response times [6], [13], [34]. In particular, the compact system design, easy maintenance, low gas crossover are advantageous features comparing to the mature alkaline electrolysis technology [6], [35], [36]. PEM electrolysers use a dense membrane that allows a very fast protonic conduction between the negative and positive electrode. Figure 1.17 shows the generation of protons and electrons from water that lead to the evolution of oxygen (OER) at the anode, while hydrogen is evolved at the cathode (HER).

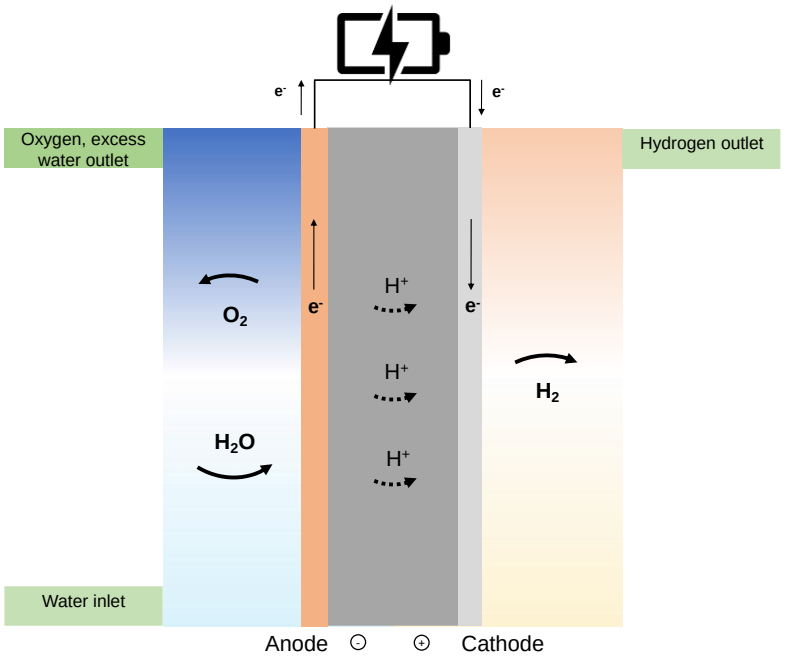


Figure 1.17 - Basic operation principles of a PEM electrolyser including the main reactants and products as well as flow paths of protons and electrons.

Due to the acidic behaviour of PEMs, transition metals like Ni, Fe or Co display an immediate loss of activity caused by the highly oxidative and corrosive conditions. Instead, both sides of the membrane are coated with a thin layer of material containing precious metal catalysts (Pt, Pd, Ir and Ru are the most common examples) [37]. PEM electrolysis capital costs are higher than alkaline electrolysis thanks to the use of precious metals as catalysts and corrosion resistant materials (typically Ti-based) in the anode bipolar plate and porous transport layer (PTL) [38], [39]. But, PEM electrolysers can operate at higher current density (> 2 A cm^{-2}), compared to alkaline electrolysis (*ca.* 300 mA cm^{-2}), and have a significant potential for cost reduction owing to the more compact system design [6].

Despite the market for PEM electrolysers is gaining traction they are not still at the same technology readiness level (TRL) of PEM fuel cells. More demanding needs at the anode require materials that are stable under harsh conditions like acidic environment and high electrode potential, where the carbon-based components are not stable. Many

alternatives have been proposed, but most of them rely on using platinum group metals (PGMs) as electrocatalysts and Ti-based bipolar plates and current collectors [29]. The development of highly active and stable components that are low-cost and scalable is still on-going.

As for fuel cells, the MEA is also the core component of a PEM electrolyser. Typically, carbon supported platinum or palladium nanoparticles are used in the cathode side due to their remarkable HER activity and stability in acidic medium [15,16]. But, the OER governs the efficiency of water electrolysis, as most of the potential losses are related to the anodic electrochemical processes. The most active material for OER in acidic medium is ruthenium oxide; however, it exhibits very poor stability due to the formation of gaseous RuO_4/soluble RuO_4^- during OER [40], [41]. Iridium oxides are considered as the state-of-the-art catalysts as they possess the best trade-off between electrochemical activity and stability [42], [43]. Unfortunately, current iridium price of *ca.* 150 € g^{-1} (price in January 2022) is roughly 5 times higher than that of Pt. This is related to iridium scarcity (less than 10 tonnes produced per year) and it will become a bottleneck in the development and commercialization of PEM electrolysers if their Ir loading is not substantially lowered or a replacement is not found [44].

To achieve higher gravimetric specific activity, smaller particles of iridium have been stabilized by supporting them on corrosion resistant ceramic particles like titanium or tin oxides [45]. The harsh anode environment causes fast corrosion of carbon-based materials, making unpractical their use as electrocatalyst supports which have been already developed for PEM fuel cells. Nonetheless, compared to carbon, metal oxides typically have lower surface area and inferior electric conduction. A compensation in terms of electronic conductivity can be made by adding dopants like antimony, indium or fluorine.

In theory, electrolyser performance would be increased by increasing the catalyst loading, especially on the anode. In some extent it is true, however there is an optimum catalyst loading in terms of overpotentials. Above the optimum catalyst loading, ionic transport losses in the catalyst layer become dominant [46]; a catalytic particle is only electrochemically active if three conditions are ensured: free pathways for

reactants/products diffusion, electrical conduction, and ionic conduction. Like for fuel cells, to extend ionic conduction away from the membrane, a solubilized form of the membrane is dispersed through the catalyst layer, called ionomer.

In PEM electrolysers, cathode and anode have different demands for bipolar plates, transport layers and electrodes. At the cathode, local potentials are close to zero (*vs* RHE), thus it is possible to use carbon-based materials widely used in PEM fuel cells. But the anode corrosive environment makes carbon undergoing fast electrochemical oxidation. Steel is also not stable, so porous titanium structures typically used to withstand long-term electrical conductivity. The main drawbacks of these materials are the formation of oxide insulating layers and their high cost [47].

Titanium is the main component used in bipolar plates and diffusion layers for anode. A coating with platinum is used to increase electrical conductivity [48]. Considering the cost breakdown for PEM electrolysis system and stack (Figure 1.18), it becomes clear that the latter accounts for most of the system cost shares, with plates and transport layers requiring more than half of the stack cost.

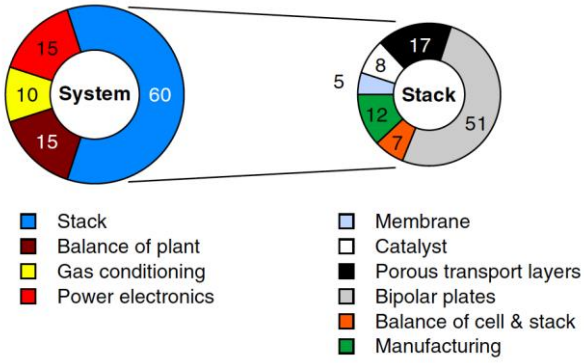


Figure 1.18 - System and stack cost breakdown of PEM electrolysis (adapted from [49]).

1.4. REDOX FLOW BATTERIES

In an energy scenario where renewables will play a dominant role, energy management becomes a central part of the decarbonization strategy. When the demand for renewable electricity is different from its production, energy management requires energy storage systems different from conventional power plants. To mitigate the instability and poor reliability caused by renewable energy sources, traditional grids will be replaced by

smart grids that will allow to integrate the behaviour and actions of electricity generators, consumers and those that are both at the same time. Smart grids consist in intelligent infrastructures that will ensure economic efficiency, sustainable power systems with less energy losses and that are more reliable and safer [50]. Energy storage systems are an essential piece for these new electricity networks and a wide portfolio of technologies will be needed depending on their efficiency, power density, response time and cost [2]. Any battery used to balance electricity grids must be reliable and its performance must be predictable to deliver electricity on demand and to store it efficiently during peak production periods.

A redox flow battery (RFB) is an electrochemical storage device in which two separate liquid electrolytes containing redox active species flow through two half-cell separated by a membrane. Figure 1.19 shows the redox couples circulating in each electrode set a potential difference that can be directly related to the battery state-of-charge (SoC). The two half-cells are typically separated by an ion-exchange membrane (either cationic or anionic) that electrically insulates both electrodes and is responsible to transport ionic species involved in each electrochemical reaction. The positive and negative electrolyte are stored in external tanks and are pumped into each half-cell. The electrodes of a RFB are usually inert, serving as the site for redox reactions of the active species which remain soluble in the electrolyte [51]. Individual RFB cells are connected in series to form stacks to generate voltages suitable for application. The stack together with the tanks of the electrolyte and the balance of plant constitute a RFB system (Figure 1.19). The electricity is stored by means of an electron exchange involving oxidation of the active species at the negative electrode and reduction of the active species in the positive electrode. The electrolytes and thus the energy may be transported and stored externally, in tanks.

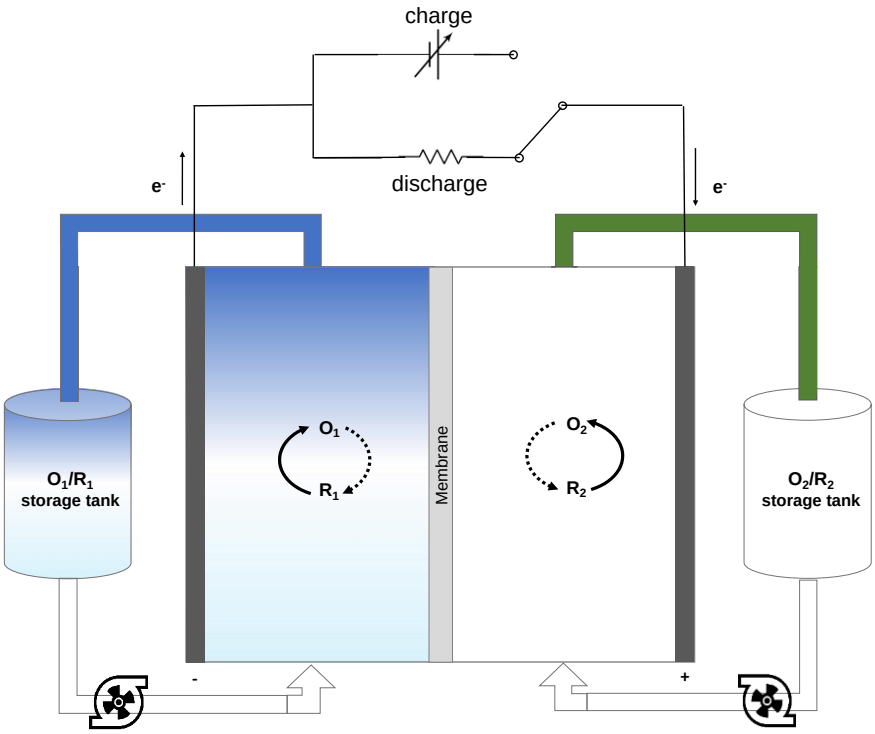


Figure 1.19 - Schematic of a RFB components and design.

While the energy storage capacity of redox flow batteries is, in principle, easily scalable, current systems still exhibit low energy and power densities and, thus, require large systems in terms of weight and volume. Known RFBs are found in or designed for stationary applications rather than on portable or mobile applications. Several redox species have been investigated in the last decades to be used in RFBs. Some of the popular chemistries for RFBs are vanadium-vanadium, iron-chromium, zinc-bromine, zinc-iron, and hydrogen-bromine. Among these chemistries, the all-vanadium redox flow battery (VRFB) has the unique advantage of the flexibility provided by using the same element in both electrodes.

VRFBs are especially suited for medium to large scale electricity storage due to their low-cost, easy scalability, longevity, high round-trip efficiency, stable capacity and safety [52]. Initial developments were led by the group of M. Skyllas-Kazacos at the University of New South Wales in Australia since 1985 [53], [54]. Despite considerable advances achieved in the last decades, the deployment of VRFBs still requires improvement in stack power density to decrease the cost per kW of power output. The

main on-going challenges are related to increasing electrode activity, reducing cell resistance, improving membrane selectivity and ionic conductivity [51].

The VRFB is an electrochemical cell that converts electrical energy into chemical energy during charge, and chemical energy into electrical energy during discharge. Both modes consist on single-electron redox processes: V(II)/V(III) at the negative electrode and V(IV)/V(V) at the positive electrode. The electrochemical reactions during the charging or discharging in each half cell occur as follows in Table 1.2.

Table 1.2 - Half-cell and combined reactions and redox potentials for VRFBs.

Positive	$VO^{2+} + H_2O \rightleftharpoons VO_2^+ + 2H^+ + 2e^-$	$E^0 = 1.00\ V$ vs RHE	(1.25)
Negative	$V^{3+} + e^- \rightleftharpoons V^{2+}$	$E^0 = -0.26\ V$ vs RHE	(1.26)
Combined	$V^{3+} + VO^{2+} + H_2O \rightleftharpoons V^{2+} + VO_2^+ + 2H^+$	$E^0_{cell} = 1.26\ V$	(1.27)

Charging mode considers the direct reaction direction while the inverse direction corresponds to the discharge. To enable oxidation and reduction of vanadium ions in aqueous media, protons are formed or consumed depending on the electrode and operation mode. There is then competition with parasitic hydrogen or oxygen evolution reactions that can decrease the faradaic efficiency of the VRFB.

The main drawbacks of a VRFB are the limited energy density of electrolytes containing divalent/trivalent vanadium, and the slow rate of reactions. In addition, the electrolyte solution of VRBs usually comprises important amounts of acid, requiring appropriate safety and environmental measures. Like for other chemistries, the VRFB requires unique materials with special design and electrical properties. The major parameters that govern performance of VRFB are electrode materials, their pre-treatment and compression in the assembly. The addition of electrolyte additives, operating temperature, flow field design, and membrane characteristics are other important parameters that need to be considered [55]. These improvements need to be aided by numerous physical, electrochemical and chemical characterisation techniques, which are mostly done *ex-situ*. However, *ex-situ* characterization is often unpractical, requiring cell disassembly and proper handling of the materials. Even more important is to provide in-depth insights on changes of the cell during normal operation. Thus, *in-situ* diagnostic

tools are essential to provide information related to the cell design, materials and operation parameters.

1.5. OBJECTIVES AND OUTLINE OF THIS WORK

In recent decades, research in the field of electrochemistry has become crucial since these technologies are expected to play key roles in the energy transition that is already on the way. Fuel cells and electrolysers are expected to balance the intermittency of renewable energy sources in sectors in which common batteries have important drawbacks. Nevertheless, the combination of these technologies (hydrogen and batteries) will be needed to avoid the use of fossil fuels for power generation, while being considerably safer and more environmentally friendly than nuclear power generation. To achieve industrialization readiness there is the need to develop high performance stack components that are cheaper and more abundant. The continuous replacement of precious metals and hazard substances in systems is then of paramount importance for the market implementation of these technologies. This thesis aims then to contribute with cost-competitive and easy-scalable manufacturing of components and to demonstrate an interplay between the need for new materials and new characterization tools that share similarities and that will help leveraging different technologies in parallel.

Chapter 1 introduces the different storage technologies that are addressed in this thesis, namely electrolytic hydrogen or redox flow batteries, and that are promising to couple with the production of renewable electricity (*i.e.* wind, solar and geothermal). An overview on the materials and characterization techniques is provided as well as the main advantages and disadvantages of each type of electrolyser, fuel cell or redox flow battery depending on the energy sector and application.

Chapter 2 describes the first work carried out during this thesis in which a fabrication route of MEA for PEM electrolysers was studied and developed. This includes the use of screen printing of electrocatalytic and ionomer materials directly on a proton exchange membrane followed by morphological and electrochemical analyses. From a more fundamental point of view, the properties of suitable solvents are directly correlated with the performance of the MEA operating in an electrolyser set-up.

Chapter 3 concerns to PEM fuel cells and strategies to mitigate poisoning of the anode catalyst by small traces of carbon monoxide present in the hydrogen feed. These include internal air bleeding, where small amounts oxygen is promoted to permeate from the cathode through the membrane, and the direct blending of controlled concentrations of air in the hydrogen stream. Both are able minimize catalyst poisoning by oxidizing carbon monoxide but with different efficiency depending on relevant parameters like, oxygen partial pressure, membrane thickness and pressure difference between cathode and anode. **Chapter 4** refers to the synthesis of graphene-supported Pt catalysts to be used at the cathode of a fuel cell. The loading of Pt on graphene is varied, leading to electrocatalysts with different platinum coverage, particle size and degree of crystallinity. Their performance is tested both in a three-electrode (RDE) and single cell configurations and they are subjected to an accelerated stress protocol to differentiate them in terms of ORR stability. **Chapter 5** focuses on oxygen reduction degradation phenomena of a graphene-supported electrocatalyst subjected to accelerated stress protocols. Three different protocols that are typically used in three-electrodes configurations are coupled with electrochemical and morphological measurements to deconvolute the different origins of degradation, either directly related to the carbon-based support or the platinum nanoparticles.

Chapter 6 explains the development of a useful *in-situ* method to quantify the membrane crossover of vanadium oxidized species in redox flow batteries. It uses the electric current generated during voltammetry scan and is validated and confirmed with typical external measurements. The method is demonstrated using membranes with different thickness and capability to transport cations or anions.

REFERENCES

[1] IRENA, *WORLD ENERGY TRANSITIONS OUTLOOK - 1.5º C PATHWAY*. 2021, isbn: 978-92-9260-334-2.

[2] R. Shan, J. Reagan, S. Castellanos, S. Kurtz, and N. Kittner, "Evaluating emerging long-duration energy storage technologies," *Renew. Sustain. Energy Rev.*, vol. 159, p. 112240, May 2022, doi: 10.1016/j.rser.2022.112240.

[3] B. Dunn, H. Kamath, and J.-M. Tarascon, "Electrical Energy Storage for the Grid: A Battery of Choices," *Science (80-.).*, vol. 334, no. 6058, pp. 928 LP – 935, Nov. 2011, doi: 10.1126/science.1212741.

[4] L. Alves, V. Pereira, T. Lagarteira, and A. Mendes, "Catalytic methane decomposition to boost the energy transition: Scientific and technological advancements," *Renew. Sustain. Energy Rev.*, vol. 137, p. 110465, March 2021, doi: 10.1016/j.rser.2020.110465.

[5] V. Mehta and J. S. Cooper, "Review and analysis of PEM fuel cell design and manufacturing," *Journal of Power Sources*, vol. 114, no. 1. pp. 32–53, Feb. 25, 2003, doi: 10.1016/S0378-7753(02)00542-6.

[6] M. Carmo, D. L. Fritz, J. Mergel, and D. Stolten, "A comprehensive review on PEM water electrolysis," *International Journal of Hydrogen Energy*, vol. 38, no. 12. pp. 4901–4934, 2013, doi: 10.1016/j.ijhydene.2013.01.151.

[7] M. Skyllas-Kazacos, L. Cao, M. Kazacos, N. Kausar, and A. Mousa, "Vanadium Electrolyte Studies for the Vanadium Redox Battery—A Review," *ChemSusChem*, vol. 9, no. 13, pp. 1521–1543, Jul. 2016, doi: 10.1002/cssc.201600102.

[8] J. Song, H. Song, B. Kim, and J. Oh, "Towards Higher Rate Electrochemical CO2 Conversion: From Liquid-Phase to Gas-Phase Systems," *Catalysts*, vol. 9, no. 3, p. 224, Mar. 2019, doi: 10.3390/catal9030224.

[9] D. T. Whipple and P. J. A. Kenis, "Prospects of CO2 Utilization via Direct Heterogeneous Electrochemical Reduction," *J. Phys. Chem. Lett.*, vol. 1, no. 24, pp. 3451–3458, Dec. 2010, doi: 10.1021/jz1012627.

[10] C. Rae, S. Kerr, and M. M. Maroto-Valer, "Upscaling smart local energy

systems: A review of technical barriers," *Renew. Sustain. Energy Rev.*, vol. 131, p. 110020, Oct. 2020, doi: 10.1016/j.rser.2020.110020.

[11] Deutscher; Brennstoffzellenverband und Wasserstoff; Enagás; Engie; Equinor; Air Liquide S.A; BMW Group; and Power; et al., "Hydrogen Roadmap Europe", 2019, doi: 10.2843/341510.

[12] IRENA, "Hydrogen: a renewable energy perspective," 2019, isbn: 978-92-9260-151-5.

[13] F. Barbir, "PEM electrolysis for production of hydrogen from renewable energy sources," *Sol. Energy*, vol. 78, no. 5, pp. 661–669, 2005, doi: 10.1016/j.solener.2004.09.003.

[14] A. Tang, J. Bao, and M. Skyllas-Kazacos, "Dynamic modelling of the effects of ion diffusion and side reactions on the capacity loss for vanadium redox flow battery," *J. Power Sources*, vol. 196, no. 24, pp. 10737–10747, Dec. 2011, doi: 10.1016/j.jpowsour.2011.09.003.

[15] P. A. Boettcher, E. Agar, C. R. Dennison, and E. C. Kumbur, "Modeling of Ion Crossover in Vanadium Redox Flow Batteries: A Computationally-Efficient Lumped Parameter Approach for Extended Cycling," *J. Electrochem. Soc.* , vol. 163, no. 1, pp. A5244–A5252, Jan. 2016, doi: 10.1149/2.0311601jes.

[16] R. Hefner III, "The age of energy gases," *Int. J. Hydrogen Energy*, vol. 27, no. 1, pp. 1–9, Jan. 2002, doi: 10.1016/S0360-3199(01)00079-9.

[17] A. Lajunen and T. Lipman, "Lifecycle cost assessment and carbon dioxide emissions of diesel, natural gas, hybrid electric, fuel cell hybrid and electric transit buses," *Energy*, vol. 106, pp. 329–342, 2016, doi: 10.1016/j.energy.2016.03.075.

[18] J. Zhang *et al.*, "High temperature PEM fuel cells," *J. Power Sources*, vol. 160, no. 2, pp. 872–891, Oct. 2006, doi: 10.1016/j.jpowsour.2006.05.034.

[19] X. Cheng *et al.*, "A review of PEM hydrogen fuel cell contamination: Impacts, mechanisms, and mitigation," *J. Power Sources*, vol. 165, no. 2, pp. 739–756, 2007, doi: 10.1016/j.jpowsour.2006.12.012.

[20] Air liquide S.A.; BMW Group.; Deutscher Wasserstoff - und

Brennstoffzellenverband.; Enagás.; Engie.; Equinor ASA.; Hydrogenics.; ITM Power; Michelin.; NEL Hydrogen.; Plastic Omnium.; Salzgitter AG.; Solid Power.; Total SA.; Toyota Motor Europe.; Verbund, "Hydrogen Roadmap Europe : A sustainable pathway for the European Energy transition," Belgium, 2019, doi: 10.2843/341510.

[21] E. Padgett *et al.*, "Mitigation of PEM Fuel Cell Catalyst Degradation with Porous Carbon Supports," *J. Electrochem. Soc.* , vol. 166, no. 4, pp. F198–F207, Jan. 2019, doi: 10.1149/2.0371904jes.

[22] M. K. Debe, "Tutorial on the Fundamental Characteristics and Practical Properties of Nanostructured Thin Film (NSTF) Catalysts," *J. Electrochem. Soc.* , vol. 160, no. 6, pp. F522–F534, Jan. 2013, doi: 10.1149/2.049306jes.

[23] Z. Hua, Z. Zheng, E. Pahon, M.-C. Péra, and F. Gao, "A review on lifetime prediction of proton exchange membrane fuel cells system," *J. Power Sources*, vol. 529, p. 231256, May 2022, doi: 10.1016/j.jpowsour.2022.231256.

[24] DOE, "Technical Targets for Polymer Electrolyte Membrane Fuel Cell Components," 2017, url: https://www.energy.gov/eere/fuelcells/doe-technical-targets-polymer-electrolyte-membrane-fuel-cell-components.

[25] C. A. Reiser *et al.*, "A Reverse-Current Decay Mechanism for Fuel Cells," *Electrochem. Solid-State Lett.*, vol. 8, no. 6, p. A273, 2005, doi: 10.1149/1.1896466.

[26] L. L. Atanasoska, G. Vernstrom, G. M. Haugen, and R. Atanasoski, "Catalyst Durability for Fuel Cells under Start-Up and Shutdown Conditions: Evaluation of Ru and Ir Sputter-Deposited Films on Platinum in PEM Environment," *ECS Trans.*, vol. 41, no. 1, pp. 785–795, Oct. 2011, doi: 10.1149/1.3635612.

[27] I. C. Halalay, S. Swathirajan, B. Merzougui, M. P. Balogh, G. C. Garabedian, and M. K. Carpenter, "Anode Materials for Mitigating Hydrogen Starvation Effects in PEM Fuel Cells," *J. Electrochem. Soc.*, vol. 158, no. 3, p. B313, 2011, doi: 10.1149/1.3530796.

[28] M. N. Tsampas, A. Pikos, S. Brosda, A. Katsaounis, and C. G. Vayenas, "The effect of membrane thickness on the conductivity of Nafion," *Electrochim. Acta*,

vol. 51, no. 13, pp. 2743–2755, Mar. 2006, doi: 10.1016/j.electacta.2005.08.021.

[29] M. Schalenbach, G. Tjarks, M. Carmo, W. Lueke, M. Mueller, and D. Stolten, "Acidic or Alkaline? Towards a New Perspective on the Efficiency of Water Electrolysis," *J. Electrochem. Soc.* , vol. 163, no. 11, pp. F3197–F3208, Jan. 2016, doi: 10.1149/2.0271611jes.

[30] Y. Shao, G. Yin, and Y. Gao, "Understanding and approaches for the durability issues of Pt-based catalysts for PEM fuel cell," *J. Power Sources*, vol. 171, no. 2, pp. 558–566, Sep. 2007, doi: 10.1016/j.jpowsour.2007.07.004.

[31] M. Breitwieser, M. Klingele, S. Vierrath, R. Zengerle, and S. Thiele, "Tailoring the Membrane-Electrode Interface in PEM Fuel Cells: A Review and Perspective on Novel Engineering Approaches," *Adv. Energy Mater.*, vol. 8, no. 4, p. 1701257, Feb. 2018, doi: 10.1002/aenm.201701257.

[32] Mylène Robert. "Impact of degradation and aging on properties of PFSA membranes for fuel cells." Mechanics of materials. Université de Lorraine, 2021, url: https://hal.univ-lorraine.fr/tel-03203250/document

[33] Z. Xu, D. Qiu, P. Yi, L. Peng, and X. Lai, "Towards mass applications: A review on the challenges and developments in metallic bipolar plates for PEMFC," *Prog. Nat. Sci. Mater. Int.*, vol. 30, no. 6, pp. 815–824, Dec. 2020, doi: 10.1016/j.pnsc.2020.10.015.

[34] K. A. Friedrich, "PlanDelyKad: Study on Large Scale Water Electrolysis and Hydrogen Storage (in German). German Federal Ministry for Economic Affairs and Energy (BMWi), Berlin," 2015.

[35] K. E. Ayers, C. Capuano, and E. B. Anderson, "Recent Advances in Cell Cost and Efficiency for PEM-Based Water Electrolysis," *ECS Trans.* , vol. 41, no. 10, pp. 15–22, May 2012, doi: 10.1149/1.3684798.

[36] K. E. Ayers *et al.*, "Research Advances towards Low Cost, High Efficiency PEM Electrolysis," *ECS Trans.* , vol. 33, no. 1, pp. 3–15, Oct. 2010, doi: 10.1149/1.3484496.

[37] S. Cherevko *et al.*, "Oxygen and hydrogen evolution reactions on Ru, RuO2, Ir, and IrO2 thin film electrodes in acidic and alkaline electrolytes: A comparative

study on activity and stability," *Catal. Today*, vol. 262, pp. 170–180, 2016, doi: https://doi.org/10.1016/j.cattod.2015.08.014.

[38] P. Lettenmeier *et al.*, "Comprehensive investigation of novel pore-graded gas diffusion layers for high-performance and cost-effective proton exchange membrane electrolyzers," *Energy Environ. Sci.*, vol. 10, no. 12, pp. 2521–2533, 2017, doi: 10.1039/c7ee01240c.

[39] P. Lettenmeier *et al.*, "Low-Cost and Durable Bipolar Plates for Proton Exchange Membrane Electrolyzers," *Sci. Rep.*, vol. 7, p. 44035, Mar. 2017, doi: 10.1038/srep44035.

[40] R. Kötz, S. Stucki, D. Scherson, and D. M. Kolb, "In-situ identification of RuO4 as the corrosion product during oxygen evolution on ruthenium in acid media," *J. Electroanal. Chem. Interfacial Electrochem.*, vol. 172, no. 1–2, pp. 211–219, Aug. 1984, doi: 10.1016/0022-0728(84)80187-4.

[41] S. Cherevko, A. R. Zeradjanin, A. A. Topalov, N. Kulyk, I. Katsounaros, and K. J. J. Mayrhofer, "Dissolution of Noble Metals during Oxygen Evolution in Acidic Media," *ChemCatChem*, vol. 6, no. 8, pp. 2219–2223, Aug. 2014, doi: 10.1002/cctc.201402194.

[42] T. Reier, M. Oezaslan, and P. Strasser, "Electrocatalytic Oxygen Evolution Reaction (OER) on Ru, Ir, and Pt Catalysts: A Comparative Study of Nanoparticles and Bulk Materials," *ACS Catal.*, vol. 2, no. 8, pp. 1765–1772, Aug. 2012, doi: 10.1021/cs3003098.

[43] E. Fabbri, A. Habereder, K. Waltar, R. Kötz, and T. J. Schmidt, "Developments and perspectives of oxide-based catalysts for the oxygen evolution reaction," *Catal. Sci. Technol.*, vol. 4, no. 11, pp. 3800–3821, 2014, doi: 10.1039/C4CY00669K.

[44] A. E. Hughes, N. Haque, S. A. Northey, and S. Giddey, "Platinum Group Metals: A Review of Resources, Production and Usage with a Focus on Catalysts," *Resources*, vol. 10, no. 9, p. 93, Sep. 2021, doi: 10.3390/resources10090093.

[45] P. Lettenmeier *et al.*, "Nanosized IrOx-Ir Catalyst with Relevant Activity for Anodes of Proton Exchange Membrane Electrolysis Produced by a Cost-

Effective Procedure," *Angew. Chemie*, vol. 128, no. 2, pp. 752–756, Jan. 2016, doi: 10.1002/ange.201507626.

[46] C. K. Mittelsteadt, "PEM Electrolysis: Ready for Impact," *ECS Trans.*, vol. 69, no. 17, pp. 205–211, Sep. 2015, doi: 10.1149/06917.0205ecst.

[47] P. Lettenmeier, R. Wang, R. Abouatallah, F. Burggraf, A. S. Gago, and K. A. Friedrich, "Coated Stainless Steel Bipolar Plates for Proton Exchange Membrane Electrolyzers," *J. Electrochem. Soc.*, vol. 163, no. 11, pp. F3119–F3124, Jul. 2016, doi: 10.1149/2.0141611jes.

[48] A. S. Gago *et al.*, "Protective coatings on stainless steel bipolar plates for proton exchange membrane (PEM) electrolysers," *J. Power Sources*, vol. 307, pp. 815–825, Mar. 2016, doi: 10.1016/j.jpowsour.2015.12.071.

[49] U. Babic, M. Suermann, F. N. Büchi, L. Gubler, and T. J. Schmidt, "Critical Review—Identifying Critical Gaps for Polymer Electrolyte Water Electrolysis Development," *J. Electrochem. Soc.* , vol. 164, no. 4, pp. F387–F399, Jan. 2017, doi: 10.1149/2.1441704jes.

[50] D. Fan, Y. Ren, Q. Feng, Y. Liu, Z. Wang, and J. Lin, "Restoration of smart grids: Current status, challenges, and opportunities," *Renew. Sustain. Energy Rev.*, vol. 143, p. 110909, Jun. 2021, doi: 10.1016/j.rser.2021.110909.

[51] R. K. Sankaralingam, S. Seshadri, J. Sunarso, A. I. Bhatt, and A. Kapoor, "Overview of the factors affecting the performance of vanadium redox flow batteries," *J. Energy Storage*, vol. 41, p. 102857, Sep. 2021, doi: 10.1016/j.est.2021.102857.

[52] P. C. Ghimire, A. Bhattarai, T. M. Lim, N. Wai, M. Skyllas-Kazacos, and Q. Yan, "In-Situ Tools Used in Vanadium Redox Flow Battery Research—Review," *Batteries*, vol. 7, no. 3, p. 53, Aug. 2021, doi: 10.3390/batteries7030053.

[53] E. Sum and M. Skyllas-Kazacos, "A study of the V(II)/V(III) redox couple for redox flow cell applications," *J. Power Sources*, vol. 15, no. 2–3, pp. 179–190, Jun. 1985, doi: 10.1016/0378-7753(85)80071-9.

[54] F. Grossmith, P. Llewellyn, A. Fane, and M. Kazacos, "Evaluation of membranes for all-vanadium redox cell," in *Proceedings of Electrochemical Society*

Symposium, 1988, p. 363.

[55] I. Derr, M. Bruns, J. Langner, A. Fetyan, J. Melke, and C. Roth, "Degradation of all-vanadium redox flow batteries (VRFB) investigated by electrochemical impedance and X-ray photoelectron spectroscopy: Part 2 electrochemical degradation," *J. Power Sources*, vol. 325, pp. 351–359, 2016, doi: 10.1016/j.jpowsour.2016.06.040.

[56] M. Jouny, W. Luc, and F. Jiao, "General Techno-Economic Analysis of CO2 Electrolysis Systems," *Ind. Eng. Chem. Res.*, vol. 57, no. 6, pp. 2165–2177, Feb. 2018, doi: 10.1021/acs.iecr.7b03514.

[57] R. Costa *et al.*, "Power-to-X with High Temperature Solid Oxide Cells: Concepts, Challenges & Prospects," *ECS Trans.* , vol. 85, no. 10, pp. 1–11, Apr. 2018, doi: 10.1149/08510.0001ecst.

[58] M. Gattrell, N. Gupta, and A. Co, "Electrochemical reduction of CO2 to hydrocarbons to store renewable electrical energy and upgrade biogas," *Energy Convers. Manag.*, vol. 48, no. 4, pp. 1255–1265, 2007, doi: 10.1016/j.enconman.2006.09.019.

[59] B. Endrődi, G. Bencsik, F. Darvas, R. Jones, K. Rajeshwar, and C. Janáky, "Continuous-flow electroreduction of carbon dioxide," *Prog. Energy Combust. Sci.*, vol. 62, pp. 133–154, 2017, doi: 10.1016/j.pecs.2017.05.005.

[60] J.-P. Jones, G. K. S. Prakash, and G. A. Olah, "Electrochemical CO2 Reduction: Recent Advances and Current Trends," *Isr. J. Chem.*, vol. 54, no. 10, pp. 1451–1466, Sep. 2014, doi: 10.1002/ijch.201400081.

[61] M. Alvarez-Guerra, A. Del Castillo, and A. Irabien, "Continuous electrochemical reduction of carbon dioxide into formate using a tin cathode: Comparison with lead cathode," *Chem. Eng. Res. Des.*, vol. 92, no. 4, pp. 692–701, 2014, doi: 10.1016/j.cherd.2013.11.002.

[62] D. Kopljar, N. Wagner, and E. Klemm, "Transferring Electrochemical CO2 Reduction from Semi-Batch into Continuous Operation Mode Using Gas Diffusion Electrodes," *Chem. Eng. Technol.*, vol. 39, no. 11, pp. 2042–2050, Jul. 2016, doi: 10.1002/ceat.201600198.

[63] J. Wu, F. G. Risalvato, P. P. Sharma, P. J. Pellechia, F.-S. Ke, and X.-D. Zhou, "Electrochemical Reduction of Carbon Dioxide: II. Design, Assembly, and Performance of Low Temperature Full Electrochemical Cells ," *J. Electrochem. Soc.* , vol. 160, no. 9, pp. F953–F957, Jan. 2013, doi: 10.1149/2.030309jes.

[64] S. Pérez-Rodríguez, F. Barreras, E. Pastor, and M. J. Lázaro, "Electrochemical reactors for CO2 reduction: From acid media to gas phase," *Int. J. Hydrogen Energy*, vol. 41, no. 43, pp. 19756–19765, 2016, doi: 10.1016/j.ijhydene.2016.06.130.

[65] I. Merino-Garcia, J. Albo, and A. Irabien, "Productivity and Selectivity of Gas-Phase CO2 Electroreduction to Methane at Copper Nanoparticle-Based Electrodes," *Energy Technol.*, vol. 5, no. 6, pp. 922–928, Dec. 2016, doi: 10.1002/ente.201600616.

[66] A. Pătru, T. Binninger, B. Pribyl, and T. J. Schmidt, "Design Principles of Bipolar Electrochemical Co-Electrolysis Cells for Efficient Reduction of Carbon Dioxide from Gas Phase at Low Temperature," *J. Electrochem. Soc.*, vol. 166, no. 2, pp. F34–F43, Jan. 2019, doi: 10.1149/2.1221816jes.

CHAPTER 2

HIGHLY ACTIVE SCREEN-PRINTED IR-Ti_4O_7 ANODES FOR PROTON EXCHANGE MEMBRANE ELECTROLYZERS

2

HIGHLY ACTIVE SCREEN-PRINTED IR-Ti_4O_7 ANODES FOR PROTON EXCHANGE MEMBRANE ELECTROLYSERS

Tiago Lagarteira, Feng Han, Tobias Morawietz, Renate Hiesgen, Daniel Garcia, Adélio Mendes, Aldo Gago and Rémi Costa

Adapted from the International Journal of Hydrogen Energy, 2018, 43(35)

ABSTRACT

Electroceramic support materials can help reducing the noble-metal loading of iridium in membrane electrodes assembly (MEA) of proton exchange membrane (PEM) electrolysers. Highly active anodes containing Ir-black catalyst and submicron Ti_4O_7 are manufactured through screen printing technique. Several vehicle solvents, including ethane-1,2-diol; propane-1,2-diol and cyclohexanol are investigated.

Suitable functional anodic layers with iridium loading as low as 0.4 mg cm^{-2} are obtained. Surface properties of the deposited layers are investigated by atomic force microscopy (AFM). The most homogeneous coating with the highest electronic conductivity is obtained using cyclohexanol. Tests in PEM electrolyser operating at 1.7 V and 40 °C demonstrate that the MEAs prepared with this solvent achieve 35 % higher Ir-mass activity compared to the commercial MEA.

Keywords: Proton exchange membrane water electrolysis; Membrane electrodes assembly; Catalyst coated membrane; Cost; Iridium loading; Ceramic support; Ti_4O_7; Screen printing; Oxygen evolution reaction.

2.1. INTRODUCTION

The penetration of PEM electrolyser systems at the megawatt scale will be hindered by the high cost and scarcity of catalyst materials. Together with the manufacturing of the membrane electrodes assembly (MEA), they represent approximately 20 % of the overall cost of the PEM electrolyser stack [6]. Therefore, there is a potential for cost reduction by decreasing the used amount of precious group metals (PGM) and optimizing the catalyst coating process in the production of MEAs.

A reduction in the catalyst loadings is not only important due to the high price of the precious metals but also to the scarcity of platinum and mainly iridium [7]. Despite some recent advances that took several years of research [8,9], the state-of-the-art anode still requires high iridium loadings of *ca.* 2-4 mg cm^{-2} [10,11], to balance the sluggish kinetics and the high charge transfer overpotential caused by the oxygen evolution reaction (OER). Ceramic supports like Magnéli-phase titanium sub-oxides (TiO_2, Ti_4O_7 and Ti_5O_9) are promising catalyst supports because they provide higher catalytic stability and resistance to corrosion in the harsh environment of the electrolyser anode in comparison to the typical carbon-based supports used in PEM fuel cells [12–20].

For the manufacturing, screen printing is a widespread and common cost-efficient printing technique that can be used to produce catalyst coated membranes (CCM-MEA), where the catalysts are directly deposited on a proton exchange membrane – typically Nafion. Some reports on the fabrication of MEAs for PEM fuel cells with screen printing are available. But in most of them, the catalyst deposition is carried out on the porous transport layer (PTL) or on PTFE sheets for posterior decal transfer to the membrane. This is the usual strategy to avoid typical processing issues like membrane swelling when it contacts with organic solvents [21–24]. The overcome of the swelling issue is a key challenge as direct catalyst deposition on the membrane provides better contact between the catalyst layer and the electrolyte thus reducing interfacial contact resistances. Kim and co-workers proposed a treatment [25] in which the membrane was exchanged from the H^+ form to Na^+ form before coating. The protonic reconversion was performed after the catalyst layer was deposited and dried. Nonetheless, no report is found in the

literature of screen-printed catalyst layers directly on the membrane for PEM electrolysers [11].

Composition of the catalyst ink affects not only the coating process itself - by governing the rheological properties - but also affects the microstructure of the coated layer. The properties of the catalyst ink should be optimized not only for the coating process but also for maximizing the connection of catalytic sites to both electronic and ionic conducting phases, thus ensuring the overall performance of the electrolyser. The idea of using solubilized Nafion ionomer in catalyst inks or suspensions has been widely used for extending the protonic vehicular conduction through the 3D-structures of the catalyst layers [26–28]. More recently, Chan and Eikerling reported that ionomer-free ultra-thin catalyst layers (20 - 500 nm thick) rely entirely on liquid water for proton conduction [29]. Therefore, a fully humidified catalyst layer would be beneficial, enabling proton conduction exclusively by the Grotthuss mechanism [30]. In the case of screen-printed catalyst layers, with thickness in the micrometer range, ionomer distribution and its orientation should be tuned for maximizing the number of active sites connected to the protonic conductive phase while not hindering electronic conductivity of the catalyst support and mass diffusion in the porous structure of the catalyst layer [31].

In this work, highly-active anodes with inexpensive catalyst support and low iridium loading were fabricated via a cost-effective and scalable screen printing technique. Moreover, the properties of the developed layers were characterized and investigated through diagnosis tools such as TGA, AFM and electrochemical single cell tests.

2.2. EXPERIMENTAL

2.2.1. CCM FABRICATION

2.2.1.1 SCREEN PRINTING OF THE ANODE

In the preparation of the screen printing inks, summarized in Table 2.1, 30 wt.% Iridium Black (Umicore) was mixed with 70 wt.% Ti_4O_7 catalyst support (Changsha Purong Chemical Engineering Inc.) using a mortar and a pestle. Ethane-1,2-diol (Sigma Aldrich), propane-1,2-diol (VWR) and cyclohexanol (VWR) were used as organic

solvents for the inks (physicochemical properties shown in Table 2.2). The ratio between Nafion ionomer and the total solid particles was kept at 30 wt.% [32]. The solvents from a 20 wt.% Nafion solution (Sigma Aldrich) were evaporated during the mixing and, only then, the chosen organic solvent was added. The solid content in the screen printing inks was kept at 37.5 wt.%, except for the ink used in to study the effectiveness of the membrane swelling treatment which contained a lower (but not determined) weight ratio of solid particles.

Table 2.1 - Screen printing ink formulations; ratios based on the total weight of the ink.

Ink formulations	**Catalyst (7.875 wt%)**	**Catalyst support (18.375 wt%)**	**Binder (11.25 wt%)**	**Solvent (62.5 wt%)**
A	Ir Black	Ti_4O_7	Nafion ionomer	Ethane-1,2-diol
B	Ir Black	Ti_4O_7	Nafion ionomer	Propane-1,2-diol
C	Ir Black	Ti_4O_7	Nafion ionomer	Cyclohexanol

Table 2.2 - Physical properties of organic solvents used in screen printing inks.

Solvent	**Viscosity * 10^{-3} (Pa s) @ 298 K**	**Vapor pressure (Pa) @ 293 K**	**Relative permittivity (ε)**	**Boiling temperature (K @ 10^5 Pa)**
Ethane-1,2-diol	16.13	8	37 @ 298 K	470.75
Propane-1,2-diol	42.00	17.3	32 @ 293 K	461.35
Cyclohexanol	54.60	133.3	15 @ 293 K	434.15

Nafion 212 membrane was cut into squares with a size 7 cm x 7 cm and, after removing the protection foils and conditioning at ambient humidity, they were weighted. Subsequently, they were placed on a porous metal substrate, enabling the use of a vacuum positioning and fixing system during the coating process. An Aurel 900 screen printer equipped with a Koenen Typ-10 M6 mesh (4 cm^2 of open area) was used for

coating the anodes of the CCMs. The printing pressure was set to 1.5 N cm^{-2} and the distance between the screen and the substrate was 0.8 mm.

After coating, the samples were dried firstly on the screen printing holder for 10 minutes under infrared radiation produced by an incandescent lamp (40 W, distance 10 cm) to remove most of the solvent, and then dried at 348 K for 30 minutes in a drying oven. After conditioning at ambient humidity, the one-side coated membranes were again weighted for the catalyst loading calculation. The iridium loading was calculated based on weight difference of the membranes before and after the anode coating, and further confirmed by thermal gravimetric analysis (TGA).

2.2.1.2 WET SPRAYING OF THE CATHODE

Since the focus of this work was the anode processing, the cathode was deposited by the state-of-the-art and widely used wet spray coating method. Thus, the differences in performance could be only related to the screen printing conditions. This technique was selected for processing the platinum-based cathodes since it allows achieving high performances with good reproducibility [33–35]. The spraying suspension was prepared by mixing 60 wt.% Pt/C (Johnson Matthey) with 50 vol.% water in isopropanol, considering the solvents from a 5 wt.% Nafion solution (Ion Power). First, HPLC purity grade water was added the catalyst powder to avoid nanoparticles ignition when in contact with low molecular alcohols. Nafion ionomer content was kept at 35 wt% relatively to the solids in the spraying suspension. The total solid content in the suspension was 0.8 wt%. A heated vacuum table at 378 K was used during the wet spray deposition to dry the suspension solvents and simultaneously avoiding membrane swelling. After the cathode was coated, the CCM was hot pressed at 1.75 MPa and 398 K during 5 minutes.

2.2.1.3 MEMBRANE SWELLING TREATMENT

A membrane treatment reported by Kim and co-workers [24,25,36] was used to avoid swelling of the Nafion membrane caused by ethane-1,2-diol. In short, the membrane was boiled in an aqueous solution of 0.25 M NaOH for 15 minutes. After exchanging from

protonic to sodium ionic form, the membrane was washed and boiled in deionized water for 10 minutes before being screen-printed. Following, the membrane was coated, dried and hot pressed to produce the CCM. Finally, the CCM was boiled in an aqueous solution of H_2SO_4 (0.5 M) for 30 minutes for the needed reprotonation. The CCM was then rinsed three times, one minute each, in deionized water to remove any remaining acid traces before testing. The iridium loading of the two anodes used for assessing the effectiveness of the membrane swelling treatment were equal, however they were not calculated.

2.2.2. CATALYST LOADING CALCULATION THROUGH THERMAL GRAVIMETRIC ANALYSIS (TGA)

The anode-coated membrane with the ink using propane-1,2-diol as solvent was cut in circular samples of 5 mm in diameter for the TGA measurement. The analysis was performed using a thermal gravimetric analyzer (Netzsch STA 449 C) and a DSC/TG pan Pt under air atmosphere, heated from 303 K to 1073 K at 5 K min^{-1}.

2.2.3. SURFACE MORPHOLOGY ANALYSIS WITH ATOMIC FORCE MICROSCOPY (AFM)

The local properties of the surface were investigated by atomic force microscopy (AFM). For the AFM measurements performed with a Multimode 8 AFM (Bruker, Karlsruhe), a piece of the MEA was cut out of the center with a razorblade. The CCM sample was glued with conductive adhesive tape onto a steel disc with the anode facing to the top. The anode was additionally connected with silver paste to ensure a low electrical resistance. Platinum/iridium coated AFM tips (PPP-NCHPt), with a nominal spring constant of 42 N m^{-1}, were used in conductive tapping mode (PF-TUNA, Bruker). In PF-TUNA mode, a force distance curve is evaluated at every image point to reveal adhesion, stiffness and deformation. A built-in lock-in amplifier averaged the simultaneously measured current. Images with a length scale of 5 µm and 512 x 512 pixel were recorded at a scan rate of 0.5 Hz. The relative humidity during measurements was 30 ± 5 %. Evaluation of the porosity was performed with the bearing analysis tool of the Bruker nanoscope analysis software. For each anode, three 25 μm^2 measurements were

performed. For the porosity determination, the 25 μm^2-sized measurements were evaluated at 4 areas of 6.25 µm side length. For the conductive area evaluation, the threshold was set to 0.1 nA and the applied voltage was 2 V. The threshold for the adhesion force and deformation evaluation was derived by profile lines across high and low value areas. The adhesion force/deformation values determined by the turning points were used as threshold values, respectively.

2.2.4. SINGLE CELL MEASUREMENTS

The investigation of the dynamic response of the developed CCMs was performed on a in-house single cell PEM electrolyser test rig with an electrode area of 4 cm^2 [37]. The cell temperature was maintained at 313 K and it was fed with HPLC purity grade water. A potentiostat/galvanostat equipped with an electrochemical impedance spectroscopy (EIS) module (Zahner Instruments) was used to evaluate the performance of the electrolyser in a single-cell configuration.

Ti-coated stainless steel bipolar plates by vacuum plasma spraying [38–40] without flow field were used for the cell assembly. At the anode side, a Ti mesh was put between the bipolar plate and a sintered titanium porous transport layer (PTL) of *ca.* 1 mm thickness, > 40% porosity, coated with Pt-IrOx (Magneto Special Anodes B.V.). At the cathode side, three carbon PTLs (Toray paper 030) were used as gas diffusion layer (GDL) to prevent the destruction of the carbon paper upon the pressure increase caused by the evolution of H_2. A protocol of measurements was defined using mild conditions for electrolyser operation to avoid a possible fast degradation of the produced CCMs. The evolution of the current density was measured at 1.7 V in potentiostatic conditions.

EIS was performed at 35 mA cm^{-2} to enable a stable recording using a small perturbation of 5 mV. The parameters of the EIS spectra were fitted with an equivalent circuit [41] with (RQ) elements, representing a parallel combination of resistance and pseudo-capacitance for each catalyst layer. For the sake of convergence and getting relevant data, the *n* value was not fitted and was set to 0.5, which corresponds to a 45º phase angle. The fitted parameters are displayed in Table 2.3. R_S corresponds to the high frequency region in which the major contribution is assigned to the electrolyte. R_1 and R_2 are associated to charge transfer resistances of HER and OER, respectively. The onset

of mass diffusion effects was not included in the fittings. A previously activated commercial CCM (E300 from Greenerity) was also tested under the same cell configuration, containing 2.25 mg cm^{-2} of iridium at the anode, 1.25 mg cm^{-2} of platinum at the cathode and a Nafion 212 membrane.

2.3. RESULTS AND DISCUSSION

2.3.1. THE ROLE OF THE SCREEN PRINTING SOLVENTS

Figure 2.1 shows the anode-coated membranes, after being screen-printed and dried. The red circles point out the membrane swelling spots. The thickness of the anodes was *ca.* 13 µm. The ink using cyclohexanol was the only one that did not generate any visible membrane swelling. The ink using ethane-1,2-diol generated more membrane swelling when compared with the ink using propane-1,2-diol. After hot pressing, swelling spots (red circles) could not be seen in all CCMs. However, only the sample using cyclohexanol presented uniform coating which could guaranty homogeneous catalyst loading.

The generation of swelling is related to the affinity between hydroxyl groups of the solvents and sulfonated groups of Nafion. Cyclohexanol has just one hydroxyl group and a heavier closed carbon chain while propane-1,2-diol and ethane-1,2-diol have two hydroxyl groups. A heavier carbon chain decreases the polarity of the molecule thus decreasing its interaction with sulfonated groups of Nafion.

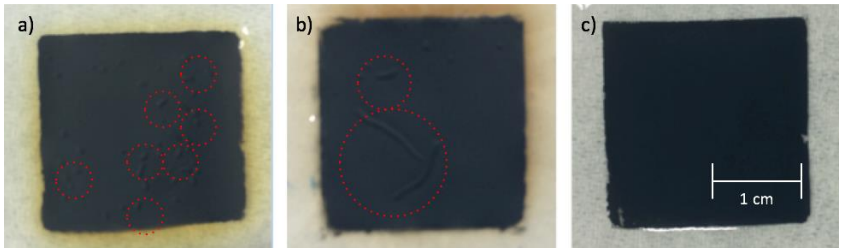


Figure 2.1 - Images of the anodes, before hot press, coated using different solvents: a) ethane-1,2-diol; b) propane-1,2-diol; c) cyclohexanol.

The membrane treatment procedure proposed by Kim et al. [25], proved to be effective for minimizing membrane swelling. Figure 2.2a shows the chronoamperometries at 1.7 V of two CCMs with anode coated with ethane-1,2-diol as solvent of the screen printing ink. The replacement of protons by heavier Na^+ reduced the affinity between Nafion sulfonated groups and ethane-1,2-diol. A larger cation ($Na^+ > H^+$) not only limits the free space for sulfonated groups to move, but also disables those sites for hydrogen-type bonds with the solvent hydroxyl groups. The two curves display different starting points and slopes before steady-state behavior, but the electrochemical activity of both CCMs equalizes for longer times. At the end of tests, the swelling treated CCM slightly outperformed the CCM without treatment, indicating that the ionic form modification and posterior reprotonation does not hinder the electrochemical performance of the CCM.

Figure 2.2b presents the impedance spectra (at 35 mA cm^{-2}) of CCMs subjected and not subjected to membrane treatment, recorded at the end of tests.

The overall impedance of the electrolyser with treated CCM is smaller than that with the untreated CCM (difference of *ca.* 800 mΩ cm^2) and the largest contribution for the overall impedance is assigned to charge transfer resistances of OER with values of 2.1 Ω cm^2 and 2.5 Ω cm^2, respectively [41–44]. The high frequency resistance (HFR) is 250 mΩ cm^2 for the treated CCM, that is even lower than that of the untreated CCM - 300 mΩ cm^2. This indicates that the swelling treatment has not a negative effect on the ohmic resistance and on the membrane conductivity.

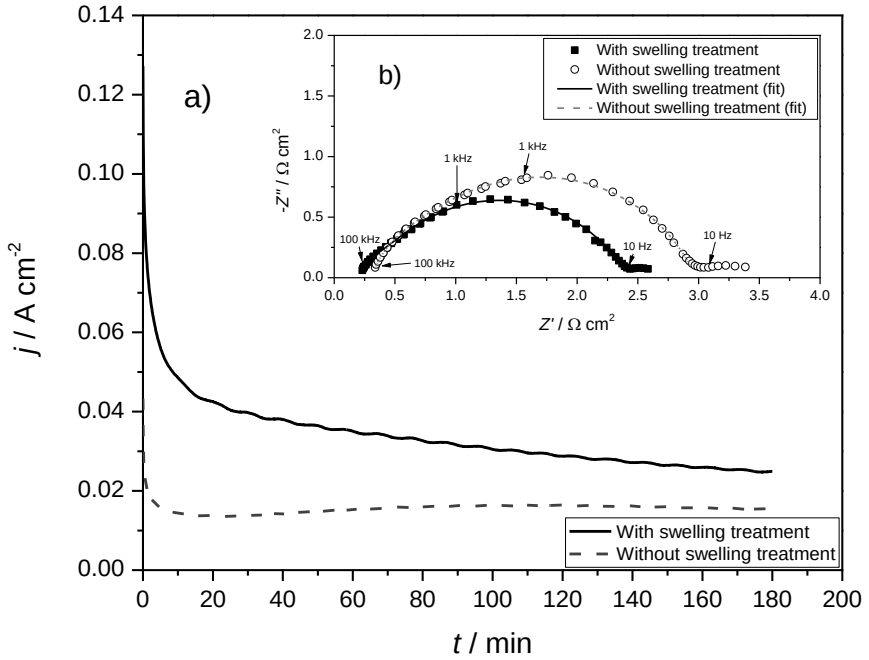


Figure 2.2 - a) Chronoamperometries (at 1.7 V and 40 ºC) of CCMs with and without swelling treatment. b) Impedance spectra (at 35 mA cm^{-2} and 40 ºC) of CCMs with and without swelling treatment.

The influence of the solvents used on the surface structure of the anodes is visible in the AFM topography measurements in Figure 2.3. In Figure 2.3a and Figure 2.3c, prepared using cyclohexanol and using propane-1,2-diol, respectively; more pores are present at the surface when compared to Figure 2.3b, prepared using ethane-1,2-diol. At this anode, beside a few open pores, regions with a smooth surface are present, and are most-likely Nafion ionomer. The adhesion force and deformation mappings given in Figure 2.4 reveal the distribution of catalyst and ionomer. Ionomer can be discerned from the catalyst and support particles by its high adhesion (bright areas in Figure 2.4, a-c), high deformation values (bright areas in Figure 2.4, d-f), and low DMT modulus (stiffness) - Figure S2 in Supplementary Information [45–47].

The surface porosity of the three 25 μm^2 topography images of the prepared anodes was evaluated. The porosity of the anode prepared using cyclohexanol solvent was the highest of the three samples, 26 ± 2 %, followed by the sample prepared using propane-1,2-diol with 20 ± 2 %. The anode prepared using ethane-1,2-diol had the lowest porosity with 13 ± 2 %. Due to the restriction to horizontal geometry, the AFM-determined porosity values are generally lower than those determined by other methods.

The coatings prepared using cyclohexanol and using propane-1,2-diol as solvents presented a comparably good distribution of ionomer and catalyst particles at the surface, as illustrated in Figure 2.4. The maximum size of connected ionomer particle area was determined from particle analysis of the adhesion image evaluation. For anodes prepared using cyclohexanol as solvent, the size was the smallest, 1280 ± 170 nm^2; for anodes prepared using propane-1,2-diol, the size was 1900 ± 240 nm^2; and the largest size was displayed by anodes prepared using ethane-1,2-diol, 3420 ± 40 nm^2. In conclusion, the catalyst particle distribution of the anode surface prepared using ethane-1,2-diol was the least homogeneous.

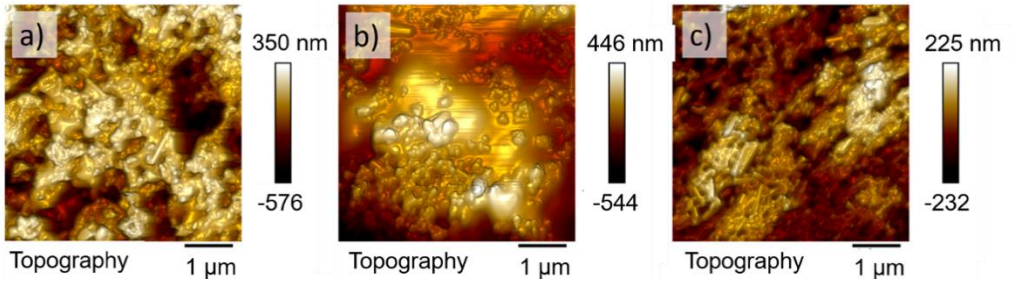


Figure 2.3 - AFM topography images of anodes prepared using different solvents: a) cyclohexanol, b) ethane-1,2-diol, c) propane-1,2-diol.

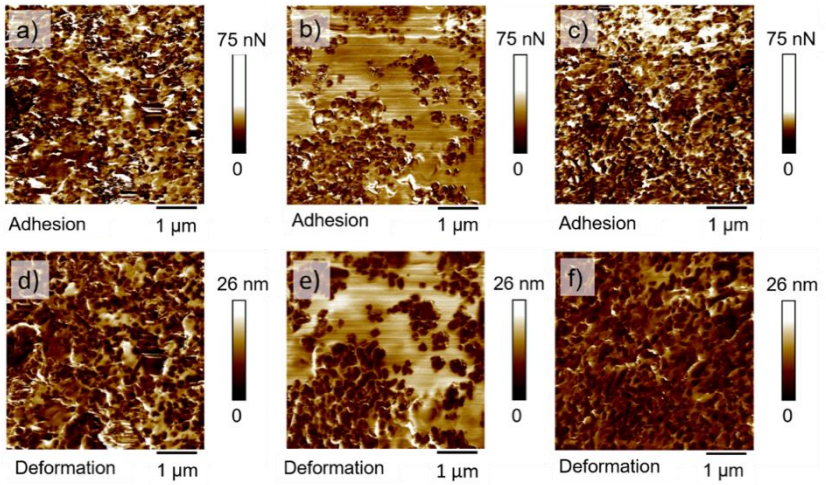


Figure 2.4 - AFM adhesion force measurements at the anodes prepared using different solvents. a) cyclohexanol, b) ethane-1,2-diol, c) propane-1,2-diol. Correlated deformation measurements for the anodes prepared using different solvents: d) cyclohexanol, e) ethane-1,2-diol, f) propane-1,2-diol.

2.3.2. CATALYST LOADING CALCULATION

The manufactured anodes contained Ir-loadings of 0.4 ± 0.02 mg cm^{-2} according to the differences in the weight of the membrane before and after coating the anodes. TGA was performed to the anode coated using propane-1,2-diol for validation of the weight difference calculation. The mass-losses at 400 ºC correspond to the Nafion membrane and ionomer decomposition. These results are in accordance with the work of Deng and co-workers [48] who noted major decomposition between 355 °C–560 °C corresponding to HF, carbonyl fluorides, and species exhibiting C–F stretching vibrations. In the work by Chen et al. [49], Ti_4O_7 does not show any thermal oxidation below 300 ºC. More recently, Senevirathne and co-workers [50] reported that Ti_4O_7 oxidizes to the more stable TiO_2 at 550 ºC with a weight gain of 6.2 % (higher than the theoretical value of 5.3 %). Iridium nanoparticles oxidize to IrO_2 during the TGA measurements under airflow, which additionally increases the total weight gain.

The remaining mass after the TGA measurement was found to be *ca.* 5.3 % of the initial mass of 4.90 mg. Since the species present after TGA are not Ir and Ti_4O_7, but instead IrO_2 and TiO_2, different oxygen uptake by the two species was considered to calculate

IrO_2 mass content at the end of TGA. The original mass fraction of Ir in the mixture of Ir/Ti_4O_7 was 30 wt.%. After the TGA, the theoretical mass fraction of IrO_2 in the mixture of IrO_2/TiO2 would be 32.2 wt.% (calculation in Supplementary Information). Finally, from the remaining TGA mass (correspondent to IrO_2 and TiO_2) and the area of the TGA sample, one can obtain the Ir-loading of 0.42 mg cm^{-2}.

The cathode of the CCM was sprayed with 100 µl cm^{-2} of catalyst suspension, and estimated Pt loading was 0.5 mg cm^{-2}, assuming 10 % of suspension loss in the gun and borders of the spraying area.

2.3.3. ELECTRICAL SURFACE CONDUCTIVITY

In Figure 2.5, the fraction of high deformation, high adhesion and non-conductive surface area of the three differently prepared anodes is given. When measuring the ionomer coverage, the highly deformable area fraction is the most significant signal because, by surface deformation values, only regions with approximately more than 30 nm thick ionomer layers at the surface are counted. Due to the high surface sensitivity to the adhesion force, the area measured by adhesion contrast also includes particles covered by a very thin ionomer layer erroneously rated as ionomer. The ionomer area at the surface of the sample prepared using ethane-1,2-diol (42 ± 2 %) was larger than that of the two other samples, which had approximately the same ionomer area fraction of 36 ± 2 % (propane-1,2-diol) and 35 ± 2 % (cyclohexanol). In addition, the non-conductive area derived from the current measurements was much larger in all three cases. The sample prepared using propane-1,2-diol had the largest non-conductive area, followed by the samples prepared using ethane-1,2-diol and cyclohexanol, respectively. This discrepancy can be explained by the different nature of the signals. A conductive surface spot needs to be electrically connected to the back electrode, while the nanomechanical properties reflect the properties of surface and sub-surface. In conclusion, the conductive network was the best for the sample prepared with cyclohexanol, followed by the samples prepared by using ethane-1,2-diol and propane-1,2-diol, respectively.

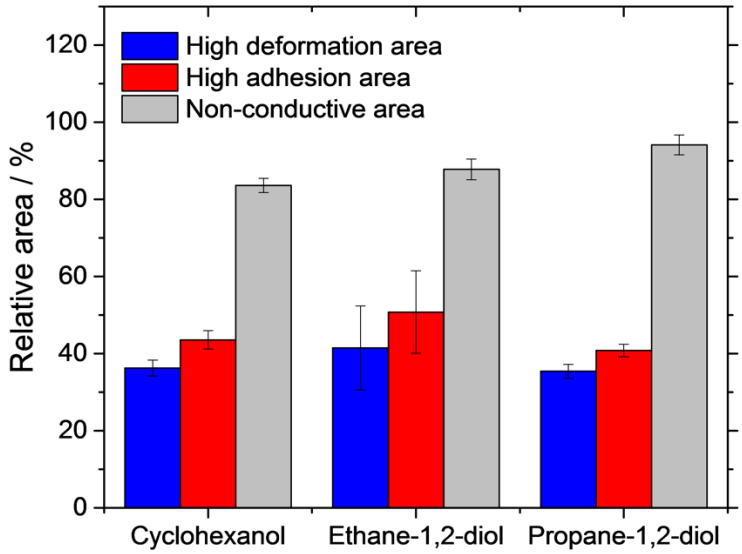


Figure 2.5 - Relative area of adhesion, deformation and non-conductive area at the surfaces of the three anodes prepared using different solvents.

The AFM-derived conductive area fractions follow the same slope as the current revealed by the polarization measurements of the anodes after a short running period (Figure 2.6). Examples of the AFM current measurements are given in Figure 2.7; a correlation between electronic conductivity and conductive surface area is apparent. Consequently, a decrease of ionomer content could enhance the electrolyser performance.

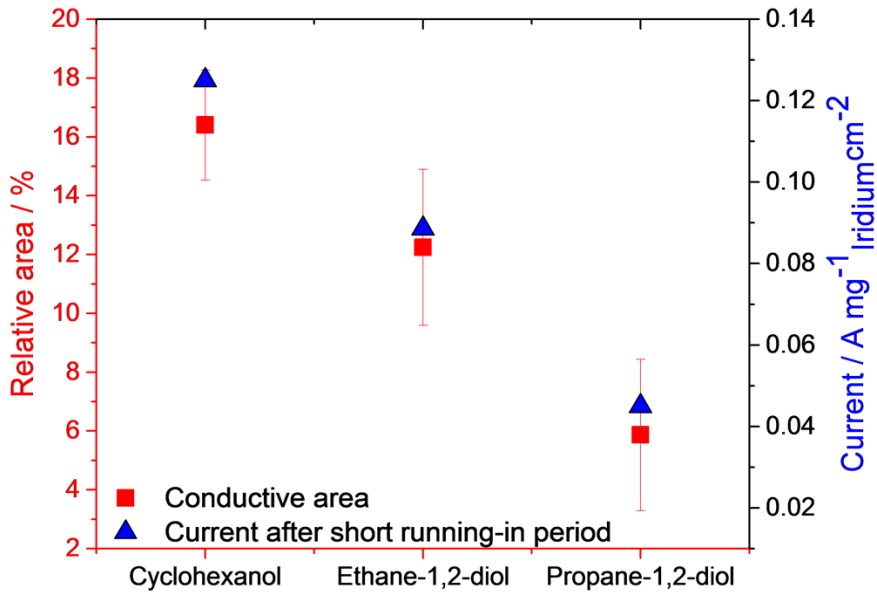


Figure 2.6 - Comparison of AFM-derived conductive area and current after short running-in period for the three differently prepared anodes.

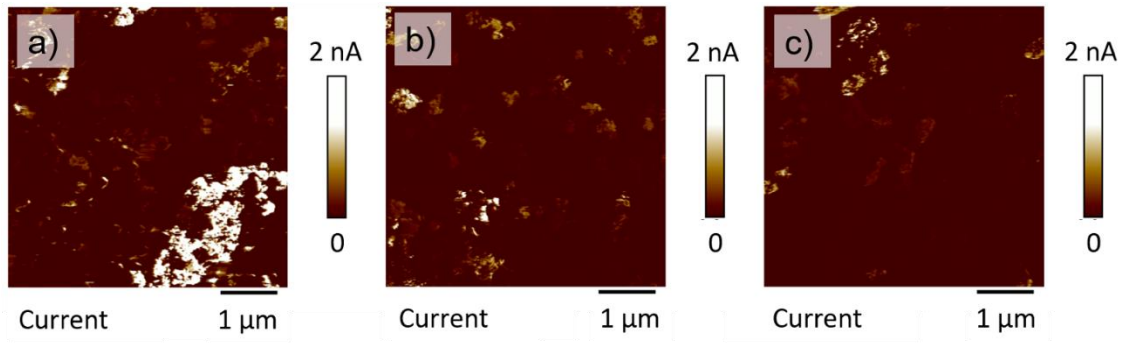


Figure 2.7 - AFM measurements of conductive area for the anodes prepared using different solvents: a) cyclohexanol, b) ethane-1,2-diol, c) propane-1,2-diol.

In Figure 2.8, the surface topography of 400 μm^2 of the three different surface structures is shown; the roughness was evaluated from the AFM topography images. The highest

roughness of 120 ± 30 nm was observed for the anode prepared using ethane-1,2-diol as solvent, followed by the sample prepared using cyclohexanol - 110 ± 10 nm; the lowest roughness was determined for the sample prepared using propane-1,2-diol, with a roughness of 54 ± 2 nm. The higher roughness of sample prepared using ethane-1,2-diol is likely caused by the large height differences between the ionomer agglomerates and the catalyst-containing phase and does not represent the roughness of the surface film; the large inhomogeneity is also indicated by the large error. The sample prepared using ethane-1,2-diol exhibited the most heterogeneous distribution, with regions of high catalyst density and large ionomer areas without any catalyst.

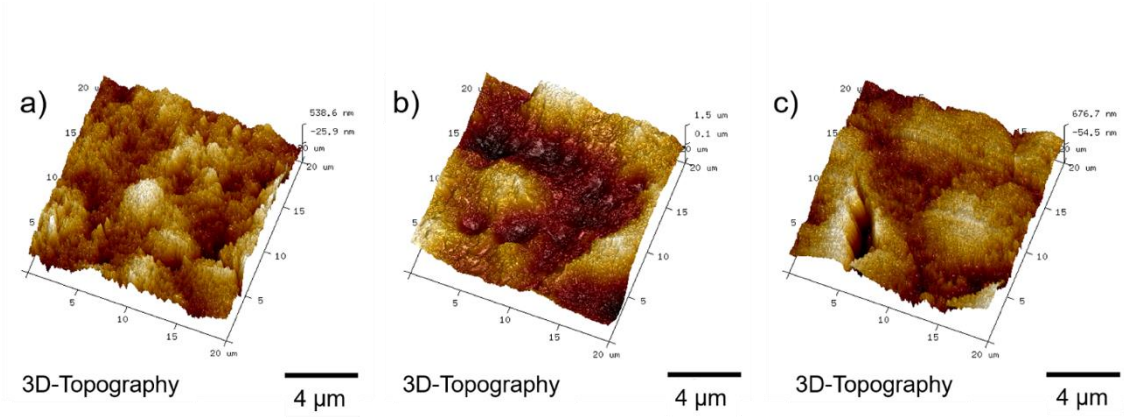


Figure 2.8 - AFM 3D-topography measurements of the anodes prepared using different solvents: a) cyclohexanol, b) ethane-1,2-diol, c) propane-1,2-diol.

2.3.4. ELECTROLYSIS MEASUREMENTS

Chronoamperometries of the CCMs with anodes coated using different solvents are depicted in Figure 2.9a. After 180 min of operation, the anode coated using cyclohexanol solvent delivered the highest current density at 1.7 V, followed by the anode coated using propane-1,2-diol. The relative permittivity of the ink solvents impacts on the ionomer conformation and distribution in the catalyst layer. The three solvents used in this work (with $\varepsilon > 10$) make Nafion ionomer remain in solution form [24]. From Figure 2.9a, electrochemical activity is higher for solvents with lower relative permittivity. This fact suggests that solvents with ε values closer to the colloidal form frontier ($3 < \varepsilon < 10$) of

the ionomer generate a better triple-phase boundary, thus promoting a better catalyst utilization.

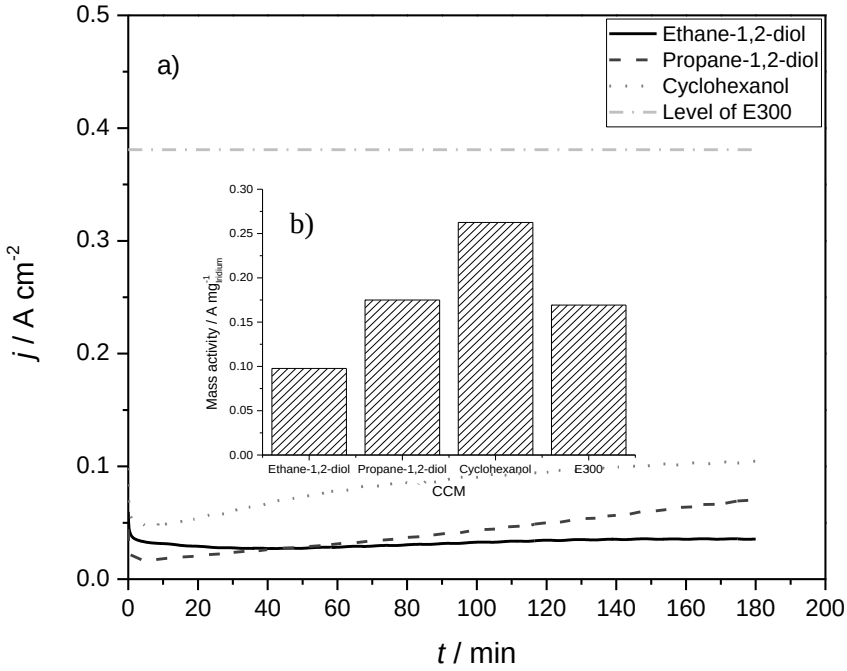


Figure 2.9 - a) Chronoamperometries at 1.7 V and 40 ºC of CCMs with anodes coated using ethane-1,2-diol propane-1,2-diol, and cyclohexanol as solvents. b) Iridium-mass activity of fabricated CCMs and E300 (Greenerity) at 1.7 V and 40 °C.

The single curve with a relatively constant current value at end of tests corresponds to the anode coated using ethane-1,2-diol as ink vehicle. The slow electrochemical activity improvement observed in Figure 2.9a can be attributed to CCM activation phenomenon, which is a typical procedure in PEM fuel cells [51]. The origin of this improvement might be related to the accommodation of the microstructure of the catalyst layer and membrane/ionomer. Additionally, high potentials typical in water electrolysis (operation above 1.4 V) enable oxidation of Ir to the more OER-active IrO_2 [52]. A commercial CCM (E300 from Greenerity) was also tested under the same conditions (Figure S3 in Supplementary Information). The commercial CCM had been previously activated by

the manufacturer. Mass activities of the fabricated CCMs are presented in Figure 2.9b. Even though the CCMs coated using propane-1,2-diol and cyclohexanol did not reach steady-state activity at end of tests, they already exceeded the iridium-mass activity of E300 at 1.7 V and 40 ºC. The screen-printed CCM using cyclohexanol as ink vehicle, delivered the highest Ir-mass activity, that is 0.26 A mg^{-1} at 1.7 V and 40 ºC. Compared to the commercial CCM, a higher catalyst utilization was observed for the screen printed CCM using cyclohexanol as a solvent.

Electrochemical impedance spectra (Figure 2.10) were recorded in galvanostatic mode (at 35 mA cm^{-2}) at end of tests. The EIS spectra were fitted with the equivalent circuit depicted in Figure 2.10 that consisted in (RQ) elements, representing a parallel combination of a resistance with a constant phase element. The high frequency resistances (R_S), associated to the electrolyte, were similar and the highest for the CCMs coated with ethane-1,2-diol and cyclohexanol (~ 0.29 Ω cm^2), the lowest for the commercial CCM (~ 0.22 Ω cm^2), followed by the CCM coated with propane-1,2-diol (~ 0.25 Ω cm^2). R_1 is associated to the HER and the lowest values were obtained for the CCM coated with cyclohexanol and commercial CCM (~ 33 mΩ cm^2), followed by the CCM coated with ethane-1,2-diol (~ 64 mΩ cm^2) and the highest for the CCM coated with propane-1,2-diol (~ 74 mΩ cm^2). Finally, R_2 is associated to the OER and is responsible for the major contribution for the overall impedances. As discussed above and following the trend observed in the chronoamperometries (Figure 2.9), the values for R_2 are higher for the anodes coated with the solvents with higher relative permittivity. Among the fabricated CCMs, the highest R_2 value was obtained for the anode coated ethane-1,2-diol (~ 1.5 Ω cm^2), followed by the anode coated with propane-1,2-diol (~ 0.98 Ω cm^2) and the lowest for the anode coated with cyclohexanol (~ 0.86 Ω cm^2). Despite the commercial CCM presented the lowest R_2 among all CCMs (~ 0.56 Ω cm^2), this difference can be attributed to the higher Ir loading and to several others factors that depend on the materials and methods used in the manufacture.

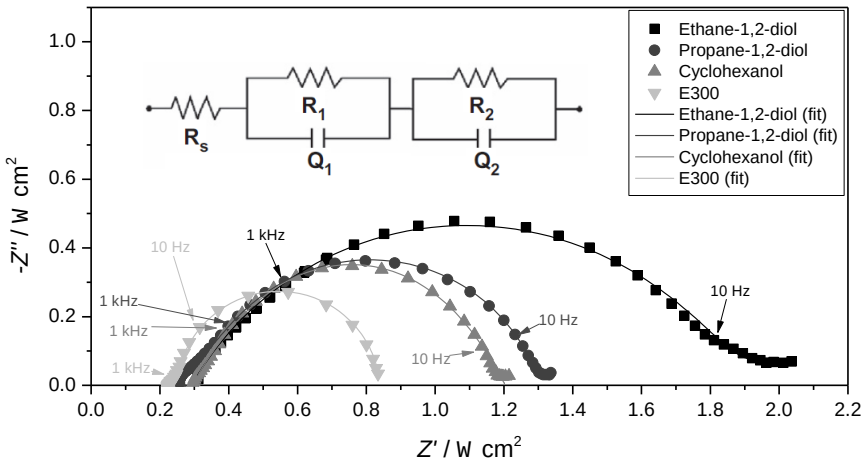


Figure 2.10 - Impedance spectra at 35 mA cm^{-2} and 40 ºC of E300 (Greenerity) and fabricated CCMs with anodes coated using ethane-1,2-diol; propane-1,2-diol; and cyclohexanol as solvents.

Table 2.3 - Parameters evaluated from EIS data fitting to equivalent circuit shown in Fig. 10 for the fabricated and commercial CCMs.

CCMs	R_S / mΩ	R_1 / mΩ	Q_1 / mF	R_2 / mΩ	Q_2 / mF
With swelling treatment	49.4	32.0	0.433	522.6	0.579
Without swelling treatment	75.8	51.2	0.364	617.8	0.290
Ethane-1,2-diol	74.1	16.0	1.48	374	0.999
Propane-1,2-diol	63.4	18.4	2.35	245	3.95
Cyclohexanol	73.5	8.41	4.26	214	4.77
E300	55.3	8.30	48.7	146	306

2.4. CONCLUSIONS

Catalyst coated membranes for PEM electrolysers were successfully fabricated by screen printing technique using three different solvents in the inks and a mixture of Ir-black

catalyst and Ti_4O_7 support. As the electronic conductivity is correlated to the conductive surface area derived by AFM, a decrease of ionomer content could lead to a higher electrochemical performance.

This work unveils promising OER activities from inexpensive and easy-scalable screen-printed anodes with reduced iridium loadings of 0.4 ± 0.02 mg cm^{-2}, which is 82 % lower than that of the commercial reference. The membrane swelling treatment was found to be effective, minimizing the membrane swelling during the coating process using ethane-1,2-diol as solvent of the paste, without hindering the electrolyser performance.

Cyclohexanol was found to be a suitable single solvent for coating anodes directly on the membrane. It did not cause any noticeable swelling of the membrane thus enabling to skip the membrane swelling treatment. PEM electrolyser tests at constant 1.7 V showed that the screen-printed CCM, using cyclohexanol as ink vehicle, delivers the highest current among all the prepared samples. Furthermore, this CCM also delivered 35 % higher Ir-mass activity than the commercial reference.

REFERENCES

[1] M. Carmo, D. L. Fritz, J. Mergel, and D. Stolten, "A comprehensive review on PEM water electrolysis," *International Journal of Hydrogen Energy*, vol. 38, no. 12. pp. 4901–4934, 2013, doi: 10.1016/j.ijhydene.2013.01.151.

[2] K. A. Friedrich, "PlanDelyKad: Study on Large Scale Water Electrolysis and Hydrogen Storage (in German). German Federal Ministry for Economic Affairs and Energy (BMWi), Berlin," 2015.

[3] F. Barbir, "PEM electrolysis for production of hydrogen from renewable energy sources," *Sol. Energy*, vol. 78, no. 5, pp. 661–669, 2005, doi: 10.1016/j.solener.2004.09.003.

[4] K. E. Ayers, C. Capuano, and E. B. Anderson, "Recent Advances in Cell Cost and Efficiency for PEM-Based Water Electrolysis," *ECS Trans.* , vol. 41, no. 10, pp. 15–22, May 2012, doi: 10.1149/1.3684798.

[5] K. E. Ayers *et al.*, "Research Advances towards Low Cost, High Efficiency PEM Electrolysis," *ECS Trans.* , vol. 33, no. 1, pp. 3–15, Oct. 2010, doi: 10.1149/1.3484496.

[6] L. Bertuccioli *et al.*, "Study on development of water electrolysis in the EU by E4tech Sàrl with Element Energy Ltd for the Fuel Cells and Hydrogen Joint Undertaking," Feb. 2014, url: https://www.sintef.no/contentassets/1ac5d74dbeac4e5ea19aa3079df0997a/01-05_lehner_e4tech.pdf.

[7] U. Babic, M. Suermann, F. N. Büchi, L. Gubler, and T. J. Schmidt, "Critical Review—Identifying Critical Gaps for Polymer Electrolyte Water Electrolysis Development," *J. Electrochem. Soc.* , vol. 164, no. 4, pp. F387–F399, Jan. 2017, doi: 10.1149/2.1441704jes.

[8] K. A. Lewinski, D. van der Vliet, and S. M. Luopa, "NSTF Advances for PEM Electrolysis - the Effect of Alloying on Activity of NSTF Electrolyzer Catalysts and Performance of NSTF Based PEM Electrolyzers," *ECS Trans.* , vol. 69, no. 17, pp. 893–917, Sep. 2015, doi: 10.1149/06917.0893ecst.

[9] S. M. Alia, S. M. Shulda, C. Ngo, S. Pylypenko, and B. S. Pivovar, "Iridium Nanowires As Highly Active, Oxygen Evolution Reaction Electrocatalysts," *Meet. Abstr.* , vol. MA2017-02, no. 37, p. 1655, Sep. 2017, url:

http://ma.ecsdl.org/content/MA2017-02/37/1655.abstract.

[10] P. Lettenmeier *et al.*, "Durable Membrane Electrode Assemblies for Proton Exchange Membrane Electrolyzer Systems Operating at High Current Densities," *Electrochim. Acta*, vol. 210, pp. 502–511, Aug. 2016, doi: 10.1016/j.electacta.2016.04.164.

[11] B. Bladergroen, H. Su, S. Pasupathi, and V. Linkov, "Overview of Membrane Electrode Assembly Preparation Methods for Solid Polymer Electrolyte Electrolyzer," in *Electrolysis*, 2012, doi: 10.5772/52947.

[12] G. Chen, S. R. Bare, and T. E. Mallouk, "Development of Supported Bifunctional Electrocatalysts for Unitized Regenerative Fuel Cells," *J. Electrochem. Soc.* , vol. 149, no. 8, pp. A1092–A1099, Aug. 2002, doi: 10.1149/1.1491237.

[13] S. Siracusano, V. Baglio, C. D'Urso, V. Antonucci, and A. S. Aricò, "Preparation and characterization of titanium suboxides as conductive supports of IrO2 electrocatalysts for application in SPE electrolysers," *Electrochim. Acta*, vol. 54, no. 26, pp. 6292–6299, 2009, doi: 10.1016/j.electacta.2009.05.094.

[14] R. E. Fuentes, J. Farell, and J. W. Weidner, "Multimetallic Electrocatalysts of Pt, Ru, and Ir Supported on Anatase and Rutile TiO2 for Oxygen Evolution in an Acid Environment," *Electrochem. Solid-State Lett.* , vol. 14, no. 3, pp. E5–E7, Mar. 2011, doi: 10.1149/1.3528163.

[15] P. Mazúr, J. Polonský, M. Paidar, and K. Bouzek, "Non-conductive TiO2 as the anode catalyst support for PEM water electrolysis," *Int. J. Hydrogen Energy*, vol. 37, no. 17, pp. 12081–12088, 2012, doi: 10.1016/j.ijhydene.2012.05.129.

[16] A. Stoyanova, G. Borisov, E. Lefterova, and E. Slavcheva, "Oxygen evolution on Ebonex-supported Pt-based binary compounds in PEM water electrolysis," *Int. J. Hydrogen Energy*, vol. 37, no. 21, pp. 16515–16521, 2012, doi: 10.1016/j.ijhydene.2012.02.032.

[17] E. Slavcheva, G. Borisov, E. Lefterova, E. Petkucheva, and I. Boshnakova, "Ebonex supported iridium as anode catalyst for PEM water electrolysis," *Int. J. Hydrogen Energy*, vol. 40, no. 35, pp. 11356–11361, 2015, doi: 10.1016/j.ijhydene.2015.03.005.

[18] L. Wang *et al.*, "Nanostructured Ir-supported on Ti4O7 as cost effective anode for proton exchange membrane (PEM) electrolyzers," *Phys. Chem. Chem. Phys.*, vol. 18, no. 6, pp. 4487–4495, Dec. 2016, doi: 10.1039/c5cp05296c.

[19] T. Ioroi and K. Yasuda, "Iridium Nanoparticles Supported on Magneli Phase Ti4O7 for PEM Water Electrolyzers," *Meet. Abstr.* , vol. MA2016-02, no. 38, p. 2419, Sep. 2016, url: http://ma.ecsdl.org/content/MA2016-02/38/2419.abstract.

[20] J.-E. Won *et al.*, "PtIr/Ti4O7 as a bifunctional electrocatalyst for improved oxygen reduction and oxygen evolution reactions," *J. Catal.*, vol. 358, pp. 287–294, 2018, doi: 10.1016/j.jcat.2017.12.013.

[21] M. Uchida, Y. Aoyama, N. Eda, and A. Ohta, "New Preparation Method for Polymer-Electrolyte Fuel Cells," *J. Electrochem. Soc.* , vol. 142, no. 2, pp. 463–468, Feb. 1995, doi: 10.1149/1.2044068.

[22] T. T. Ngo, T. L. Yu, and H. L. Lin, "Influence of the composition of isopropyl alcohol/water mixture solvents in catalyst ink solutions on proton exchange membrane fuel cell performance," *J. Power Sources*, vol. 225, pp. 293–303, 2013, doi: 10.1016/j.jpowsour.2012.10.055.

[23] R. Yudianti, H. Onggo, and A. Syampurwadi, "Molecular Conformation of Nafion Ionomer on Electrocatalyst Layer Prepared by Screen Printing Technique," *Int. J. Electrochem. Sci*, vol. 9, pp. 3047–3059, 2014, doi: 10.1016/s1452-3981(23)07990-7.

[24] W. Wang, S. Chen, J. Li, and W. Wang, "Fabrication of catalyst coated membrane with screen printing method in a proton exchange membrane fuel cell," *Int. J. Hydrogen Energy*, vol. 40, no. 13, pp. 4649–4658, 2015, doi: 10.1016/j.ijhydene.2015.02.027.

[25] C. S. Kim, Y. G. Chun, D. H. Peck, and D. R. Shin, "Method for fabricating membrane and electrode assembly for polymer electrolyte membrane fuel cells." Google Patents, 2001, url: https://www.google.pt/patents/US6180276.

[26] E. Antolini, L. Giorgi, A. Pozio, and E. Passalacqua, "Influence of Nafion loading in the catalyst layer of gas-diffusion electrodes for PEFC," *J. Power Sources*, vol. 77, no. 2, pp. 136–142, 1999, doi: 10.1016/s0378-7753(98)00186-4.

[27] E. Passalacqua, F. Lufrano, G. Squadrito, A. Patti, and L. Giorgi, "Nafion content in the catalyst layer of polymer electrolyte fuel cells: effects on structure and performance," *Electrochim. Acta*, vol. 46, no. 6, pp. 799–805, 2001, doi: 10.1016/s0013-4686(00)00679-4.

[28] T. E. Springer, M. S. Wilson, and S. Gottesfeld, "Modeling and Experimental Diagnostics in Polymer Electrolyte Fuel Cells," *J. Electrochem. Soc.* , vol. 140, no. 12, pp. 3513–3526, Dec. 1993, doi: 10.1149/1.2221120.

[29] K. Chan and M. Eikerling, "Water balance model for polymer electrolyte fuel cells with ultrathin catalyst layers," *Phys. Chem. Chem. Phys.*, vol. 16, no. 5, pp. 2106–2117, 2014, doi: 10.1039/c3cp54849j.

[30] N. Agmon, "The Grotthuss mechanism," *Chem. Phys. Lett.*, vol. 244, no. 5–6, pp. 456–462, Oct. 1995, doi: 10.1016/0009-2614(95)00905-j.

[31] M. J. Eslamibidgoli, J. Huang, T. Kadyk, A. Malek, and M. Eikerling, "How theory and simulation can drive fuel cell electrocatalysis," *Nano Energy*, vol. 29, pp. 334–361, 2016, doi: 10.1016/j.nanoen.2016.06.004.

[32] K.-H. Kim *et al.*, "The effects of Nafion® ionomer content in PEMFC MEAs prepared by a catalyst-coated membrane (CCM) spraying method," *Int. J. Hydrogen Energy*, vol. 35, no. 5, pp. 2119–2126, 2010, doi: 10.1016/j.ijhydene.2009.11.058.

[33] S. Siracusano, N. Van Dijk, E. Payne-Johnson, V. Baglio, and A. S. Aricò, "Nanosized IrOx and IrRuOx electrocatalysts for the O2 evolution reaction in PEM water electrolysers," *Appl. Catal. B Environ.*, vol. 164, pp. 488–495, 2015, doi: 10.1016/j.apcatb.2014.09.005.

[34] H.-S. Oh, H. N. Nong, T. Reier, M. Gliech, and P. Strasser, "Oxide-supported Ir nanodendrites with high activity and durability for the oxygen evolution reaction in acid PEM water electrolyzers," *Chem. Sci.*, vol. 6, no. 6, pp. 3321–3328, 2015, doi: 10.1039/c5sc00518c.

[35] P. Lettenmeier *et al.*, "Nanosized IrOx-Ir Catalyst with Relevant Activity for Anodes of Proton Exchange Membrane Electrolysis Produced by a Cost-Effective Procedure," *Angew. Chemie*, vol. 128, no. 2, pp. 752–756, Jan. 2016, doi: 10.1002/ange.201507626.

[36] Z. Hou, P. Ming, D. Xing, S. Song, K. Zhang, and Y. Zhang, "Preparing method for integrated membrane-catalyst coated layer membrane electrode for a fuel cell." Google Patents, 2012, url: https://www.google.pt/patents/US20120279648.

[37] P. Lettenmeier *et al.*, "Comprehensive investigation of novel pore-graded gas diffusion layers for high-performance and cost-effective proton exchange membrane electrolyzers," *Energy Environ. Sci.*, vol. 10, no. 12, pp. 2521–2533, 2017, doi: 10.1039/c7ee01240c.

[38] P. Lettenmeier *et al.*, "Low-Cost and Durable Bipolar Plates for Proton Exchange Membrane Electrolyzers," *Sci. Rep.*, vol. 7, p. 44035, Mar. 2017, doi:

10.1038/srep44035.

[39] P. Lettenmeier, R. Wang, R. Abouatallah, F. Burggraf, A. S. Gago, and K. A. Friedrich, "Coated Stainless Steel Bipolar Plates for Proton Exchange Membrane Electrolyzers," *J. Electrochem. Soc.*, vol. 163, no. 11, pp. F3119–F3124, Jul. 2016, doi: 10.1149/2.0141611jes.

[40] A. S. Gago *et al.*, "Protective coatings on stainless steel bipolar plates for proton exchange membrane (PEM) electrolysers," *J. Power Sources*, vol. 307, pp. 815–825, Mar. 2016, doi: 10.1016/j.jpowsour.2015.12.071.

[41] S. Siracusano, V. Baglio, F. Lufrano, P. Staiti, and A. S. Aricò, "Electrochemical characterization of a PEM water electrolyzer based on a sulfonated polysulfone membrane," *J. Memb. Sci.*, vol. 448, no. Supplement C, pp. 209–214, 2013, doi: 10.1016/j.memsci.2013.07.058.

[42] C. Rozain and P. Millet, "Electrochemical characterization of Polymer Electrolyte Membrane Water Electrolysis Cells," *Electrochim. Acta*, vol. 131, pp. 160–167, Jan. 2014, doi: 10.1016/j.electacta.2014.01.099.

[43] I. Dedigama *et al.*, "In situ diagnostic techniques for characterisation of polymer electrolyte membrane water electrolysers – Flow visualisation and electrochemical impedance spectroscopy," *Int. J. Hydrogen Energy*, vol. 39, no. 9, pp. 4468–4482, Mar. 2014, doi: 10.1016/j.ijhydene.2014.01.026.

[44] K. Elsøe, L. Grahl-Madsen, G. G. Scherer, J. Hjelm, and M. B. Mogensen, "Electrochemical Characterization of a PEMEC Using Impedance Spectroscopy," *J. Electrochem. Soc.* , vol. 164, no. 13, pp. F1419–F1426, Jan. 2017, doi: 10.1149/2.0651713jes.

[45] S. Helmly, R. Hiesgen, T. Morawietz, X.-Z. Yuan, H. Wang, and K. Andreas Friedrich, "Microscopic Investigation of Platinum Deposition in PEMFC Cross-Sections Using AFM and SEM," *J. Electrochem. Soc.* , vol. 160, no. 6, pp. F687–F697, Jan. 2013, doi: 10.1149/2.130306jes.

[46] R. Hiesgen, T. Morawietz, M. Handl, and K. A. Friedrich, "Structure and conductivity of fuel cell membranes and catalytic layers investigated by AFM," *MRS Proc.*, vol. 1774, pp. 19–24, 2015, doi: 10.1557/opl.2015.725.

[47] T. Morawietz, A. Singraber, C. Dellago, and J. Behler, "How van der Waals interactions determine the unique properties of water," *Proc. Natl. Acad. Sci.* , vol. 113, no. 30, pp. 8368–8373, Jul. 2016, doi: 10.1073/pnas.1602375113.

[48] Q. Deng, C. A. Wilkie, R. B. Moore, and K. A. Mauritz, "TGA–FTi.r.

investigation of the thermal degradation of Nafion® and Nafion®/[silicon oxide]-based nanocomposites," *Polymer (Guildf).*, vol. 39, no. 24, pp. 5961–5972, 1998, doi: 10.1016/s0032-3861(98)00055-x.

[49] G. Chen, S. R. Bare, and T. E. Mallouk, "Development of Supported Bifunctional Electrocatalysts for Unitized Regenerative Fuel Cells," *J. Electrochem. Soc.*, vol. 149, no. 8, p. A1092, 2002, doi: 10.1149/1.1491237.

[50] K. Senevirathne, R. Hui, S. Campbell, S. Ye, and J. Zhang, "Electrocatalytic activity and durability of Pt/NbO2 and Pt/Ti4O7 nanofibers for PEM fuel cell oxygen reduction reaction," *Electrochim. Acta*, vol. 59, pp. 538–547, 2012, doi: 10.1016/j.electacta.2011.11.005.

[51] Z. Qi and A. Kaufman, "Activation of low temperature {PEM} fuel cells," *J. Power Sources*, vol. 111, no. 1, pp. 181–184, 2002, doi: 10.1016/S0378-7753(02)00273-2.

[52] S. Siracusano, V. Baglio, S. A. Grigoriev, L. Merlo, V. N. Fateev, and A. S. Aricò, "The influence of iridium chemical oxidation state on the performance and durability of oxygen evolution catalysts in PEM electrolysis," *J. Power Sources*, vol. 366, no. Supplement C, pp. 105–114, 2017, doi: 10.1016/j.jpowsour.2017.09.020.

CHAPTER 3

AIR BLEEDING STRATEGIES TO INCREASE THE EFFICIENCY OF PROTON EXCHANGE MEMBRANE FUEL CELL STATIONARY APPLICATIONS FUELLED WITH CO PPM-LEVELS

3

AIR BLEEDING STRATEGIES TO INCREASE THE EFFICIENCY OF PROTON EXCHANGE MEMBRANE FUEL CELL STATIONARY APPLICATIONS FUELLED WITH CO PPM-LEVELS

Sofia Delgado, Tiago Lagarteira and Adélio Mendes

Adapted from the International Journal of Electrochemical Science, 2020, 15

ABSTRACT

The use of proton exchange membrane fuel cells (PEMFCs) as efficient electric generators for residential and tertiary sectors to replace conventional internal combustion engines greatly depends on the recent advances in purification technologies. Preferential oxidation and pressure swing adsorption offer reformate hydrogen streams with CO concentrations down to fractional ppm-level. However, even small traces of CO cause reversible and irreversible performance losses of the PEMFC stack due to poisoning of the anode Pt catalyst. This work reports the performance loss upon H_2 contamination down to the ppm level and the efficiency gains after applying internal and external air bleeding to the anode of the fuel cell. By adding solely 1 % of air bleed to a 10 ppm CO-contaminated hydrogen stream, the full performance recovery is achieved without compromising the stability of the cell. Moreover, a performance loss of less than 1 % – US DoE target value for reformate streams – can be met using Pt-Ru based anode catalysts allied to a minimal air bleed concentration. Long term experiments, of *ca.* 80 h, are performed to assess the stability of the fuel cells fed with contaminated hydrogen and compare the long-term impacts of both internal and external air bleeding.

Keywords: Proton exchange membrane fuel cell; Membrane electrodes assembly; CO poisoning; Air bleeding.

3.1. INTRODUCTION

Low-temperature proton exchange membrane fuel cells (PEMFCs) are considered an attractive candidate to power small stationary units including off-grid energy, backup power systems and combined heat and power (CHP) systems for industry and buildings. CHP systems based on fuel cells are expected to replace natural gas heaters for domestic cogeneration, because of their higher fuel efficiency, modularity, and environmentally friendly operation [1]. However, some challenges still hinder the widespread commercialization of the technology. The core component of the fuel cell, the membrane-electrodes assembly (MEA), plays a crucial role on the overall cost of fuel stacks due to the need of highly active and durable catalysts and electrodes. In parallel to the high cost of the precious-metal catalysts, the small world-wide production of highly pure hydrogen is a major drawback [2].

Systems for stationary applications usually adopt a fuel processor to produce hydrogen from fossil (natural gas, LPG) or renewable (bioethanol, biogas, etc.) fuels [3]. The reforming of hydrocarbons followed by water-gas shift and purification is the most common production route of hydrogen. Nonetheless, this production route still delivers contaminants (CO_2, H_2S and mainly CO) in the hydrogen stream that poison platinum catalyst activity and durability [4], [5]. Therefore, ISO 14687-3 details hydrogen quality requirements for PEM fuel cells for stationary applications. It defines three categories: two with $H_2 \geq 50$ % and CO ≤ 10 ppm, and one with $H_2 \geq 99.9$ % and CO ≤ 0.2 ppm. Hydrogen produced by conventional fuel processors can only fulfil the requirements of the first two categories. Japan appears as the world leader on micro-combined heat and power systems based on fuel cells (m-CHP-PEMFC) for buildings with over 140 000 units sold; likewise, Europe is expected to promote the exponential growing of m-CHP-PEMFC [6], [7]. The chemisorption of CO on Pt catalyst particles surface reduces the number of active sites for H_2 electro-oxidation [8], [9] and hence the fuel cell power output and its useful life. The performance of the fuel cell anode is then highly sensitive to small traces of CO (down to fractional ppm-level) and dependent on operating conditions such as temperature, the exposure time to CO, pressure, current density, relative humidity and fuel stoichiometry [10]. Carbon dioxide has a minimal affinity for

the Pt catalyst and therefore does not affect the performance of the cell at low current densities (< 300 mA cm^{-2}), behaving as an inert specie [11].

In the last two decades, several works have been published focusing on the mitigation of CO poisoning in PEM fuel cells [10], [12]–[14]. The most conventional approach is to use CO-tolerant catalysts at the anode, normally obtained by combining Pt with other metals. Pt-Ru alloy is typically used as CO-tolerant catalyst albeit some impact on the fuel cell durability due to Ru dissolution and migration to the cathode [15], [16]. The CO tolerance evidenced by Pt-Ru catalysts is mainly attributed to two mechanisms, the electronic tuning of Pt d-band structure (ligand effect) and/or the acceleration of CO oxidation to CO_2 by providing oxygen species to CO adsorbed on Pt surfaces [17]. The ligand effect consists in the modification of Pt electronic structure that either weakens the Pt-CO bond thus promoting CO oxidation by nearby OH groups; or improves Pt-H_2O activation that leads to direct oxidation of CO on the Pt sites [18].

Another approach to inhibit CO poisoning is to introduce trace concentrations of oxygen in the anode. Oxygen can be supplied to the anode by: i) internal oxygen/air bleeding from the cathode through the membrane; ii) external oxygen/air bleeding; iii) introduction of H_2O_2 in the anode bubbler [10]. Oxygen permeation through the membrane is commonly described in terms of sorption-diffusion mechanisms [19]; specifically, during PEMFC operation oxygen sorbs into the membrane and diffuses from the cathode to the anode side preferably through its hydrated pathways. The membrane permeability to oxygen is proportional to the product of Fick's diffusion coefficient and solubility coefficient [20],[21]. The membrane permeability to oxygen increases with the operating temperature and with the membrane humidification [22]–[25]. On the other hand, oxygen permeation increases with the partial pressure difference between the two sides of the membrane but decreases for thicker membranes [26]. The permeated oxygen is partly responsible for the oxidation of CO to CO_2 at the anode catalyst particles surface through heterogeneous catalysis described by the Langmuir-Hinshelwood mechanism [27]. Yet, some negative aspects may arise from the presence of excessive O_2 at the anode such as higher anode overpotential caused by water production from the hydrogen oxidation, catalyst sintering due to the highly exothermic

hydrogen oxidation, and membrane degradation from the side-production of H_2O_2 [16]. Therefore, air (or oxygen) bleeding must be tuned depending on the CO contamination levels [28].

In this work, the impacts of two different techniques for the mitigation of CO poisoning are assessed, internal and external air bleeding. For both techniques, oxygen traces at the anode were tuned to determine the minimum amount able to fully recover the efficiency drop caused by CO poisoning. Longer operation under CO contamination was compared for both techniques to assess the degradation through potential decay. To the best of the authors' knowledge, these techniques are compared for the first time under PEMFC operating conditions suitable for stationary applications, such as m-CHP-PEMFC.

3.2. EXPERIMENTAL

The electrochemical measurements were carried out in a 25 cm^2 fuel cell purchased to Pragma Industries. The graphite flow fields used in both the anode and cathode were single channel type. The cell compression was set to *ca.* 2 MPa to guarantee the electrical contact between the gas diffusion electrodes (GDE) and the bipolar plates.

MEA#1 was made of a Nafion 212 membrane (N212, 51 μm of thickness) sandwiched by two GDEs, all purchased to Quintech. The anode catalyst layer contained 0.5 mg cm^{-2} of PtRu and the cathode catalyst layer had 0.5 mg cm^{-2} of Pt. The GDEs were hot-pressed to the membrane at 120 °C and 17 bar for 5 minutes. The French Alternative Energies and Atomic Energy Commission (CEA) provided MEA#2 that employs a Nafion reinforced-stabilized HP membrane (NRHP) with 22 μm of thickness. The catalyst layers contained 0.585 mg cm^{-2} of PtRu (66 wt.% of Pt) in the anode and PtCo alloy with 0.468 mg cm^{-2} of Pt in the cathode. The gas diffusion layers of both MEAs (Sigracet 28 BC, SGL Carbon) were 220 μm thick.

The mass flow rates of the reactants, humidification and temperatures of the lines were controlled with a test station. The anode was fed with either high purity H_2 (99.999 %), mixtures of CO/H_2 or synthetic air whilst the cathode was fed with synthetic air. CO was supplied from a cylinder containing a mixture of H_2 balanced with 100 ppm of CO

(Linde). Anode and cathode were humidified by bubbling the feed gases into ultra-pure water; the relative humidity was set to 50 % for both the anode and cathode. The stoichiometries of the reactants were set to 1.5/2 for the anode and cathode, respectively. Subsequently, the reactant flow rates were calculated using Faraday's equation, assuming a coulombic efficiency of 100 %.

An electrochemical workstation (Zahner IM6eX) coupled with a PP-240 power potentiostat was used to perform the electrochemical measurements. The MEAs were subjected to break-in at 500 mA cm^{-2}. The conditions for the break-in and experiments of interest are described in

Table 3.**1**. The break-in step (conditions of Run #1) was considered completed when the cell potential variation was less than 5 mV h^{-1} at 500 mA cm^{-2}.

After achieving steady-state performance, a polarization curve was recorded in galvanostatic mode. The cell potential was recorded (Run #2) as a function of the current density with a dwell time of 3 minutes. Chronopotentiometries were performed at 500 mA cm^{-2} following the conditions of Run #2-Run #10 to evaluate the magnitude of performance loss due to CO exposure and the performance gains after implementing each bleeding technique.

Electrochemical impedance spectroscopy (EIS) was performed in galvanostatic mode at 500 mA cm^{-2}, with a perturbation amplitude of 40 mA cm^{-2} between 10 kHz and 100 mHz. Figure 3.1 depicts the equivalent circuit of elements used to fit the electrochemical impedance spectra. The equivalent circuit chosen comprises two simple circuits, each with a constant phase element ($Q_{a/c}$) and a resistor ($R_{a/c}$) in parallel, along with a resistor connected in series (R_m) [29]. R_m accounts mostly for the resistance associated to protonic conduction through the membrane, R_a and R_c are the charge transfer resistances associated to anode and cathode, respectively. For the sake of convergence and getting relevant data, the *n* value was not fitted and was set to 0.5, which corresponds to a 45º phase angle. EIS low frequency data, related to mass transfer overpotential, was not included in the fittings since it was not relevant for this study.

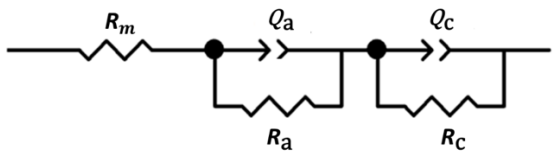


Figure 3.1 - Schematic representation of the equivalent circuit for the PEMFC.

In-situ cyclic voltammetry (CV) was performed to both anode and cathode of the MEAs to estimate the electrochemical surface area (ECSA) at the beginning and end of experiments. The working electrode was purged with N_2 to remove any adsorbed O_2, and the counter electrode was fed with H_2, maintaining the stoichiometry and flow rates calculated for 100 mA cm^{-2} between H_2/O_2. The relative humidity was set to 50 %, the back pressure was set to 1.5 bar for both electrodes, the scan rate was set to 50 mV s^{-1} and the cell temperature was kept at 70 °C.

Table 3.1 - Performed tests and corresponding operating conditions.

#	MEA#	*p* H_2	*p* Air	RH H_2	RH Air	Fuel	Temperature
1 – Break-in	1 / 2	1.5	1.5	80 %	80 %	Pure H_2	80 °C
2 - Reference	1 / 2	1.2	1.2	50 %	50 %	Pure H_2	70 °C
3	1 / 2	1.2	1.2	50 %	50 %	H_2 + 10 ppm CO	70 °C
4	1 / 2	1.1	1.2	50 %	50 %	H_2 + 10 ppm CO	70 °C
5	1 / 2	1.1	1.3	50 %	50 %	H_2 + 10 ppm CO	70 °C
6	2	1.1	1.3	50 %	50 %	H_2 + 20 ppm CO	70 °C
7	2	1.1	1.3	50 %	50 %	H_2 + 30 ppm CO	70 °C
8	1	1.2	1.2	50 %	50 %	H_2 + 10 ppm CO + 0.5 % Air	70 °C
9	1 / 2	1.2	1.2	50 %	50 %	H_2 + 10 ppm CO + 1 % Air	70 °C

10	1	1.2	1.2	50 %	50 %	H_2 + 10 ppm CO + 1.5 % Air	70 °C

3.3. RESULTS AND DISCUSSION

3.3.1. ELECTROCHEMICAL PERFORMANCE WITH PURE HYDROGEN

The polarization curves (Figure 3.2a) and EIS spectra at 500 mA cm^{-2} (Figure 3.2b) of MEA#1 and MEA#2 were obtained for Reference conditions –

Table 3.**1**. MEA#2 outperformed MEA#1 at current densities higher than 300 mA·cm^{-2}. The higher thickness of membrane N212, in MEA#1, compared with membrane NRHP, inserted in MEA#2, makes its ohmic overpotential higher, limiting the protonic conduction and decreasing the power output [30]. Nafion HP is a sandwich type membrane, similar to its predecessor Nafion XL (*ca.* 28 µm), comprising an inner layer of PTFE-rich reinforcing mesh that provides mechanical stability, coated with two ultra-thin layers of Nafion in each side (ca. 7 µm thick each). This membrane provides high proton conductivity with better chemical/mechanical durability compared to the benchmark counterparts (*e.g.* Nafion 212 or Nafion 115) [31]–[33]. Nonetheless, the activation overpotential (< 100 mA·cm^{-2}) of MEA#2 is higher comparing to MEA#1, thanks to the higher Pt loading of the latter. Nevertheless, ohmic losses are smaller for MEA#2 (Figure 3.2a). From the EIS spectra (Figure 3.2b), the difference in the ohmic resistances of MEA#2 and MEA#1 – 107.4 mΩ cm^2 vs 221.4 mΩ cm^2, respectively – was assigned to the membranes thickness where MEA#2 is equipped with a membrane *ca.* 50 % thinner (22 µm) than MEA#1 (51 µm); these results are in line with previous studies [30], [34]. Ohmic losses tend to increase linearly with membrane thickness [35]. Additionally, the lower mass transport overpotential of MEA#2 suggests the existence of better gas and liquid diffusion-pathways in the cathode catalyst layer.

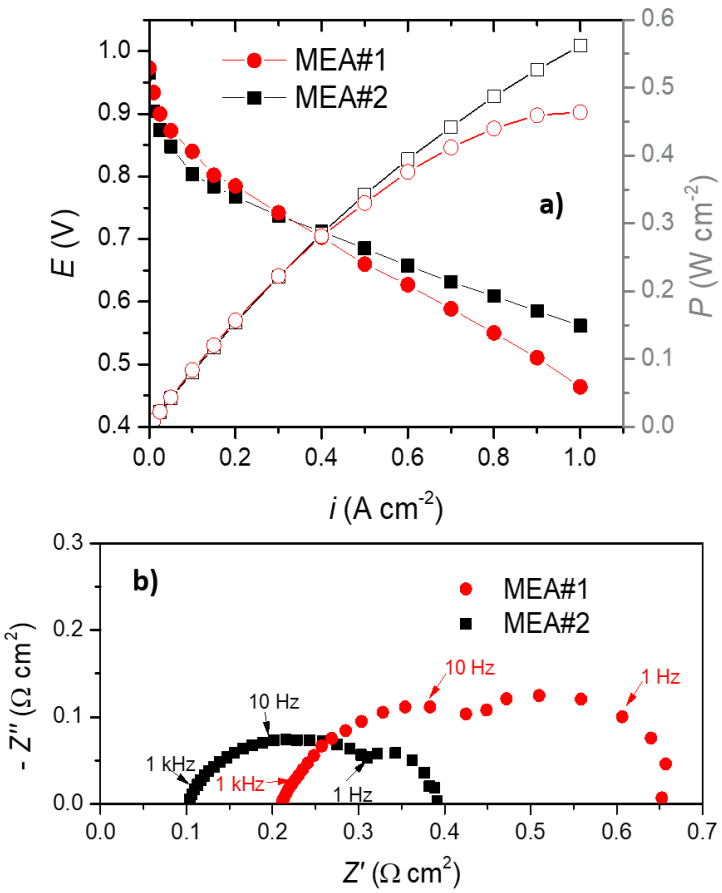


Figure 3.2 - Comparison between the two tested MEAs under the conditions of Run#2 (from Table 3.1) by a) a polarization curve; b) EIS at 500 mA·cm^{-2}.

Hereafter both MEA#1 and MEA#2 will be used to assess the defined strategies to mitigate CO contamination – internal and air bleeding – under the operating conditions shown in Table 3.1, Runs #3 - #13.

3.3.2. INTERNAL AIR BLEEDING

Internal air bleeding was controlled by setting a pressure difference between the two electrodes. The solubility of oxygen in water, which controls the oxygen transport to the anode, is related to its partial pressure. Therefore, the cathode side pressure must be higher to promote oxygen permeation through the membrane [26]. Figure 3.3a shows

chronopotentiometries of MEA#1, at 500 mA cm^{-2}, for pure hydrogen feed (Run #2) and for hydrogen with 10 ppm of CO feed (Runs #3, #4 and #5). With the introduction of CO at the anode, a linear loss of cell potential was observed until reaching a new steady-state. The effect of the internal air bleeding was not evident up to 0.1 bar of pressure difference. At 0.2 bar of cathode over-pressure, the steady-state cell potential increased *ca.* 20 mV, denoting a partial recovery of catalyst poisoning by CO of *ca.* 50 %.

The impedance spectra obtained at 500 mA cm^{-2}, were fitted to an equivalent circuit shown in Figure 3.1 to better diagnose the effect of the CO poisoning mitigation strategies. From the EIS spectra (Figure 3.3b), in the high-frequency region the anodic charge transfer resistance increased significantly when CO was fed with no internal bleeding – R_a = 67.8 mΩ cm^2 vs R_a =120 mΩ cm^2. When an internal bleeding is employed, ΔP = 0.2 bar, the anodic charge transfer resistance decreased significantly, R_a = 82.9 mΩ cm^2 (Table 3.2).

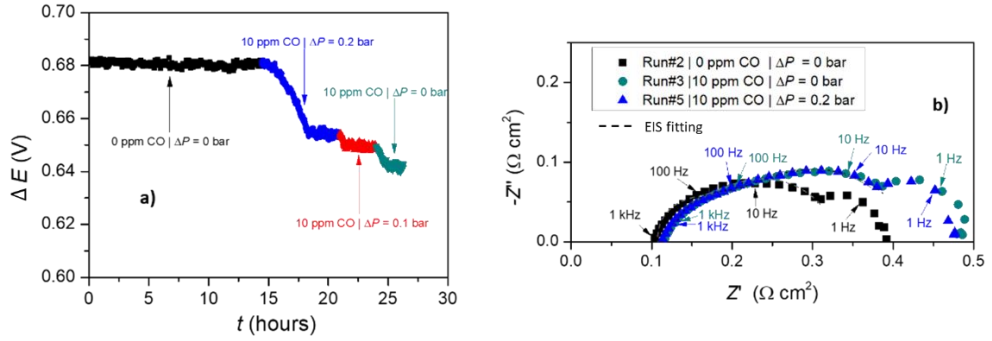


Figure 3.3 - Effect of internal air bleeding a) chronopotentiometry and b) EIS at 500 mA cm^{-2} of MEA#1.

Runs #2, #3, #4 and #5 were repeated with MEA#2. Figure 3.4a displays the chronopotentiometries of MEA#2 at 500 mA cm^{-2}. After CO contamination, the steady-state cell potential increased with the cathode over-pressure (*ca.* 10 ± 2 mV per 0.1 bar). Therefore, internal air bleeding effect is hardly noticeable in EIS (Figure 3.4b), since the spectra of Runs #3 and #5 almost overlap. Moreover, the effect of internal air bleeding with an over-pressure of 0.2 bar allows a recovery of 25 % of the initial performance and

a reduction of anode charge transfer resistance of *ca.* 10 mΩ cm^2, comparing with Run #3, according to the EIS fitting - Table 3.2.

Table 3.2 - Summary of fitted values from EIS data using the equivalent circuit shown in Figure 3.1 for MEA#1 and#2; (Frequency range of the EIS fitted data: 2.5 kHz – 10 Hz).

MEA	#	R_m / mΩ cm^2	R_a / mΩ cm^2	Q_a / F cm^{-2}	R_c / mΩ cm^2	Q_c / F cm^{-2}
1	**2 -** 0 ppm CO	221.4	67.8	639 m	293.2	789 m
	3 - 10 ppm CO	243	117.7	294 m	347.5	443.8 m
	5 - 10 ppm CO | Δ*P* =0.2 bar	233.2	82.9	146.9 m	326.5	254.9 m
	10 - 10 ppm CO + 1.5% air bleed	213.1	67.5	681.5 m	278.3	790.5 m
2	**2 -** 0 ppm CO	107.4	49.5	16.1	174	23.7
	3 - 10 ppm CO	125.4	237.4	11	315.8	6.3
	5 - 10 ppm CO | Δ*P*=0.2 bar	122.5	224.3	7.9	252.5	9.4
	9 - 10 ppm CO + 1% air bleed	109.4	44.6	15.6	160.7	22.4

Oxygen bleeding on several membranes has been a subject of several studies, which report that CO poisoning mitigation is lower for thicker membranes like Nafion 115 (127 μm) [27]; the work of Wang and co-workers [36] reported higher oxygen bleeding when the cathode over-pressure increases in ultra-thin membranes (5 μm and 25 μm). This supports that performing internal bleeding for CO poisoning mitigation is more effective when thin membranes are used. By promoting back diffusion of water dissolved oxygen through thin membranes (internal bleeding), more CO present at the anode can be oxidized to CO_2, thus reducing the anode overpotential caused by CO poisoning. Increments on the cathode total pressure promote CO oxidation [36] but only *ca.* 0.25 %

of the crossed oxygen molecules oxidize CO to CO_2 [36]. In the present study, a similar performance gain was achieved for both MEA#1 and MEA#2, as seen in Figure 3.3a and Figure 3.4b. Nonetheless, no more than 40 % of the initial performance could be re-established; pressure gradients higher than 200 mbar between the electrodes were not employed to avoid excessive mechanical stress that could lead to pinholes in the membrane and consequent gas crossover or internal short-circuits.

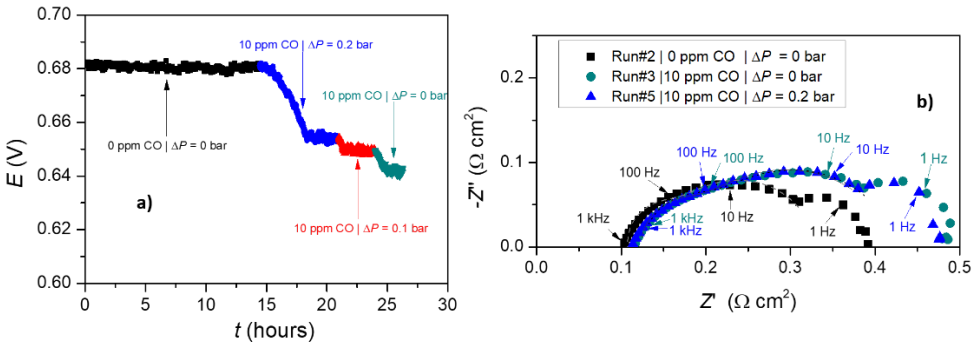


Figure 3.4 - Effect of internal bleeding in MEA#2 on a) chronopotentiometry at 500 mA·cm^{-2} and b) EIS at 500 mA·cm^{-2}.

There is no agreement whether Nafion-PTFE composite membranes display better gas barrier properties compared with plain Nafion membranes (*e.g.* Nafion 115, Nafion 117 among others); several works [37]–[39] report higher permeabilities of Nafion/PTFE composite membranes to oxygen and nitrogen. The PTFE mesh in the composite membrane allows to reduce the overall membrane thickness (from typical *ca.* 185 µm - Nafion 117 - to less than 40 µm) while ensuring the mechanical stability. These authors observed higher composite membrane permeabilities to gas relatively to thicker non-reinforced membranes [40]. On the other hand, Yu and co-workers developed a Nafion/PTFE composite with an overall thickness of 20 ± 5 µm and, upon scanning electron microscopy analysis, they confirmed that PTFE pores were filled with the Nafion resin. The permeability of the composite membrane to nitrogen was reduced when comparing to non-reinforced Nafion 112, 115 or 117 [38].

In the present study, the use of a thinner membrane (Nafion HP in MEA#2) did not provide better internal bleeding-based performance recovery than thicker Nafion 212 membrane (MEA#1). Nafion HP membranes are reinforced with a backbone that makes them not only mechanically more stable but also less permeable to both hydrogen and oxygen. The lower permeability to oxygen limits internal bleeding and thus CO mitigation is less effective comparing to non-reinforced membranes of similar thickness. Higher concentrations of CO in the fuel stream were also tested together with internal bleeding. The pressure difference between cathode and anode was set to 200 mbar to enable internal air bleeding under different CO contaminations. Figure 3.5a shows the chronopotentiometries for four levels of CO contamination (0, 10, 20 and 30 ppm). The efficiency of the cell equipped with MEA#1 at 500 mA cm^{-2} and 80 °C dropped from the initial value, feeding pure H_2 to progressively lower efficiencies, with increasing concentrations of CO. In this regard, the steady state potential decreased with the CO concentration, mainly because of increasing anode overpotential.

The impedance spectra (Figure 3.5b), obtained after each chronopotentiometry, unveils that higher CO concentrations increase the overall impedance. The differences are clear for frequencies lower than 1 Hz, in which gradual increments of 10 ppm in the CO concentration led to two-fold higher anode charge transfer resistances, *i.e.*, the resistance increases *ca.* 20 mΩ cm^2 when CO concentrations increases from 10 ppm to 20 ppm, and *ca.* 40 mΩ cm^2 when increasing from 20 ppm and 30 ppm of CO.

The work of Dhar [41] reported that the apparent activation energy of the HOR increases with the CO concentration thus leading to higher anode polarizations losses. Oetjen [42] studied the effect of different CO concentrations (25 to 250 ppm of CO) on the performance a PEMFC at 80 ºC. These authors concluded that feeding hydrogen with increasing CO contents causes a more negative slope on the polarization curve compared to that measured with pure hydrogen; this effect was more noticeable for higher current densities (> 300 mA cm^2). Similar results were reported by other authors [43], [44].

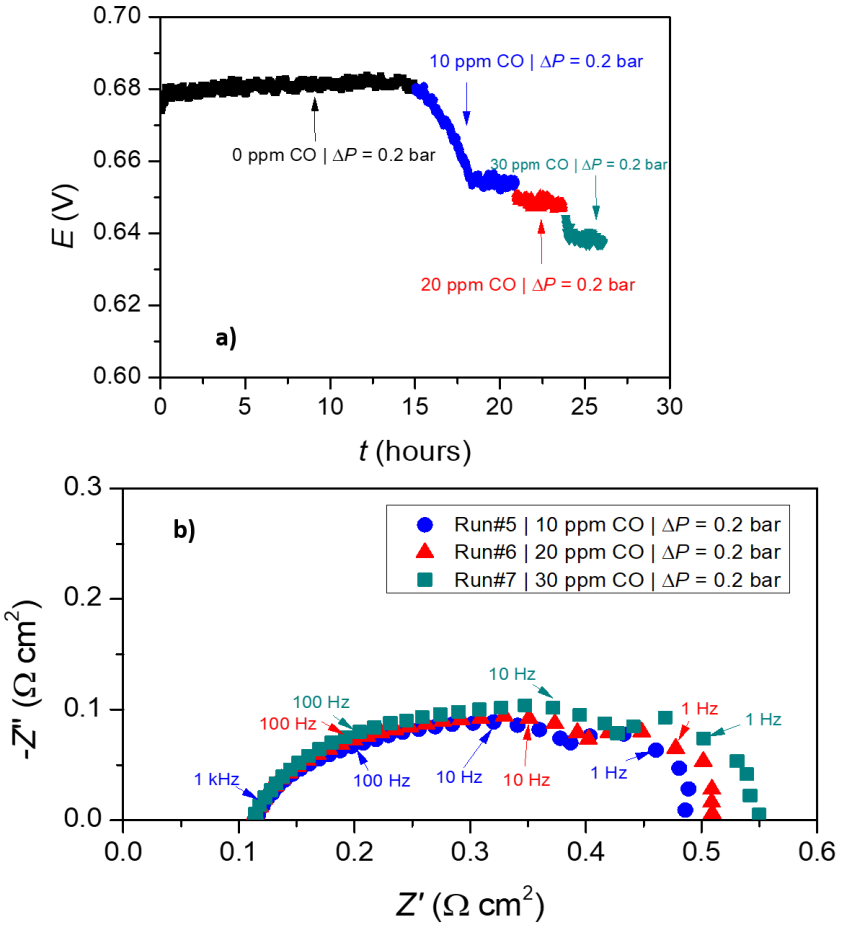


Figure 3.5 - Effect of different CO concentrations in MEA#2 on a) chronopotentiometry at 500 mA·cm^{-2} and on b) EIS at 500 mA·cm^{-2}.

The potential needed to oxidize hydrogen (potential range of 0 to 0.2 V *vs* RHE) is inferior to that needed to oxidize CO (a minimum of 350 mV on Pt/Ru) [45], [46]; the latter occupies the active sites following a Tempkin adsorption isotherm behaviour. If the temperature is kept constant, the CO coverage increases with its concentration in the feed, progressively blocking the active sites for the HOR, resulting in lower performance [41].

3.3.3. EXTERNAL AIR BLEEDING

The cell potential behaviour before and after introducing 10 ppm of CO together with gradually higher concentrations (volumetric ratios) of air (0.5 %, 1 % and 1.5 %) in the fuel stream is depicted in Figure 3.6a. 0.5 % of air is enough to cause significant gains in the performance (*ca.* 45 %) while 1.5 % of air in the anode is sufficient to mitigate the CO poisoning – Run #10.

EIS spectra for Runs #2, #3 and #10. Runs #2 and #10 are shown in Figure 3.6b, displaying approximately the same anodic charge transfer resistance $R_a \approx 68$ mΩ cm^2 and the same series resistance $R_m \approx 217 \pm 4$ mΩ cm^2; the fuel feed of Run #10 contains 1.5 % of air (*ca.* 0.32 % of oxygen), 10 ppm of CO and the balance of hydrogen, this last from air.

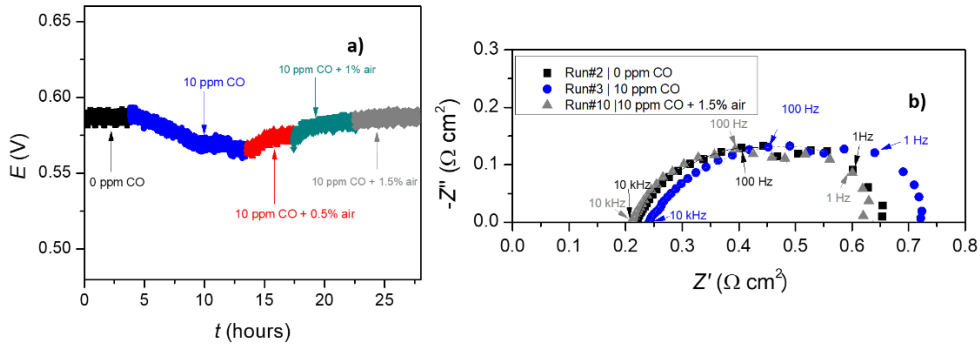


Figure 3.6 - Effect of external bleeding in MEA#1 on a) chronopotentiometry at 500 mA cm^{-2} and b) on EIS at 500 mA cm^{-2} .

The effect of external air bleeding was also assessed using MEA#2. For this MEA, 1 % of air was enough to fully recover the reference potential (Run#2 and #9 in Figure 3.7a). Impedance spectra for Runs #2, #3 and #9 are depicted in Figure 3.7b; spectra of Runs #2 and #9 overlap, confirming that the recovery from the CO poisoning was complete, in agreement with the characteristic curve results. Moreover, ohmic resistance increases when CO is added to the feed (Run #3) and returns to the reference value when external bleeding is provided (Run #9): R_m is *ca.* 125.4 mΩ cm^2 for Run #3 and R_m of 107 ± 2 mΩ cm^2 for Run #2 and #9).

Several works in the literature report that the addition of a fraction of air to a CO contaminated hydrogen stream allows the recovery of the fuel cell performance as if it was operating with pure hydrogen [47]–[52]. Higher CO concentrations typically require higher levels of air bleeding; for example, anode air bleeding of 15 % (*ca.* 3 % of oxygen) is not enough to fully recover the performance of a cell fed with a 53 ppm CO-contaminated hydrogen stream [53]. However, excessive air bleeding (>15 %) is dangerous and leads to the fast membrane ageing and to the decrease of the output power since a significant amount of fuel oxidizes to water at the anode side. Nevertheless, the work by Wilson and his co-workers [54] is one of the few to report the effect of external air bleeding for mitigating CO poisoning present at low concentrations. These authors reported the use of an external bleeding stream of air (2 %) for fully recover the performance of a PEMFC fed with hydrogen contaminated with 5 ppm and 20 ppm of CO; the anode was loaded with 0.14 mg cm^{-2} of Pt-Ru. A similar work comprehended the use of an external bleeding of 6.7 % (air) for a recovery of 80 % with a 10 ppm CO-contaminated hydrogen stream while using a 0.45mg cm^{-2} Pt-Ru anode [53].

The oxygen reaction with the adsorbed CO on the catalyst surface produces CO_2. As soon as the CO is oxidized and removed, the catalyst sites become available for the HOR. Here, it is reported that 1 – 1.5 % of anode air bleed is sufficient to completely recover the performance of a 10 ppm CO-contaminated fuel stream under typical operating conditions, *i.e.* m-CHP systems. To safely supply oxygen (or air) into the anode, its concentration should be kept always below the limiting oxygen concentration, which for 1 bar and room temperature is *ca.* 5 % of oxygen [55]. Furthermore, such oxygen content at the anode did not impact the open circuit potential of the cell, thus it does not contribute for lowering the PEMFC performance.

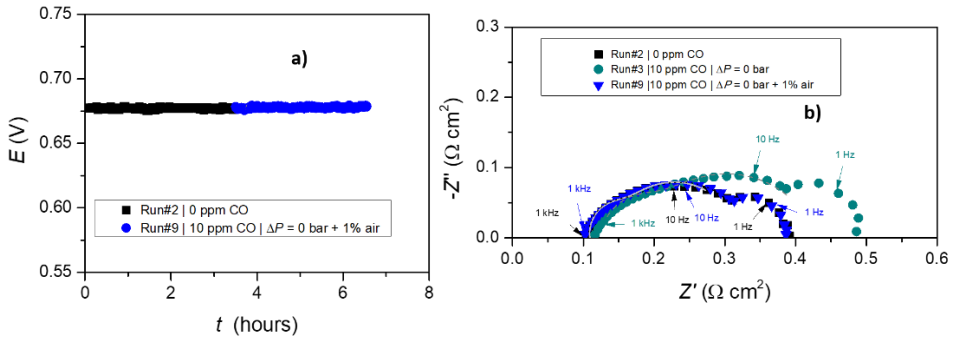


Figure 3.7 - Effect of external air bleeding in MEA#2 on a) chronopotentiometry at 500 mA cm^{-2} and on b) EIS at 500 mA cm^{-2}.

3.3.4. STABILITY UPON IMPLEMENTATION OF BLEEDING STRATEGIES

A comparison between long-term chronopotentiometries of Run #5 and Runs #9 and #10 with internal and external air bleeding for both MEAs is shown in Figure 3.8a and Figure 3.8b. After reaching the steady-state potential at a current density of 500 mA·cm^{-2}, the potential loss history was recorded for assessing the long-term stability. A potential loss rate of $1.58 \cdot 10^{-4}$ V h^{-1} is observed for an internal bleeding of 200 mbar of cathode over-pressure – Run #5 in MEA#1; on the other hand, after *ca.* 80 h of operation, MEA#2 displays a potential loss rate of $9.45 \cdot 10^{-5}$ V h^{-1} under the same operating conditions. After *ca.* 8 h of operation the performance loss of MEA#1 under external bleeding is negligible (loss rate of *ca.* $4.30 \cdot 10^{-6}$ V h^{-1}) – Run #10, while MEA#2 displays a potential loss rate of $8.04 \cdot 10^{-5}$ V h^{-1} – Run #9. At reference conditions, for a CO free hydrogen feeding, the observed potential loss rate was $9.43 \cdot 10^{-7}$ V h^{-1} for MEA#1 and $9.00 \cdot 10^{-6}$ V h^{-1} for MEA#2. These values are similar to the ones obtained for the external bleeding experiments, showing that this method is not only sufficient to recover the performance of the cell but also causes less cell potential decay than internal bleeding; nonetheless, some authors have reported a detrimental effect in long-term performance when using external air bleeding due to H_2O_2 formation [16]. The results of Figure 3.8 demonstrate that MEA#1, that uses a thicker membrane, displays a better long-term stability even at higher air bleed concentrations than MEA#2 – 1.5 % air bleed in MEA#1 vs. 1 % of air in MEA#2.

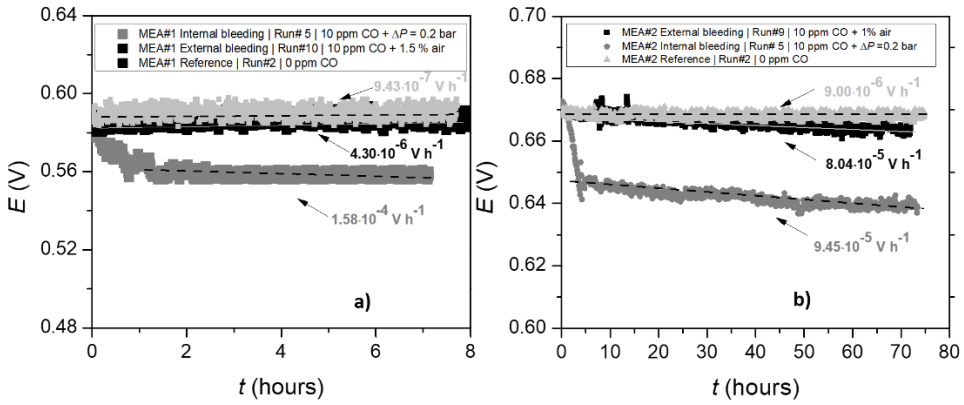


Figure 3.8 - Long-term chronopotentiometry of two types of air bleeding at 500 mA cm^{-2} in a) MEA#1 and b) MEA#2.

Cyclic voltammetry was performed to assess the impact of CO contamination over both anode and cathode ECSA after a complete set of experiments (Runs# 3 to 9) with MEA#2. Figure 3.9a and b depict the beginning of life (BoL) CV, and the end of life (EoL) CV for the anode and cathode of MEA#2, respectively. The voltammograms present distinct shapes due to the different catalysts present in each electrode. The peak areas reflect the amount of Pt active sites to hydrogen adsorption/desorption. The anode CVs display solely one peak typical of Pt-Ru catalysts [56]. On the other hand, the cathode displays two peaks at the anodic currents region ($i > 0$) accounting for the H desorption on Pt (111) at ~ 110 mV and Pt (100) at ~ 215 mV [57]. The reduction process is electrochemically reversible since the difference between the anodic and cathodic peak potentials is lower than 59 mV. After performing all tests involving CO coverage, the electrochemically active surface area seems to be kept intact with no signs of loss on catalytic activity, Figure 3.9c. This result confirms the great stability of Pt-Ru alloy towards CO contaminated hydrogen streams [58]. Moreover, Wagner and Schulze [59] confirmed by EIS analysis the excellent properties of Pt-Ru/C anodes as CO-tolerant electrocatalysts for the HOR; not only they provide less anodic charge transfer resistance but also generate less mass transfer resistance compared to Pt/C based anodes. However, there is an evident loss of active surface area of Pt at the cathode, nearly 16 %, due to

the typical catalyst layer degradation that comprehends Pt dissolution/sintering, carbon corrosion and ionomer dissolution [60].

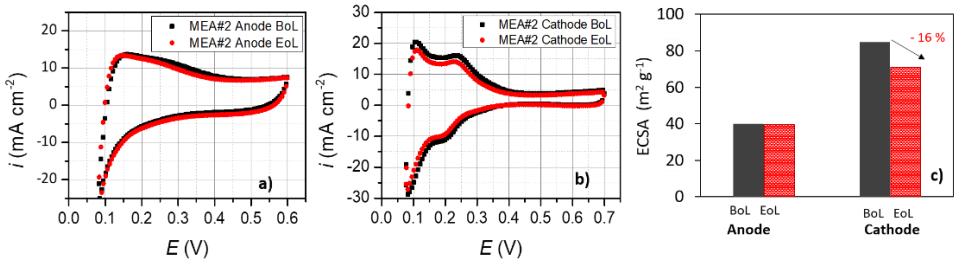


Figure 3.9 - Cyclic voltammograms at beginning of life (BoL) and end of life (EoL) of a) anode and b) cathode of MEA#2; scan: 50 mV s^{-1}; RH: 50 %; Stoic: 1.5/2 (H_2/O_2) at 100 ml min^{-1}).

3.4. CONCLUSIONS

In the present study, the performance of PEMFCs was evaluated while feeding H_2 and CO (10 ppm) to a Pt-Ru based anode and compared with the performance with pure hydrogen at 70 °C. Oxygen concentrations were tuned and applied to the anode – by means of internal air or external air bleeding - to assess the minimum concentration to mitigate CO poisoning. Simultaneously, the long-term stability of the cells was monitored to ascribe the potential decay with each air bleeding strategy.

The potential drop caused by feeding H_2 contaminated with 10 ppm of CO was 3 % at 500 mA·cm^{-2} for the fuel cells equipped with Nafion HP membrane and a Nafion 212 membrane; nonetheless, the dynamic response to the addition of 10 ppm of CO was slow, reaching the new steady state performance after *ca.* 5 h. The air feed over-pressure of 0.2 bar at the cathode allowed the re-activation of the poisoned catalyst and a cell potential recovery of over 30 % in both MEAs. The success of internal bleeding towards CO oxidation along with the stability was found to depend on the mechanical strength of each membrane that equipped the MEAs. Thinner but reinforced and stabilized Nafion HP membrane displayed lower performance recovery but higher stability during mid-term diagnosis, in contrast to the non-reinforced and thicker Nafion 212 membrane.

Performing external air bleeding proved to be the most effective approach. In fact, adding an air bleed of 1 % and 1.5 % in the fuel stream for both MEAs promoted full

CO oxidation and thus nearly 100 % recovery of cell performance (comparing to neat hydrogen). Accordingly, up to 1.5 % of air in the anode side showed to be harmless for long-term operation. This strategy is then recommendable for stationary applications, namely for residential power generation, whenever the feeding hydrogen contains up to *ca.* 10 ppm.

REFERENCES

[1] J. Tjønnås, F. Zenith, I. J. Halvorsen, M. Klages, and J. Scholta, "Control of Reversible Degradation Mechanisms in Fuel Cells: Mitigation of CO contamination," *IFAC-PapersOnLine*, vol. 49, no. 7, pp. 302–307, 2016, doi: 10.1016/j.ifacol.2016.07.309.

[2] C. A. Rice, P. Urchaga, A. O. Pistono, B. W. McFerrin, B. T. McComb, and J. Hu, "Platinum Dissolution in Fuel Cell Electrodes: Enhanced Degradation from Surface Area Assessment in Automotive Accelerated Stress Tests," *J. Electrochem. Soc.*, vol. 162, no. 10, pp. F1175–F1180, Jan. 2015, doi: 10.1149/2.0371510jes.

[3] S. Foresti, G. Manzolini, and S. Escribano, "Experimental investigation of PEM fuel cells for a m-CHP system with membrane reformer," *Int. J. Hydrogen Energy*, vol. 42, no. 40, pp. 25334–25350, 2017, doi: 10.1016/j.ijhydene.2017.08.046.

[4] T. J. Park, S.M.; O'Brien, "Effects of several trace contaminants on fuel cell performance," 1979. doi: 10.2172/5205079.

[5] N. Hayter, P R; Mitchell, P; Dams, R A.J.; Dudfield, C; Gladding, "The effect of contaminants in the fuel and air streams on the performance of a solid polymer fuel cell," 1997, url: https://www.osti.gov/etdeweb/biblio/572962.

[6] P. E. Dodds *et al.*, "Hydrogen and fuel cell technologies for heating: A review," *Int. J. Hydrogen Energy*, vol. 40, no. 5, pp. 2065–2083, Feb. 2015, doi: 10.1016/j.ijhydene.2014.11.059.

[7] I. Staffell, "Zero carbon infinite COP heat from fuel cell CHP," *Appl. Energy*, vol. 147, pp. 373–385, Jun. 2015, doi: 10.1016/j.apenergy.2015.02.089.

[8] R. A. Lemons, "Fuel cells for transportation," *J. Power Sources*, vol. 29, no. 1–2, pp. 251–264, Jan. 1990, doi: 10.1016/0378-7753(90)80024-8.

[9] H. Igarashi, T. Fujino, and M. Watanabe, "Hydrogen electro-oxidation on platinum catalysts in the presence of trace carbon monoxide," *J. Electroanal. Chem.*, vol. 391, no. 1–2, pp. 119–123, Jul. 1995, doi: 10.1016/0022-0728(95)03914-3.

[10] X. Cheng *et al.*, "A review of PEM hydrogen fuel cell contamination: Impacts, mechanisms, and mitigation," *J. Power Sources*, vol. 165, no. 2, pp. 739–756, 2007, doi: 10.1016/j.jpowsour.2006.12.012.

[11] Z. Qi, C. He, and A. Kaufman, "Effect of CO in the anode fuel on the performance of PEM fuel cell cathode," *J. Power Sources*, vol. 111, no. 2, pp. 239–247, 2002, doi: 10.1016/s0378-7753(02)00300-2.

[12] R. J. Bellows, E. M. Soos, and R. P. Reynolds, "The Mechanism of CO Mitigation in Proton Exchange Membrane Fuel Cells Using Dilute H2O in the Anode Humidifier," *Electrochem. Solid-State Lett.*, vol. 1, no. 2, p. 69, Aug. 1999, doi: 10.1149/1.1390639.

[13] L. P. L. Carrette, K. A. Friedrich, M. Huber, and U. Stimming, "Improvement of CO tolerance of proton exchange membrane (PEM) fuel cells by a pulsing technique," in *Physical Chemistry Chemical Physics*, 2001, doi: 10.1039/b005843m.

[14] C.-C. Chung, C.-H. Chen, and D.-Z. Weng, "Development of an air bleeding technique and specific duration to improve the CO tolerance of proton-exchange membrane fuel cells," *Appl. Therm. Eng.*, vol. 29, no. 11–12, pp. 2518–2526, Aug. 2009, doi: 10.1016/j.applthermaleng.2008.12.021.

[15] R. Bashyam, P. He, S. Wessel, and S. Knights, "Impacts of Cathode Loading on Ru Crossover Related PEFC Durability," in *ECS Transactions*, 2011, doi: 10.1149/1.3635617.

[16] S. Knights *et al.*, "PEMFC MEA and System Design Considerations," *ECS Trans.*, vol. 41, no. 1, pp. 39–53, Oct. 2011, doi: 10.1149/1.3635542.

[17] M. J. Lee *et al.*, "Understanding the Bifunctional Effect for Removal of CO Poisoning: Blend of a Platinum Nanocatalyst and Hydrous Ruthenium Oxide as a Model System," *ACS Catal.*, vol. 6, no. 4, pp. 2398–2407, 2016, doi: 10.1021/acscatal.5b02580.

[18] S. Alayoglu, A. U. Nilekar, M. Mavrikakis, and B. Eichhorn, "Ru-Pt core-shell nanoparticles for preferential oxidation of carbon monoxide in hydrogen," *Nat. Mater.*, vol. 7, pp. 333–338, 2008, doi: 10.1038/nmat2156.

[19] A. H. Thomason, T. R. Lalk, and A. J. Appleby, "Effect of current pulsing and 'self-oxidation' on the CO tolerance of a PEM fuel cell," *J. Power Sources*, vol. 135, no. 1-2, pp. 204-211, 2004, doi: 10.1016/j.jpowsour.2004.03.070.

[20] Y. Kurihara, T. Mabuchi, and T. Tokumasu, "Molecular Analysis of Structural Effect of Ionomer on Oxygen Permeation Properties in PEFC," *J. Electrochem. Soc.*, vol. 164, pp. F628, 2017, doi: 10.1149/2.1301706jes.

[21] T. Kawakami, I. Shigemoto, and N. Matubayasi, "Free-energy analysis of water affinity in polymer studied by atomistic molecular simulation combined with the theory of solutions in the energy representation," *J. Chem. Phys.*, vol. 137, no. 23, 2012, doi: 10.1063/1.4770334.

[22] A. T. Haug and R. E. White, "Oxygen diffusion coefficient and solubility in a new proton exchange membrane," *J. Electrochem. Soc.*, vol. 147, pp. 980, 2000, doi: 10.1149/1.1393300.

[23] P. Gode, G. Lindbergh, and G. Sundholm, "In-situ measurements of gas permeability in fuel cell membranes using a cylindrical microelectrode," *J. Electroanal. Chem.*, vol. 518, no. 2, pp. 115–122, 2002, doi: 10.1016/S0022-0728(01)00698-2.

[24] K. Lee, A. Ishihara, S. Mitsushima, N. Kamiya, and K. Ota, "Effect of Recast Temperature on Diffusion and Dissolution of Oxygen and Morphological Properties in Recast Nafion," *J. Electrochem. Soc.*, vol. 151, pp. A639, 2004, doi: 10.1149/1.1652052.

[25] V. A. Sethuraman, S. Khan, J. S. Jur, A. T. Haug, and J. W. Weidner, "Measuring oxygen, carbon monoxide and hydrogen sulfide diffusion coefficient and solubility in Nafion membranes," *Electrochim. Acta*, vol. 54, no. 27, pp. 6850–6860, 2009, doi: 10.1016/j.electacta.2009.06.068.

[26] S. S. Kocha, J. D. Yang, and J. S. Yi, "Characterization of gas crossover and its implications in PEM fuel cells," *AIChE J.*, vol. 52, no. 5, 2006, doi: 10.1002/aic.10780.

[27] J. Zhang, T. Thampan, and R. Datta, "Influence of Anode Flow Rate and Cathode Oxygen Pressure on CO Poisoning of Proton Exchange Membrane Fuel Cells," *J. Electrochem. Soc.*, vol. 149, pp. A765, 2002, doi: 10.1149/1.1475686.

[28] M. Murthy *et al.*, "Performance of a Polymer Electrolyte Membrane Fuel Cell Exposed to Transient CO Concentrations," *J. Electrochem. Soc.*, vol. 148, pp. A1141, 2001, doi: 10.1149/1.1402119.

[29] Y. V. Pleskov, Y. E. Evstefeeva, M. D. Krotova, V. V. Elkin, A. M. Baranov, and A. P. Dement'Ev, "Electrochemical behavior of amorphous carbon films: Kinetic and impedance-spectroscopy studies," *Diam. Relat. Mater.*, vol. 8, no. 1, pp. 64–72, 1999, doi: 10.1016/s0925-9635(98)00367-7.

[30] X.-Z. Yuan *et al.*, "Degradation of a polymer exchange membrane fuel cell stack with Nafion® membranes of different thicknesses: Part I. In situ diagnosis," *J. Power Sources*, vol. 195, no. 22, pp. 7594–7599, Nov. 2010, doi: 10.1016/j.jpowsour.2010.06.023.

[31] L. Yu, F. Lin, L. Xu, and J. Xi, "Structure–property relationship study of Nafion XL membrane for high-rate, long-lifespan, and all-climate vanadium flow batteries," *RSC Adv.*, vol. 7, no. 50, pp. 31164–31172, Jun. 2017, doi: 10.1039/c7ra04996j.

[32] DuPont Fuel Cells, "DuPont™ Nafion® PFSA Membranes NR-211 and NR-212, "2008, url: http://www.hesen.cn/userfiles/bochi/file/212%E3%80%81211%E5%8F%82%E6%95%B0.pdf.

[33] DuPont Fuel Cells, "DuPont™ Nafion® PFSA Membranes : Nafion HP membrane," 2010, url: http://www.hesen.cn/userfiles/bochi/file/HP%20Product%20Brochure.pdf.

[34] S. Slade, S. A. Campbell, T. R. Ralph, and F. C. Walsh, "Ionic Conductivity of an Extruded Nafion 1100 EW Series of Membranes," *J. Electrochem. Soc.*, vol. 149, no. 12, p. A1556, Dec. 2002, doi: 10.1149/1.1517281.

[35] M. N. Tsampas, A. Pikos, S. Brosda, A. Katsaounis, and C. G. Vayenas, "The effect of membrane thickness on the conductivity of Nafion," *Electrochim. Acta*, vol. 51, no. 13, pp. 2743–2755, Mar. 2006, doi: 10.1016/j.electacta.2005.08.021.

[36] W. Wang, "The effect of internal air bleed on CO poisoning in a proton exchange membrane fuel cell," *J. Power Sources*, vol. 191, no. 2, pp. 400–406, 2009, doi:

10.1016/j.jpowsour.2009.02.058.

[37] K. M. Nouel and P. S. Fedkiw, "Nafion®-based composite polymer electrolyte membranes," *Electrochim. Acta*, vol. 43, no. 16–17, pp. 2381–2387, May 1998, doi: 10.1016/s0013-4686(97)10151-7.

[38] F. Liu, B. Yi, D. Xing, J. Yu, and H. Zhang, "Nafion/PTFE composite membranes for fuel cell applications," *J. Memb. Sci.*, vol. 212, no. 1–2, pp. 213–223, Feb. 2003, doi: 10.1016/s0376-7388(02)00503-3.

[39] J. Shim, H. Y. Ha, S.-A. Hong, and I.-H. Oh, "Characteristics of the Nafion ionomer-impregnated composite membrane for polymer electrolyte fuel cells," *J. Power Sources*, vol. 109, no. 2, pp. 412–417, Jul. 2002, doi: 10.1016/s0378-7753(02)00106-4.

[40] H.-L. Lin, T. L. Yu, L.-N. Huang, L.-C. Chen, K.-S. Shen, and G.-B. Jung, "Nafion/PTFE composite membranes for direct methanol fuel cell applications," *J. Power Sources*, vol. 150, pp. 11–19, Oct. 2005, doi: 10.1016/j.jpowsour.2005.02.016.

[41] H. P. Dhar, L. G. Christner, A. K. Kush, and H. C. Maru, "Performance Study of a Fuel Cell Pt-on-C Anode in Presence of CO and CO 2, and Calculation of Adsorption Parameters for CO Poisoning," *J. Electrochem. Soc.* , vol. 133, no. 8, pp. 1574–1582, Aug. 1986, doi: 10.1149/1.2108971.

[42] U. Oetjen, H.-F., Schmidt, V.M , Stimming, "Performance Data of a Proton Exchange Membrane Fuel Cell Using H2/CO as Fuel Gas," *J. Electrochem. Soc.*, vol. 143, no. 12, p. 3838, 1996, doi: 10.1149/1.1837305.

[43] V. M. Schmidt, R. Ianniello, H.-F. Oetjen, H. Reger, U. Stinuning, and F. Trila, "Oxidation of H2/CO in a Proton Exchange Membrane Fuel Cell," *ECS Proc. Vol.* , vol. 1995–23, pp. 1–11, Jan. 1995, doi: 10.1149/199523.0001pv.

[44] Y. Si, R. Jiang, J.-C. Lin, H. R. Kunz, and J. M. Fenton, "CO Tolerance of Carbon-Supported Platinum-Ruthenium Catalyst at Elevated Temperature and Atmospheric Pressure in a PEM Fuel Cell," *J. Electrochem. Soc.*, vol. 151, no. 11, pp. A1820–A1824, 2004, doi: 10.1149/1.1796446.

[45] Y. Takasu, T. Kawaguchi, W. Sugimoto, and Y. Murakami, "Effects of the surface area of carbon support on the characteristics of highly-dispersed Pt-Ru

particles as catalysts for methanol oxidation," *Electrochim. Acta*, vol. 48, no. 25–26, pp. 3861–3868, 2003, doi: 10.1016/s0013-4686(03)00521-8.

[46] T. Gu, W.-K. Lee, J. W. Van Zee, and M. Murthy, "Effect of Reformate Components on PEMFC Performance," *J. Electrochem. Soc.*, vol. 151, no. 12, pp. A2100–A2105, 2004, doi: 10.1149/1.1811080.

[47] L. Y. Sung, B. J. Hwang, K. L. Hsueh, and F. H. Tsau, "Effects of anode air bleeding on the performance of CO-poisoned proton-exchange membrane fuel cells," *J. Power Sources*, vol. 195, no. 6, pp. 1630–1639, 2010, doi: 10.1016/j.jpowsour.2009.09.062.

[48] T. Tingelöf, L. Hedström, N. Holmström, P. Alvfors, and G. Lindbergh, "The influence of CO2, CO and air bleed on the current distribution of a polymer electrolyte fuel cell," *Int. J. Hydrogen Energy*, vol. 33, no. 8, pp. 2064–2072, 2008, doi: 10.1016/j.ijhydene.2008.02.002.

[49] L. Y. Sung, B. J. Hwang, K. L. Hsueh, W. N. Su, and C. C. Yang, "Comprehensive study of an air bleeding technique on the performance of a proton-exchange membrane fuel cell subjected to CO poisoning," *J. Power Sources*, vol. 242, pp. 264–272, 2013, doi: 10.1016/j.jpowsour.2013.05.042.

[50] F. a. Uribe, J. a. Valerio, F. H. Garzon, and T. a. Zawodzinski, "PEMFC Reconfigured Anodes for Enhancing CO Tolerance with Air Bleed," *Electrochem. Solid-State Lett.*, vol. 7, no. 10, p. A376, 2004, doi: 10.1149/1.1795633.

[51] R. C. Urian, A. F. Gullá, and S. Mukerjee, "Electrocatalysis of reformate tolerance in proton exchange membranes fuel cells: Part I," *J. Electroanal. Chem.*, vol. 554–555, pp. 307–324, 2003, doi: 10.1016/s0022-0728(03)00241-9.

[52] T. Morawietz, M. Handl, C. Oldani, K. A. Friedrich, and R. Hiesgen, "Quantitative in Situ Analysis of Ionomer Structure in Fuel Cell Catalytic Layers," *ACS Appl. Mater. Interfaces*, vol. 40, no. 8, pp. 27044–27054, 2016, doi: 10.1021/acsami.6b07188.

[53] X. Cheng *et al.*, "A review of PEM hydrogen fuel cell contamination: Impacts, mechanisms, and mitigation," *J. Power Sources*, vol. 165, no. 2, pp. 739–756,

Mar. 2007, doi: 10.1016/j.jpowsour.2006.12.012.

[54] S. F. . Wilson, M.S., Derouin, C.R., Valerio, J.A., and Gottesfeld, "Electrocatalysis issues in polymer electrolyte fuel cells," in *Conference: 28. intersociety energy conversion engineering conference, Atlanta, GA (United States), 8-13 Aug 1993*, 1193, url: https://www.osti.gov/biblio/10158639.

[55] I. A. Zlochower and G. M. Green, "The limiting oxygen concentration and flammability limits of gases and gas mixtures," *J. Loss Prev. Process Ind.*, vol. 22, no. 4, pp. 499–505, 2009, doi: 10.1016/j.jlp.2009.03.006.

[56] S. J. Yoo, T. Y. Jeon, K. S. Kim, T. H. Lim, and Y. E. Sung, "Multilayered Pt/Ru nanorods with controllable bimetallic sites as methanol oxidation catalysts," *Phys. Chem. Chem. Phys.*, vol. 46, no. 12, pp. 15240–15246, 2010, doi: 10.1039/c0cp00737d.

[57] W. Sheng, Z. Zhuang, M. Gao, J. Zheng, J. G. Chen, and Y. Yan, "Correlating hydrogen oxidation and evolution activity on platinum at different pH with measured hydrogen binding energy," *Nat. Commun.*, vol. 6, no. 1, p. 5848, May 2015, doi: 10.1038/ncomms6848.

[58] H.-F. Oetjen, "Performance Data of a Proton Exchange Membrane Fuel Cell Using H2/CO as Fuel Gas," *J. Electrochem. Soc.*, 1996, doi: 10.1149/1.1837305.

[59] N. Wagner and M. Schulze, "Change of electrochemical impedance spectra during CO poisoning of the Pt and Pt–Ru anodes in a membrane fuel cell (PEFC)," *Electrochim. Acta*, vol. 48, no. 25–26, pp. 3899–3907, Nov. 2003, doi: 10.1016/S0013-4686(03)00528-0.

[60] X. Yu and S. Ye, "Recent advances in activity and durability enhancement of Pt/C catalytic cathode in PEMFC: Part II: Degradation mechanism and durability enhancement of carbon supported platinum catalyst," *J. Power Sources*, vol. 172, no. 1, pp. 145–154, Oct. 2007, doi: 10.1016/j.jpowsour.2007.07.048.

CHAPTER 4

THE ROLE OF PT LOADING ON REDUCED GRAPHENE OXIDE SUPPORT IN THE POLYOL SYNTHESIS OF CATALYSTS FOR OXYGEN REDUCTION REACTION

4

THE ROLE OF PT LOADING ON REDUCED GRAPHENE OXIDE SUPPORT IN THE POLYOL SYNTHESIS OF CATALYSTS FOR OXYGEN REDUCTION REACTION

Tiago Lagarteira, Sofia Delgado, Celina Fernandes, Cátia Azenha, Cecilia Pedrero and Adélio Mendes

Adapted from the International Journal of Hydrogen Energy, 2020, 45(40)

ABSTRACT

Common carbon-blacks have shown insufficient stability as cathodic catalyst supports for proton exchange membrane fuel cells (PEMFCs). In this regard, alternative supports have been proposed and, specifically graphene or reduced graphene oxide (rGO), have attracted special attention. Herein, a set of electrocatalysts using reduced graphene oxide (rGO) as support are synthetized by a modified polyol method. The influence of the Pt loading on the support is studied and compared with conventional supports, considering Pt particle morphologies and oxygen reduction reaction (ORR) performance in rotating disk electrode (RDE). Despite Pt average particle size typically increases with the Pt loading, 30 wt.% of Pt on rGO is the optimal Pt loading, demonstrating the highest ORR activity among the rGO-supported electrocatalysts. These results show that both Pt loading and type of support greatly impact on the morphology and electrochemical performance of Pt nanoparticles.

Keywords: Proton exchange membrane fuel cell; Oxygen reduction reaction; Catalyst durability; Reduced graphene oxide support.

4.1. INTRODUCTION

Proton exchange membrane fuel cells (PEMFCs) are recognized as a promising power source for both transport and stationary applications owing to the high power density, high efficiency and compact design [1]–[3]. Moreover, the technology is environmentally friendly since electricity is generated by the direct electrochemical conversion of hydrogen and oxygen into water. Pt-based catalysts, supported on conductive materials, commonly on carbon blacks, are used as electrodes [4]. Particularly, the sluggish kinetics and high overpotential of oxygen reduction reaction (ORR) require high-performance catalysts to achieve high power output with ultra-low Pt loading [5]. The continuous decrease in Pt loading has been a subject of paramount importance among the scientific community; it means a significant reduction in the overall-cost and sustainability of PEMFC stacks, due to the limited world reserves of platinum [6]. Despite some reports [7]–[11] met the target for ORR mass-specific activity set by the US Department of Energy (0.44 A mg^{-1}_{Pt} @ 0.9 $V_{i\text{-}R\ free}$), stability remains one of the major issues for the widespread commercialization of PEMFCs [12]. Different strategies have been employed to boost ORR activity while reducing the amount of Pt, either by alloying Pt with other metals, dealloying Pt-M alloys to obtain skeleton-like structures or synthetizing core-shell structures. Nevertheless, just the downsizing of Pt particles, by dispersing them on carbon supports, has shown great potential to increase the electrochemical surface area (ECSA) and thus the Pt utilization [5]. Pt nanoparticles smaller than 2-3 nm are thermodynamically unstable [13], displaying a non-defined crystallographic structure and making them less attractive both in terms of stability and activity (particle-size effect) [14]–[16]. Additionally, the interaction between the support material and the metal catalyst also influences the activity and stability of the supported-catalyst, either from electronic or geometric effects [17], [18]. Hence, the main challenge is to support the metallic catalyst in materials with good electrical conductivity, corrosion resistance and suitable porosity to provide reactive sites and enhanced diffusion paths to the reactants [19].

Recently, new carbon materials such as ordered mesoporous carbons, carbon aerogels, carbon nanotubes (CNTs) [20], [21], carbon nanohorns [22] and carbon nanofibers [23], [24] have been tested as supports to meet the above referred criteria. Among those, graphene, a two-dimensional one-atom-thick planar sheet of sp^2-bonded carbon atoms, can be considered as the building block for all fullerene allotropic dimensionalities [25], [26]. Graphene, has great potential for many applications, serving from recently discovered anticorrosion additive for solar absorber films to resilient catalyst supports [27]–[29]. Most studies that report the use of graphene supports, aim to develop not only functional electrocatalysts for ORR but also for anodes of direct methanol fuel cells (DMFCs) due to improved CO tolerance [30]–[34]. However, there is a huge dispersion of results concerning ECSA values in literature, ranging from ca. 35 to 80 $m_{Pt}^2\ g_{Pt}^{-1}$, some of them obtained using very similar preparation methods [30], [33], [35]–[39]. This suggests that the electrochemical performance of graphene-supported is highly sensitive not only to the synthesis method (Pt precursor, Pt/carbon ratio, pH, reaction duration, reducing agent, surfactants) but also to post-synthesis treatments and methods used to functionalize the supports.

To the best of authors' knowledge, this work reports for the first time the influence of Pt loading on rGO using the widely spread polyol electrocatalysts synthesis. The electrochemical performance of the electrocatalysts is correlated with ex-situ analysis carried out to disclose Pt particle size, crystallography and dispersion over rGO. Moreover, other types of carbon materials are used and compared with rGO-supported catalyst with similar Pt loading. The synthetized electrocatalysts and commercial references are analyzed with TEM, TGA, XRD and BET, and characterized electrochemically to measure their ECSA and ORR activity. Finally, the stability of the best-performing electrocatalysts upon accelerated degradation is also assessed.

4.2. EXPERIMENTAL

4.2.1. MODIFIED POLYOL SYNTHESIS

The catalysts were prepared by chemical reduction of Pt precursor in ethane-1,2-diol solution. Graphene oxide (Nanoinnova), Vulcan XC-72R (Cabot) and multi-wall carbon nanotubes (Sigma-Aldrich) were used as-received in a typical polyol synthesis. 100 mg of each carbon support was first added to ethane-1,2-diol (VWR, 99 %), and the resultant suspension was sonicated for 3 h to obtain a homogenous solution. Following, required amounts of chloroplatinic acid hexahydrate (ACS, ≥ 37.5 %) and deionized water were added to the above dispersion to obtain 5 vol.% of water in ethane-1,2-diol. The synthesis was then carried out for 5 h under reflux at 150 °C with constant stirring. Finally, upon cooling to room temperature, the resulting colloid was filtered and washed extensively with water before being dried in an oven at 120 °C.

The catalysts were named according to their composition, using the following nomenclature, XPtY, where X represents the Pt loading (wt.%) and Y the carbon support (Vulcan – Vulcan XC-72R; CNTs – multi-wall carbon nanotubes; and rGO – reduced graphene oxide). Electrocatalysts that were subjected to accelerated degradation were identified with "AD".

4.2.2. PHYSICOCHEMICAL CHARACTERIZATION

Thermogravimetric analysis (TGA) was performed using a thermogravimetric analyzer (TG 209 F1 iris, NETZSCH) under 20 ml min^{-1} of air flow, heating from room temperature to 900 ºC at 2 ºC min^{-1}. In each analysis, ca. 4 - 7 mg of sample was used.

The synthetized catalysts were examined using a transmission electron microscope (TEM), a Jeol JEM 1400. Samples for TEM analysis were prepared by placing a single drop of ultrasonicated sample suspension onto a copper grid. TEM images were processed with Image J software. To calculate the average particle size, 30 platinum particles were measured in each electrocatalyst sample.

The structure of the catalysts was studied using XRD. The X-ray pattern of the samples was collected using a PANanlytical X'Pert Pro operating in Bragg-Bretano focusing geometry and using Cu Kα radiation at wavelengths Cu Kα1 = 1.5406 Å and Cu Kα2 = 1.54443 Å. The data was collected at 2θ angles (15-95°), with a step size of 0.017°. The

obtained X-ray scans were compared to those of standard database and the phases were assigned comparing the data available in literature. The crystallite size of platinum phases present in the investigated catalysts was based on X-ray diffraction line broadening and calculated by Williamson-Hall method after peak refining.

The textural properties of the samples were evaluated by N_2 physisorption at -196 ºC in a Quantachrome Autosorb-1 Instruments apparatus. The surface area (S_{BET}) was calculated using the Brunauer-Emmett-Teller (BET) equation in the nitrogen partial pressure range (P/P^0) from 0.05 to 0.15. Prior to the analysis, the samples (40 mg) were outgassed in vacuum at 200 °C overnight.

4.2.3. ELECTROCHEMICAL CHARACTERIZATION

ORR measurements were performed in a Gamry RDE equipped with an Eurocell Electrochemical Kit. A Zahner IM6-ex was used as potentiostat and impedance spectrometer. The glassy carbon electrode (GCE) was polished with 0.05 µm alumina-particle solution prior to each film deposition. Catalyst inks were prepared by keeping constant the mass of carbon (2 mg), 7.96 ml of ultra-pure water, 2 ml isopropanol (Alfa Aesar) and 40 µl Nafion (5 wt.%, Quintech). The catalyst inks were ultrasonicated (50 W, Hielscher UP50H) in an ice-bath for 15 min. Two drops of 10 µl each were deposited on the GCE and dried at 700 rotations per minute (RPM) and room temperature. Immediately after dipping the working electrode (GCE of *ca.* 0.2 cm^2) into the electrolyte (0.1 M $HClO_{4(aq)}$, 70 % conc. Sigma Aldrich), the potential was maintained at 0.4 V *vs* RHE to avoid exposure to open circuit potential (OCP). An Ag/AgCl reference electrode was used. The following protocol was chosen considering previous reports [5], [40]–[44]. The electrode was first conditioned in Ar during 100 cycles between 50 mV - 1 V (*vs.* RHE) at 100 mV s^{-1} and 0 RPM. The electrochemical surface area (ECSA) was then determined by H_{UPD} method at 20 mV s^{-1} and 0 RPM, with charge integration of the hydrogen adsorption/desorption peak from the third negative scan and using 210 µC cm^{-2} as the charge generated by a fully H_2-covered Pt monolayer. Electrochemical impedance spectroscopy (EIS) was performed in potentiostatic mode (0.4 V *vs.* RHE) using a 5 mV perturbation between 1 kHz – 0.1 Hz to measure the ohmic resistance of

the electrolyte. Linear sweep voltammetry (LSV), between 50 mV – 1 V (*vs.* RHE) at 20 mV s^{-1}, was carried out to measure the background currents (in Ar) and ORR activity (in O_2) both at 1600 RPM. The electrolyte was saturated by bubbling 100 ml min^{-1} of gas during 30 min. Gas blanketing was used to prevent electrolyte contamination from the exterior of the cell. A commercial catalyst was used to compare the performance of the synthesized catalysts: 20 % Pt/C ETEK from BASF.

The protocol for studying the catalyst stability comprehends 10 000 cycles, between 20 and 925 mV (vs. RHE), at 500 mV s^{-1} in O_2-saturated electrolyte. The samples were then subjected to a new conditioning in Ar, before measuring the ECSA and ORR activities.

4.3. RESULTS AND DISCUSSION

4.3.1. SUITABILITY OF THE POLYOL METHOD

20PtVulcan was prepared using the polyol method and ORR performance is compared with a commercial sample (20PtETEK) in Figure 4.1. Despite the synthetized 20PtVulcan presents lower ECSA, it displayed higher area and mass specific activities at 0.9 V (vs. RHE) compared with the commercial sample. After confirming the suitable use of the polyol method for preparing functional electrocatalysts, the rGO and CNTs-supported platinum catalysts were then prepared and characterized.

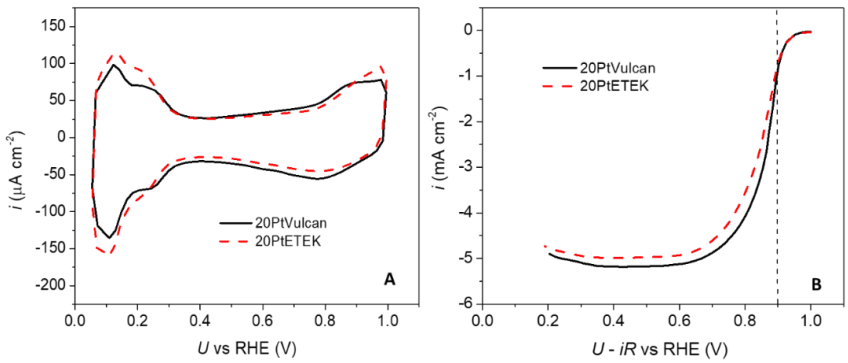


Figure 4.1 – ECSA and ORR activity measurements of synthesized 20PtVulcan and commercial sample: a) cyclic voltammograms in Ar at 20 mV s^{-1}; b) linear sweep voltammograms in O_2 at 1600 RPM and 20 mV s^{-1}.

4.3.2. INFLUENCE OF THE CARBON SUPPORT

The thermal stability and Pt loading of the synthetized electrocatalysts were determined by TGA under air flow. A sample of reduced graphene oxide, submitted to the polyol protocol but without Pt precursor, was tested to assess if any remaining material, besides platinum, would be present at the end of the analysis. The obtained results indicate a weight loss of almost 100 % showing, therefore, that the residual mass of the supported catalysts after TGA corresponds to the Pt content. The influence of the type of support employed is depicted in Figure 4.2a. Pt/CNTs displays the highest thermal stability followed by Pt/rGO. Chiang et al. observed that the maximum rates of weight loss of their graphene oxide (GO) and Vulcan XC-72R take place at ca. 715 °C; they also found that Pt/rGO was more thermally stable than Pt/Vulcan [45]. These authors strengthened that when Pt is nucleated in a carbon support, the maximum rate of weight loss decreases significantly.

The influence of the Pt content on the thermal stability of the rGO-supported catalysts is depicted in Figure 4.2b. The thermograms suggest that Pt increases the thermal stability of the supported catalyst in comparison to the support alone. However, this should be assigned to the reduction of most oxygenated groups during the polyol synthesis, increasing the crystallinity of the support. After the synthesis of 35PtrGO, the filtrate presented a yellow colour due to the presence of unreacted precursor, suggesting that all anchoring sites were already occupied [46]. Under the conditions of the synthesis, it seems unfeasible to achieve ratios of Pt/rGO higher than 30 – 35 wt.%. Few works in the literature succeeded to obtain higher Pt loadings on rGO (60 – 80 wt.%) and they achieved through either support functionalization [47], [48] or more complex synthesis methods [34], [49].

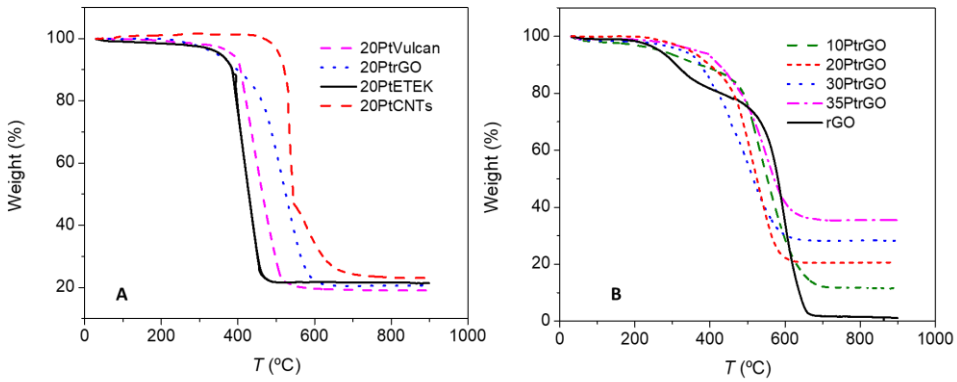


Figure 4.2 – Thermal gravimetric analysis (20 ml min^{-1} of air, 2 ºC min^{-1}) to assess the influence of a) the carbon support on the thermal stability of carbon-supported Pt catalysts; b) the Pt loading on the thermal stability of Pt/rGO catalysts.

The synthetized electrocatalysts were analyzed by TEM – Figure 4.3 – to evaluate the average size and dispersion of Pt particles. The average Pt particle size is given in Table 4.1. The catalysts synthetized with 20 wt.% of Pt in the three selected supports present an average Pt particle size of 6-7 nm. In the rGO-supported catalysts, the average Pt particle size increases with the Pt loading, ranging from 4 to 9 nm. The polyol synthesis allows to achieve Pt particles of small average sizes, between 2 and 4 nm; however, precise pH control throughout the synthesis is employed.

Table 4.1 - Average Pt particle size of synthetized electrocatalysts measured by TEM.

Catalyst sample	Average Pt particle size (nm)
20PtETEK	2-3*
20PtVulcan	5.9
20PtCNTs	6.6
10PtrGO	4.3
20PtrGO	6.3
30PtrGO	8.4
35PtrGO	9.5

*Information from the manufacturer

The higher Pt particle size obtained in this work can be explained by slightly different pH conditions from those reported by other studies [50], [51]. The effect of pH has been a subject of interest but there is not a full agreement in the literature. Some studies report that an acidic pH provided by the glycolate anion can alter the electrostatic forces between the support and the Pt colloid thus increasing the metal particle final size [46], [52]. Nonetheless, Liu *et al*. report a similar Pt particle mean size distribution, of ca 4.5 nm, also produced by a modified polyol method with no pH control [53].

Despite some agglomeration located especially at the edges of rGO sheets (Figure 4.3e), the 30PtrGO sample presents similar dispersion of Pt particles to those supported in Vulcan and CNTs. Nevertheless, the dispersion of Pt particles in the 20PtrGO sample is poor, due to the relatively low BET surface area of the carrier compared to other carbon supports. The intense black zone that is visible in some of the Pt/rGO samples corresponds to the wrinkling of the rGO sheets.

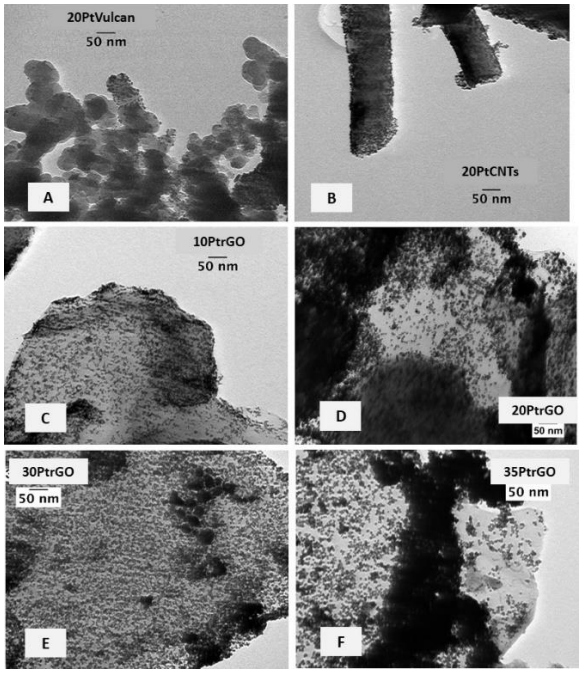


Figure 4.3 - TEM images of synthetized catalysts with different carbon supports and Pt loading on rGO – 200 000x of magnification.

For all the electrocatalysts, the incorporation of platinum causes a loss of BET specific area (ca. 50 – 70 %), suggesting that the texture of the supports is somehow altered by the Pt particles, Table 4.2.

Table 4.2 – Results from BET surface area determination.

Sample	**Surface area (m^2 g^{-1})**
Vulcan XC72-R	272.2
Graphene oxide	62.3
Reduced graphene oxide	103
CNTs	220
20PtETEK	191.9
20PtVulcan	185.2
20PtrGO	33.4
20PtCNTs	15.1

The X-ray diffractograms of the carbon-supported Pt catalysts are presented in Figure 4.4. For the rGO sample, the characteristic (0 0 2) peak assigned to graphitic carbon (JCPDS 75-1621) appears at ca. 26.0 º meaning that the functional surface groups of GO (anchoring sites) were partially reduced after the polyol protocol. In the GO sample, the characteristic (1 0 0) peak is dominant over the (0 0 2) [54], [55]. One fact that stands out is the high crystallinity evidenced by the sharp peak at ca. 25.0° for the sample 20PtCNTs [56]. The diffraction peaks at 40.0º, 46.0º, 67.5º and 81.4º correspond to the characteristic (1 1 1), (2 0 0), (2 2 0) and (3 1 1) crystalline planes of Pt (JCPDS 04-0802) of a face-centered-cubic structure [30].

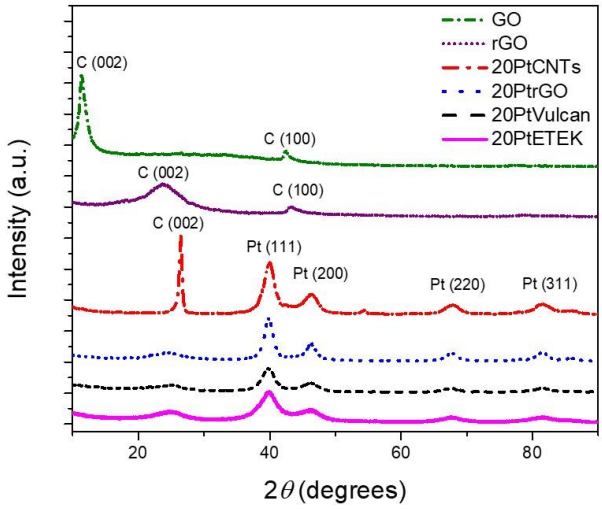


Figure 4.4 - X-ray diffraction patterns of the carbon-supported Pt catalysts; graphitic carbon (JCPDS 75-1621), Pt (JCPDS 04-0802).

The crystallite size of each catalyst was obtained by the Williamson-Hall method and listed in Table 4.3. The mean Pt crystallite size of the synthesized catalysts was determined to be ca. 5-7 nm, regardless of the carbon support, in good agreement with the TEM results.

Table 4.3 – Pt mean crystallite size determined from XRD.

Catalyst sample	**Pt mean crystallite size (nm)**
20PtETEK	5.3 ± 0.5
20PtVulcan	5.7 ± 0.5
20PtrGO	6.5 ± 0.5
20PtCNTs	6.9 ± 1

This suggests that the carbon support has no major influence in the resulting the Pt crystallite sizes. ECSA and ORR activity in RDE of the prepared Vulcan XC-72R, CNTs and rGO-based catalysts are summarized in Table 4.4. The highest ECSA (64 $m^2\ g^{-1}$)

was obtained for 20PtVulcan, followed by 20PtCNTs and 20PtrGO, respectively. The geometric activity at 0.4 V *vs.* RHE typically displays the diffusion-limited activity; the results obtained for 20PtVulcan and 20PtCNTs were similar and lower for 20PtrGO. A performance-microstructure dependence is evident and rGO seems to generate diffusion problems in which O_2 molecules struggle more to reach the active sites [57]. Moreover, the linear scan does not present the plateau that is observed in the other catalysts, which also suggests the existence of increased mass transport losses, Figure 4.5b.

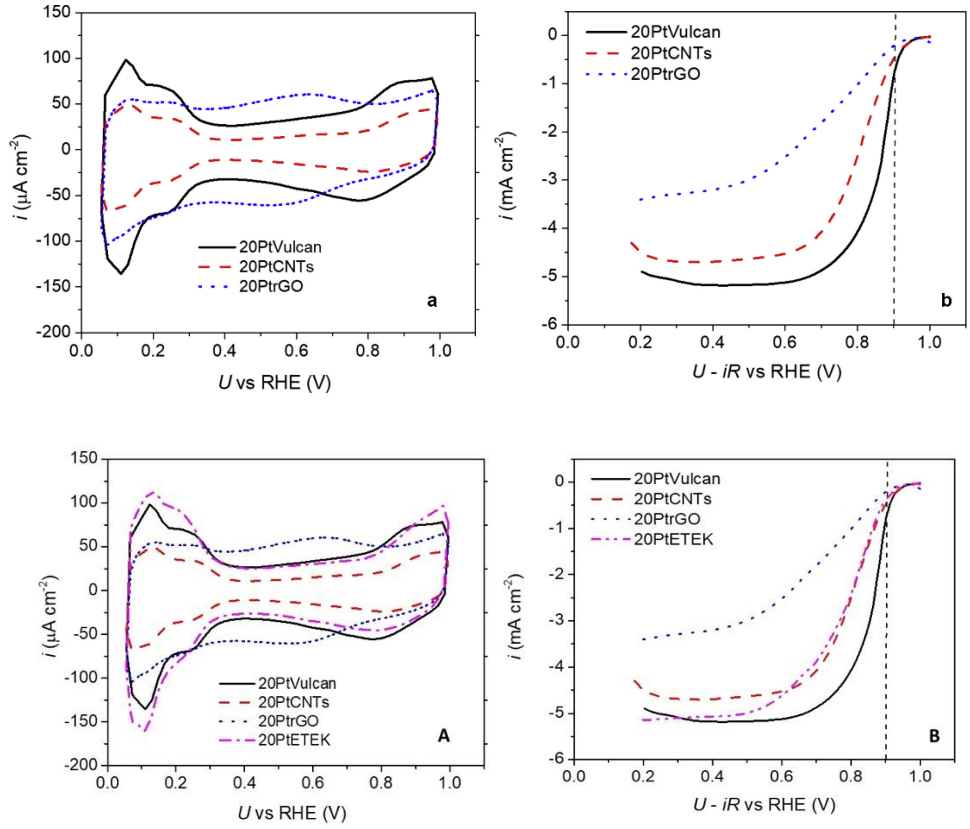


Figure 4.5 - ECSA and ORR activity measurement of electrocatalysts synthesized with different supports: a) cyclic voltammograms in Ar at 20 mV s^{-1}; b) linear sweep voltammograms in O_2 at 1600 RPM and 20 mV s^{-1}.

Analysing the electrochemical results summarized in Table 4.4, 30PtrGO displayed the highest area-specific activity (0.66 mA cm^{-2}_{Pt}) outperforming 20PtVulcan (0.33 mA cm^{-}

$^{2}_{Pt}$); on the other hand, the latter presents higher mass-specific activity (0.21 A mg$^{-1}_{Pt}$) than the former (0.17 A mg$^{-1}_{Pt}$). The work by Debe [58] provides an interesting explanation about the geometry effects that influence ORR specific activities. The author concluded that polycrystalline single crystal bulk surfaces, possess 5 to 10 times higher oxygen reduction area-specific activity than smaller spheroid metal catalyst particles; this effect balances the lower surface area of the platelet-like metal particles. ORR mechanisms are dependent on the electrode's surface area per unit of volume (cm$^{2}_{Pt}$/cm$^{3}_{Pt}$) and, in the Knudsen regime, the electrode microstructure influences the number of chemisorption bounds established per unit of time. Pt/rGO seems to possess a microstructure that behaves closer to a platelet-like catalyst owing to its high area-specific activity but low mass-specific activity.

Table 4.4 – Summary of results from RDE measurements.

Catalyst	**ECSA (m^2_{Pt} g^{-1}_{Pt})**	**Area-specific activity @ 0.9 V (mA cm^{-2}_{Pt})**	**Mass-specific activity @ 0.9 V (A mg^{-1}_{Pt})**	**Diffusion-limited activity (mA cm_{geo}^{-2})**	**Loading (µg cm_{geo}^{-2})**
20PtVulcan	64	0.33	0.21	5.3	8
20PtVulcanAD	51 (-20 %)	0.26	0.13 (-37 %)	4.5 (-15 %)	8
20PtCNTs	42	0.29	0.12	4.8	8
20PtrGO	27	0.38	0.10	3.8	8
10PtrGO	36	0.30	0.11	2.8	4
30PtrGO	26	0.66	0.17	4.1	12
30PtrGOAD	22 (-15 %)	0.25	0.05 (-69 %)	3.8 (-7 %)	12
35PtrGO	29	0.36	0.10	3.8	14
25|75 PtrGO|PtVulcan	37	0.42	0.16	5	9
50|50 PtrGO|PtVulcan	46	0.39	0.18	4.5	10

50|50 PtrGO|PtVulcanAD	37 (-14 %)	0.36	0.13 (-28%)	4.2 (-7 %)	10
20PtETEK	81	0.22	0.18	5	8

Due to the self-similar geometries of dispersed catalysts with respect to surface area and loading, they are more dependent on the catalyst loading than the platelet-like catalyst. A reduction in the Pt loading will then generate a higher loss of surface area for Pt/Vulcan than for Pt/rGO. Xin *et al.* reported higher ORR activities for Pt supported on graphene when compared with Pt supported on Vulcan XC-72, both synthetized using $NaBH_4$ as reducing agent [31]. Shao *et al.* compared the performance of two catalysts synthetized using a modified polyol method, in alkaline conditions, using graphene and CNTs as supports. The catalysts displayed lower ECSA values (of ca. 40 $m^2_{Pt}\ g^{-1}_{Pt}$) than the commercial 20 wt.% Pt/C. Nonetheless the Pt/graphene catalyst presented the best performance after running the degradation protocol, consisting in 10 000 potential cycles [59]. Jafri *et al.* used $NaBH_4$ as reducing agent to synthetize Pt/graphene and Pt/CNTs. They measured high ECSA values (in a single-cell) of 95.1 and 77.4 $m^2\ g^{-1}$, respectively [60]. Li *et al.* reported the synthesis of Pt/rGO and Pt/CNTs by the polyol method and measured lower ECSAs, 36.3 and 33.4 $m^2\ g^{-1}$, respectively [30]. These results indicate that the synthesis methods are very sensitive to the operating conditions and to the electrochemical characterization procedure.

4.3.3. INFLUENCE OF PT LOADING IN RGO

The Pt loading on carbon supports plays a decisive role in the Pt particle size and dispersion as well as in ECSA and ORR activity of the catalysts. Figure 4.6 depicts ECSA and ORR measurements of the prepared catalysts on rGO as a function of the Pt mass fraction. 10PtrGO displays the highest ECSA (36 $m^2\ g^{-1}$), followed by 35PtrGO (29 $m^2\ g^{-1}$), 20PtrGO (27 $m^2\ g^{-1}$) and the lowest for 30PtrGO (26 $m^2\ g^{-1}$); the values of ECSA do not follow the trend of the Pt/rGO mass fraction. In terms of ORR activity at 0.9 V *vs.* RHE, the 30PtrGO sample displays the highest area and mass-specific

activities. The diffusion-limited activity (at 0.4 V *vs.* RHE) increases with the Pt loading, peaking for 30PtrGO, and decreasing afterwards for 35PtrGO. The increasing Pt loadings allows "processing" more reactant per unit of time but, when Pt particles are too big, they may block the micropores of the electrode thus decreasing the diffusion pathways and consequently the diffusion-limited activity. Additionally, a Koutecky – Levich study was performed to one of the rGO-supported electrocatalyst to estimate the number of electrons transferred during the ORR, considering a C_0 of 1.18×10^{-6} mol cm^{-3} – bulk concentration of O_2 in the electrolyte, a D_0 of 1.9×10^{-5} cm^2 s^{-1} – O_2 effective diffusion coefficient and a kinematic viscosity of the electrolyte (v) of 9.87×10^{-3} cm^2 s^{-1} at 25 ºC for a 0.1 M $HCLO_{4(aq)}$ [61]. An overall electron-transfer number of 3.94 was estimated, which confirmed a direct 4-electron transfer pathway for the rGO-supported catalysts. Thus, a minimal and despicable portion of the electron-transfer process happens through a 2-electron transfer pathway from O_2 to H_2O_2.

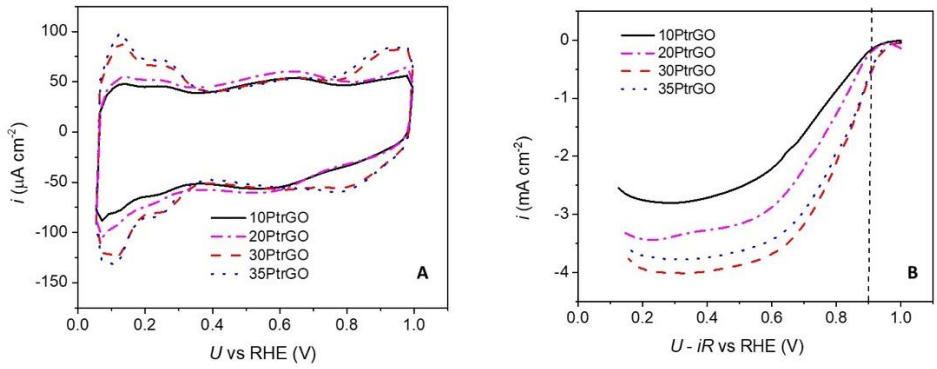


Figure 4.6 - ECSA and ORR activity measurement of electrocatalysts synthesized with different Pt loadings on rGO: a) cyclic voltammograms in Ar at 20 mV s^{-1}; b) linear sweep voltammograms in O_2 at 1600 RPM and 20 mV s^{-1}.

Speder *et al.*, studied the influence of the mass fraction of Pt on Vulcan and obtained increased ECSA values as Pt/C ratio decreases [62]. The same trend was reported by Choi *et al.* using surface-modified graphene, instead of Vulcan, as catalyst support [63]. Daş *et al.* studied the Pt loading on graphene and reported a linear dependence between Pt particle size and Pt/graphene mass fraction; surprisingly, the ECSA values obtained

did not follow the same behaviour of the two previous works [64]. The results obtained in this work greatly depend on the properties of the GO used in the synthesis and since there are several methods to produce GO with different qualities, a big discrepancy can be expected in terms of electrochemical performances. The rGO sheets used in this work measure *ca.* 10-20 µm in length whereas the diameter of Vulcan carbon particles is ca. 30 nm. To obtain a homogeneous catalyst layer is much easier with smaller particles and it influences the catalytic performance.

4.3.4. HYBRID SUPPORT TO AVOID RGO-STACKING

Several works in the literature reported the advantage of mixing catalysts with different supports, namely graphene with carbon black [35]–[37], [65] or with carbon nanotubes [60]. The idea is to use the second catalyst as a "spacer" of the carbon platelets characteristic of the graphene supported platinum catalysts. More interesting is the fact that some of these works measured higher ECSAs using mixed catalysts of different supports than those measured for the individual catalyst types. Şanlı *et al.* found that rGO:Vulcan mass ratio of 75:25 offers the highest ECSA [65]. The ECSA and ORR activities of different mixed rGO-based catalysts with Vulcan-based ones are shown in Figure 4.7.

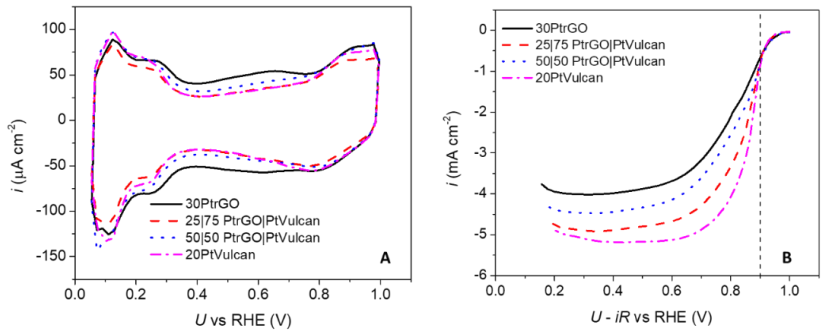


Figure 4.7- ECSA and ORR activities of 30PtrGO, 20PtVulcan and mixtures of rGO and Vulcan-based electrocatalysts: a) cyclic voltammograms in Ar at 20 mV s^{-1}; b) linear sweep voltammograms in O_2 at 1600 RPM and 20 mV s^{-1}

Both ECSA and ORR activity of the mixtures remain within the values of the catalysts that form the mixture. This is in accordance with the single cell measurements by Jung *et al.* where the only advantage they found of mixing the two catalysts was to increase the stability upon accelerated degradation [35]. The fact that the use of Vulcan to act as a "spacer" did not generate valuable results may be related to the big length of the rGO sheets. The dimensions of the two types of support are very different and such small spherical particles are not able to prevent re-stacking of rGO sheets.

4.3.5. STABILITY UPON ACCELERATED DEGRADATION

An accelerated stress test, consisting of 10 000 cycles between 50 mV and 925 mV (*vs.* RHE) at 500 mV/s in O_2-saturated electrolyte, was imposed to the best performing catalysts among those that were synthetized - Figure 4.8. Catalysts 20PtVulcan, 30PtrGO and 50|50 PtrGO|PtVulcan were characterized.

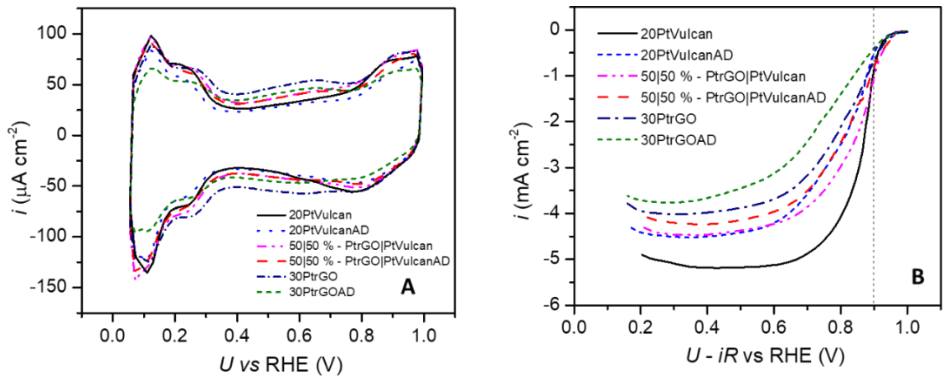


Figure 4.8 - Comparison between mixtures of 20PtVulcan and 30PtrGO pristine and upon degradation: a) cyclic voltammograms in Ar at 20 mV s^{-1}; b) linear sweep voltammograms in O_2 at 1600 RPM and 20 mV s^{-1}.

The highest ECSA loss at the end of this test was recorded for 20PtVulcan (-20 %), followed by 30PtrGO (-15 %) and finally the hybrid support (-14 %), the loss of mass activity was significantly higher for the latter (-69 %), followed by the former (-37 %) and the lowest for the hybrid support (-28 %). Nonetheless, the hybrid catalyst displays

the least loss rate of ECSA (14 %) and mass activity (28 %), meaning that it proves valuable to combine these two supports in terms of stability. In the work by Jun *et al.* it is reported that a Pt/GO catalyst is more stable than Pt/C (losses in ECSA were 45 % and 15 %, respectively) after imposing a degradation protocol, consisting in cycling between high potentials (0.4 – 1.2 V *vs.* RHE), which affects mainly the support [35].

Shao *et al.* also reported the same trend for both ECSA and ORR activity for Pt/graphene and commercial 20 wt.% Pt/C, after imposing a similar degradation protocol [59]. The degradation protocol of this work consisted in a broader range of potential for ORR but did not include potentials above 925 mV *vs.* RHE. Carbon corrosion should not be as extensive as in the reports mentioned before, meaning that the main degradation should be associated to Pt particles growth by sintering or Ostwald ripening. Despite the small drop in ECSA of the sample 30PtrGO, the loss of specific mass activity was very high; this suggests changes in the metallic structure of platinum, exposing less-reactive planes but with small loss of metal surface area. The smaller loss in diffusion-limited activity compared to 20PtVulcan suggest a lower change in the microstructure after the degradation protocol, keeping most of oxygen diffusion pathways.

4.4. CONCLUSIONS

Functional ORR catalysts were produced through a simple and easy-scalable synthesis route like the polyol method. Higher Pt loading on rGO led to bigger but more crystalline Pt particles.

The area-specific activities of rGO-supported catalysts were the highest, evidencing a behaviour closer to that of a bulk-like catalyst, in which the active sites seem to "work harder" if compared to dispersed particles. 30 wt.% on rGO was found to be the optimal Pt loading leading to higher ORR activity and best Pt dispersion in the support.

Upon accelerated degradation the 30PtrGO sample presented higher loss of ORR mass-specific activity when compared to 20PtVulcan. Still, it possessed much higher area-specific activity, a promising indicator regarding the use rGO-supported catalysts in

increasingly thinner catalyst layers due to their lower performance sensitivity to the reduction of catalyst loading in the fuel cell cathode.

REFERENCES

[1] P. Costamagna and S. Srinivasan, "Quantum jumps in the PEMFC science and technology from the 1960s to the year 2000: Part II. Engineering, technology development and application aspects," *J. Power Sources*, vol. 102, no. 1–2, pp. 253–269, Dec. 2001, doi: 10.1016/s0378-7753(01)00808-4.

[2] J. M. Andújar and F. Segura, "Fuel cells: History and updating. A walk along two centuries," *Renew. Sustain. Energy Rev.*, vol. 13, no. 9, pp. 2309–2322, Dec. 2009, doi: 10.1016/j.rser.2009.03.015.

[3] Y. Wang, K. S. Chen, J. Mishler, S. C. Cho, and X. C. Adroher, "A review of polymer electrolyte membrane fuel cells: Technology, applications, and needs on fundamental research," *Appl. Energy*, vol. 88, no. 4, pp. 981–1007, Apr. 2011, doi: 10.1016/j.apenergy.2010.09.030.

[4] E. Antolini, "Formation of carbon-supported PtM alloys for low temperature fuel cells: a review," *Mater. Chem. Phys.*, vol. 78, no. 3, pp. 563–573, Feb. 2003, doi: 10.1016/s0254-0584(02)00389-9.

[5] H. A. Gasteiger, S. S. Kocha, B. Sompalli, and F. T. Wagner, "Activity benchmarks and requirements for Pt, Pt-alloy, and non-Pt oxygen reduction catalysts for PEMFCs," *Appl. Catal. B Environ.*, vol. 56, no. 1–2, pp. 9–35, Mar. 2005, doi: 10.1016/j.apcatb.2004.06.021.

[6] A. Holewinski, J.-C. Idrobo, and S. Linic, "High-performance Ag–Co alloy catalysts for electrochemical oxygen reduction," *Nat. Chem.*, vol. 6, p. 828, Aug. 2014, [Online]. Available: http://dx.doi.org/10.1038/nchem.2032.

[7] S. M. Alia, S. Pylypenko, A. Dameron, K. C. Neyerlin, S. S. Kocha, and B. S. Pivovar, "Oxidation of Platinum Nickel Nanowires to Improve Durability of Oxygen-Reducing Electrocatalysts," *J. Electrochem. Soc.* , vol. 163, no. 3, pp. F296–F301, Jan. 2016, doi: 10.1149/2.0081605jes.

[8] S. M. Alia *et al.*, "Platinum-Coated Nickel Nanowires as Oxygen-Reducing Electrocatalysts," *ACS Catal.*, vol. 4, no. 4, pp. 1114–1119, Apr. 2014, doi: 10.1021/cs401081w.

[9] M. Li *et al.*, "Ultrafine jagged platinum nanowires enable ultrahigh mass activity for the oxygen reduction reaction," *Science (80-.).*, Nov. 2016, [Online]. Available: http://science.sciencemag.org/content/early/2016/11/16/science.aaf9050.abstract.

[10] C. Zhang, S. Y. Hwang, and Z. Peng, "Platinum Alloy Nanocatalyst with Manipulated Particle Composition and Morphology for Improved ORR Property," *Meet. Abstr.* , vol. MA2016-01, no. 35, p. 1698, Apr. 2016.

[11] N. Lindahl *et al.*, "High Specific and Mass Activity for the Oxygen Reduction Reaction for Thin Film Catalysts of Sputtered Pt3Y," *Adv. Mater. Interfaces*, vol. 4, no. 13, p. 1700311, May 2017, doi: 10.1002/admi.201700311.

[12] R. Borup *et al.*, "Scientific Aspects of Polymer Electrolyte Fuel Cell Durability and Degradation," *Chem. Rev.*, vol. 107, no. 10, pp. 3904–3951, Oct. 2007, doi: 10.1021/cr050182l.

[13] J. Xie, D. L. Wood, D. M. Wayne, T. A. Zawodzinski, P. Atanassov, and R. L. Borup, "Durability of PEFCs at High Humidity Conditions," *J. Electrochem. Soc.* , vol. 152, no. 1, pp. A104–A113, Jan. 2005, doi: 10.1149/1.1830355.

[14] K. Kinoshita, "Particle Size Effects for Oxygen Reduction on Highly Dispersed Platinum in Acid Electrolytes," *J. Electrochem. Soc.* , vol. 137, no. 3, pp. 845–848, Mar. 1990, doi: 10.1149/1.2086566.

[15] M. Watanabe, H. Sei, and P. Stonehart, "The influence of platinum crystallite size on the electroreduction of oxygen," *J. Electroanal. Chem. Interfacial Electrochem.*, vol. 261, no. 2, pp. 375–387, Apr. 1989, doi: 10.1016/0022-0728(89)85006-5.

[16] A. Kabbabi, F. Gloaguen, F. Andolfatto, and R. Durand, "Particle size effect for oxygen reduction and methanol oxidation on Pt/C inside a proton exchange membrane," *J. Electroanal. Chem.*, vol. 373, no. 1–2, pp. 251–254, Aug. 1994, doi: 10.1016/0022-0728(94)03503-2.

[17] B. Zhang and D. S. Su, "Probing the Metal–Support Interaction in Carbon-Supported Catalysts by using Electron Microscopy," *ChemCatChem*, vol. 7, no. 22, pp. 3639–3645, Oct. 2015, doi: 10.1002/cctc.201500666.

[18] C. T. Campbell, "Electronic perturbations," *Nat. Chem.*, vol. 4, p. 597, Jul. 2012, [Online]. Available: http://dx.doi.org/10.1038/nchem.1412.

[19] C. Wang *et al.*, "A unique platinum-graphene hybrid structure for high activity and durability in oxygen reduction reaction," *Sci. Rep.*, vol. 3, p. 2580, Sep. 2013, [Online]. Available: http://dx.doi.org/10.1038/srep02580.

[20] D. Kaewsai, H.-L. Lin, Y.-C. Liu, and T. L. Yu, "Platinum on pyridine-polybenzimidazole wrapped carbon nanotube supports for high temperature proton exchange membrane fuel cells," *Int. J. Hydrogen Energy*, vol. 41, no. 24, pp. 10430–10445, 2016, doi: https://doi.org/10.1016/j.ijhydene.2015.09.066.

[21] B. P. Vinayan, R. I. Jafri, R. Nagar, N. Rajalakshmi, K. Sethupathi, and S. Ramaprabhu, "Catalytic activity of platinum–cobalt alloy nanoparticles decorated functionalized multiwalled carbon nanotubes for oxygen reduction reaction in PEMFC," *Int. J. Hydrogen Energy*, vol. 37, no. 1, pp. 412–421, 2012, doi: https://doi.org/10.1016/j.ijhydene.2011.09.069.

[22] M. Boaventura, L. Brandão, and A. Mendes, "Single-Wall Nanohorns as Electrocatalyst Support for High Temperature PEM Fuel Cells," *J. Electrochem. Soc.* , vol. 158, no. 4, pp. B394–B401, Apr. 2011, doi: 10.1149/1.3551495.

[23] M. Ghasemi, S. Shahgaldi, M. Ismail, B. H. Kim, Z. Yaakob, and W. R. Wan Daud, "Activated carbon nanofibers as an alternative cathode catalyst to platinum in a two-chamber microbial fuel cell," *Int. J. Hydrogen Energy*, vol. 36, no. 21, pp. 13746–13752, 2011, doi: https://doi.org/10.1016/j.ijhydene.2011.07.118.

[24] A. M. Zainoodin, S. K. Kamarudin, M. S. Masdar, W. R. W. Daud, A. B. Mohamad, and J. Sahari, "High power direct methanol fuel cell with a porous carbon nanofiber anode layer," *Appl. Energy*, vol. 113, pp. 946–954, 2014, doi: https://doi.org/10.1016/j.apenergy.2013.07.066.

[25] A. K. Geim and K. S. Novoselov, "The rise of graphene," in *Nanoscience and Technology*, Co-Published with Macmillan Publishers Ltd, UK, 2009, pp. 11–19.

[26] D. Chen, L. Tang, and J. Li, "Graphene-based materials in electrochemistry," *Chem. Soc. Rev.*, vol. 39, no. 8, pp. 3157–3180, 2010, doi: 10.1039/b923596e.

[27] E. Sani, J. P. Vallejo, D. Cabaleiro, and L. Lugo, "Functionalized graphene nanoplatelet-nanofluids for solar thermal collectors," *Sol. Energy Mater. Sol. Cells*, vol. 185, pp. 205–209, Oct. 2018, doi: 10.1016/j.solmat.2018.05.038.

[28] E. Šest, G. Dražič, B. Genorio, and I. Jerman, "Graphene nanoplatelets as an anticorrosion additive for solar absorber coatings," *Sol. Energy Mater. Sol. Cells*, vol. 176, pp. 19–29, Mar. 2018, doi: 10.1016/j.solmat.2017.11.016.

[29] M. Vaqueiro-Contreras *et al.*, "Graphene oxide films for field effect surface passivation of silicon for solar cells," *Sol. Energy Mater. Sol. Cells*, vol. 187, pp. 189–193, Dec. 2018, doi: 10.1016/j.solmat.2018.08.002.

[30] Y. Li, W. Gao, L. Ci, C. Wang, and P. M. Ajayan, "Catalytic performance of Pt nanoparticles on reduced graphene oxide for methanol electro-oxidation," *Carbon N. Y.*, vol. 48, no. 4, pp. 1124–1130, Apr. 2010, doi: 10.1016/j.carbon.2009.11.034.

[31] Y. Xin *et al.*, "Preparation and characterization of Pt supported on graphene with enhanced electrocatalytic activity in fuel cell," *J. Power Sources*, vol. 196, no. 3, pp. 1012–1018, Feb. 2011, doi: 10.1016/j.jpowsour.2010.08.051.

[32] D. Krishnan *et al.*, "Energetic graphene oxide: Challenges and opportunities," *Nano Today*, vol. 7, no. 2, pp. 137–152, Apr. 2012, doi: 10.1016/j.nantod.2012.02.003.

[33] D. He *et al.*, "Highly Active Platinum Nanoparticles on Graphene Nanosheets with a Significant Improvement in Stability and CO Tolerance," *Langmuir*, vol. 28, no. 8, pp. 3979–3986, Feb. 2012, doi: 10.1021/la2045493.

[34] S. H. Hsieh, M. C. Hsu, W. L. Liu, and W. J. Chen, "Study of Pt catalyst on graphene and its application to fuel cell," *Appl. Surf. Sci.*, vol. 277, pp. 223–230, Jul. 2013, doi: 10.1016/j.apsusc.2013.04.029.

[35] J. H. Jung, H. J. Park, J. Kim, and S. H. Hur, "Highly durable Pt/graphene oxide and Pt/C hybrid catalyst for polymer electrolyte membrane fuel cell," *J. Power Sources*, vol. 248, pp. 1156–1162, Feb. 2014, doi: 10.1016/j.jpowsour.2013.10.055.

[36] S. Park *et al.*, "Design of graphene sheets-supported Pt catalyst layer in PEM fuel cells," *Electrochem. commun.*, vol. 13, no. 3, pp. 258–261, Mar. 2011, doi:

10.1016/j.elecom.2010.12.028.

[37] D. He, K. Cheng, T. Peng, M. Pan, and S. Mu, "Graphene/carbon nanospheres sandwich supported PEM fuel cell metal nanocatalysts with remarkably high activity and stability," *J. Mater. Chem. A*, vol. 1, no. 6, pp. 2126–2132, 2013, doi: 10.1039/c2ta00606e.

[38] L. I. Şanlı, V. Bayram, B. Yarar, S. Ghobadi, and S. A. Gürsel, "Development of graphene supported platinum nanoparticles for polymer electrolyte membrane fuel cells: Effect of support type and impregnation–reduction methods," *Int. J. Hydrogen Energy*, vol. 41, no. 5, pp. 3414–3427, Feb. 2016, doi: 10.1016/j.ijhydene.2015.12.166.

[39] L. Pak Hoe, M. Boaventura, T. Lagarteira, L. Kee Shyuan, and A. Mendes, "Polyol synthesis of reduced graphene oxide supported platinum electrocatalysts for fuel cells: Effect of Pt precursor, support oxidation level and pH," *Int. J. Hydrogen Energy*, vol. 43, no. 35, pp. 16998–17011, Jun. 2018, doi: 10.1016/j.ijhydene.2018.05.147.

[40] Y. Garsany, J. Ge, J. St-Pierre, R. Rocheleau, and K. E. Swider-Lyons, "Analytical Procedure for Accurate Comparison of Rotating Disk Electrode Results for the Oxygen Reduction Activity of Pt/C," *J. Electrochem. Soc.* , vol. 161, no. 5, pp. F628–F640, Jan. 2014, doi: 10.1149/2.036405jes.

[41] T. J. Schmidt, H. A. Gasteiger, G. D. Stäb, P. M. Urban, D. M. Kolb, and R. J. Behm, "Characterization of High-Surface-Area Electrocatalysts Using a Rotating Disk Electrode Configuration," *J. Electrochem. Soc.* , vol. 145, no. 7, pp. 2354–2358, Jul. 1998, doi: 10.1149/1.1838642.

[42] U. A. Paulus, T. J. Schmidt, H. A. Gasteiger, and R. J. Behm, "Oxygen reduction on a high-surface area Pt/Vulcan carbon catalyst: a thin-film rotating ring-disk electrode study," *J. Electroanal. Chem.*, vol. 495, no. 2, pp. 134–145, 2001, doi: https://doi.org/10.1016/s0022-0728(00)00407-1.

[43] Y. Garsany, I. L. Singer, and K. E. Swider-Lyons, "Impact of film drying procedures on RDE characterization of Pt/VC electrocatalysts," *J. Electroanal.*

Chem., vol. 662, no. 2, pp. 396–406, 2011, doi: https://doi.org/10.1016/j.jelechem.2011.09.016.

[44] Y. Garsany, O. A. Baturina, K. E. Swider-Lyons, and S. S. Kocha, "Experimental Methods for Quantifying the Activity of Platinum Electrocatalysts for the Oxygen Reduction Reaction," *Anal. Chem.*, vol. 82, no. 15, pp. 6321–6328, Aug. 2010, doi: 10.1021/ac100306c.

[45] Y.-C. Chiang, C.-C. Liang, and C.-P. Chung, "Characterization of Platinum Nanoparticles Deposited on Functionalized Graphene Sheets," *Materials* , vol. 8, no. 9. 2015, doi: 10.3390/ma8095318.

[46] X. Li, W.-X. Chen, J. Zhao, W. Xing, and Z.-D. Xu, "Microwave polyol synthesis of Pt/CNTs catalysts: Effects of pH on particle size and electrocatalytic activity for methanol electrooxidization," *Carbon N. Y.*, vol. 43, no. 10, pp. 2168–2174, Aug. 2005, doi: 10.1016/j.carbon.2005.03.030.

[47] S. M. Choi, M. H. Seo, H. J. Kim, and W. B. Kim, "Synthesis of surface-functionalized graphene nanosheets with high Pt-loadings and their applications to methanol electrooxidation," *Carbon N. Y.*, vol. 49, no. 3, pp. 904–909, Mar. 2011, doi: 10.1016/j.carbon.2010.10.055.

[48] L. Xin *et al.*, "Understanding Pt Nanoparticle Anchoring on Graphene Supports through Surface Functionalization," *ACS Catal.*, vol. 6, no. 4, pp. 2642–2653, Apr. 2016, doi: 10.1021/acscatal.5b02722.

[49] H.-W. Ha, I. Y. Kim, S.-J. Hwang, and R. S. Ruoff, "One-Pot Synthesis of Platinum Nanoparticles Embedded on Reduced Graphene Oxide for Oxygen Reduction in Methanol Fuel Cells," *Electrochem. Solid-State Lett.* , vol. 14, no. 7, pp. B70–B73, Jul. 2011, doi: 10.1149/1.3584092.

[50] F. Fievet, J. P. Lagier, B. Blin, B. Beaudoin, and M. Figlarz, "Homogeneous and heterogeneous nucleations in the polyol process for the preparation of micron and submicron size metal particles," *Solid State Ionics*, vol. 32–33, pp. 198–205, Feb. 1989, doi: 10.1016/0167-2738(89)90222-1.

[51] W. X. Chen, J. Y. Lee, and Z. Liu, "Microwave-assisted synthesis of carbon supported Pt nanoparticles for fuel cell applications," *Chem. Commun.*, no. 21, pp. 2588–2589, Oct. 2002, doi: 10.1039/b208600j.

[52] H.-S. Oh, J.-G. Oh, and H. Kim, "Modification of polyol process for synthesis of highly platinum loaded platinum–carbon catalysts for fuel cells," *J. Power Sources*, vol. 183, no. 2, pp. 600–603, Sep. 2008, doi: 10.1016/j.jpowsour.2008.05.070.

[53] Z. Liu, X. Y. Ling, X. Su, J. Y. Lee, and L. M. Gan, "Preparation and characterization of Pt/C and PtRu/C electrocatalysts for direct ethanol fuel cells," *J. Power Sources*, vol. 149, pp. 1–7, Sep. 2005, doi: 10.1016/j.jpowsour.2005.02.009.

[54] H.-K. Jeong *et al.*, "Evidence of Graphitic AB Stacking Order of Graphite Oxides," *J. Am. Chem. Soc.*, vol. 130, no. 4, pp. 1362–1366, Jan. 2008, doi: 10.1021/ja076473o.

[55] C.-C. Chien and K.-T. Jeng, "Effective preparation of carbon nanotube-supported Pt–Ru electrocatalysts," *Mater. Chem. Phys.*, vol. 99, no. 1, pp. 80–87, 2006, doi: https://doi.org/10.1016/j.matchemphys.2005.09.080.

[56] P. V Shanahan, L. Xu, C. Liang, M. Waje, S. Dai, and Y. S. Yan, "Graphitic mesoporous carbon as a durable fuel cell catalyst support," *J. Power Sources*, vol. 185, no. 1, pp. 423–427, 2008, doi: https://doi.org/10.1016/j.jpowsour.2008.06.041.

[57] R. Kou *et al.*, "Enhanced activity and stability of Pt catalysts on functionalized graphene sheets for electrocatalytic oxygen reduction," *Electrochem. commun.*, vol. 11, no. 5, pp. 954–957, May 2009, doi: 10.1016/j.elecom.2009.02.033.

[58] M. K. Debe, "Nanostructured Thin Film Electrocatalysts for PEM Fuel Cells - A Tutorial on the Fundamental Characteristics and Practical Properties of NSTF Catalysts," *ECS Trans.* , vol. 45, no. 2, pp. 47–68, Apr. 2012, doi: 10.1149/1.3701968.

[59] Y. Shao *et al.*, "Highly durable graphene nanoplatelets supported Pt nanocatalysts for oxygen reduction," *J. Power Sources*, vol. 195, no. 15, pp. 4600–4605, Aug. 2010, doi: 10.1016/j.jpowsour.2010.02.044.

[60] R. I. Jafri, T. Arockiados, N. Rajalakshmi, and S. Ramaprabhu, "Nanostructured

Pt Dispersed on Graphene-Multiwalled Carbon Nanotube Hybrid Nanomaterials as Electrocatalyst for PEMFC," *J. Electrochem. Soc.* , vol. 157, no. 6, pp. B874–B879, Jun. 2010, doi: 10.1149/1.3374353.

[61] A. Onoda, Y. Tanaka, T. Ono, S. Takeuchi, A. Sakai, and T. Hayashi, "Myoglobin-based non-precious metal carbon catalysts for an oxygen reduction reaction," *J. Porphyr. Phthalocyanines*, vol. 19, no. 01–03, pp. 510–516, Jan. 2015, doi: 10.1142/s108842461550039x.

[62] J. Speder *et al.*, "Comparative degradation study of carbon supported proton exchange membrane fuel cell electrocatalysts – The influence of the platinum to carbon ratio on the degradation rate," *J. Power Sources*, vol. 261, pp. 14–22, Sep. 2014, doi: 10.1016/j.jpowsour.2014.03.039.

[63] S.-H. Kim *et al.*, "Synthesis of noble metal/graphene nanocomposites without surfactants by one-step reduction of metal salt and graphene oxide," *J. Colloid Interface Sci.*, vol. 389, no. 1, pp. 85–90, Jan. 2013, doi: 10.1016/j.jcis.2012.08.064.

[64] E. Daş, S. Alkan Gürsel, L. Işıkel Şanlı, and A. Bayrakçeken Yurtcan, "Thermodynamically controlled Pt deposition over graphene nanoplatelets: Effect of Pt loading on PEM fuel cell performance," *Int. J. Hydrogen Energy*, vol. 42, no. 30, pp. 19246–19256, Jul. 2017, doi: 10.1016/j.ijhydene.2017.06.108.

[65] L. Işıkel Şanlı, V. Bayram, S. Ghobadi, N. Düzen, and S. Alkan Gürsel, "Engineered catalyst layer design with graphene-carbon black hybrid supports for enhanced platinum utilization in PEM fuel cell," *Int. J. Hydrogen Energy*, vol. 42, no. 2, pp. 1085–1092, Jan. 2017, doi: 10.1016/j.ijhydene.2016.08.210.

CHAPTER 5

OXYGEN REDUCTION STABILITY OF GRAPHENE-SUPPORTED ELECTROCATALYST: ELECTROCHEMICAL AND MORPHOLOGICAL EVIDENCES

5

OXYGEN REDUCTION STABILITY OF GRAPHENE-SUPPORTED ELECTROCATALYST: ELECTROCHEMICAL AND MORPHOLOGICAL EVIDENCES

Tiago Lagarteira, Sofia Delgado, Gema Garcia, Alfredo Ortiz and Adélio Mendes

Adapted from the International Journal of Hydrogen Energy, 2023, 48(54)

ABSTRACT

The insufficient Oxygen Reduction Reaction (ORR) stability demonstrated by common carbon supports has been hindering the widespread commercialization of automotive Proton Exchange Membrane Fuel cells (PEMFCs). To meet the stability targets set by the US DoE, other supports are needed with greater corrosion stability, surface area and electronic conductivity.

Graphene has been proposed as support or as co-support for electrocatalysts due to its high electronic conductivity, corrosion stability and high specific surface area compared to common carbon blacks, such as Vulcan. Despite such outstanding properties, comprehensive studies on long-term stability of graphene-supported ORR catalysts are still unavailable or limited.

The stability of graphene as support is now studied and compared with carbon black in terms of electrochemical performance and degradation mechanisms. Catalytic layers with Pt/G were prepared and subjected to a set of three different Accelerated Stress Tests (ASTs) (cycling at high potentials, Open Circuit Potential (OCP) holding and cycling at low potentials) to assess if and why graphene is a better candidate as support. The Pt/G catalyst outperformed the reference catalyst in all ASTs, delivering both higher electrochemical active surface area (ECSA) and ORR mass-specific activity. Such

electrochemical performance was correlated with several degradation mechanisms associated to the support itself and with Pt nanoparticles.

Keywords: Oxygen Reduction Reaction, carbon support, Graphene, Stability, specific-area activity.

5.1. INTRODUCTION

Hydrogen has emerged as a promising option for at-scale decarbonization of energy sectors such as transport, industry and buildings [1]. Proton exchange membrane fuel cells (PEMFCs) will play an important role, mainly at the heavy-duty transport sector due to their high-power density, cold-start withstand and ability to operate at low temperature with high efficiency and power output [2]. PEMFCs are especially suited for powering large cars, trucks, buses, ships, trains and even air-planes due to their extended range and quick refueling time. Despite both efficiency and environmental advantages of fuel cells had been already demonstrated, it is still a challenge to meet the cost and durability of competing technologies [2].

Platinum (or its alloys [3]–[6]) is the catalyst of choice for driving both hydrogen oxidation reaction (HOR) and oxygen reduction reaction (ORR), due to its unmatchable activity and stability in acidic medium. For increasing the specific electrochemical surface area (ECSA), state-of-the-art PEMFC electrocatalysts consist in the very small metal nanoparticles supported onto high-surface area and electrically conductive carbon materials (typically Vulcan and Ketjen). Despite the catalyst support has not relevant catalytic activity, it may play a significant role in the stability and activity of the Pt nanoparticles due to geometric and electronic effects. More recently, new materials such as ordered mesoporous carbons, carbon aerogels, carbon nanotubes (CNTs), carbon nanocoils and carbon nanofibers have emerged as promising catalyst supports. The building block of these materials is graphene, a two-dimensional one-atom-thick planar sheet of sp2-bonded carbon atoms.

Some great efforts done in the past decade, especially the alloying of Pt with transition metals, allowed to exceed ORR activity targets set by the EU and US DoE (440 $mA \cdot mg_{Pt}^{-1}$ at 0.9 $V_{iR\text{-free}}$) [7], [8]. However, current PEMFC catalysts cannot withstand the harsh operating conditions, including high potentials, start/stop cycles, low pH, cold starts, low relative humidity and even fuel starvation [9]. The insufficient electrocatalytic stability of the cathode, trigger the irreversible loss of performance throughout the PEMFC

lifetime due mainly, to losses of electrochemical surface area (ECSA), increased hydrophilicity, or lower electronic conductivity triggered by the poor interaction between the support, the catalyst and the ionomer. Degradation mechanisms including the corrosion of the carbon support, Pt migration, Pt detachment and others in a smaller extent, are directly related to the stability of the support [10], [11].

Carbon corrosion rate is significantly accelerated above 1.15 V or during high overvoltage periods that take place at start and stop conditions, even though carbon oxidation is thermodynamically possible at potentials above 0.207 V *vs* SHE. Below 0.9 V *vs* SHE the kinetics of the reaction is extremely slow, still, the presence of Pt promotes oxidation to occur in the potential range of typical PEMFC operation (0.6 V - 0.7 V) [12]. This degradation mechanism may include partial oxidation or multi-step oxidation to CO_2.

Currently, multiple accelerated stress test (AST) protocols are available in the literature [13], including potential cycling below 1.2 V (triangular wave, squared wave and asymmetric wave forms), potential cycling at high potentials (1 V - 1.6 V *vs* RHE) to simulate start-and-stops that sharply accelerate carbon corrosion and potential holding at open circuit potential (OCP). A combination of the three types of ASTs is the most suited comparison to distinguish the ORR stability of PEMFC electrocatalysts. In the search of novel supports to replace carbon blacks, graphene has been widely suggested. Nonetheless, there are insufficient evidences concerning the resulting graphene's morphology influence on the integrity of Pt sites, especially when subjected to sets of different ASTs in ORR conditions. Thereafter, there is a lack of understanding on the degradation mechanisms that govern a Pt/graphene catalyst.

This work compares the stability of a graphene-supported catalyst with a widely used commercial electrocatalyst (Pt/H) under three different types of ASTs. The stability of the electrocatalysts is sequentially unveiled based on electrochemical characterization techniques, such as ECSA, double-layer capacitance and ORR activity. Moreover, through transmission electron microscopy (TEM) and inductively coupled plasma mass spectrometry (ICP-MS), Pt particle growth and Pt dissolution in the electrolyte were quantified. A relationship between electrochemical and physicochemical analyses is

proposed aiming at deconvoluting the most relevant degradation mechanisms, as well as their extension, in a graphene supported PEMFC electrocatalyst.

5.2. EXPERIMENTAL

5.2.1 MATERIALS

Two electrocatalysts were studied, 40 wt.% Pt/graphene (Pt/G) from Premetek Co. and 40 wt.% Pt/HiSPEC (Pt/H) from Alfa Aesar. Table 5.1 details the materials and operating conditions used in this study. Electrochemical measurements were performed in a Gamry RDE coupled with an Eurocell Electrochemical Kit. A Zahner IM6-ex was used as potentiostat and impedance spectrometer. The glassy carbon (GC) electrode was polished with 0.05 µm alumina-particle solution, prior to each film deposition. Immediately after dipping the working electrode (GC of *ca.* 0.2 cm^2) into the electrolyte (0.1 M $HClO4_{(aq)}$), the potential was set to 0.4 V *vs* RHE to avoid exposure to OCP which could generate carbon corrosion after a short time.

Table 5.1 - Materials used for RDE measurements.

Ink composition 5 mg of electrocatalyst 7.96 ml H_2O 2 ml isopropanol 40 µl Nafion (5 wt. %)	**Temperature / °C** 20 **Ar gas purity** Linde, 99.999 % **Oxygen gas purity** Linde, 99.995 % **Reference electrode** Ag/AgCl **Counter electrode** Graphite rod **Electrolyte** 70 % conc. $HClO_4$, 99.999 % trace metal bases, Sigma Aldrich
Ink application 20 µl – 4 μg_{Pt} electrode 700 RPM	
Ultrasound equipment Hielscher UP50H (50 W) Ultrasound probe treatment 15 min @ 20 % amplitude in ice bath	

5.2.2 ELECTROCHEMICAL MEASUREMENTS

The electrode was first conditioned in Ar during 100 cycles between 0.05 V and 1 V (*vs* RHE) at 100 mV s^{-1} and 0 rotations per minute (RPM). Hydrogen underpotential deposition analysis was carried out with cyclic voltammetry (CV) at 20 mV s^{-1} and 0 RPM (from 0.05 - 1 V in Ar) to estimate the ECSA and Pt utilization of each electrocatalyst. The anodic charge attained from 0.05 V to 0.40 V *vs.* RHE refers to desorption of hydrogen from the available Pt active sites. The latter was normalized by 210 µC cm^{-2} which was assumed as the charge generated by a fully covered Polycrystalline Pt (111) monolayer [14].

EIS was performed in potentiostatic mode using a 5 mV perturbation at high frequency range (20 kHz - 3 kHz) to measure the ohmic resistance of the electrolyte. Linear sweep voltammetry (50 mV - 1 V *vs* RHE at 20 mV s^{-1}) was used to measure the background currents (in Ar) and ORR activity (in O_2) both at 1600 RPM. The electrolyte was saturated using 100 ml min^{-1} of each gas, for 30 min. During the measurements, a gas blanketing was set to prevent electrolyte contamination from the exterior of the cell.

5.2.3 ACCELERATED STRESS TESTS

Figure 5.1 depicts the three AST protocols employed in this study. AST1 consisted in triangular wave cycling between 1.0 V - 1.6 V *vs* RHE, at 20 °C with a scan rate of 100 mV s^{-1} in O_2; AST2 corresponded to 4 h of OCP holding in O_2. CV and ORR activity were measured in intervals of 2 h. Finally, AST3 comprised triangular wave cycling between 0.6 V - 1 V, at 20 °C at a scan rate of 100 mV s^{-1} in O_2. ASTs 1 and 3 consisted in sets of 2000 potential cycles, including a new break-in step in Ar atmosphere prior to retrieve both the ECSA and ORR back currents activities, followed by saturation of the electrolyte with O_2 to finally retrieve the ORR activity.

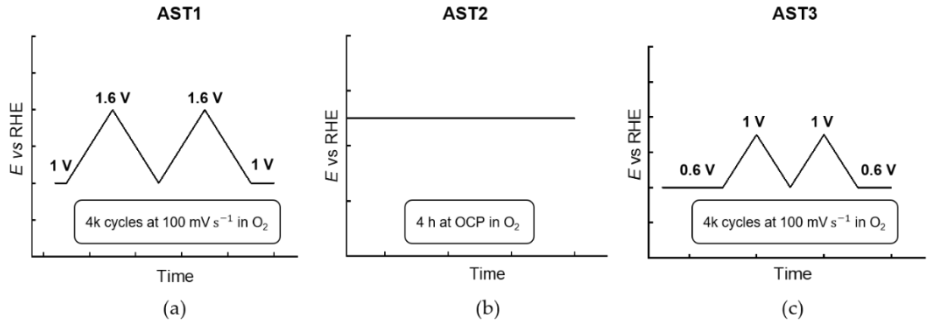


Figure 5.1 - Scheme for the three AST protocols used for the stability study: (a) Triangular wave cycling at high potentials (1.0 V – 1.6 V); (b) Open circuit potential holding; (c) Triangular wave cycling at low potentials (0.6 V – 1.0 V).

5.2.4 PHYSICAL MEASUREMENTS

Pt particle size and dispersion were analyzed for the three electrocatalysts before and after each degradation protocol, using a transmission electron microscope (Jeol JEM 1400). The magnification was set to 600 000 times. To quantify the average particle size distribution, *ca.* 300 Pt nanoparticles were measured from 4 different zones of each TEM image using ImageJ software. The structure of the pristine catalysts was analyzed by X-ray diffraction (XRD). A PANalytical X'Pert Pro device operating in Bragg-Bretano focusing geometry served to collect the X-ray patterns of the samples. The average crystallite size of Pt was calculated based on the broadening Pt reflection using Scherrer's equation (Equation 1) [14]:

$$d = \frac{K\,\lambda}{\beta\cos\theta} \qquad (1)$$

where d is the average size of the Pt crystallites (nm), K is the crystallite-shape factor while λ stands for the wavelength of the Kα radiation of Cu (λ = 1.5418 Å), θ is the Bragg angle, and the broadening of the diffraction line measured at half maximum intensity (FWHM) is represented by β. The average Pt crystallite size was calculated assuming an identical spherical shape and size, so that the K factor was chosen to be 0.9.

The concentration of platinum present in the electrolyte was measured after AST3 using an inductively coupled plasma mass spectrometer (ICP-MS), Agilent 7500 CE.
Raman spectra of the two electrocatalyst samples were obtained using a using a Witec alpha300, excited by a 532 nm laser with an electric current of 0.5 mA.
X-ray photoelectron spectroscopy (XPS) measurements were performed with a hemispherical analyser-type X-ray photoelectron spectrometer (Kratos Axis Ultra HSA) with monochromatic Al, 90W X-ray source power where 15 kV power and 30 mA were used for all measurements. The spectra were obtained by applying pass energy of 80 eV and 20 eV for survey region and specific peak region respectively. The resultant XPS spectra were analysed by using CasaXPS software.

5.3. RESULTS AND DISCUSSION

5.3.1 MORPHOLOGICAL AND ELECTROCHEMICAL MEASUREMENTS AT BEGINNING OF LIFE

XRD patterns of 40 wt.% Pt supported on HiSPEC (Pt/H) and 40 wt.% Pt supported on graphene (Pt/G) powders are shown in Figure 5.2. The diffraction peaks in XRD of both electrocatalysts at 2θ of 39°, 46°, 68°, 81° and 86º correspond to the (111), (200), (220), (311) and (222) lattice planes of the face-centered cubic structures of platinum [15], which is in accordance with the reference card of cubic Pt (JCPDS-04-0802). The broader peak at $2\theta < 30°$ shown in both diffractograms corresponds to carbon (JCPDS 75-1621). For both samples, the broad carbon peak unveils a disordered amorphous structure when compared to the sharp peak typical for graphitic carbon. Although this is expected for spherical nanoparticles (*e.g.* carbon black), in the case of graphene, it was already reported that exfoliation and re-stacking of graphene sheets decreases the degree of graphitization when compared to original graphite [16].
Using Scherrer's equation, a Pt crystallite size of *ca.* 1.8 nm was calculated for Pt/G. Similarly, calculated Pt crystallite size is twice larger when Pt nanoparticles are supported on HiSPEC (*ca.* 3.7 nm), which is in reasonable agreement with that reported by the manufacturer (maximum of 4.5 nm). Regarding ORR activity, the two most active

crystal planes are Pt (111) and (200). For both electrocatalysts, these peaks correspond to *ca.* 70 % of the total sum of Pt crystal planes peaks. These values are summarized in Table 5.2.

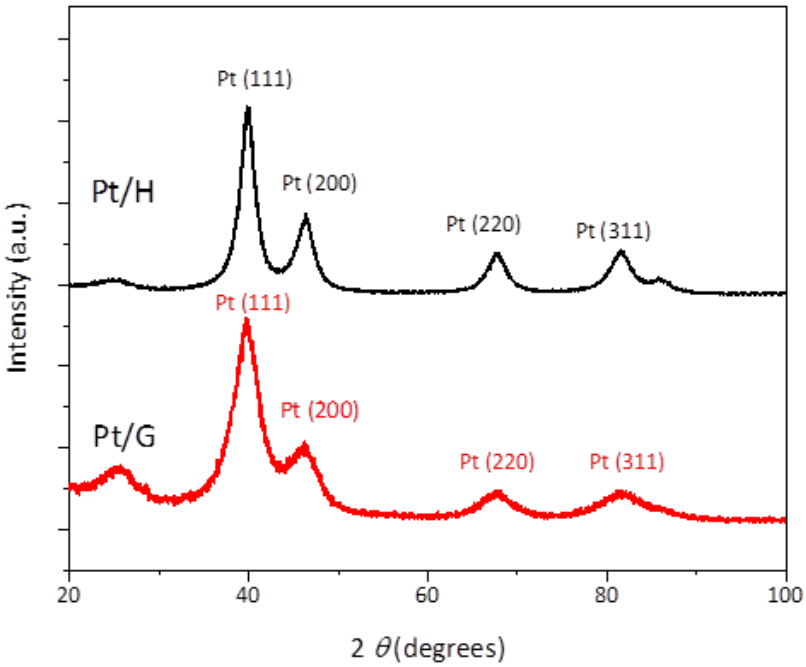


Figure 5.2 - X-ray diffraction patterns of pristine Pt/H and Pt/G; graphitic carbon (JCPDS 75-1621), Pt (JCPDS 04-0802).

Table 5.2 - Summary of X-ray diffraction results: relative peak area and crystallite size.

	Pt (111) / %	**Pt (200) / %**	**Pt (220) / %**	**Pt (311) / %**	**Crystallite size / nm**
Pt/H	47	23	13	17	3.7
Pt/G	51	19	13	17	1.8

Pt average particle size was measured from TEM images (Figure 5.3). The histograms (Figure 5.3 a-b) show that the particle size distribution fits a Gaussian distribution. The TEM images corresponding to Pt/H depict uniform dispersion of Pt particles despite the presence of some Pt agglomerates, while fewer were observed for Pt/G sample (see Figure S3). The platinum particle size of the two pristine electrocatalysts was different, 4.1 nm for Pt/H and 2.6 nm for Pt/G, which renders higher specific surface area for the latter. Pt/G displays the smallest crystallite size (1.8 nm), compared with Pt/H (3.7 nm). Kinetically, both higher Pt crystallinity and smaller particle sizes generate higher ORR activity; typically, the preferred lattice plane is Pt (111) plane for extended crystallinity [17] and Pt/G demonstrates slightly higher relative amount of such facets compared to than Pt/H.

The support of Pt/H catalyst, Figure 5.3 (a), consists of spherical-like carbon particles with diameter ranging from 10 to 30 nm. Such carbon particles display high surface area, high hydrophobicity and high electronic conductivity. The existence of pseudo-capacitive groups on the carbon surface caused by the application of pretreatments (in situ electrochemical oxidations, thermal or chemical attacks) may modify the above-mentioned properties [18]. The carbon support of Pt/G, Figure 5.3 (b), graphene, consists in the ordered arrangement of carbon atoms in two-dimensional structures. Depending on the synthesis or functionalization applied, graphene can contain some functional groups, based on N, O, S, among others. The existence of more capacitive groups in pristine Pt/G is shown in the Raman spectra (Figure S1); the I_D and I_G peaks are much broader than for Pt/H despite the similar peak intensity ratio [19]. For both carbon materials, functional groups are important during the synthesis of Pt/C catalysts. They serve as anchoring sites for nucleating small Pt particles and lead to more uniform Pt dispersion over carbon [20]. After the synthesis, Raman and XPS analyses (Figures S1 and S2) reveal similar graphitization degree and number of oxygenated species present at the near surface of both Pt/H and Pt/G [21] (results are summarized in Table S1).

The Pt particle size distribution for both electrocatalysts reveals a smaller average size for Pt/G (2.6 nm) than on Pt/H (4.1 nm). This hints for the existence of more anchoring sites on graphene that provide better dispersion of Pt particles, which yields smaller Pt average particle size [22]. XPS analysis shows similar C1s spectra, but higher

differences are observed in the Pt4f high resolution spectra. The peaks corresponding to Pt valence >+2 are larger for Pt/G which indicates the presence of stronger and more abundant bonds between Pt sites and the support [23]. This is typically observed for samples with better Pt dispersion with smaller particle sizes. Moreover, there is a positive shift in the metallic Pt (Pt^0) peak of 0.2 eV, which is commonly associated to higher ORR activity due to a decrease in the binding strength Pt and the reaction adsorbates [24].

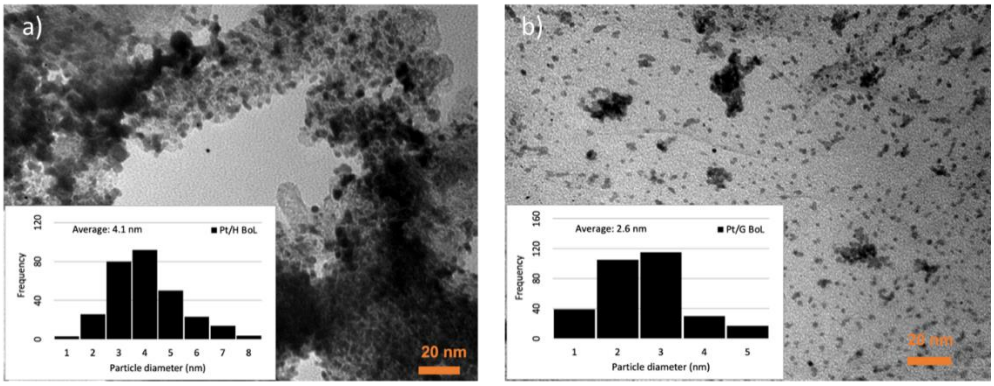


Figure 5.3 - TEM images and particle size distribution of pristine: (a) Pt/H and (b) Pt/G.

The initial performance of the two electrocatalysts was evaluated using a rotating disk electrode. The Pt loading on the glassy carbon electrode was kept at 42 $\mu g_{Pt} \cdot cm^{-2}$. ORR activities were measured at 0.9 V *vs* RHE. The ECSA at beginning of life (BoL) of both catalysts was calculated from the cyclic voltammograms shown in Figure 5.4 (a). The capacitance is similar for both catalysts. Yet, the hydrogen desorption/adsorption charge (0.05 V to 0.4 V *vs* RHE) is larger for Pt/G, which is directly related to the existence of more active sites. The higher ECSA obtained for Pt/G (96.2 $m_{Pt}^2 \cdot g_{Pt}^{-1}$) means that Pt is utilized more efficiently in comparison to the Pt/H catalyst (80.2 $m_{Pt}^2 \cdot g_{Pt}^{-1}$). This difference can be explained by many factors but the most important refers to the lower Pt average particle size, which ensure higher Pt utilization due to more electroactive Pt sites exposed and availability to form more triple-phase boundaries [25].

ORR activity was measured in an O_2-saturated electrolyte (0.1 M $HClO_4$) by linear sweep voltammetry (LSV) at 20 $mV \cdot s^{-1}$ and a rotation speed of 1600 RPM; the mass-specific activity (MA), diffusion-limited activity (j_{lim}) and area-specific activity (SA) of each catalyst were calculated. The ohmic drop assigned to the liquid electrolyte was measured by EIS and used to correct the *j-V* curves. The latter not only enables a direct comparison with other results in the literature but also excludes the changing of electrolyte properties after long-term experiments [26]. The resulting *jR*-corrected LSVs are shown in Figure 5.4 (b) – the background currents measured in Ar-purged 0.1 M $HClO_4$ were also subtracted to the curves recorded in O_2-saturated atmosphere. To calculate both mass- and area-specific activities, the net kinetic current (j_k) was determined using Equation (2) [27]:

$$j_k = \frac{j_{\text{lim}} j_{0.9}}{j_{\text{lim}} - j_{0.9}} \quad (2)$$

where $j_{0.9}$ is the current density at 0.9 V and j_{lim} is the measured diffusion-limited current. The highest mass-specific activity was achieved for Pt/G, 323.4 ± 47.3 $mA \cdot g_{Pt}^{-1}$, compared to 268.3 ± 35.2 $mA \cdot g_{Pt}^{-1}$ of Pt/H. Though mass-specific activities depend on several factors such as the Pt average particle size, catalyst-support interaction, and Pt crystal structure, it is noticeable that higher ECSA and lower Pt particle size are directly associated to the larger mass-specific activity obtained for Pt/G, which is also supported by the previously mentioned positive shift (see Table S1) of metallic Pt observed in the XPS analysis [28]. In terms of ORR specific-activity, 340.3 ± 29.9 $\mu A \cdot cm_{Pt}^{-2}$ was achieved for Pt/G and 348.6 ± 18.7 $\mu A \cdot cm_{Pt}^{-2}$ for Pt/H, since both electrocatalysts display similar contribution from the most active crystalline planes (111 and 200) measured by XRD [29].

Tafel plots were obtained from plotting the electrode potential as function of the logarithm of current density and considering low values of overpotential (up to 330 mV), which excludes the diffusion-limited regime, Figure 5.4 (c) [30]. The Tafel slope was calculated for both electrocatalysts before subjecting them to accelerated degradation, therefore, the reached values greatly depend on the type of electrocatalyst support. The Tafel slope (b) for Pt/H (54 $mV \cdot dec^{-1}$) is similar to other electrocatalyst in which Pt

particles are supported on carbon nanoparticles [31], [32]. The lower Tafel slope measured for Pt/G (40 $mV \cdot dec^{-1}$) indicates faster ORR kinetics either due to higher changer-transfer rates or decreased binding energy to reaction adsorbates.

Table 5.3 - Electrochemical active surface area (ECSA), mass-specific activity, area-specific activity and diffusion limited activity of Pt/H and Pt/G catalysts.

	ECSA ($m_{Pt}^2 \cdot g_{Pt}^{-1}$)	**Mass-specific activity ($mA \cdot g_{Pt}^{-1}$) @ 0.9 V *vs* RHE**	**Area-specific activity ($\mu A \cdot cm_{Pt}^{-2}$) @ 0.9 V *vs* RHE**	**Diffusion-limited activity ($mA \cdot cm_{geo}^{-2}$)**
Pt/H	80.7	303.6	376	5.1
Pt/G	95.5	386.5	405	5.1

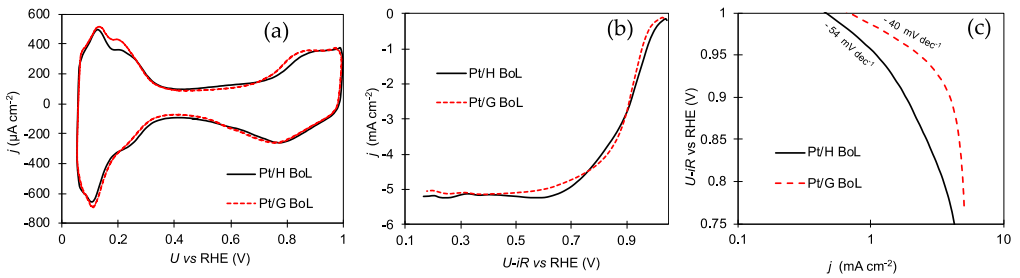


Figure 5.4 - RDE results at beginning of life for Pt/H and Pt/G: (a) cyclic voltammograms at 20 $mV \cdot s^{-1}$ in Ar; (b) Linear sweep voltammograms at 20 $mV \cdot s^{-1}$ and 1600 RPM in O_2; (c) Tafel plots measured using 0.1 M $HClO_4$ at 20 $mV \cdot s^{-1}$ and 1600 rpm in O_2-saturated electrolyte; (Pt loading: 42 $\mu g_{Pt} \cdot cm^{-2}$).

5.3.2 TRIANGULAR WAVE CYCLING AT HIGH POTENTIALS (AST1)

In automotive fuel cells, the cathode is often exposed to high potentials (up to *ca.* 1.5 V) mainly due to a "reverse-current" generated from a sudden potential increase during startups and shutdowns [33]. This is a result of the simultaneous presence of hydrogen

and oxygen at the electrode surface takin place in case of membrane failure or when the anode is blown with hydrogen at the start-up and with air during shut-off. This is called as fuel starvation and is typically studied through simulated start-stop cycles through thousands of voltage cycles above 1 V *vs* RHE using a fast scan rate [34]. From the perspective of the carbon support, this AST is aggressive mainly due to the presence of platinum and a highly acidic environment which accelerate degradation mechanisms. Aged carbon structures typically show massive changes in their morphology, loss of electrical conductivity and increased hydrophilicity. Carbon corrosion has been considered one of the two major degradation mechanisms in PEMFCs together with Pt dissolution.

Apart from degradation mechanisms solely associated to the support, there are others associated to platinum nanoparticles that are also indirectly associated to the support. When exposed to high potentials and low pH, like those found in PEMFC cathodes, Pt nanoparticles are oxidized and may dissolve into the electrolyte (membrane and/or ionomer) or be found in water outlet stream. Wang *et al.* concluded that the equilibrium concentration of dissolved Pt increases monotonically from 0.65 to 1.1 V and then decreases above 1.1 V. Pt dissolution was shown to be highly dependent on Pt particle size under simulated start-stop cycling; Meier *et al.* stated that, under such conditions, smaller Pt particles were more likely to dissolve [35]. Strongly linked to Pt dissolution, Ostwald ripening and particle agglomeration are secondary degradation mechanisms. Dissolved Pt ions can also migrate and nucleate in already existing Pt clusters, leading to particle growth. Particle growth can also take place by the migration and sintering of similar Pt particles [36]. Moreover, carbon corrosion also promotes agglomeration as close Pt particles become in contact upon support shrinking [11].

As mentioned before, graphene is a great candidate for a stable catalyst support since its highly ordered carbon structure not only ensures higher electrical conductivity but also higher resistance to corrosion when compared to amorphous carbon blacks. On the other hand, Pt/G is loaded with smaller Pt particles than Pt/H. Figures 5.5 (a) and (d) show cyclic voltammograms obtained after subjecting the electrocatalysts to the accelerated stress test (AST1). CVs were recorder before and after 2000 cycles between 1 -1.6 V *vs* RHE at 500 mV s^{-1}. Three different regions are present in the cyclic voltammograms and

they provide information about which phenomena have the most important influence on ORR performance: Pt-H adsorption/desorption region (below 0.4 V *vs* RHE), double-layer region (0.4 - 0.6 V *vs* RHE) and Pt-OH interaction region (above 0.6 V *vs* RHE) [37].

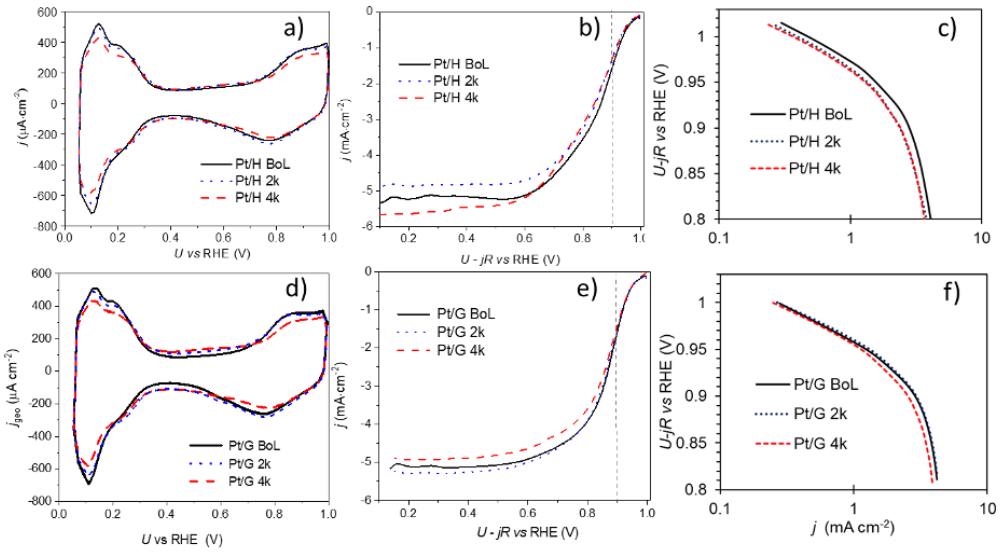


Figure 5.5 - RDE results at beginning of life and upon 2k cycles and 4k potential cycles between 1.0 V and 1.6 V in an O_2-saturated electrolyte for Pt/H and Pt/G, respectively - vertical plots: (a,d) cyclic voltammograms at 20 mV s^{-1} in Ar; (b,e,) Linear sweep voltammograms at 20 mV s^{-1} and 1600 RPM in O_2; (c,f,) Tafel plots.

Electrochemical surface area (ECSA) is an important parameter since it is directly related the Pt utilization by the quantification of the electrochemically active sites in electrocatalytic films. Almost all degradation mechanisms contribute to a decrease in ECSA. Pt dissolution, agglomeration or Ostwald ripening lead to lower ECSA due to the loss of active Pt or by Pt particle growth. Support corrosion also reduces the ECSA; Pt particles may simply detach from the support and migrate inside the membrane/ionomer acting there as an electrical insulator. ECSA losses after 2000 cycles are similar but Pt/H presents much lower ECSA (63.7 $m^2 \cdot g_{Pt}^{-1}$) at the end of tests. Remarkably, Pt/G showed minor ECSA loss after 4000 cycles (76.5 $m^2 \cdot g_{Pt}^{-1}$).

Typically, higher ECSA values account for higher ability to generate larger current densities; a similar conclusion can be taken from the limiting current density in LSVs - Figures 5.5 (b) and (e), but only the former LSVs corresponding to Pt/H, allow to unveil changes in the diffusion limiting current. At low potentials (below 0.6 V *vs* RHE), the current reaches a plateau which corresponds to the electrode response limited by mass-diffusion for a rotation of 1600 RPM. The absence of a current plateau is associated to oxygen concentration gradients that are not constant with potential and this is highly associated to changes in the microstructure of the electrocatalyst. The loss of porosity [38] and the formation of excessive oxygen functional groups at the HiSPEC surface increase the hydrophilicity of the support. This enhances flooding effects that limit oxygen diffusion to the active sites [39].

The double layer capacitance of an electrode with Pt supported on carbon depends on the surface morphology and type of anchored functional groups in the support. Such functional groups decrease electrical conductivity and increase affinity to water. In particular, the latter may contribute to a more challenging water removal from the fuel cell which actively promotes support corrosion and mostly Pt dissolution. An increase in the double layer capacitance on Pt/G is evident after degradation, and it is three times higher than the increase observed for Pt/H. Compared to spherical carbon particles, the planar structure of graphene facilitates the uptake of oxygen functional groups, mainly on the edges of the graphene sheets [40]. The existence of more capacitive groups in pristine Pt/G was already shown in the Raman spectra (Figure S1). Commercial carbon Vulcan XC72 (present in HiSPEC 4000) is also known to possess many defective surfaces (edges and corners of basal planes) with high concentration of oxygenated functional groups at the surface which is evidenced in XPS measurements [41] (see Table S1). Although surface defects had been proven to enhance the ORR activity and to allow better Pt dispersion, long-term observations shown that these properties also led to carbon corrosion due to unsaturated valences and free σ-electrons [42] and to the adverse effect of highly electronegative oxygen functional groups which are prone to partially oxidize the Pt NPs and trigger their sintering and dissolution mechanisms [43].

Linear sweep voltammetry was performed to obtain the ORR activity, measured at 0.9 V *vs* RHE. The exchange current density and Tafel slope (Figures 5 (b), (e), (c) and (f))

were used to compare the performance of ORR electrocatalysts. ORR activity is normally presented in two forms: normalized by the catalytic loading (mA g_{Pt}^{-1}) or by the catalytic surface area (μA cm_{Pt}^{-2}). These allow a direct comparison between electrocatalysts excluding morphological effects (area-specific activity) or catalytic loading (mass-specific activity). At first glance, it is noticeable that the two electrocatalysts present considerable loss of mass activity at 0.9 V *vs* RHE. Yet, Pt/H not only displays the most pronounced loss of mass activity upon 4000 potential cycles (32 %), but also the highest loss in specific-area activity (32 %), see Figure 5.6 (a). On the other hand, Pt/G presents an increase in specific-area activity (*ca.* 3.6 %), which suggests particle growth to more acicular-shaped and crystalline Pt particles (Figure 5.6 (c)) which yield higher specific activity. Previous works report the increase of specific activity with increasing platinum particle sizes for Pt/C catalysts after being subjected to 1500 potential cycles [44]; the same trend is verified in a variety of studies for Pt-alloys supported on carbon subjected to potential cycling (> 1.25 V) [45], [46]. Thus, the greater attained specific-area activity of Pt/G was assigned to the increase in the average particle size, from 2.6 nm, at BoL, to 3.2 nm, at EoL (see Table S2). Pt nanoparticles smaller than 2-3 nm are thermodynamically unstable. Below the threshold in which Pt utilization would drop considerably, larger Pt particles are typically more stable and display a larger specific area of facets (111) and (200), the most ORR active facets [20]. Figure 5.6 (a) and 5.6 (b) shows TEM images of Pt/H and Pt/G after being subjected to the first accelerated stress test (AST1). The particle size increased *ca.* 15 % for Pt/H and *ca.* 35 % for Pt/G, relatively to their original size; it is noticeable a broader distribution of nanoparticle sizes (2 - 8 nm) for both electrocatalysts, which was assigned to the Ostwald ripening and/or particle coalescence. The presence of Pt dissolved in the electrolyte was measured using ICP-MS. High concentrations of dissolved Pt were detected in the liquid electrolyte (0.4 and 0.8 $\mu g \cdot dm^{-3}$ for Pt/H and Pt/G, respectively). Pt dissolved into the electrolyte can also lead to particle growth following a re-precipitation mechanism [35].

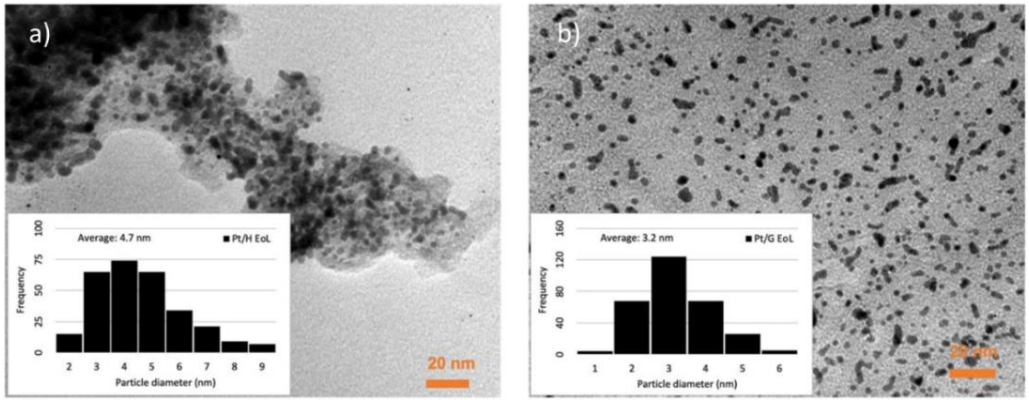


Figure 5.6 - TEM images and particle size distribution of (a) Pt/H and (b) Pt/G at EoL after 4000 cycles from 1.0 V to 1.6 V..

Table 5.4 summarizes the results of the two electrocatalyst during and after subjected to accelerated degradation through potential cycling between 1 V - 1.6 V (*vs* RHE). Pt/G presents lower losses in ECSA, mass-specific (MA) and area-specific (SA) activities. It also reached higher diffusion-limited currents than Pt/H. These are clear signs of graphene's improved stability, showing higher stability and losing two times less mass-specific activity after 4000 cycles, when compared to Pt/H. Remarkably, the area-specific activity of Pt/G was maintained after 4000 cycles.

Table 5.4 - Summary of results for ECSA, Mass-specific activity (MA), Area-specific activity (SA) and Double-layer (dl) variation of Pt/G and Pt/H, subjected to AST1.

Catalyst	**ECSA variation at 2k cycles/2h (%)**	**ECSA variation at EoL (%)**	**MA loss at 2k cyles /2h (%)**	**MA loss at EoL (%)**	**SA loss at EoL (%)**	**DL variation at EoL (%)**
Pt/G	-7.6	-21.5	1.6	-17.2	3.6	42.0
Pt/H	-8.4	-21.6	-18.2	-32.2	-13.3	12.2

5.3.3 OPEN CIRCUIT POTENTIAL HOLDING (AST2)

During the lifetime of a PEMFC system (*ca.* 6000 h), the cathode is exposed to harsh conditions, namely when no power is supplied to the propulsion system and the only power drawn from the cell is that required to withstand the auxiliary systems (*e.g.* cooling pumps). In these periods, the cathode potential reaches *ca.* 0.90 V *vs* RHE [47]. At open circuit potential (OCP), where no current is drawn from the stack, the cathode also reaches high potentials either prior to a fuel cell shutdown or immediately after a start-up. Such realistic situations cause severe degradation thus causing a significant reduction to the lifetime of the electrocatalyst [48]. In this regard, potential holding at OCP was performed to both electrocatalysts.

Figure 5.7 (a) displays the CVs for Pt/H and Pt/G after 4 h at OCP. The ECSA loss at the end of life was considerably higher for Pt/H (*ca.* 42 %) when compared to Pt/G (*ca.* 22 %). The double layer capacitance of both Pt/G and Pt/H decreased (*ca.* 10 % of their original size), which indicates the removal of anchored surface species or corrosion of carbon material to carbon dioxide [10]. Pt/H display a round shape, suggesting migration and agglomeration as they are *ca.* 1.5-fold larger than their original size (Figure 5.8 (a) and Table S2). On the other hand, the coalescence of individual Pt particles can be observed in the TEM images of Pt/G at EoL, Figure 5.8 (b).

Table 5.5 summarizes the results of the two electrocatalysts exposed to open circuit potential. Pt/G displayed interesting results in terms of ORR mass-specific activity; after 2 h of potential hold, it increased but it then decreased after 4 h. This is likely to occur due to a beneficial increase of the particle size to an optimum size (3 - 4 nm), in which the most active crystal facets allow higher rates of oxygen reduction. However, with persisting continuous potential cycling, the electrocatalyst lost ORR mass-specific activity but gained ORR area-specific activity. Similar results were previously reported by Kinoshita et al., where the specific activity of ORR was shown to be a function of the particle size and of the surface average distribution of Pt crystal facets. It is also mentioned a maximum ORR mass-specific activity for Pt particle sizes between 3 - 4 nm [49]. During prolonged operation under OCP, the catalyst support is partially or fully

oxidized during the startup and shutdown processes. Simultaneously, the Pt particle growth may follow two of the above mentioned mechanisms: agglomeration/growth or dissolution followed by re-deposition [50].

The concentration of dissolved Pt in the electrolyte obtained after 4 h of OCP (*ca.* 0.925 V) in O_2 is similar for the two catalysts (Table S2). This can be attributed to the growth of a protective oxide layer that retrains the dissolution process though it typically is reported to be formed at potentials higher than 1.0 V *vs* RHE [51]. Nevertheless, some studies consider that such Pt oxides play a dual effect of protection against Pt dissolution even being as well, such oxides susceptible to dissolution [52].

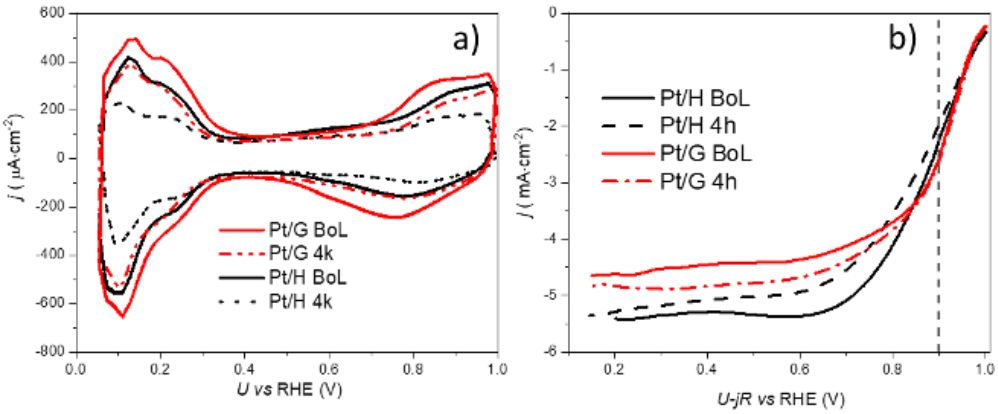


Figure 5.7 - RDE electrochemical results for Pt/H and Pt/G aging (4h at OCP); (a) Cyclic voltammograms at 20 mV·s^{-1}; (b) LSVs in O_2-saturated electrolyte at 1600 RPM.

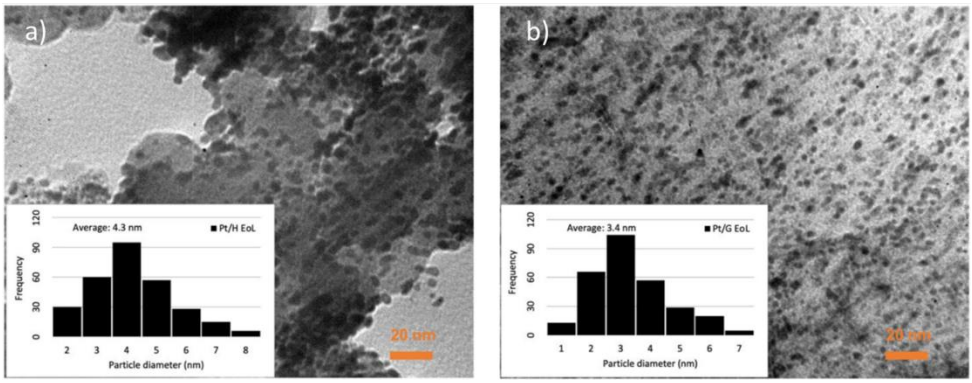


Figure 5.8 - TEM images and particle size distribution of aged (4 h at OCP): (a) Pt/H; (b) Pt/G.

Table 5.5 - Summary of results for ECSA, Mass-specific activity (MA), Area-specific activity (SA) and Double-layer (dl) variation of Pt/G and Pt/H, subjected to AST2.

Catalyst	ECSA variation at 2k cycles/2h (%)	ECSA variation at EoL (%)	MA loss at 2k cyles /2h (%)	MA loss at EoL (%)	SA loss at EoL (%)	DL variation at EoL (%)
Pt/G	-4.4	-11.9	-10.4	-17.3	-6.1	*ca.* 0
Pt/H	-9.7	-25.7	-30.2	-59.0	-44.9	*ca.* 0

5.3.4 TRIANGULAR WAVE CYCLING AT LOW POTENTIALS (AST3)

The previous AST protocols were performed to evaluate mainly the carbon corrosion, which also promotes agglomeration/detachment of Pt nanoparticles as well as morphological changes in the electrode's microstructure such as higher hydrophilicity and loss of porosity. The combination of such effects results not only on the loss of Pt utilization but also lead to mass transport limitations. To study degradation as consequence of variations in power demands on the stability of Pt catalysts, potential cycling from 0.6 V to 1.0 V *vs* RHE was performed during 4000 cycles. This protocol is very similar to that defined by the US Drive (US FCTT), in collaboration with the US

Department of Energy load-cycling protocol, which uses potential cycling from 0.65 V - 1.0 V *vs* RHE.

Figure 5.9 shows TEM images of the two electrocatalysts after subjected to potential cycling between 0.6 - 1 V (*vs* RHE). Pt/G microstructure appears to be kept intact and the average size of the particles identical to BoL conditions (3.4 nm after AST3 vs. 2.6 nm at BoL – see Table S2). Likewise, the Pt particle size of Pt/H did not increase but more Pt agglomerates are present in Pt/H compared to Pt/G. The concentration of dissolved Pt in the electrolyte is very low ($< 0.1 \pm 0.05$ mg dm^{-3}); see Table S2. Compared to others accelerated stress tests, AST3 appears to be milder in terms support corrosion and loss of Pt surface area. Some works in the literature reported that Pt dissolution occurs both during anodic and cathodic potential scans and especially when the upper potential limit of cycling is ≥ 1.1 V *vs* RHE [36]. On the other hand, other works report that cycling at lower potentials, corresponding to the regions of oxide formation and reduction to metallic particles (0.6 - 1.0 V *vs* RHE), tend to endorse higher dissolution rates instead of holding the potential in the oxide formation region (*ca.* 0.9 V *vs* RHE) or even cycling it at higher potentials [53]. This mechanism consists in the formation and disruption of a place-exchanged oxide film that ultimately leads to mobile platinum species [54].

Figures 5.10 (a) and (b) show cyclic and linear voltammograms after 4 000 potential cycles from 0.6 V - 1.0 V *vs* RHE. Clearly, Pt/G again presents a remarkable stability with the lowest loss of ECSA and the highest ORR activity at 0.9 V *vs* RHE, after degradation. Compared to the other AST protocols, both Pt/H and Pt/G lost more ECSA (27 % and 12 %, respectively). A similar AST protocol was set by Nissan´s technical lab in which they tested a 40 wt.% Pt supported on a high surface area carbon under load cycle conditions of 0.6 - 0.95 V *vs* RHE, at 80° [55]. They report major ECSA losses (49 % for Pt/H, which was not assigned to platinum dissolution and agglomeration. The authors refer, however, in the framework of cell and stack failure, that the stability of the support is far more important than the stability of the platinum particles that are loaded onto it. Similarly, in the present work, it is clearly shown that electrocatalyst support corrosion triggered during start-up and shutdown (AST1 in this study) is by far more important in terms of degradation than platinum dissolution.

From the results summarized in Table 5.6, there were no changes in the double layer capacitance on both catalysts. This confirms that by cycling at lower potentials promotes less surface functionalization of the carbon structure, when compared to AST1. On the other hand, the decrease in ORR activity (mass- and area-specific activities) at the end of measurements was the highest, mainly for Pt/H (60 % and 45 %, respectively). In the case of Pt/G, the loss of ORR activities was similar to that of AST1 and much lower than those observed for Pt/H. The low average particle size increase on both electrocatalysts (Figure 5.9) suggests that the loss of ORR activity was triggered by electronic effects. These turned the Pt sites (mainly on HiSPEC) less active or unavailable to form triple-phase boundaries, as evidenced by the drop in ECSA.

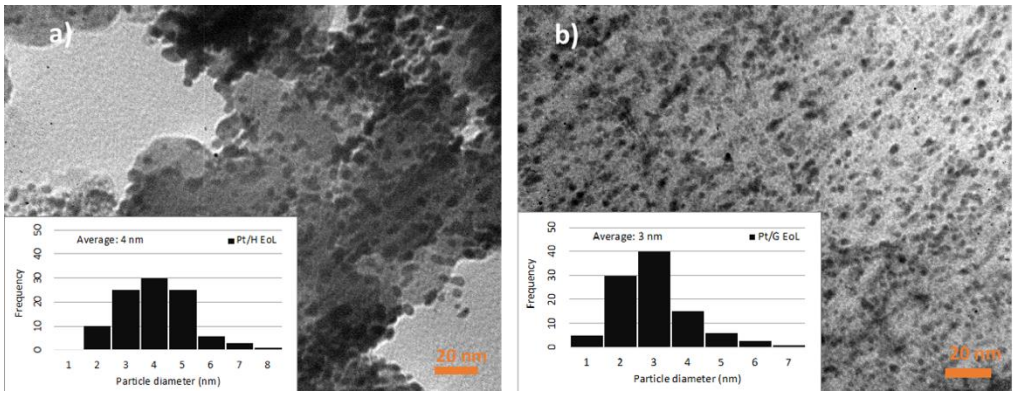


Figure 5.9 - TEM images and particle size distribution of aged (4k cycles 0.6 V – 1.0 V): (a) Pt/H; (b) Pt/K; (c) Pt/G at 600k.

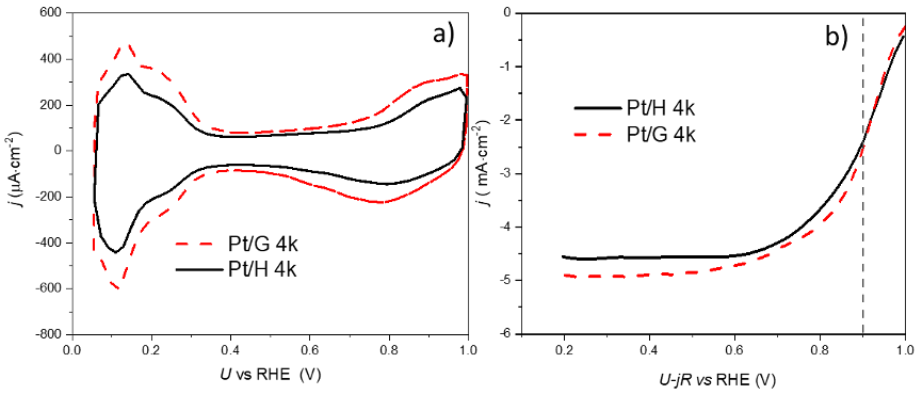


Figure 5.10 - RDE electrochemical results for Pt/H, Pt/K and Pt/G aging (4k cycles between 0.6 V – 1.0 V); (a) Cyclic voltammograms at 20 mV·s^{-1}; (b) LSVs in O_2-saturated electrolyte at 1600 RPM.

Table 5.6 - Summary of results for ECSA, Mass-specific activity (MA), Area-specific activity (SA) and Double-layer (DL) variation of Pt/G and Pt/H, subjected to AST3.

Catalyst	**ECSA variation at 2k cycles/2h (%)**	**ECSA variation at EoL (%)**	**MA loss at 2k cyles /2h (%)**	**MA loss at EoL (%)**	**SA loss at EoL (%)**	**DL variation at EoL (%)**
Pt/G	-4.4	-11.9	-10.4	-17.3	-6.1	*ca.* 0
Pt/H	-9.7	-25.7	-30.2	-59.0	-44.9	*ca.* 0

5.4. CONCLUSIONS

The degradation protocols caused clear differences in terms of ORR stability of two catalysts supported on carbon black and graphene. Pt supported on graphene not only outperformed Pt supported on HiSPEC in terms of initial ORR activity and ECSA but also after being subjected to the degradation protocols.

Despite the larger particle growth, Pt/G was able to maintain most of its initial ECSA and mass-specific activity after potential cycling between 1 V - 1.6 V (*vs* RHE). Lowest

stability and performance of commercial Pt/H could be attributed to the loss of porosity at the catalyst layer coupled to the generation of O_2 imbalanced concentration gradients arising from the detachment of carbon support into the bulk electrolyte.

When subjected to OCP holding, the double layer capacitance of both catalysts increased because of the introduction of pseudo-capacitive groups on the surface of graphene. Nevertheless, Pt/G presented slightly larger particle growth than Pt/H after 4 h of OCP. Potential cycling between 0.6 V - 1 V (*vs* RHE), typical PEMFC operation conditions, was more harmful for Pt/H than for Pt/G; three times higher ORR mass- specific activity and seven times higher area-specific activity losses. This degradation protocol caused less average particle growth and ECSA loss similar to AST1.

The superior performance of Pt/G is evident in terms of ECSA and ORR activity and upheld in morphological evidence, shows the benefits of this supported catalyst as alternative to common carbon blacks to be used as cathodic support for automotive PEMFCs.

REFERENCES

[1] International Energy Agency, “No Title,” 2015.

[2] B. G. Pollet, S. S. Kocha, and I. Staffell, “Current status of automotive fuel cells for sustainable transport,” *Curr. Opin. Electrochem.*, vol. 16, pp. 90–95, Aug. 2019, doi: 10.1016/j.coelec.2019.04.021.

[3] C. Chen *et al.*, “Highly crystalline multimetallic nanoframes with three-dimensional electrocatalytic surfaces,” *Science (80-.).*, vol. 343, no. 6177, pp. 1339–1343, 2014, doi: 10.1126/science.1249061.

[4] S. M. Alia *et al.*, “Platinum-Coated Nickel Nanowires as Oxygen-Reducing Electrocatalysts,” *ACS Catal.*, vol. 4, no. 4, pp. 1114–1119, Apr. 2014, doi: 10.1021/cs401081w.

[5] X. Huang *et al.*, “High-performance transition metal-doped Pt3Ni octahedra for oxygen reduction reaction,” *Science (80-.).*, vol. 348, no. 6240, pp. 1230–1234, Jun. 2015, doi: 10.1126/science.aaa8765.

[6] B. Lim *et al.*, “Pd-Pt Bimetallic Nanodendrites with High Activity for Oxygen Reduction,” *Science (80-.).*, vol. 324, no. 5932, pp. 1302 LP – 1305, Jun. 2009, [Online]. Available: http://science.sciencemag.org/content/324/5932/1302.abstract.

[7] DOE, “Technical Targets for Polymer Electrolyte Membrane Fuel Cell Components,” 2017.

[8] G. Tsotridis, A. Pilenga, G. De Marco, and T. Malkow, *EU Harmonised Test Protocols for PEMFC MEA Testing in Single Cell Configuration for Automotive Applications; JRC Science for Policy report*. 2015.

[9] D. Schonvogel *et al.*, “Stability of Pt nanoparticles on alternative carbon supports for oxygen reduction reaction,” *J. Electrochem. Soc.*, vol. 164, no. 9, pp. F995–F1004, 2017, doi: 10.1149/2.1611709jes.

[10] A. Riese, D. Banham, S. Ye, and X. Sun, “Accelerated Stress Testing by Rotating Disk Electrode for Carbon Corrosion in Fuel Cell Catalyst Supports,” *J. Electrochem. Soc.*, vol. 162, no. 7, pp. F783–F788, Apr. 2015, doi: 10.1149/2.0911507jes.

[11] L. Castanheira, W. O. Silva, F. H. B. Lima, A. Crisci, L. Dubau, and F. Maillard, "Carbon Corrosion in Proton-Exchange Membrane Fuel Cells: Effect of the Carbon Structure, the Degradation Protocol, and the Gas Atmosphere," *ACS Catal.*, vol. 5, no. 4, pp. 2184–2194, Apr. 2015, doi: 10.1021/cs501973j.

[12] K. Saikia, B. K. Kakati, B. Boro, and A. Verma, "Current Advances and Applications of Fuel Cell Technologies," in *Recent Advancements in Biofuels and Bioenergy Utilization*, Singapore: Springer Singapore, 2018, pp. 303–337, doi: https://doi.org/10.1007/978-981-13-1307-3_13.

[13] S. Stariha *et al.*, "Recent Advances in Catalyst Accelerated Stress Tests for Polymer Electrolyte Membrane Fuel Cells," *J. Electrochem. Soc.*, vol. 165, no. 7, pp. F492–F501, May 2018, doi: 10.1149/2.0881807jes.

[14] S. Trasatti and O. A. Petrii, "Real surface area measurements in electrochemistry," *Pure Appl. Chem.*, vol. 63, no. 5, pp. 711–734, Jan. 1991, doi: 10.1351/pac199163050711.

[15] Y. Li, L. Tang, and J. Li, "Preparation and electrochemical performance for methanol oxidation of pt/graphene nanocomposites," *Electrochem. commun.*, vol. 11, no. 4, pp. 846–849, Apr. 2009, doi: 10.1016/j.elecom.2009.02.009.

[16] B. P. Vinayan and S. Ramaprabhu, "Facile Synthesis of Platinum Decorated Graphene Wrapped Multiwalled Carbon Nanotube and Its Hydrogen Storage Properties," *Nano Commun.*, vol. 1, no. 1, pp. 4–10, Jun. 2014, doi: 10.1166/nano.2014.1003.

[17] H. Sun *et al.*, "Pt nanodendrites with (111) crystalline facet as an efficient, stable and pH-universal catalyst for electrochemical hydrogen production," *Chinese Chem. Lett.*, vol. 31, no. 9, pp. 2478–2482, Sep. 2020, doi: 10.1016/j.cclet.2020.03.032.

[18] I. Jiménez-Morales *et al.*, "Correlation between the surface characteristics of carbon supports and their electrochemical stability and performance in fuel cell cathodes," *Carbon Energy*, vol. 3, no. 4, pp. 654–665, Aug. 2021, doi: 10.1002/cey2.109.

[19] J.-B. Wu, M.-L. Lin, X. Cong, H.-N. Liu, and P.-H. Tan, "Raman spectroscopy of graphene-based materials and its applications in related devices," *Chem. Soc. Rev.*, vol. 47, no. 5, pp. 1822–1873, 2018, doi: 10.1039/c6cs00915h.

[20] T. Lagarteira, S. Delgado, C. Fernandes, C. Azenha, C. Mateos-Pedrero, and A. Mendes, "The role of Pt loading on reduced graphene oxide support in the polyol synthesis of catalysts for oxygen reduction reaction," *Int. J. Hydrogen Energy*, vol. 45, no. 40, pp. 20594–20604, 2020, doi: 10.1016/j.ijhydene.2020.02.022.

[21] P. Toth, "Nanostructure quantification of turbostratic carbon by HRTEM image analysis: State of the art, biases, sensitivity and best practices," *Carbon N. Y.*, vol. 178, pp. 688–707, Jun. 2021, doi: 10.1016/j.carbon.2021.03.043.

[22] S. M. Choi, M. H. Seo, H. J. Kim, and W. B. Kim, "Synthesis of surface-functionalized graphene nanosheets with high Pt-loadings and their applications to methanol electrooxidation," *Carbon N. Y.*, vol. 49, no. 3, pp. 904–909, Mar. 2011, doi: 10.1016/j.carbon.2010.10.055.

[23] P. Dhanasekaran, A. Shukla, S. V. Selvaganesh, S. Mohan, and S. D. Bhat, "Silica-decorated carbon-Pt electrocatalyst synthesis via single-step polyol method for superior polymer electrolyte fuel cell performance, durability and stack operation under low relative humidity," *J. Power Sources*, vol. 438, p. 226999, Oct. 2019, doi: 10.1016/j.jpowsour.2019.226999.

[24] Y. Takasu *et al.*, "Size effects of platinum particles on the electroreduction of oxygen," *Electrochim. Acta*, vol. 41, no. 16, pp. 2595–2600, Jan. 1996, doi: 10.1016/0013-4686(96)00081-3.

[25] J. M. Doña Rodríguez, J. A. Herrera Melián, and J. Pérez Peña, "Determination of the Real Surface Area of Pt Electrodes by Hydrogen Adsorption Using Cyclic Voltammetry," *J. Chem. Educ.*, vol. 77, no. 9, p. 1195, Sep. 2000, doi: 10.1021/ed077p1195.

[26] C. Costentin and J.-M. Savéant, "Ohmic drop correction in electrochemical techniques. Multiple potential step chronoamperometry at the test bench," *Energy Storage Mater.*, vol. 24, pp. 1–3, Jan. 2020, doi: 10.1016/j.ensm.2019.07.029.

[27] S. Song, Y. Wang, and P. K. Shen, "Pulse-microwave assisted polyol synthesis

of highly dispersed high loading Pt/C electrocatalyst for oxygen reduction reaction," *J. Power Sources*, vol. 170, no. 1, pp. 46–49, Jun. 2007, doi: 10.1016/j.jpowsour.2007.04.012.

[28] A. Holewinski and S. Linic, "Elementary Mechanisms in Electrocatalysis: Revisiting the ORR Tafel Slope," *J. Electrochem. Soc.*, vol. 159, no. 11, pp. H864–H870, Jan. 2012, doi: 10.1149/2.022211jes.

[29] H. A. Gasteiger, S. S. Kocha, B. Sompalli, and F. T. Wagner, "Activity benchmarks and requirements for Pt, Pt-alloy, and non-Pt oxygen reduction catalysts for PEMFCs," *Appl. Catal. B Environ.*, vol. 56, no. 1–2, pp. 9–35, Mar. 2005, doi: 10.1016/j.apcatb.2004.06.021.

[30] Y. Garsany, I. L. Singer, and K. E. Swider-Lyons, "Impact of film drying procedures on RDE characterization of Pt/VC electrocatalysts," *J. Electroanal. Chem.*, vol. 662, no. 2, pp. 396–406, 2011, doi: https://doi.org/10.1016/j.jelechem.2011.09.016.

[31] A. Damjanovic and V. Brusic, "Electrode kinetics of oxygen reduction on oxide-free platinum electrodes," *Electrochim. Acta*, vol. 12, no. 6, pp. 615–628, Jun. 1967, doi: 10.1016/0013-4686(67)85030-8.

[32] M. R. Tarasevich, A. Sadkowski, and E. Yeager, "Oxygen Electrochemistry," in *Comprehensive Treatise of Electrochemistry*, Boston, MA: Springer US, 1983, pp. 301–398, doi: 10.1007/978-1-4613-3584-9_6.

[33] C. A. Reiser *et al.*, "A Reverse-Current Decay Mechanism for Fuel Cells," *Electrochem. Solid-State Lett.*, vol. 8, no. 6, p. A273, 2005, doi: 10.1149/1.1896466.

[34] W. R. Baumgartner, P. Parz, S. D. Fraser, E. Wallnöfer, and V. Hacker, "Polarization study of a PEMFC with four reference electrodes at hydrogen starvation conditions," *J. Power Sources*, vol. 182, no. 2, pp. 413–421, Aug. 2008, doi: 10.1016/j.jpowsour.2008.01.001.

[35] J. C. Meier *et al.*, "Degradation Mechanisms of Pt/C Fuel Cell Catalysts under Simulated Start–Stop Conditions," *ACS Catal.*, vol. 2, no. 5, pp. 832–843, May

2012, doi: 10.1021/cs300024h.

[36] A. A. Topalov, S. Cherevko, A. R. Zeradjanin, J. C. Meier, I. Katsounaros, and K. J. J. Mayrhofer, "Towards a comprehensive understanding of platinum dissolution in acidic media," *Chem. Sci.*, vol. 5, no. 2, pp. 631–638, 2014, doi: 10.1039/C3SC52411F.

[37] Y. Garsany, O. A. Baturina, K. E. Swider-Lyons, and S. S. Kocha, "Experimental Methods for Quantifying the Activity of Platinum Electrocatalysts for the Oxygen Reduction Reaction," *Anal. Chem.*, vol. 82, no. 15, pp. 6321–6328, Aug. 2010, doi: 10.1021/ac100306c.

[38] H. Schulenburg *et al.*, "3D Imaging of Catalyst Support Corrosion in Polymer Electrolyte Fuel Cells," *J. Phys. Chem. C*, vol. 115, no. 29, pp. 14236–14243, Jul. 2011, doi: 10.1021/jp203016u.

[39] T. N. V. Matthew M. Mench, Emin Caglan Kumbur, *Polymer Electrolyte Fuel Cell Degradation*. 2012, doi: https://doi.org/10.1016/c2010-0-67819-9.

[40] T. Lagarteira, S. Delgado, C. Fernandes, C. Azenha, C. Mateos-Pedrero, and A. Mendes, "The role of Pt loading on reduced graphene oxide support in the polyol synthesis of catalysts for oxygen reduction reaction," *Int. J. Hydrogen Energy*, vol. 45, no. 40, pp. 20594–20604, Feb. 2020, doi: 10.1016/j.ijhydene.2020.02.022.

[41] B. Fang, J. H. Kim, M. S. Kim, and J. S. Yu, "Hierarchical nanostructured carbons with meso-macroporosity: Design, characterization, and applications," *Acc. Chem. Res.*, vol. 46, no. 7, pp. 1397–1406, Jul. 2013, doi: 10.1021/ar300253f.

[42] T.-N. Tran *et al.*, "Iron Phosphide Incorporated into Iron-Treated Heteroatoms-Doped Porous Bio-Carbon as Efficient Electrocatalyst for the Oxygen Reduction Reaction," *ChemElectroChem*, vol. 5, no. 14, pp. 1944–1953, Jul. 2018, doi: 10.1002/celc.201800091.

[43] S. Maass, F. Finsterwalder, G. Frank, R. Hartmann, and C. Merten, "Carbon support oxidation in PEM fuel cell cathodes," *J. Power Sources*, vol. 176, no. 2, pp. 444–451, Feb. 2008, doi: 10.1016/j.jpowsour.2007.08.053.

[44] J. H. Kim, J. Y. Cheon, T. J. Shin, J. Y. Park, and S. H. Joo, "Effect of surface

oxygen functionalization of carbon support on the activity and durability of Pt/C catalysts for the oxygen reduction reaction," *Carbon N. Y.*, vol. 101, pp. 449–457, May 2016, doi: 10.1016/j.carbon.2016.02.014.

[45] S. Mukerjee, S. Srinivasan, M. P. Soriaga, and J. McBreen, "Effect of preparation conditions of Pt alloys on their electronic, structural, and electrocatalytic activities for oxygen reduction. XRD, XAS, and electrochemical studies," *J. Phys. Chem.*, vol. 99, no. 13, pp. 4577–4589, 1995, doi: 10.1021/j100013a032.

[46] B. C. Beard and P. N. Ross, "The Structure and Activity of Pt-Co Alloys as Oxygen Reduction Electrocatalysts," *J. Electrochem. Soc.*, vol. 137, no. 11, pp. 3368–3374, 1990, doi: 10.1149/1.2086223.

[47] F. N. Büchi, M. Inaba, and T. J. Schmidt, Eds., *Polymer Electrolyte Fuel Cell Durability*. New York, NY: Springer New York, 2009, doi: 10.1007/978-0-387-85536-3.

[48] X. Cheng *et al.*, "A review of PEM hydrogen fuel cell contamination: Impacts, mechanisms, and mitigation," *J. Power Sources*, vol. 165, no. 2, pp. 739–756, Mar. 2007, doi: 10.1016/j.jpowsour.2006.12.012.

[49] K. Kinoshita, "Particle Size Effects for Oxygen Reduction on Highly Dispersed Platinum in Acid Electrolytes," *J. Electrochem. Soc.* , vol. 137, no. 3, pp. 845–848, Mar. 1990, doi: 10.1149/1.2086566.

[50] K. J. J. Mayrhofer *et al.*, "Fuel cell catalyst degradation on the nanoscale," *Electrochem. commun.*, vol. 10, no. 8, pp. 1144–1147, Aug. 2008, doi: 10.1016/j.elecom.2008.05.032.

[51] S. G. Rinaldo, J. Stumper, and M. Eikerling, "Physical Theory of Platinum Nanoparticle Dissolution in Polymer Electrolyte Fuel Cells," *J. Phys. Chem. C*, vol. 114, no. 13, pp. 5773–5785, Apr. 2010, doi: 10.1021/jp9101509.

[52] E. F. Holby, Y. Shao-Horn, W. Sheng, and D. Morgan, "Oxide formation and removal on Pt surfaces under potential cycled conditions," in *ECS Transactions*, 2009, vol. 25, no. 1 PART 1, pp. 583–592, doi: 10.1149/1.3210609.

[53] D. C. Johnson, D. T. Napp, and S. Bruckenstein, "A ring-disk electrode study of

the current/potential behaviour of platinum in 1.0 M sulphuric and 0.1 M perchloric acids," *Electrochim. Acta*, vol. 15, no. 9, pp. 1493–1509, Sep. 1970, doi: 10.1016/0013-4686(70)80070-6.

[54] X. Wang, R. Kumar, and D. J. Myers, "Effect of voltage on platinum dissolution relevance to polymer electrolyte fuel cells," *Electrochem. Solid-State Lett.*, vol. 9, no. 5, 2006, doi: 10.1149/1.2180536.

[55] J. Parrondo *et al.*, "Platinum supported on titanium-ruthenium oxide is a remarkably stable electrocatayst for hydrogen fuel cell vehicles," *Proc. Natl. Acad. Sci. U. S. A.*, vol. 111, no. 1, pp. 45–50, 2014, doi: 10.1073/pnas.1319663111.

Supplementary information

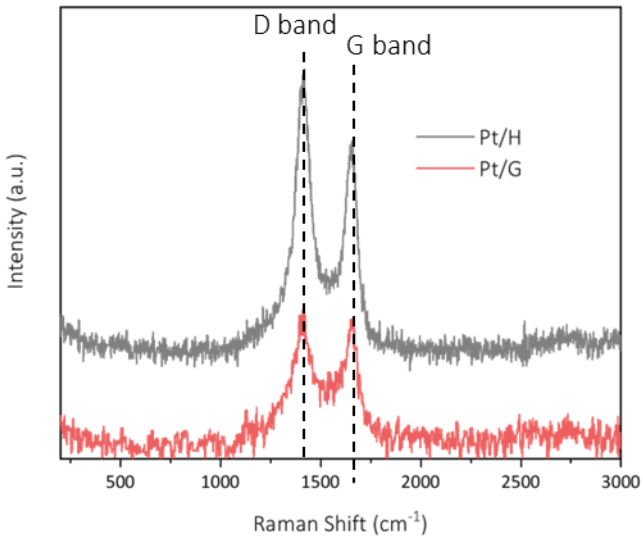


Figure S1 – Raman spectra obtained for pristine Pt/H and Pt/G samples.

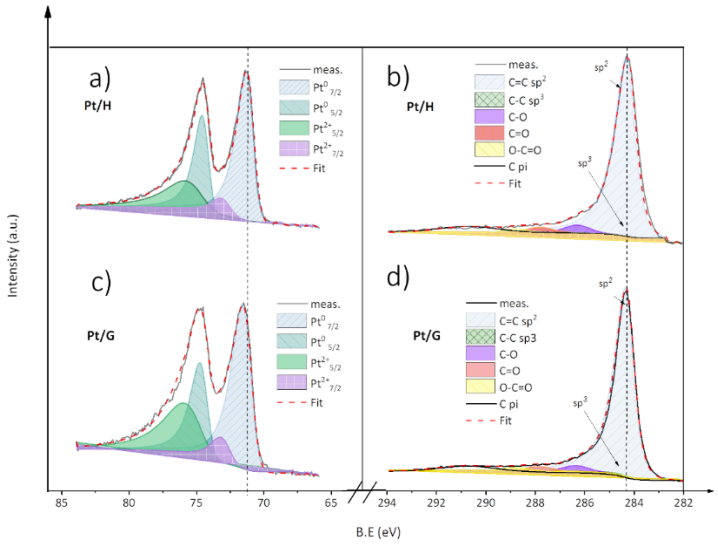


Figure S2 – High resolution XPS analysis of (a,c) Pt 4f of pristines Pt/H and Pt/G respectively, (b,d) C1s of Pt/H and Pt/G, respectively.

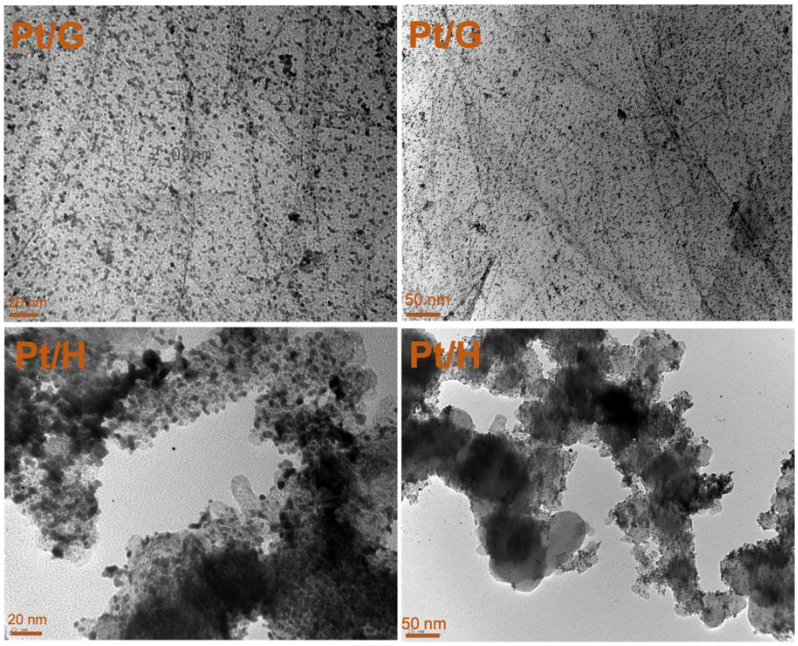


Figure S3 – TEM images with different magnifications for Pt/G and Pt/H.

Table S1 – Fittings for peak binding energy of orbitals 4f and C1s from Pt/H and Pt/G.

Pt/G **Pt 4f orbital**	**Be/ eV**	**FWHM**	**Line Shape**	**At. %**
$Pt^0_{7/2}$	71.1	1.45	LA(1.2,85,70)	43.40
$Pt^0_{5/2}$	74.3	1.3	LA(1.2,85,70)	22.80
$Pt^{2+}_{7/2}$	72.7	1.54	LA(1.2,85,70)	7.23
$P^{2+}_{5/2}$	75.0	2.8	LA(1.2,85,70)	26.57
Pt/H **Pt4f orbital**	**Be/ eV**	**FWHM**	**Line Shape**	**At. %**
$Pt^0_{7/2}$	70.9	1.26	LA(1.2,85,70)	46.8
$Pt^0_{5/2}$	74.2	1.1	LA(1.2,85,70)	26.7
$Pt^{2+}_{7/2}$	72.7	1.5	LA(1.2,85,70)	6.50
$P^{2+}_{5/2}$	74.9	2.8	LA(1.2,85,70)	20.0

Pt/G **C1s orbital**	**Be/ eV**	**FWHM**	**Line Shape**	**At. %**
C=C sp^2	284.31	0.75	LA(1.2,2.5,5)	87.2
C-C sp^3	284.81	1.2	GL(30)	0.4
C-O	286.31	1.2	GL(30)	2.8
C=O	287.81	1.2	GL(30)	2.1
O-C=O	288.81	1.2	GL(30)	1.4
C π*	290.72	2.7	GL(30)	6.1
Pt/H **C1s orbital**	**Be/ eV**	**FWHM**	**Line Shape**	**At. %**
C=C sp^2	284.26	0.8	LA(1.2,2.5,5)	86.4
C-C sp^3	284.76	1.2	GL(30)	0.01
C-O	286.26	1.2	GL(30)	3.7
C=O	287.76	1.2	GL(30)	2.39
O-C=O	288.76	1.2	GL(30)	1.52
C π*	290.67	2.7	GL(30)	6.0

Table S2 – Pt average particle sizes and dissolved Pt in the electrolyte for Pt/H and Pt/G.

Pt average size	**Pt/H**	**Pt/G**
BoL (nm)	4.1	2.6
AST 1 (nm)	4.7 (+114.6 %)	3.2 (+123.1 %)
AST 2 (nm)	6.0 (+146.3 %)	1.2 (+184.6 %)
AST3 (nm)	4.3 (+104.9 %)	1.2 (+130.8 %)
Pt dissolution	**Pt/H**	**Pt/G**
Initial mass (µg)	4.000	4.000
AST 1 (µg)	0.062 (1.54 %)	0.123 (3.08 %)
AST 2 (µg)	0.0195 (0.49 %)	0.024 (0.60 %)
AST 3 (µg)	0.006 (0.15 %)	0.015 (0.38 %)

CHAPTER 6

IN-SITU MEASUREMENT OF VANADIUM CROSSOVER FOR THE VANADIUM REDOX FLOW BATTERY

6

IN-SITU MEASUREMENT OF VANADIUM CROSSOVER FOR THE VANADIUM REDOX FLOW BATTERY

Tiago Lagarteira, Pedro Pacheco, Carlos Almeida, Anders Bentien, Ricardo Monteiro and Adélio Mendes

Adapted from the Journal of Electrochemical Society, 2020, 15

ABSTRACT

A simple *in-situ* method for the quantification of the crossover in redox flow batteries, adapted from an electrochemical method currently used for quantifying the hydrogen crossover in fuel cells, is proposed and used for characterizing a vanadium redox flow battery. A linear sweep voltammetry (LSV) scan is performed with the pertinent redox species in one side of the electrochemical cell, while in the other side is the supporting electrolyte. The LSV plot should display a plateau where the current is limited by the crossover of the selected species. The crossover results were compared with an external analytical method using MP-AES, showing very good agreement with a maximum relative difference of 6 %. This method was used to quantify the crossover of all vanadium species using both cation and anion exchange membranes. The proposed method can be applied for assisting the development and characterization of ion-exchange membranes for redox flow batteries and for *in-situ* diagnosis of component degradation and failure in RFB systems without disassembling them.

6.1. INTRODUCTION

The increasing widespread of electricity production from renewable sources led to the critical need of grid-scale energy storage systems to balance the intermittent nature of wind and solar power [1]–[3]. In this regard, redox flow batteries (RFBs) have emerged due to the advantage of decoupled power and energy scaling, long operation lifetime, easy maintenance, simple manufacture and low cost of energy storage [4]–[6]. Particularly, all-vanadium redox flow batteries (VRFBs) have the unique feature of using, in both electrodes, redox pairs based in the same chemical element. Also, the used electrolyte is very stable, and, in theory, it can be reused indefinitely [7], [8]. This is an important advantage compared to other RFBs since the detrimental crossover of active species through the membrane can be periodically mitigated by remixing the electrolyte [9]. VRFBs have been successfully implemented in stationary applications such as for remote areas, back-up power supply, regulation of grid power quality and frequency control, and in distributed power generation systems [10]. After generating significant commercial interest, VRFBs are now requiring the development of quality control tools, besides the ongoing development of mass production solutions.

Some of the most important causes for performance degradation and system shut-down of VRFBs are the vanadium crossover and existence of internal short-circuits [11], [12]. The permeation of unreacted vanadium ions through the membrane (crossover) is problematic since it leads to the (reversible) loss of capacity and self-discharge, thus requiring periodical remixing of the electrolyte. Despite the influence of the operational conditions, such as temperature and flow rate, the membrane type and aging have the biggest impact on vanadium crossover [13]. Different types of membranes used in VRFBs include cationic and anionic exchange membranes; the most commonly reported are perfluorinated cation exchange membranes such as Nafion [14], [15]. Regardless of the membrane type, vanadium crossover is inevitable, making it a topic of great interest among the VRFB research community not only to assess but also to mitigate its detrimental effects in the performance and lifespan of the battery.

The crossover in VRFBs is driven by the different electrochemical potentials of each species in the two sides of the membrane, with transport occurring from higher to lower

potential. Two contributions are discernible: chemical potential gradients are responsible for diffusive processes, and electric potential gradients cause migration of charged species and solvent molecules (electro-osmotic drag) [16], [17]. If a porous membrane is employed instead of an ion exchange membrane, bulk convection of the electrolyte can also occur. The most widely reported method for crossover quantification in VRFBs makes use of a diffusion cell, where only one of the two chambers, separated by the membrane, contains vanadium ions in the electrolyte [18], [19]. The blank side, initially containing supporting electrolyte, is periodically sampled for posterior analysis to quantify the vanadium concentrations. A simple mass balance to the blank electrolyte yields the following relation:

$$J = \frac{V}{A}\frac{dc}{dt} \tag{1}$$

where J (mol s^{-1}) is molar flux of vanadium species through the membrane, V (m^3) stands for the total volume of blank electrolyte, A is the membrane area (m^2), c (mol m^{-3}) is the concentration of vanadium in the blank electrolyte and t (s) is time. The mass transfer rate of vanadium ions through the membrane remains approximately constant and the concentration increases linearly throughout the experiment, according to Fick's law. Thus, the slope of concentration/time relationship can be used to calculate the molar flux of vanadium through the membrane.

The use of diffusion cells does not allow to account for the contribution of migration driven crossover, since there is no electrical field applied. Other approaches have been proposed to consider migration along with diffusion contributions but none is able to measure vanadium crossover *in-situ* [20], [21]. Moreover, all *in-situ* methods in literature require the use of an external analytic method for the determination of the vanadium concentration of the electrolyte samples, such as UV-Vis spectroscopy [11], [15], potentiometric titration [15], [22], [23], or inductively coupled plasma atomic emission spectrometry (ICP-AES) [19], [24], among others [23]. In real applications, the use of external analytical methods for quality control proves often to be unpractical and

time-consuming. Therefore, RFBs are still lacking an *in-situ*, simple, accurate and reliable methodology for crossover determination.

The PEMFC community make use of a standard procedure to measure hydrogen crossover through the membrane [25]–[27]. This procedure consists of performing linear sweep voltammetry at very low scan rate to a PEMFC fed with hydrogen to the anode and inert nitrogen to the cathode. The faradaic response corresponds to the oxidation of hydrogen at the working electrode (WE) that permeated through the membrane. After reaching the steady state, the faradaic current is limited by the flow rate of H_2 through the membrane, despite the linearly increasing potential difference applied on the cell. At this stage, the limiting current is proportional to the rate of hydrogen permeation, as expressed by Faraday's law:

$$J = \frac{j_l}{zF} \tag{2}$$

where J (mol s^{-1}) is the flow rate of hydrogen through the membrane, j_l (A) is the limiting current, z is the number of electrons exchanged in the electrochemical reaction, and F (96 485 C mol^{-1}) is Faraday's constant.

Inspired in the hydrogen crossover diagnosis for PEMFCs, this work discloses an *in-situ* method to quantify electrochemically the vanadium crossover in VRFBs. The accuracy and reliability of the proposed method is highlighted with the use of different membranes – cation and anion exchange membranes – and the crossover quantification of all vanadium ion species; this new adaption of the method for RFBs was then validated using an external analytical method. The simplicity of the method, named hereafter electrochemical method, coupled with the fact that it does not require analytical equipment other than an electrochemical workstation, makes it very attractive for the quantification of species crossover in any kind of redox flow batteries. It can be applied to a redox flow cell or stack without disassembly, unlike other methods reported in literature. This method provides not only an effective tool for membrane characterization and development but also for diagnosing failure, enabling the monitoring of active species crossover throughout the lifetime of a redox flow battery.

6.2. EXPERIMENTAL

6.2.1. MATERIALS AND CELL COMPONENTS

Vanadium electrolyte was sourced from GfE (1.6 M at a 1:1 V^{3+}/V^{4+} ratio). An electrochemical cell was used to charge the two electrolytes to a state of charge (SoC) of *ca.* 98%, yielding a V^{2+} enriched negalyte and a VO_2^+ enriched posilyte. A 4 M H_2SO_4 aqueous solution was prepared by diluting 95.0 - 97.0 wt.% H_2SO_4 (Honeywell International Inc., USA) in deionized water, to be used as blank electrolyte. PAN-based carbon felt (Chemshine Carbon Co., Ltd., China) was employed as the electrode material, with a thickness of 6 mm and 95 % porosity when uncompressed. The electrodes were cut to size and treated according to the procedure reported by Monteiro *et al.* [28]. Shortly, the electrodes were thermally treated at 415 ºC during 12 h under air atmosphere. Cation exchange membranes (Nafion 117, 115 and 212) were purchased from Ion Power (Germany). Anion exchange membrane (Fumasep FAP-450) was purchased from Fumatech BWT GmbH (Germany). Prior to assembly, Nafion membranes were immersed in deionized water during 10 minutes for mechanical conditioning while FAP 450 was assembled in dry condition. The electrochemical cell used for the crossover measurements had a geometric active area of 16 cm^2. The electrodes were compressed to 60 % of their original thickness. Apart from membrane and electrodes, the cell was composed by two steel endplates, two insulating PVC plates, two copper current collectors and graphite bipolar plates machined in a flow-through design, along with EPDM gaskets.

6.2.2. EXPERIMENTAL SET-UP

The electrolyte was pumped from the reservoirs to the cell by means of two Watson-Marlow Qdos 120 Universal peristaltic pumps. To prevent oxidation of V^{2+} by oxygen in air, Verdeflex tubing (4.8 mm inner diameter) was used owing to its low oxygen permeability, and nitrogen gas was employed to purge both electrolyte reservoirs. Electrochemical measurements were performed with a Zahner Zennium workstation

(Zahner Elektrik, Germany). The cell was connected to the electrochemical workstation in a two-electrode configuration, where the working electrode (WE) was connected to the positive half-cell, and the counter electrode (CE) was connected to the negative half-cell. The reference electrode (RE) lead was connected to the CE. The experimental set-up is schematized in Figure 6.1.

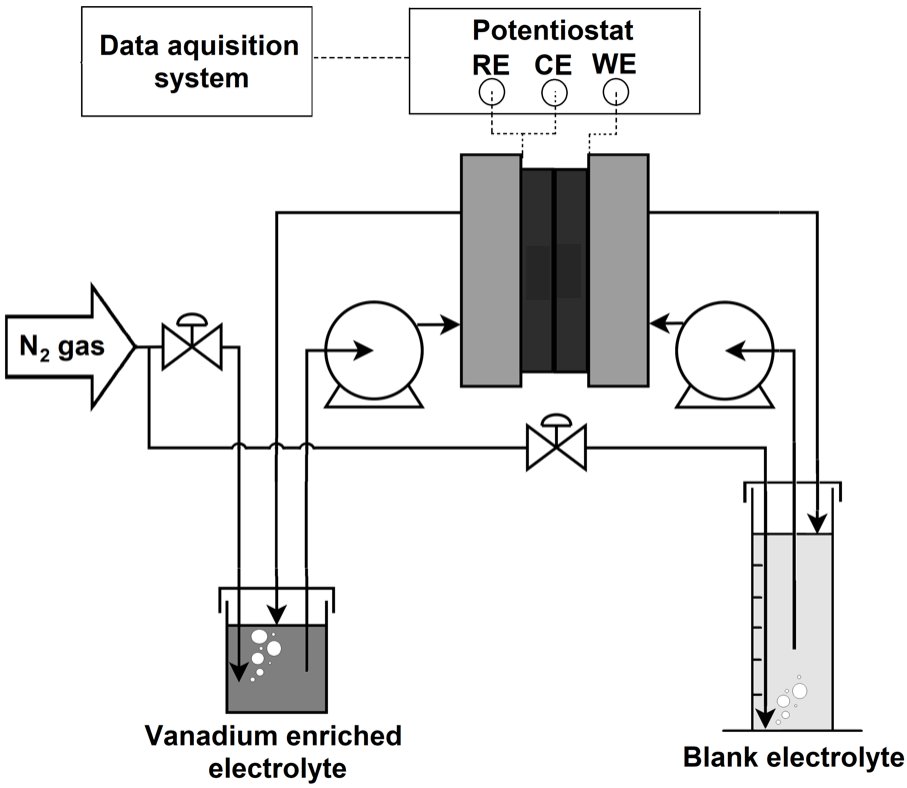


Figure 6.1 - Schematic diagram of the experimental set-up for crossover measurement.

6.2.3. CROSSOVER MEASUREMENT

The negative half-cell was connected to a reservoir of V^{2+} enriched electrolyte, and the positive half-cell was connected to a 100 cm^3 graduated cylinder used as a blank electrolyte reservoir. The positive half-cell was washed thoroughly with blank electrolyte before each experiment. A low flowrate of 0.5 cm^3 min^{-1} was maintained in both sides during the LSV for crossover measurement. The potential was swept from a lower limit corresponding to the open circuit potential (OCP) of the cell to an upper limit of 250 mV.

For the scan rate study, scan rates of 50, 75 and 100 μV s^{-1} were employed. For the study with different membranes, Nafion 212, 115 and 117, and FAP-450 were used. The scan rate in the membrane study was 75 μV s^{-1}. To show the method response in case of internal short-circuit, a scalpel was used to perforate a Nafion 212 membrane in 5 locations (in the center and in the four corners, creating incisions of ca. 2 mm in length). This measurement was also performed at 75 μV s^{-1}.

6.2.4. CROSSOVER DIAGNOSIS AFTER AGING

The degradation study was performed with Nafion 212 membrane. After the LSV for crossover measurement, as detailed in the previous section, there was a substitution of the electrolytes for fresh ones. The flowrate was set to 50 cm^3 min^{-1}. Fresh electrolytes were charged to *ca.* 100 % SoC, and the cell was then subjected to galvanostatic charge-discharge cycling (CDC) for an extended period to impose degradation to the Nafion 212 membrane. CDC was performed at a current density of 80 mA cm^{-2}, with cut-off voltages of 0.7 V and 1.65 V, for 28 cycles. After CDC, another crossover measurement was performed. Data from CDC allowed for the calculation of charge, voltage and energy efficiencies (CE, VE and EE, respectively), along with discharge capacity loss (DCL) and voltage efficiency loss (VEL) for each cycle:[29]

$$\mathrm{CE}_i = \frac{\int_{t_{\mathrm{d,o}}}^{t_{\mathrm{d,f}}} I_{\mathrm{d}}(t)\,dt}{\int_{t_{\mathrm{c,o}}}^{t_{\mathrm{c,f}}} I_{\mathrm{c}}(t)\,dt} \tag{3}$$

$$\mathrm{VE}_i = \frac{\int_{t_{\mathrm{d,o}}}^{t_{\mathrm{d,f}}} E_{\mathrm{d}}(t)\,dt}{\int_{t_{\mathrm{c,o}}}^{t_{\mathrm{c,f}}} E_{\mathrm{c}}(t)\,dt} \cdot \frac{(t_{\mathrm{c,f}} - t_{\mathrm{c,o}})}{(t_{\mathrm{d,f}} - t_{\mathrm{d,o}})} \tag{4}$$

$$\mathrm{EE}_i = \mathrm{CE}_i \cdot \mathrm{VE}_i \tag{5}$$

$$\mathrm{DCL}_i = \frac{\int_{t_{\mathrm{d,o}}}^{t_{\mathrm{d,f}}} I_{\mathrm{d}}(t)\,dt\Big|_{\text{cycle 1}} - \int_{t_{\mathrm{d,o}}}^{t_{\mathrm{d,f}}} I_{\mathrm{d}}(t)\,dt\Big|_{\text{cycle } i}}{\int_{t_{\mathrm{d,o}}}^{t_{\mathrm{d,o}}} I_{\mathrm{d}}(t)\,dt\Big|_{\text{cycle 1}}} \tag{6}$$

$$\mathrm{VEL}_i = \frac{\mathrm{VE}_1 - \mathrm{VE}_i}{\mathrm{VE}_1} \quad (7)$$

where I (A) is the current, E (V) is the cell potential, t (s) stands for time, subscript i stands for cycle number, subscript c for charge, subscript d for discharge, subscript 0 for initial and subscript f for final. DCL and VEL are measures of the percentage loss in charge capacity and voltage efficiency, respectively, for cycle *i,* relative to the initial values (cycle 1). Additionally, after charge-discharge cycling, both membranes submerged in Millipore water for a period of 12 h, and subsequently dried at 60 ºC during 24h, when their thicknesses were measured. The measurements were performed with a micrometer (Mitutoyo Digimatic Micrometer 293-805), in eight points on both the pristine and aged membranes. These correspond to the four corners of the membranes (*ca.* 3 mm from the edges of the active area), four points in a cross pattern near the center (*ca.* 1.5 cm from the edges), and one point in the center.

6.2.5. DETERMINATION OF VANADIUM CONCENTRATION

During the crossover measurement of the cell assembled with Nafion 115, samples of 1 cm^3 were periodically taken from the blank electrolyte reservoir and diluted by a factor of 10 with Millipore water. The total volume of blank electrolyte contained in the cell and reservoir was 143 cm^3. Elemental vanadium concentration was determined by Microwave Plasma coupled with Atomic Emission Spectroscopy (MP-AES, Agilent 4200), at a wavelength of 437.9 nm.

6.3. RESULTS AND DISCUSSION

6.3.1. OPTIMIZATION OF PARAMETERS

The WE compartment was washed carefully to remove any traces of vanadium which directly impact the starting point of the LSV. The supporting electrolyte used in washing was stored for further recycling and use. After washing the WE with blank electrolyte, the OCP of the cell sat typically within the range of 0 – 100 mV, slowly decreasing due to traces V^{2+} from immediate crossover. The difference in potential across the two half-

cells is assigned to the differing concentrations of V^{2+} and V^{3+}, as the cell effectively behaves as a concentration cell. After starting the LSV, the redox reactions occurring in the cell, as the potential in the WE is swept, are:

Counter electrode (vanadium electrolyte): $V^{3+} + e^{-} \rightarrow V^{2+}$ (8)

Working electrode (blank electrolyte): $V^{2+} \rightarrow V^{3+} + e^{-}$ (9)

Preliminary tests were performed with wider potentials to determine the most suitable potential range for running the LSV. Considering that the standard oxidation potentials of V^{2+} to V^{3+} and V^{3+} to V^{4+} are separated by 600 mV, an upper potential of 250 mV was found to be adequate, since, in one hand, this potential the reaction is not electrochemically limited, and in the other it does not enable the further oxidation of V^{3+} to V^{4+}. To investigate whether the blank electrolyte was indeed electrochemically inert or if hydrogen evolution would not take place within the LSV potential range, as initially hypothesized, a blank test was performed. The resulting voltammogram displayed a nearly negligible constant current of *ca.* 6 µA cm^{-2}, as shown in Figure S1.

Following, for optimizing the scan rate value, several LSVs were performed at different scan rates. In Figure S2, are shown voltammograms obtained with scan rates of 50, 75 and 100 µV s^{-1}. A scan rate of 75 µV s^{-1} was found to be adequate as it generated a well-defined current plateau and was adopted for all subsequent crossover measurements. Higher scan rates result in a pronounced peak current leading to a less well-defined current plateau due to fast oxidation of accumulated V^{2+} in the blank electrolyte while shorter scan rates result in longer test durations for the same potential range. No variation in the volume of blank electrolyte was observed during the LSV measurements, which typically lasted from 30 to 50 minutes.

6.3.2. ELECTROCHEMICAL METHOD *VS EX-SITU* VANADIUM QUANTIFICATION

The validation of the method for VRFBs was accomplished comparing the results obtained electrochemically over time with those obtained directly from the determination of the elemental vanadium concentration in the blank electrolyte by MP-AES.

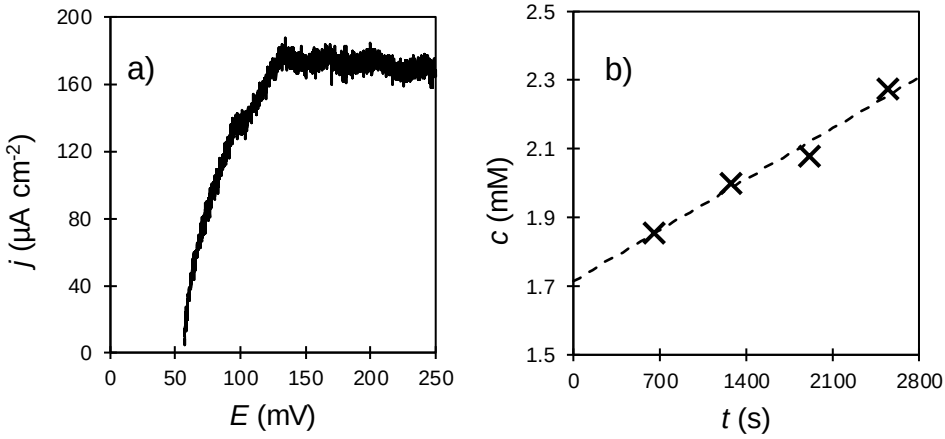


Figure 6.2 - New electrochemical vs sampling chemical analysis crossover methods: a) linear sweep voltammetry data obtained at a scan rate of 75 μV s^{-1} and b) elemental vanadium concentration plotted over elapsed time.

A stable plateau is evident in Figure 6.2a with an average limiting current density of 170 μA cm^{-2}. Throughout the electrochemical measurement, the blank electrolyte was periodically sampled and later analyzed by MP-AES. Using the concentration and collecting time of each sample, the vanadium concentration (at the initially blank electrolyte) over time can be found in Figure 6.2b, along with the linear model that fits the data; the slope of this line is directly related to the crossover rate by Equation 1, which is 6.8 μmol h^{-1} cm^{-2}.

Similarly, based on the limiting current density obtained by LSV (Equation 2), a crossover flux of 6.4 μmol h^{-1} cm^{-2} was obtained. These values differ for just 6 % (relative difference), which was within the experimental error. As for hydrogen crossover measurement for PEMFCs, the vanadium permeate flux is compensated by an

electrochemical reaction at the electrode containing higher vanadium concentration to maintain steady-state conditions and the required current is measured. Moreover, the conditions (low scan rate and low flow rate) were set to ensure that the dominant factor influencing the current response is the step of vanadium ion diffusing through the membrane, similarly as reported for H_2 crossover quantification in PEMFCs [30], [31].

6.3.3. VANADIUM CROSSOVER ON DIFFERENT MEMBRANES

The adapted method was used for comparing the crossover through membranes with different thicknesses, Nafion 212, 115 and 117, and different chemical structures, Fumasep FAP-450. Voltammograms resulting from the crossover measurements can be found in Figure 6.3a. The V^{2+} crossover rate through each membrane is displayed along with the dry membrane thickness in Table 6.1.

Table 6.1 - Comparison of crossover rates for different ion exchange membranes.

Membrane	Dry thickness / µm	V^{2+} crossover rate / µmol h^{-1} cm^{-2}
Nafion 117	183	2.90
Nafion 115	127	6.40
Nafion 212	51	29.7
Fumasep FAP-450	50	3.30

Membranes with the same chemical structure, Nafion 212, 115 and 117, displayed V^{2+} crossover inversely proportional to their thickness (Figure 6.3b), which in turn also validates the accuracy of the method. This is in agreement with the Nernst-Planck equation of mass conservation, which dictates that the diffusion and migration components of mass transfer are proportional to the inverse of the diffusion path length [32]. Despite having a similar thickness to Nafion 212, Fumasep FAP-450 has a nine-fold lower crossover. FAP-450 is an anion exchange membrane, with a high selectivity for anions, diminishing the transport of vanadium cations.[33] Moreover, it has a sterically hindered aromatic polyamine chemical structure that contains a backbone that is aromatic-based, leading to lower porosity comparing to the cation-exchange counterpart [34].

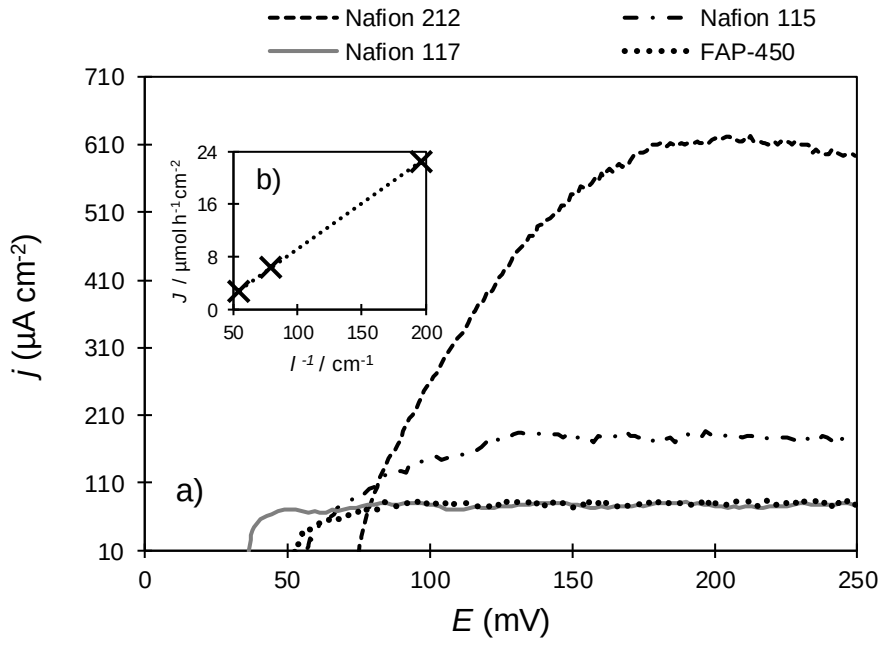


Figure 6.3 - a) LSV voltammograms performed at 75 µV s^{-1} with cells assembled with Nafion membranes with different thicknesses and FAP-450 from Fumatech. b) V^{2+} crossover flux for Nafion 212, 115 and 117, plotted against the inverse of membrane thickness.

Figure S3 illustrates the LSV response in the case of internal short-circuit caused by membrane perforation. Unlike for pristine membranes, the current response increased continuously without reaching a plateau, as it happens for PEMFC with a perforated membrane.

6.3.4. VANADIUM CROSSOVER AFTER BATTERY CYCLING

The electrochemical cell assembled with the Nafion 212 membrane in the membrane comparison study was chosen due to its smaller thickness. The use of a thinner membrane promotes a greater impact of charge-discharge cycling on increasing vanadium crossover. The charge-discharge history can be found in the supplementary material, Figure S4. Before and after battery cycling, crossover measurements were obtained as illustrated in Figure 6.4.

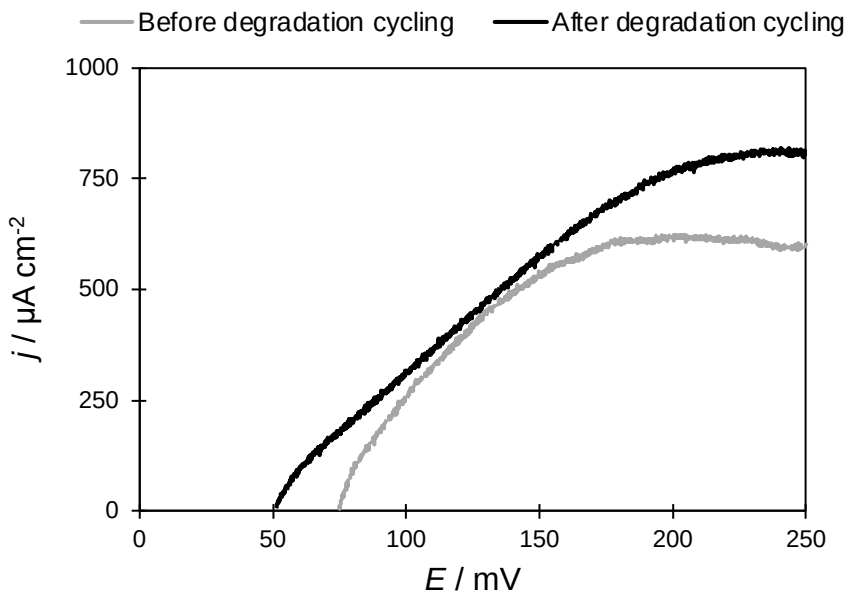


Figure 6.4 - LSV voltammograms performed at 75 µV s^{-1}, before and after charge-discharge aging.

After battery cycling, an increase of 25 % in vanadium crossover was observed. The membrane, after dissembled, displayed no perforations or pinholes. To evaluate any membrane thinning caused by battery operation, the thickness of the used Nafion 212 membrane was measured at nine points before and after charge and discharge cycles. The average measured thickness for the cycled membrane was 50.4 ± 0.9 µm, while for the pristine membrane, a value of 55 ± 0.5 µm was obtained. This represents a relative reduction of *ca.* 8 % in membrane thickness upon charge-discharge cycling that may be the reason for higher crossover after battery cycling.

Figure 6.5a plots the coulombic, voltaic and energy efficiencies (CE, VE and EE, respectively), while Figure 6.5b showcases discharge capacity loss (DCL) and voltage efficiency loss (VEL), as functions of the cycle number. These metrics were computed according to Equations 3-7. An increase in DCL can be observed starting from cycle 10 and accelerating steeply from cycle 23 onwards. DCL can result from an actual reduction in the charge capacity of the electrolytes, which can be caused by side-reactions due to

crossover, gas evolution, or electrolyte oxidation by air; however, when CDC is performed galvanostatically, DCL can result from the progressive decrease of VE. This is explained by the fact that lower VE implies higher overpotential for the same cell current. Then, the cut-off voltages for the discharge and charge processes are reached at lower SoC. Consequently, the range of SoC available during CDC is smaller, and the available charge capacity is lower. In Figure 6.5b, a strong correlation between DCL and VEL can be observed (note that VEL is scaled to have a similar magnitude to that of DCL for easier comparison), meaning that the decrease in VE is the predominating cause of the increase in DCL, not crossover. In this case, the CDC curve does not contain information regarding crossover. To isolate this phenomenon from other causes for efficiency loss, the LSV for crossover measurement is of paramount importance.

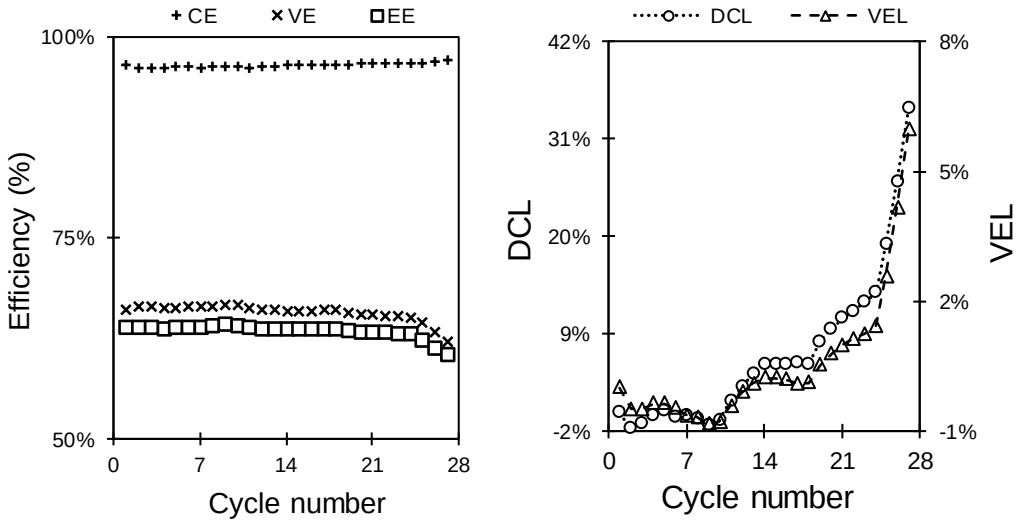


Figure 6.5 - a) Coulombic, voltaic and energy efficiency (CE, VE, EE, respectively) for each cycle. b) Discharge capacity loss and voltage efficiency loss (DCL and VEL respectively) for each cycle. CDC was performed at 80 mA cm^{-2}, with upper and lower potential limits of 1.65 and 0.7 V respectively, for 28 cycles.

6.3.5. CROSSOVER OF ALL IONIC VANADIUM STATES

Crossover measurements were also performed for the remaining vanadium species using two membranes with different chemical structure (Nafion 115 and FAP 450) – Figure

6.6. The linear voltammetry plots are shown in supplementary material, Figure S5 (Nafion 115) and Figure S6 (FAP 450), for species V^{2+}, V^{3+}, VO^{2+} and VO_2^+. The potential values were normalized and the current signal of VO_2^+ (reduced to VO^{2+} at the WE) inverted to facilitate comparing the actual crossover with each other. The crossover through FAP 450 membrane was higher for $V^{2+} > VO^{2+} > VO_2^+ > V^{3+}$.

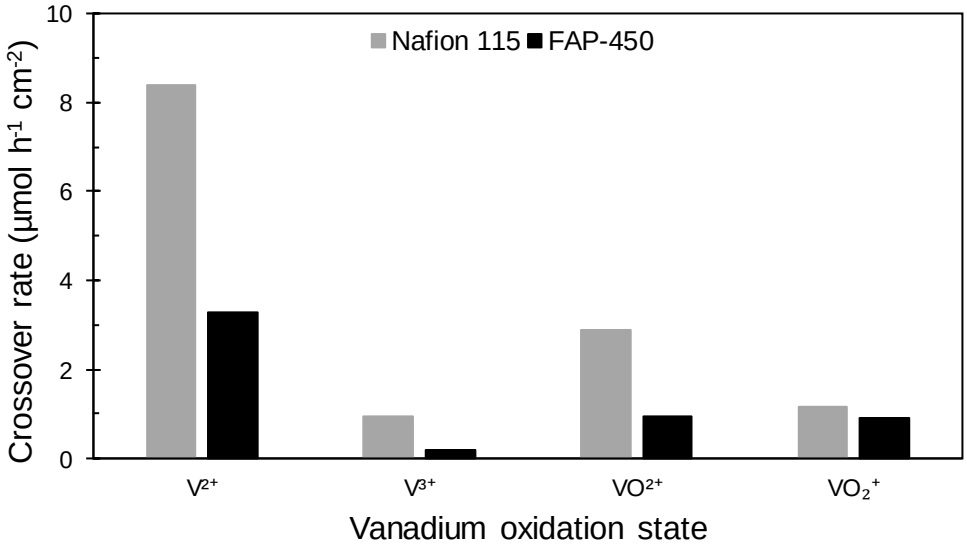


Figure 6.6 - Crossover quantification for V^{2+}, V^{3+}, VO^{2+} and VO^{2+} using a cation exchange membrane (Nafion 115) and an anion exchange membrane (FAP-450).

Such trend was also reported by Tang and co-workers [35] who studied a redox flow cell assembled using a Selemion AMV membrane. Membrane FAP 450 displayed three-fold less crossover than Nafion 115 for V^{2+}, V^{3+} and VO^{2+}; VO_2^+ crossover was also slightly lower for FAP 450. This behavior has been assigned to anion exchange nature of membrane FAP 450, which hinders the permeation of the positively charged vanadium cation ions [19], [35], [36].

The crossover through Nafion 115 membrane was $V^{2+} > VO^{2+} > VO_2^+ \approx V^{3+}$, a slightly different trend as for FAP 450 membrane. This behavior was also observed in many experimental and modelling studies using Nafion membranes [9], [13], [19], [32]. However, when vanadium crossover was experimentally studied during battery

operation, authors do not agree on the crossover trend. Darling and co-workers[10] reported higher crossover for VO^{2+} and VO_2^+ than for V^{2+} and V^{3+}, respectively. On the other hand, Agar and co-workers [9] reported a similar sequence as the one obtained in this work. Such deviations may be explained by the test conditions, namely: a) lager pressure drop between the inlet and outlet of the cell, which imposes large pressure differences through the membrane [37], b) gas evolution reactions during charge and c) air oxidation of V^{2+} [36]. The electrochemical method here reported uses very low electrolyte flowrates, minimal overpotentials and nitrogen purging when needed, such as for V^{2+}; this makes this method reliable and accurate.

6.4. CONCLUSIONS

An *in-situ* electrochemical method for determining the crossover of the redox species in redox flow batteries was successfully adapted from the widely used hydrogen crossover determination in PEMFCs and experimentally validated. The optimized potential range for the LSV applied to the V^{2+} crossover is between OCP and 250 mV and the scanning rate is 75 $\mu V\ s^{-1}$. The V^{2+} crossover increases with the potential until reaching a plateau which can then be calculated based on the Faraday's law from the diffusion-limiting current.

The new electrochemical method for RFBs was validated by MP-AES analysis and crossover results were compared for four different membranes: Nafion 212, 115 and 117 and Fumasep FAP-450, this last an anion exchange membrane. It was concluded that the two methods produce the same results within the experimental error. It was also concluded that the V^{2+} crossover varies inversely with the membrane thickness, which agrees with the Nernst-Planck equation of mass conservation. For perforated membranes the current response increases with the applied potential (internal short) without reaching a plateau.

Problems such as electrolyte imbalance, gas evolution, and V^{2+} air oxidation are avoided using the developed method. As concluded in other works that used external analytical methods, the anion exchange membrane displays lower vanadium crossover than the cation exchange counterpart due to electrostatic repulsion of positively-charged

membrane groups and vanadium cations. For Fumasep FAP-450, the crossover of the vanadium species was $V^{2+} > VO_2^+ > VO^{2+} > V^{3+}$, while for Nafion 115 it was $V^{2+} > VO^{2+} > VO_2^+ \approx V^{3+}$.

The developed *in-situ* crossover determination method is then a powerful tool for assisting the development of ion-exchange membranes for RFB, characterization of ion-exchange membranes for new redox systems and for diagnosing *in-situ* redox systems without opening them.

REFERENCES

[1] M. Skyllas-Kazacos, M. Rychcik, R. G. Robins, A. G. Fane, and M. A. Green, "New All-Vanadium Redox Flow Cell," *J. Electrochem. Soc.* , vol. 133, no. 5, pp. 1057–1058, May 1986, doi: 10.1149/1.2108706.

[2] C. Ponce de León, A. Frías-Ferrer, J. González-García, D. A. Szánto, and F. C. Walsh, "Redox flow cells for energy conversion," *J. Power Sources*, vol. 160, no. 1, pp. 716–732, 2006, doi: 10.1016/j.jpowsour.2006.02.095.

[3] T. Monai, H. Suzaki, and K. Yano, "Large-Scale Power Conditioning System for Grid Storage Battery System with Redox Flow Battery Having World's Highest Capacity Class of 60MWh," *FUJI Electr. Rev.*, vol. 63, no. 1, 2017.

[4] B. Schwenzer, J. Zhang, S. Kim, L. Li, J. Liu, and Z. Yang, "Membrane Development for Vanadium Redox Flow Batteries," *ChemSusChem*, vol. 4, no. 10, pp. 1388–1406, 2011, doi: 10.1002/cssc.201100068.

[5] R. A. Potash, J. R. McKone, S. Conte, and H. D. Abruña, "On the Benefits of a Symmetric Redox Flow Battery," *J. Electrochem. Soc.* , vol. 163, no. 3, pp. A338–A344, Jan. 2016, doi: 10.1149/2.0971602jes.

[6] M. Skyllas-Kazacos, M. H. Chakrabarti, S. A. Hajimolana, F. S. Mjalli, and M. Saleem, "Progress in Flow Battery Research and Development," *J. Electrochem. Soc.* , vol. 158, no. 8, pp. R55–R79, Aug. 2011, doi: 10.1149/1.3599565.

[7] S. C. Chieng, "Membrane processes and membrane modification for redox flow battery applications." PhD Thesis in Chemical Sciences Engineering, Faculty of Engineering UNSW, Sydney, Australia, pp. 230–301, 1993, doi: 10.26190/unsworks/4134.

[8] D. N. Buckley *et al.*, "Measurement and Computer Simulation of Catholyte Stability in Vanadium Flow Batteries (VFBs)," *J. Electrochem. Soc.* , vol. 165, no. 14, pp. A3263–A3274, Jan. 2018, doi: 10.1149/2.0091814jes.

[9] K. W. Knehr, E. Agar, C. R. Dennison, A. R. Kalidindi, and E. C. Kumbur, "A Transient Vanadium Flow Battery Model Incorporating Vanadium Crossover and Water Transport through the Membrane," *J. Electrochem. Soc.* , vol. 159, no. 9, pp. A1446–A1459, Jan. 2012, doi: 10.1149/2.017209jes.

[10] R. M. Darling, A. Z. Weber, M. C. Tucker, and M. L. Perry, "The influence of electric field on crossover in redox-flow batteries," *J. Electrochem. Soc.*, vol. 163, no. 1, pp. A5014–A5022, 2016, doi: 10.1149/2.0031601jes.

[11] F. Grossmith, P. Llewellyn, A. Fane, and M. Kazacos, "Evaluation of membranes for all-vanadium redox cell," in *Proceedings of Electrochemical Society Symposium*, 1988, p. 363.

[12] D. Schulte, J. Drillkens, B. Schulte, and D. U. Sauer, "Nafion Hybrid Membranes for Use in Redox Flow Batteries," *J. Electrochem. Soc.* , vol. 157, no. 9, pp. A989–A992, Sep. 2010, doi: 10.1149/1.3456625.

[13] X. Teng, Y. Zhao, J. Xi, Z. Wu, X. Qiu, and L. Chen, "Nafion/organically modified silicate hybrids membrane for vanadium redox flow battery," *J. Power Sources*, vol. 189, no. 2, pp. 1240–1246, 2009, doi: 10.1016/j.jpowsour.2008.12.040.

[14] E. Wiedemann, A. Heintz, and R. N. Lichtenthaler, "Transport properties of vanadium ions in cation exchange membranes:: Determination of diffusion coefficients using a dialysis cell," *J. Memb. Sci.*, vol. 141, no. 2, pp. 215–221, 1998, doi: 10.1016/S0376-7388(97)00308-6.

[15] C. Sun, J. Chen, H. Zhang, X. Han, and Q. Luo, "Investigations on transfer of water and vanadium ions across Nafion membrane in an operating vanadium redox flow battery," *J. Power Sources*, vol. 195, no. 3, pp. 890–897, 2010, doi: 10.1016/j.jpowsour.2009.08.041.

[16] E. Agar, K. W. Knehr, D. Chen, M. A. Hickner, and E. C. Kumbur, "Species transport mechanisms governing capacity loss in vanadium flow batteries: Comparing Nafion® and sulfonated Radel membranes," *Electrochim. Acta*, vol. 98, pp. 66–74, 2013, doi: 10.1016/j.electacta.2013.03.030.

[17] L. Hao, Y. Wang, and Y. He, "Modeling of Ion Crossover in an All-Vanadium Redox Flow Battery with the Interfacial Effect at Membrane/Electrode Interfaces," *J. Electrochem. Soc.* , vol. 166, no. 8, pp. A1310–A1322, Jan. 2019, doi: 10.1149/2.1061906jes.

[18] J. Xi, Z. Wu, X. Teng, Y. Zhao, L. Chen, and X. Qiu, "Self-assembled

polyelectrolyte multilayer modified Nafion membrane with suppressed vanadium ion crossover for vanadium redox flow batteries," *J. Mater. Chem.*, vol. 18, no. 11, pp. 1232–1238, 2008, doi: 10.1039/b718526j.

[19] P. K. Leung, Q. Xu, T. S. Zhao, L. Zeng, and C. Zhang, "Preparation of silica nanocomposite anion-exchange membranes with low vanadium-ion crossover for vanadium redox flow batteries," *Electrochim. Acta*, vol. 105, pp. 584–592, 2013, doi: 10.1016/j.electacta.2013.04.155.

[20] Q. Luo *et al.*, "In-situ investigation of vanadium ion transport in redox flow battery," *J. Power Sources*, vol. 218, pp. 15–20, 2012, doi: 10.1016/j.jpowsour.2012.06.066.

[21] D. C. Sing and J. P. Meyers, "Direct Measurement of Vanadium Crossover in an Operating Vanadium Redox Flow Battery," *ECS Trans.* , vol. 50, no. 45, pp. 61–72, Apr. 2013, doi: 10.1149/05045.0061ecst.

[22] J. Chen, B. Wang, and J. Yang, "Adsorption and Diffusion of VO2+ and VO2 + across Cation Membrane for All-Vanadium Redox Flow Battery," *Solvent Extr. Ion Exch.*, vol. 27, no. 2, pp. 312–327, Mar. 2009, doi: 10.1080/07366290802674614.

[23] J. S. Lawton, A. Jones, and T. Zawodzinski, "Concentration Dependence of VO2+ Crossover of Nafion for Vanadium Redox Flow Batteries," *J. Electrochem. Soc.* , vol. 160, no. 4, pp. A697–A702, Jan. 2013, doi: 10.1149/2.004306jes.

[24] X. Luo *et al.*, "Influences of Permeation of Vanadium Ions through PVDF-g-PSSA Membranes on Performances of Vanadium Redox Flow Batteries," *J. Phys. Chem. B*, vol. 109, no. 43, pp. 20310–20314, Nov. 2005, doi: 10.1021/jp054092w.

[25] Florida Solar Energy Center, "Procedure for Performing PEM Single Cell Testing," *Work Performed Under DOE Contract # DE-FC36-06GO16028*, p. 11, 2009, online: https://pt.scribd.com/document/181739885/Procedures-For-Performing-PEM-Single-Cell-Testing.

[26] K. R. Cooper, "In situ pem fuel cell fuel: Fuel crossover and electrical short circuit measurement," *Fuel Cell Magazine*, vol. 8, pp. 34–35, Aug. 2008, online:

https://dokumen.tips/documents/in-situ-pemfc-fuel-crossover-electrical-short-circuit-measurement.html.

[27] M. Inaba, T. Kinumoto, M. Kiriake, R. Umebayashi, A. Tasaka, and Z. Ogumi, "Gas crossover and membrane degradation in polymer electrolyte fuel cells," *Electrochim. Acta*, vol. 51, no. 26, pp. 5746–5753, 2006, doi: https://doi.org/10.1016/j.electacta.2006.03.008.

[28] R. Monteiro, J. Leirós, M. Boaventura, and A. Mendes, "Insights into all-vanadium redox flow battery: A case study on components and operational conditions," *Electrochim. Acta*, vol. 267, pp. 80–93, 2018, doi: https://doi.org/10.1016/j.electacta.2018.02.054.

[29] H. A.-Z. Al-Fetlawi, "The Electrolyte Monitoring of a Vanadium Redox Flow Battery," *ECS Trans.* , vol. 58, no. 36, pp. 33–48, Apr. 2014, doi: 10.1149/05836.0033ecst.

[30] B. Bensmann, R. Hanke-Rauschenbach, and K. Sundmacher, "In-situ measurement of hydrogen crossover in polymer electrolyte membrane water electrolysis," *Int. J. Hydrogen Energy*, vol. 39, no. 1, pp. 49–53, Jan. 2014, doi: 10.1016/j.ijhydene.2013.10.085.

[31] X. Cheng *et al.*, "Hydrogen crossover in high-temperature PEM fuel cells," *J. Power Sources*, vol. 167, no. 1, pp. 25–31, May 2007, doi: 10.1016/j.jpowsour.2007.02.027.

[32] P. A. Boettcher, E. Agar, C. R. Dennison, and E. C. Kumbur, "Modeling of Ion Crossover in Vanadium Redox Flow Batteries: A Computationally-Efficient Lumped Parameter Approach for Extended Cycling," *J. Electrochem. Soc.* , vol. 163, no. 1, pp. A5244–A5252, Jan. 2016, doi: 10.1149/2.0311601jes.

[33] F. G. Donnan and E. A. Guggenheim, "Die genaue thermodynamik der membrangleichgewichte," *Zeitschrift für Phys. Chemie*, vol. 162, no. 1, pp. 346–360, 1932, doi: 10.1515/zpch-1932-16225.

[34] B. Bauer *et al.*, "Anion-exchange membranes with improved alkaline stability," *Desalination*, vol. 79, no. 2-3, pp. 125–144, 1990, doi: 10.1016/0011-9164(90)85002-r.

[35] A. Tang, J. Bao, and M. Skyllas-Kazacos, "Dynamic modelling of the effects of ion diffusion and side reactions on the capacity loss for vanadium redox flow battery," *J. Power Sources*, vol. 196, no. 24, pp. 10737–10747, Dec. 2011, doi: 10.1016/j.jpowsour.2011.09.003.

[36] M. Skyllas-Kazacos and L. Goh, "Modeling of vanadium ion diffusion across the ion exchange membrane in the vanadium redox battery," *J. Memb. Sci.*, vol. 399–400, pp. 43–48, 2012, doi: 10.1016/j.memsci.2012.01.024.

[37] T. Mohammadi, S. C. Chieng, and M. Skyllas Kazacos, "Water transport study across commercial ion exchange membranes in the vanadium redox flow battery," *J. Memb. Sci.*, vol. 133, no. 2, pp. 151–159, 1997, doi: 10.1016/s0376-7388(97)00092-6.

SUPPLEMENTARY INFORMATION

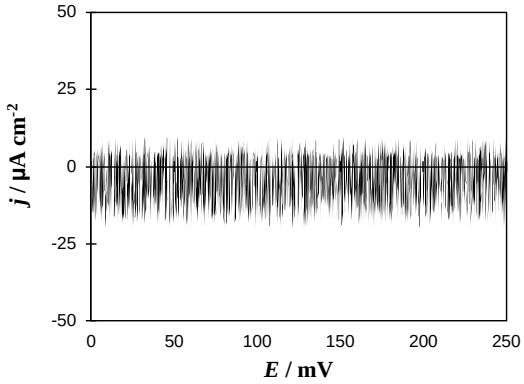


Figure S1. Effect of blank electrolyte on current during LSV measurements. The voltammogram was obtained at 75 µV s^{-1} and the potential was swept from the OCP to 250 mV.

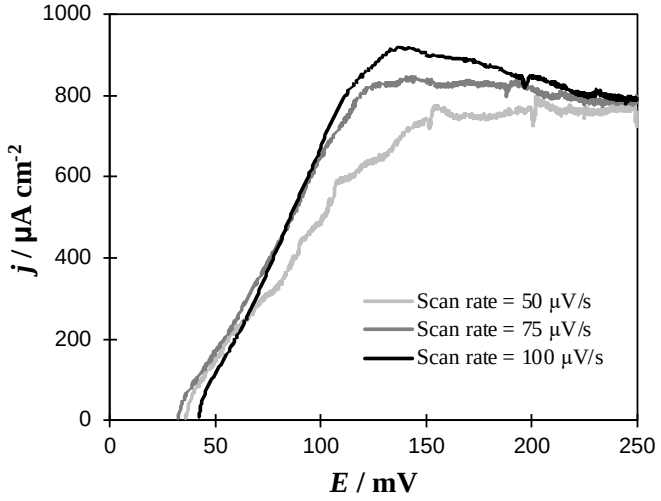


Figure S2. Effect of scan rate on voltammogram response. The voltammograms were obtained at different scan rates (see legend) and the potential was swept from the OCP to 250 mV.

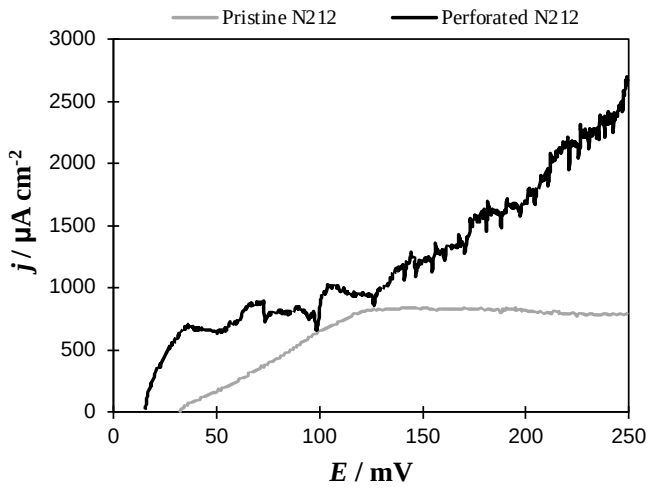


Figure S3. Comparison between the current response of pristine and perforated Nafion 212 membranes. The voltammograms were obtained at 75 µV s^{-1} and the potential was swept from the OCP to 250 mV.

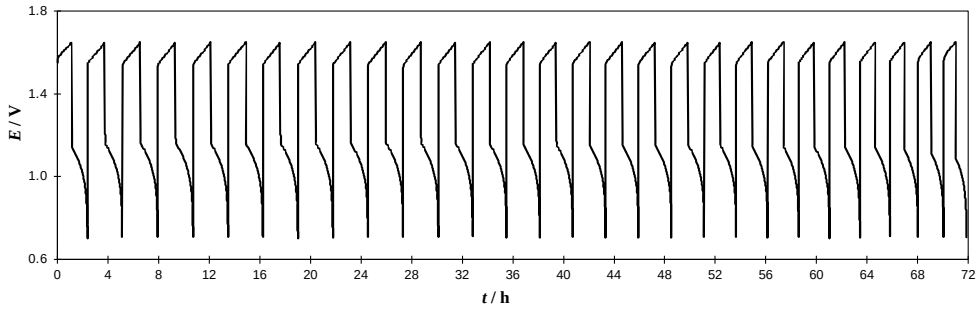


Figure S4. Charge-discharge cycling for membrane degradation, performed at 80 mA cm^{-2}, with the upper and lower potential limits set to 1.65 and 0.7 V, respectively. The cell was subjected to 28 charge-discharge cycles.

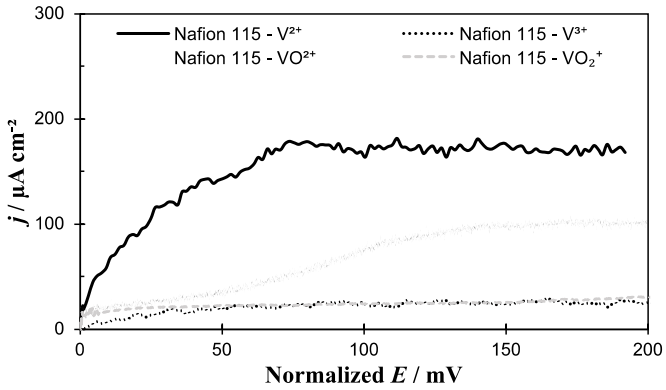


Figure S5. Comparison between the current response of all oxidation states of vanadium for Nafion 115 membrane. The voltammograms were obtained at 75 µV s^{-1} and the potential was swept from the OCP to 250 mV.

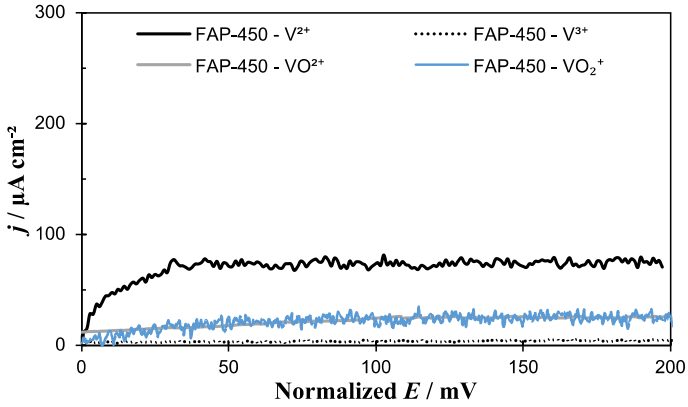


Figure S6. Comparison between the current response of all oxidation states of vanadium for FAP 450 membrane. The voltammograms were obtained at 75 µV s^{-1} and the potential was swept from the OCP to 250 mV.

CHAPTER 7

GENERAL CONCLUSIONS AND OUTLOOK

7

GENERAL CONCLUSIONS AND OUTLOOK

The present work studies electrochemical technologies that will play important roles in the upcoming energy transition. From a more general point of view, it becomes clear that these electrochemical technologies must be seen as complementary instead of competitors because all of them have advantages and disadvantages depending on the type of application. In the course of this work, structural, morphological, and electrochemical characterization of single cells or rotating disk electrode, namely polarization curves (*j*-*V*), accelerated stress tests, cyclic voltammetry, and electrochemical impedance spectroscopy (EIS), were performed to support the development of new cell components.

The development of MEAs for PEM electrolysis presented in Chapter 2 was carried out in collaboration with the German Aerospace Center (DLR) in Stuttgart, Germany. In 2017, this work was among the first ones on the fabrication of MEAs for PEM electrolysers with iridium loadings below 0.4 mg cm^{-2}. Iridium-based anodes were deposited directly on a Nafion membrane through cheap and easily scalable screen-printing technique. Ethane-1,2-diol, propane-1,2-diol and cyclohexanol were used as ink solvents to disperse a mixture of Ir particles, Ti_4O_7 as corrosion-resistant support and Nafion ionomer. The MEA fabricated with cyclohexanol produced 50 % more current density per mass of iridium (@ 1.7 V and 40 °C) than the commercial reference – E300 (Greenerity). The electrochemical performance of the developed MEAs is directly correlated with the type of solvent used in the catalytic inks and its ability to disperse the catalytic particles within the ionomer. The high relative permittivity of three solvents used in this study ensured a good dispersion of the ionomer, but cyclohexanol (with the lowest relative permittivity of the three) originated the highest electrochemically active surface area (ECSA); the observed highest ECSA is related to the ionomer forming colloids nearby the iridium sites. The correlation between the relative permittivity of the solvent and the performance of the electrolyser was realized during operation at constant power supply, but later confirmed by EIS measurements;

the impedance ascribed to oxygen evolution reaction increased with the solvent relative permittivity. Ethane-1,2-diol, with the highest permittivity value generated a MEA with the lowest performance due to a poorer catalyst/ionomer dispersion. This work is pivotal because it began the fabrication of MEAs for PEM electrolysers and also fuel cells at DLR and at the University of Porto. The two technologies share many similarities in terms of design and properties of cell components and some fabrication techniques can be adapted to bring new developments.

The work described in Chapter 3 was carried out under the framework of EU project FluidCELL. This project aimed at building a methanol steam reformer to produce hydrogen, to be later converted into electricity in a 30 kW PEMFC stack. Hydrogen produced by this process typically contains small amounts of contaminants, being CO and H_2S the most problematic ones. Carbon monoxide, for instance, is known to poison the anodic platinum catalyst; several mitigation strategies had been proposed and assessed with limited success. This thesis implemented air-bleeding strategies to mitigate the effects caused by the presence of carbon monoxide (5 – 30 ppm) in the hydrogen feed stream. The blending of small oxygen traces (1 – 3 vol.%) at the anode was found to eliminate detrimental effects of the carbon monoxide, allowing the cell to perform similarly as when pure hydrogen is fed. In the presence of oxygen, carbon monoxide oxidizes, and the resulting carbon dioxide does not harm the anode catalyst. But, due to safety reasons, only small amounts of oxygen (less than 4 %) can be directly mixed with hydrogen (external bleeding). It was then assessed the possibility to supply oxygen to the anode side, making it to permeate the membrane from the cathode side (internal bleeding). This can be achieved increasing the cathodic pressure, within the mechanical stability of membrane. The internal bleeding of oxygen is more effective in cells loaded with thinner membranes. The use of reinforced thin membranes is a proved strategy to lower the ohmic losses of a fuel cell; however, the oxygen internal bleeding strategies become more challenging due the lower membrane porosity when compared to the non-reinforced ones. This work demonstrates that combining air bleeding strategies and the introduction of ruthenium in platinum-based anode catalyst, can suppress the losses of efficiency caused by the presence carbon monoxide in hydrogen feed. Solely 1 % of air bleed to a 10 ppm CO contaminated hydrogen stream, the full performance recovery is achieved without compromising the steadiness of the cell. This approach avoids the need of using high platinum loadings at

the anode to keep its performance in the presence of small traces of carbon monoxide. In the future other sources of oxygen like H_2O_2 mixed with water vapor can also directly oxidize CO to CO_2 and mitigate catalyst poisoning. Alternatively, short exposure to OCV pulses can have a similar effect due to higher oxygen concentrations at the cathode that promote oxygen crossover to the anode.

Typical PEMFC electrocatalysts are supported on carbon particles, normally carbon black. However, long-term stability of carbon supports is insufficient mainly for automotive PEMFC applications. Support corrosion, loss of porosity or increased water affinity – partial oxidation of the carbon supports with formation of functional oxygen groups – under typical automotive loads, are common in cathodes with very low catalyst loadings. Several strategies have been considered for the development of more stable electrocatalysts and some progresses have been achieved with more complex carbon allotropes such as nanotubes, nanorods or graphene. During project PEMFC-SUDOE, the development of electrocatalysts of platinum supported on graphene was found as a promising strategy to address the insufficient stability of the state-of-the-art carbon supports. The platinum precursor content during the synthesis of the electrocatalysts was varied to obtain the optimum platinum loading on graphene; the platinum precursor was reduced using the conventional polyol method. Higher platinum loadings on graphene resulted in larger but more crystalline platinum particles. The optimum value was found to be 30 wt.% since it led to higher ORR activity and the best Pt dispersion over the surface of graphene sheets. The stability of Pt/graphene electrocatalysts was assessed based on the ECSA and on ORR activity after an accelerated aging test comprehending 10 000 potential cycles. Despite the higher ECSA, during the aging test, the Pt/graphene catalyst lost two times more ORR activity than catalyst supported on carbon black synthesized by the same method. The morphology of two-dimensional graphene sheets displays mass transport limitations. This phenomenon is known as starvation, and it accelerates the platinum sintering or detachment from the support. Finally, the two supported electrocatalysts were mixed with different proportions to avoid graphene restacking with spherical carbon particles acting as spacers. Remarkably, the hybrid catalyst was found to be the most stable catalyst among all, with the lowest losses of ECSA (14 %) and of ORR mass activity (28 %) after an accelerated stress protocol. For the future other structures and surface

modification prior to the nucleation of Pt nanoparticles should be exploited, benefiting from the knowledge gathered in this work.

Chapter 4 revisits the use of Pt/G electrocatalysts. A commercial Pt/G electrocatalyst – Premetek – was subjected to three different accelerated stress test protocols and fully compared with a standard commercial reference (Pt/C – Johnson Matthey.) using the rotating disk electrode method. Two aging protocols were considered, with thousands of potential cycles applied below or above 1 V *vs* RHE. The third protocol considered long-term exposure to open circuit potential. All of them trigger similar degradation mechanisms but with different intensities. These mechanisms are typically associated to sintering or coalescence of platinum nanoparticles, carbon support corrosion, ionomer decomposition or a combination of all. Surprisingly, the Pt/G electrocatalyst largely outperformed Pt/C in almost all criteria when both were subjected to the three degradation protocols. The superior ORR stability of Pt/G was consequence of the higher corrosion resistance of graphene, ensuring a more stable anchoring of the Pt particles and then more stable towards sintering or detachment. Apart, from the electrochemical measurements, TEM images obtained before and after the degradation protocols allowed to make a precise estimation of the average Pt particle size, which was correlated with the degradation mechanisms that are dominant. In the future, this promising Pt/G catalyst needs to be used to fabricate MEAs and to be tested in single cell configuration, to assess if mass transport limitations arise under conditions that are closer to real fuel cell operation.

While most scientific research has been done on the development of new materials, new and practical diagnosis tools are always important to assist on the development of any technology. After getting inspired from a common procedure to estimate the gas crossover through the proton exchange membrane in fuel cells, Chapter 5 describes a novel adaption of this technique to measure the crossover of vanadium species in redox flow batteries (RFBs). Up to now, this is the only technique that allows *in-situ* determination of crossover of species in redox flow batteries without the use of an external analytic equipment. This new technique allowed to estimate the crossover of V^{2+}, V^{3+}, V^{4+} and V^{5+} through the membrane from a voltammetry scan at a very low scan rate (1 – 3 mV s^{-1}). Under these conditions, the current response remains constant along the potential, and it is directly proportional to the direct crossover of vanadium ions through the membrane. To provide a glance on how this technique can benefit the

field of redox flow batteries, vanadium crossover was estimated for membranes of different thicknesses; a good inverted linear fitting was obtained. Moreover, the technique was assessed for both cation and anion exchange membranes with equally good results. This technique demonstrated to be a powerful tool not only to help on the development of new membranes for RFBs but also for membrane failure diagnosis, both in single cell and in a stack.

ANNEX 2

CO-AUTHORS AUTHORIZATION REGARDING THE FULL AGREEMENT OF THE INCLUSION OF THE MANUSCRIPTS IN THE PRESENT THESIS

To Whom it May Concern

Adélio Mendes, Professor at the Faculty of Engineering of the University of Porto (FEUP), Rémi Costa, Researcher at the German Aerospace Center (DLR), Aldo Gago, Researcher at DLR, Daniel Sanchez, Researcher at DLR, Feng Han, Researcher at DLR and Tobias Morawietz, Researcher at the University of Applied Sciences hereby authorize the PhD candidate Tiago Lagarteira to include the following publication in his doctoral Thesis entitled "Electrochemical Technologies for Renewable Energy Storage".

Highly active screen-printed Ir/Ti_4O_7 anodes for proton exchange membrane electrolyzers, International Journal of Hydrogen Energy, Volume 43, Issue 35, 2018, Pages 16824-16833, ISSN 0360-3199, https://doi.org/10.1016/j.ijhydene.2018.02.179.

(Authors: Tiago Lagarteira, Feng Han, Tobias Morawietz, Renate Hiesgen, Daniel Garcia Sanchez, Adélio Mendes, Aldo Gago, Rémi Costa)

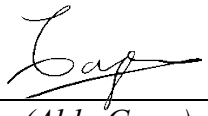
Signatures

(Adélio Mendes)

Assinado por: **ADÉLIO MIGUEL MAGALHÃES MENDES**
Num. de Identificação: 06557712
Data: 2023.03.28 13:21:46 +0100



(Rémi Costa)



(Aldo Gago)

Daniel Garcia-sanchez

Digital signiert von Daniel Garcia-sanchez
DN: CN=Daniel Garcia-sanchez, E=daniel.garciasanchez@dlr.de
Grund: Ich bin der Verfasser dieses Dokuments
Ort:
Datum: 2023.02.28 15:25:25+01'00'
Foxit PDF Reader Version: 12.1.0

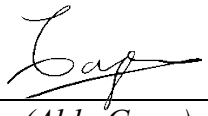
(Daniel Sanchez)



(Tobias Morawietz)



(Feng Han)



(Aldo Gago)

Daniel Garcia-sanchez

Digital signiert von Daniel Garcia-sanchez
DN: CN=Daniel Garcia-sanchez, E=daniel.garciasanchez@dlr.de
Grund: Ich bin der Verfasser dieses Dokuments
Ort:
Datum: 2023.02.28 15:25:25+01'00'
Foxit PDF Reader Version: 12.1.0

(Daniel Sanchez)



(Tobias Morawietz)



(Feng Han)

To Whom it May Concern

Adélio Mendes, Professor at the Faculty of Engineering of the University of Porto (FEUP), and Sofia Delgado, PhD student at FEUP, hereby authorize the PhD candidate Tiago Lagarteira to include the following publication in his doctoral Thesis entitled "Electrochemical Technologies for Renewable Energy Storage".

Air Bleeding Strategies to Increase the Efficiency of Proton Exchange Membrane Fuel Cell Stationary Applications Fuelled with CO ppm-levels, International Journal of Electrochemical Science, Volume 15, 2020, Pages 613-627, doi: 10.20964/2020.01.58.

(Authors: S. Delgado, T. Lagarteira, A. Mendes)

Assinado por: ADÉLIO MIGUEL MAGALHÃES MENDES
Num. de Identificação: 06557712
Data: 2023.03.28 13:22:01 +0100

Signatures

(Adélio Mendes)

(Sofia Delgado)

To Whom it May Concern

Adélio Mendes, Professor at the Faculty of Engineering of the University of Porto (FEUP), Cecilia Mateos-Pedrero, Researcher at the Collaborative Laboratory for Biorefineries CoLab (BIOREF), Cátia Azenha, Researcher at FEUP, Celina Fernandes, PhD student at FEUP and Sofia Delgado, PhD student at FEUP, hereby authorize the PhD candidate Tiago Lagarteira to include the following publication in his doctoral Thesis entitled "Electrochemical Technologies for Renewable Energy Storage".

The role of Pt loading on reduced graphene oxide support in the polyol synthesis of catalysts for oxygen reduction reaction, International Journal of Hydrogen Energy, Volume 45, Issue 40, 2020, Pages 20594-20604, ISSN 0360-3199, https://doi.org/10.1016/j.ijhydene.2020.02.022.

(Authors: Tiago Lagarteira, Sofia Delgado, Celina Fernandes, Cátia Azenha, Cecilia Mateos-Pedrero, Adélio Mendes)

Signatures

Assinado por: **ADÉLIO MIGUEL MAGALHÃES MENDES**
Num. de Identificação: 06557712
Data: 2023.03.28 13:22:31 +0100

(Adélio Mendes)

(Cecilia Mateos-Pedrero)

Assinado por: **CÁTIA SOFIA RIBEIRO AZENHA**
Num. de Identificação: 13541954
Data: 2023.03.31 09:04:19+01'00'

(Cátia Azenha)

(Celina Fernandes)

Sofia Delgado

(Sofia Delgado)

To Whom it May Concern

Adélio Mendes, Full Professor at the Faculty of Engineering of the University of Porto (FEUP), Alfredo Ortiz, Professor at University of Cantabria (UC), Gema Pérez, Researcher at UC and Sofia Delgado, PhD student at FEUP, hereby authorize the PhD candidate Tiago Lagarteira to include the following publication in his doctoral Thesis entitled "Electrochemical Technologies for Renewable Energy Storage".

Oxygen reduction stability of graphene-supported electrocatalyst and degradation mechanisms, under revision at the International Journal of Hydrogen Energy.
(Authors: Tiago Lagarteira, Sofia Delgado, Gema Garcia, Alfredo Ortiz, Adélio Mendes)

Signatures

Assinado por: ADÉLIO MIGUEL MAGALHÃES MENDES
Num. de Identificação: 06557712
Data: 2023.03.28 13:22:16 +0100

(Adélio Mendes)

ORTIZ SAINZ DE AJA ALFREDO - 72092683B
Firmado digitalmente por ORTIZ SAINZ DE AJA ALFREDO - 72092683B
Fecha: 2023.02.28 04:07:07 +01'00'

(Alfredo Ortiz)

PEREZ GARCIA GEMA - 72139121N
Firmado digitalmente por PEREZ GARCIA GEMA - 72139121N
Fecha: 2023.02.28 07:55:23 +01'00'

(Gema Pérez)

Sofia Delgado

(Sofia Delgado)

To Whom it May Concern

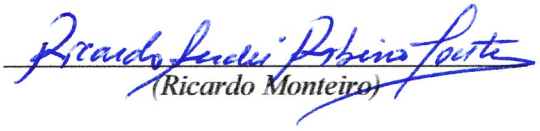
Adélio Mendes, Professor at the Faculty of Engineering of the University of Porto (FEUP), Ricado Monteiro, Researcher at Visblue, Anders Bentien, Professor at Aarhus University, Carlos Almeida, PhD student at FEUP and Pedro Pacheco, PhD student at Advanced Cyclone Systems (ACS) and FEUP, hereby authorize the PhD candidate Tiago Lagarteira to include the following publication in his doctoral Thesis entitled "Electrochemical Technologies for Renewable Energy Storage".

In-Situ Measurement of Vanadium Crossover for the Vanadium Redox Flow Battery, Journal of The Electrochemical Society, Volume 166, Issue 16, 2019, https://dx.doi.org/10.1149/2.0331916jes.
(Authors: Tiago Lagarteira, Pedro Pacheco, Carlos Almeida, Anders Bentien, Ricardo Monteiro, Adélio Mendes)

Signatures

(Adélio Mendes)

Assinado por: **ADÉLIO MIGUEL MAGALHÃES MENDES**
Num. de Identificação: 06557712
Data: 2023.03.28 13:21:04 +0100



(Ricardo Monteiro)



(Anders Bentien)

Assinado por: **Carlos Miguel Ferreira de Almeida**
Num. de Identificação: 13674023
Data: 2023.04.11 21:43:07+01'00'

(Carlos Almeida)

CHAVE MÓVEL



(Pedro Pacheco)

To Whom it May Concern

Adélio Mendes, Professor at the Faculty of Engineering of the University of Porto (FEUP), Rémi Costa, Researcher at the German Aerospace Center (DLR), Aldo Gago, Researcher at DLR, Daniel Sanchez, Researcher at DLR, Feng Han, Researcher at DLR and Tobias Morawietz, Researcher at the University of Applied Sciences hereby authorize the PhD candidate Tiago Lagarteira to include the following publication in his doctoral Thesis entitled "Electrochemical Technologies for Renewable Energy Storage".

Highly active screen-printed Ir/Ti_4O_7 anodes for proton exchange membrane electrolyzers, International Journal of Hydrogen Energy, Volume 43, Issue 35,2018, Pages 16824-16833, ISSN 0360-3199, https://doi.org/10.1016/j.ijhydene.2018.02.179.

(Authors: Tiago Lagarteira, Feng Han, Tobias Morawietz, Renate Hiesgen, Daniel Garcia Sanchez, Adélio Mendes, Aldo Gago, Rémi Costa)

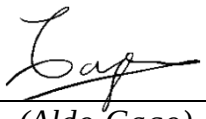
Signatures

(Adélio Mendes)

Assinado por: ADÉLIO MIGUEL MAGALHÃES MENDES
Num. de Identificação: 06557712
Data: 2023.03.28 13:21:46 +0100



(Rémi Costa)



(Aldo Gago)

Daniel Garcia-sanchez

Digital signiert von Daniel Garcia-sanchez
DN: CN=Daniel Garcia-sanchez, E=daniel.garciasanchez@dlr.de
Grund: Ich bin der Verfasser dieses Dokuments
Ort:
Datum: 2023.02.28 15:25:25+01'00'
Foxit PDF Reader Version: 12.1.0

(Daniel Sanchez)



(Tobias Morawietz)



(Feng Han)

To Whom it May Concern

Adélio Mendes, Professor at the Faculty of Engineering of the University of Porto (FEUP), and Sofia Delgado, PhD student at FEUP, hereby authorize the PhD candidate Tiago Lagarteira to include the following publication in his doctoral Thesis entitled "Electrochemical Technologies for Renewable Energy Storage".

Air Bleeding Strategies to Increase the Efficiency of Proton Exchange Membrane Fuel Cell Stationary Applications Fuelled with CO ppm-levels, International Journal of Electrochemical Science, Volume 15, 2020, Pages 613-627, doi: 10.20964/2020.01.58.

(Authors: S. Delgado, T. Lagarteira, A. Mendes)

Assinado por: **ADÉLIO MIGUEL MAGALHÃES MENDES**
Num. de Identificação: 06557712
Data: 2023.03.28 13:22:01 +0100

Signatures

(Adélio Mendes)

(Sofia Delgado)

U.PORTO FEUP FACULDADE DE ENGENHARIA UNIVERSIDADE DO PORTO — Lepabe Laboratory for Process Engineering, Environment, Biotechnology and Energy — ALiCE ASSOCIATE LABORATORY IN CHEMICAL ENGINEERING

To Whom it May Concern

Adélio Mendes, Professor at the Faculty of Engineering of the University of Porto (FEUP), Cecilia Mateos-Pedrero, Researcher at the Collaborative Laboratory for Biorefineries CoLab (BIOREF), Cátia Azenha, Researcher at FEUP, Celina Fernandes, PhD student at FEUP and Sofia Delgado, PhD student at FEUP, hereby authorize the PhD candidate Tiago Lagarteira to include the following publication in his doctoral Thesis entitled "Electrochemical Technologies for Renewable Energy Storage".

The role of Pt loading on reduced graphene oxide support in the polyol synthesis of catalysts for oxygen reduction reaction, International Journal of Hydrogen Energy, Volume 45, Issue 40, 2020, Pages 20594-20604, ISSN 0360-3199, https://doi.org/10.1016/j.ijhydene.2020.02.022.

(Authors: Tiago Lagarteira, Sofia Delgado, Celina Fernandes, Cátia Azenha, Cecilia Mateos-Pedrero, Adélio Mendes)

Assinado por: ADÉLIO MIGUEL MAGALHÃES MENDES
Num. de Identificação: 06557712 Data: 2023.03.28 13:22:31 +0100

Signatures

Assinado por: ADÉLIO MIGUEL MAGALHÃES MENDES
Num. de Identificação: 06557712
Data: 2023.03.28 13:22:31 +0100

(Adélio Mendes)

(Cecilia Mateos-Pedrero)

Assinado por: CÁTIA SOFIA RIBEIRO AZENHA
Num. de Identificação: 13541954
Data: 2023.03.31 09:04:19+01'00'

(Cátia Azenha)

(Celina Fernandes)

(Sofia Delgado)

To Whom it May Concern

Adélio Mendes, Full Professor at the Faculty of Engineering of the University of Porto (FEUP), Alfredo Ortiz, Professor at University of Cantabria (UC), Gema Pérez, Researcher at UC and Sofia Delgado, PhD student at FEUP, hereby authorize the PhD candidate Tiago Lagarteira to include the following publication in his doctoral Thesis entitled "Electrochemical Technologies for Renewable Energy Storage".

Oxygen reduction stability of graphene-supported electrocatalyst and degradation mechanisms, under revision at the International Journal of Hydrogen Energy. (Authors: Tiago Lagarteira, Sofia Delgado, Gema Garcia, Alfredo Ortiz, Adélio Mendes)

Signatures

Assinado por: ADÉLIO MIGUEL MAGALHÃES MENDES
Num. de Identificação: 06557712

Data: 2023.03.28 13:22:16 +0100

(Adélio Mendes)

ORTIZ SAINZ DE AJA ALFREDO - 72092683B
Firmado digitalmente por ORTIZ SAINZ DE AJA ALFREDO - 72092683B
Fecha: 2023.02.28 04:07:07 +01'00'

(Alfredo Ortiz)

PEREZ GARCIA GEMA -72139121N
Firmado digitalmente por PEREZ GARCIA GEMA - 72139121N
Fecha: 2023.02.28 07:55:23 +01'00'

(Gema Pérez)

Sofia Delgado

(Sofia Delgado)

To Whom it May Concern

Adélio Mendes, Professor at the Faculty of Engineering of the University of Porto (FEUP), Ricado Monteiro, Researcher at Visblue, Anders Bentien, Professor at Aarhus University, Carlos Almeida, PhD student at FEUP and Pedro Pacheco, PhD student at Advanced Cyclone Systems (ACS) and FEUP, hereby authorize the PhD candidate Tiago Lagarteira to include the following publication in his doctoral Thesis entitled "Electrochemical Technologies for Renewable Energy Storage".

In-Situ Measurement of Vanadium Crossover for the Vanadium Redox Flow Battery, Journal of The Electrochemical Society, Volume 166, Issue 16, 2019, https://dx.doi.org/10.1149/2.0331916jes.

(Authors: Tiago Lagarteira, Pedro Pacheco, Carlos Almeida, Anders Bentien, Ricardo Monteiro, Adélio Mendes)

Signatures

(Adélio Mendes)

Assinado por: **ADÉLIO MIGUEL MAGALHÃES MENDES**
Num. de Identificação: 06557712
Data: 2023.03.28 13:21:04 +0100



(Ricardo Monteiro)



(Anders Bentien)

Assinado por: **Carlos Miguel Ferreira de Almeida**
Num. de Identificação: 13674023
Data: 2023.04.11 21:43:07+01'00'

(Carlos Almeida)

CHAVE MÓVEL

Pedro Teixeira Pacheco

(Pedro Pacheco)

ANNEX 2

PUBLISHED ARTICLES

INTERNATIONAL JOURNAL OF HYDROGEN ENERGY 43 (2018) 16824–16833

Available online at www.sciencedirect.com

ScienceDirect

journal homepage: www.elsevier.com/locate/he

Highly active screen-printed Ir–Ti_4O_7 anodes for proton exchange membrane electrolyzers

Tiago Lagarteira [a,b], *Feng Han* [a,**], *Tobias Morawietz* [c], *Renate Hiesgen* [c], *Daniel Garcia Sanchez* [a], *Adélio Mendes* [b], *Aldo Gago* [a,***], *Rémi Costa* [a,*]

[a] *Institute of Engineering Thermodynamics, German Aerospace Center, Pfaffenwaldring 38-40, Stuttgart, Germany*
[b] *Laboratory for Process Engineering, Environmental, Biotechnology and Energy (LEPABE), Faculty of Engineering of University of Porto, Rua Roberto Frias s/n, 4200-465 Porto, Portugal*
[c] *University of Applied Sciences Esslingen, Dep. of Basic Science, Kanalstrasse 33, Esslingen, Germany*

ARTICLE INFO

Article history:
Received 16 August 2017
Received in revised form
19 February 2018
Accepted 27 February 2018
Available online 22 March 2018

Keywords:
Proton exchange membrane water electrolysis
Membrane electrodes assembly
Catalyst coated membrane
Iridium loading
Ceramic support
Screen printing

ABSTRACT

Electroceramic support materials can help reducing the noble-metal loading of iridium in the membrane electrodes assembly (MEA) of proton exchange membrane (PEM) electrolyzers. Highly active anodes containing Ir-black catalyst and submicronic Ti_4O_7 are manufactured through screen printing technique. Several vehicle solvents, including ethane-1,2-diol; propane-1,2-diol and cyclohexanol are investigated. Suitable functional anodic layer with iridium loading as low as 0.4 mg cm^{-2} is obtained. Surface properties of the deposited layers are investigated by atomic force microscopy (AFM). The most homogeneous coating with the highest electronic conductivity is obtained using cyclohexanol. Tests in PEM electrolyzer operating at 1.7 V and 40 °C demonstrate that the CCM with anode coated with cyclohexanol presents a 1.5-fold higher Ir-mass activity than that of the commercial CCM.

© 2018 Hydrogen Energy Publications LLC. Published by Elsevier Ltd. All rights reserved.

Introduction

Intermittency and fluctuation of renewable energy sources remain major issues for an efficient utilization, while the power flow and utility frequency of the grid need to be steadily regulated and balanced. Hydrogen can be produced through water electrolysis with the surplus from renewables when available and stored as a carbon neutral energy carrier. Proton exchange membrane (PEM) water electrolysis is a promising technology for coupling renewables with hydrogen due to the wide operating range and the fast response [1–3]. In particular, the compact system design, high efficiency and easy maintenance are advantageous features comparing to the mature alkaline electrolysis technology [1,4,5]. Yet, the penetration of PEM electrolyzer systems at the megawatt scale will be hindered by the high cost and scarcity of catalyst materials, together with the manufacturing of the membrane electrodes

* *Corresponding author.*
** *Corresponding author.*
*** *Corresponding author.*
E-mail addresses: feng.han@dlr.de (F. Han), aldo.gago@dlr.de (A. Gago), remi.costa@dlr.de (R. Costa).
https://doi.org/10.1016/j.ijhydene.2018.02.179
0360-3199/© 2018 Hydrogen Energy Publications LLC. Published by Elsevier Ltd. All rights reserved.

assembly (MEA), which currently represent approximately 20% of the overall costs of the PEM electrolyzer stack [6]. Therefore, there is a potential for cost reduction by decreasing the used amount of precious group metals (PGM) and optimizing the catalyst coating process in the production of MEAs.

A reduction in the catalyst loadings is not only important due to high price of the precious metals but also the scarcity of platinum and mainly iridium [7]. Despite some recent advances that took several years of research [8,9], the state-of-the-art anode still demands high iridium loadings of *ca.* 2–4 mg cm^{-2} [10,11], to balance the sluggish kinetics and the high charge transfer overpotential caused by the oxygen evolution reaction (OER). Ceramic supports like Magnéli-phase titanium sub-oxides (TiO_2, Ti_4O_7 and Ti_5O_9) are promising catalyst supports, providing a higher catalytic stability and resistance to corrosion in the harsh environment of the electrolyzer anode in comparison to the typical carbon-based supports used in PEM fuel cells [12–20].

For the manufacturing, screen printing is a widespread and common cost-efficient printing technique that can be used to produce catalyst coated membranes (CCM-MEA), where the catalysts are directly deposited on a proton exchange membrane – typically Nafion. Some reports on the fabrication of MEAs for PEM fuel cells with screen printing are available. But in most of them, the catalyst deposition is carried out on the gas diffusion layer (GDL) or on PTFE sheets with posterior decal transfer to the membrane. This is the usual strategy to avoid typical processing issues like membrane swelling when it contacts with organic solvents [21–24]. The overcome of the swelling issue is a key challenge as direct catalyst deposition on the membrane may provide better contact between the catalyst layer and the electrolyte thus reducing interfacial contact resistances. Kim and co-workers proposed a treatment [25] in which the membrane was exchanged from the H^+ form to Na^+ form before coating. The protonic reconversion was performed after the catalyst layer was deposited and dried. Nonetheless, no report is found in the literature of screen-printed catalyst layers directly on the membrane for PEM electrolyzers [11].

Composition of the catalyst ink affects not only the coating process itself - by governing the rheological properties - but also affects the microstructure of the coated layer. The properties of the catalyst ink should be optimized not only for the coating process but also for maximizing the connection of catalytic sites to both electronic and ionic conductive phases, thus ensuring the overall performance of the electrolyzer. The idea of using solubilized Nafion ionomer in catalyst inks or suspensions has been widely accepted for extending protonic vehicular conduction inside 3D-structures of the catalyst layers [26–28]. More recently, Chan and Eikerling reported that ionomer-free ultra-thin catalyst layers (20–500 nm thick) rely entirely on liquid water for proton conduction [29]. Therefore, a fully humidified catalyst layer would be beneficial, enabling proton conduction exclusively by the Grotthuss mechanism [30]. In the case of screen-printed catalyst layers, with thickness in the micrometer range, ionomer distribution and its orientation should be tuned for connecting the most active sites to the protonic conductive phase while not hindering electronic conductivity of the catalyst support and mass diffusion in the porous structure of the catalyst layer [31].

In this work, highly-active anodes with inexpensive catalyst support and low catalyst loading were fabricated via a cost-effective and scalable screen printing technique. Moreover, the properties of the developed layers were characterized and investigated through diagnostic tools such as TGA, AFM and electrochemical single cell tests.

Experimental

CCM fabrication

Screen printing of the anode

In the preparation of the screen printing inks, summarized in Table 1, 30 wt% Iridium Black (Umicore) was mixed with 70 wt % Ti_4O_7 catalyst support (Changsha Purong Chemical Engineering Inc.) using a mortar and a pestle. Ethane-1,2-diol (Sigma Aldrich), propane-1,2-diol (VWR) and cyclohexanol (VWR) were used as organic solvents for the inks (physicochemical properties shown in Table 2). The ratio between Nafion ionomer and the total solid particles was kept at 30 wt % [32]. The solvents from a 20 wt% Nafion solution (Sigma Aldrich) were evaporated during the mixing and, only then, the chosen organic solvent was added. The solid content in the screen printing inks was kept at 37.5 wt%, except for the ink used in the effectiveness assessment of the membrane swelling treatment which contained a lower (but not determined) weight ratio of solid particles.

Nafion 212 membrane was cut into squares with a size 7 cm × 7 cm and, after removing the protection foils and conditioning at ambient humidity, they were weighted. Subsequently, they were placed on a porous metal substrate, enabling the use of a vacuum positioning and fixing system during the coating process. An Aurel 900 screen printer equipped with a Koenen Typ-10 M6 mesh (4 cm^2 of open area) was used for coating the anodes of the CCMs. The printing pressure was set to 1.5 N cm^{-2} and the distance between the screen and the substrate was 0.8 mm.

After coating, the samples were dried firstly on the screen printing holder for 10 min under infrared radiation produced by an incandescent lamp (40 W, distance 10 cm) to remove most of the solvent, and then dried at 348 K for 30 min in a

Table 1 – Screen printing ink formulations; weight ratios based on the total weight of the ink.

Ink formulations	Catalyst (7.875 wt%)	Catalyst support (18.375 wt%)	Binder (11.25 wt%)	Solvent (62.5 wt%)
A	Ir black	Ti_4O_7	Nafion ionomer	Ethane-1,2-diol
B	Ir black	Ti_4O_7	Nafion ionomer	Propane-1,2-diol
C	Ir black	Ti_4O_7	Nafion ionomer	Cyclohexanol

Table 2 – Physical properties of organic solvents used in screen printing inks.

Solvent	Viscosity * 10^{-3} (Pa s) @ 298 K	Vapor pressure (Pa) @ 293 K	Relative permittivity (ε)	Boiling temperature (K @ 10^5 Pa)
Ethane-1,2-diol	16.13	8	37 @ 298 K	470.75
Propane-1,2-diol	42.00	17.3	32 @ 293 K	461.35
Cyclohexanol	54.60	133.3	15 @ 293 K	434.15

drying oven. After conditioning at ambient humidity, the one-side coated membranes were again weighted for catalyst loading calculation purposes. The iridium loading was calculated based on weight difference of the membranes before and after the anode coating, and confirmed by thermal gravimetric analysis (TGA).

Wet spraying of the cathode

Since the focus of this work was the anode processing, the cathode was deposited by the state-of-the-art and widely used wet spray coating method. Thus, the differences in performance could be only related to the screen printing parameters. This technique was selected for processing the platinum-based cathodes since it allows achieving high performances with good reproducibility [33–35]. The spraying suspension was prepared by mixing 60 wt% Pt/C (Johnson Matthey) with 50 vol% water in isopropanol, considering the solvents from a 5 wt% Nafion solution (Ion Power). First, HPLC purity grade water was added the catalyst powder to avoid nanoparticles ignition when in contact with low molecular alcohols. Nafion ionomer content was kept at 35 wt% relatively to the solids in the spraying suspension. The total solid content in the suspension was 0.8 wt%. A heated vacuum table at 378 K was used during the wet spray deposition to dry the suspension solvents and simultaneously avoiding membrane swelling. After the cathode was coated, the CCM was hot pressed at 1.75 MPa and 398 K for 5 min.

Membrane swelling treatment

A membrane treatment reported by Kim and co-workers [24,25,36] was used to avoid swelling of the Nafion membrane caused by ethane-1,2-diol. In short, the membrane was boiled in an aqueous solution of 0.25 M NaOH for 15 min. After exchanging from protonic to sodium ionic form, the membrane was washed and boiled in deionized water for 10 min before being screen-printed. Following, the membrane was coated, dried and hot pressed to produce the CCM. Finally, the CCM was boiled in an aqueous solution of H_2SO_4 (0.5 M) for 30 min for reprotonation. The CCM was then rinsed three times 1 min each in deionized water to remove any remaining acid traces before testing. The iridium loading of the two anodes used for assessing the effectiveness of the membrane swelling treatment were equal, however they were not calculated.

Thermal gravimetric analysis (TGA)

The anode-coated membrane with the ink using propane-1,2-diol as solvent was cut in circular samples of 5 mm in diameter for the TGA measurement. The analysis was performed using a thermal gravimetric analyzer (NETZSCH STA 449 C) and a DSC/TG pan Pt under air atmosphere, heated from 303 K to 1073 K at 5 K min^{-1}.

Atomic force microscopy (AFM)

The local properties of the surface were investigated by atomic force microscopy (AFM). For the AFM measurements performed with a Multimode 8 AFM (Bruker, Karlsruhe), a piece of the MEA was cut out of the center with a razorblade. The CCM sample was glued with conductive adhesive tape onto a steel disc with the anode facing to the top. The anode was additionally connected with silver paste to ensure a low electrical resistance. Platinum/iridium coated AFM tips (PPP-NCHPt), with a nominal spring constant of 42 N m^{-1}, were used in conductive tapping mode (PF-TUNA, Bruker). In PF-TUNA mode, a force distance curve is evaluated at every image point to reveal adhesion, stiffness and deformation. A built-in lock-in amplifier averaged the simultaneously measured current. Images with a length scale of 5 μm and 512 × 512 pixel were recorded at a scan rate of 0.5 Hz. The relative humidity during measurements was 30 ± 5%. Evaluation of the porosity was performed with the bearing analysis tool of the Bruker nanoscope analysis software. For each anode, three 25 μm^2 measurements were performed. For the porosity determination, the 25 μm^2-sized measurements were evaluated at 4 areas of 6.25 μm side length. For the conductive area evaluation, the threshold was set to 0.1 nA and the applied voltage was 2 V. The threshold for the adhesion force and deformation evaluation was derived by profile lines across high and low value areas. The adhesion force/deformation values determined by the turning points were used as threshold values, respectively.

Single cell measurements

The investigation of the dynamic response of the developed CCMs was performed on home-made single cell PEM electrolyzer test rig with an electrode area of 4 cm^2 [37]. The cell temperature was maintained at 313 K and it was fed with HPLC purity grade water. A potentiostat/galvanostat equipped with an electrochemical impedance spectroscopy (EIS) module (Zahner Instruments) was used to evaluate the performance of the electrolyzer in a single-cell configuration.

Ti-coated stainless steel bipolar plates by vacuum plasma spraying [38–40] without flow field were used for the cell assembly. At the anode side, a Ti mesh was put between the bipolar plate and a sintered porous titanium layer (PTL) current collector of *ca.* 1 mm thickness, >40% porosity coated with Pt-IrOx (Magneto Special Anodes B.V.). At the cathode side, three carbon papers (Toray paper 030) were used as gas diffusion layer (GDL) to prevent the destruction of the carbon

paper upon the pressure increase caused by the evolution of H_2. A protocol of measurements was defined using mild conditions for electrolyzer operation to avoid a possible fast degradation of the produced CCMs. The evolution of the current density was measured at 1.7 V in potentiostatic conditions. EIS was performed at 35 mA cm^{-2} to enable a stable recording using a small perturbation of 5 mV. The parameters of the EIS spectra were fitted with an equivalent circuit [41] with (RQ) elements, representing a parallel combination of resistance and pseudo-capacitance for each catalyst layer. The fitted parameters are displayed in Table 3. R_S corresponds to the HFR in which the major contribution is assigned to the electrolyte. R_1 and R_2 are associated to charge transfer resistances of HER and OER, respectively. The onset of mass diffusion effects was not included in the fittings. A previously activated commercial CCM (E300 from Greenerity), containing 2.25 mg cm^{-2} of iridium at the anode, 1.25 mg cm^{-2} of platinum at the cathode and Nafion 212 membrane, was also tested under the same cell configuration for comparison purposes.

Results and discussion

The role of solvents and membrane swelling treatment

Fig. 1 shows the anode-coated membranes, after being screen-printed and dried. The red circles point out the membrane swelling spots. The thickness of the anodes was *ca.* 13 μm. The ink using cyclohexanol was the only one that did not generate any visible membrane swelling. The ink using ethane-1,2-diol generated more membrane swelling when compared with the ink using propane-1,2-diol. After hot pressing, swelling spots (red circles) could not be seen in all CCMs. However, only the sample using cyclohexanol presented uniform coating which could guaranty homogeneous catalyst loading.

The generation of swelling is related to the affinity between hydroxyl groups of the solvents and sulfonated groups of Nafion. Cyclohexanol has just one hydroxyl group and a heavier closed carbon chain while propane-1,2-diol and ethane-1,2-diol have two hydroxyl groups. A heavier carbon chain decreases the polarity of the molecule thus decreasing its interaction with sulfonated groups of Nafion.

The membrane treatment procedure proposed by Kim et al. [25], proved to be effective for minimizing membrane swelling. Fig. 2a shows the chronoamperometries at 1.7 V of two CCMs with anode coated with ethane-1,2-diol as solvent of the screen printing ink. The replacement of protons by heavier Na^+ reduced the affinity between Nafion sulfonated groups and ethane-1,2-diol. A larger cation ($Na^+ > H^+$) not only limits the free space for sulfonated groups to move, but also disables those sites for hydrogen-type bonds with the solvent hydroxyl groups. The two curves display different starting points and slopes before steady-state behavior, but the

Table 3 – Parameters evaluated from EIS data fitting to equivalent circuit shown in Fig. 10 for the fabricated and commercial CCMs.

CCMs	R_S/Ω	R_1/Ω	Q_1/F	R_2/Ω	Q_2/F
With swelling treatment	49.4 m	31.97 m	432.8 μ	522.6 m	579 μ
Without swelling treatment	75.76 m	51.18 m	364.3 μ	617.8 m	289.5 μ
Ethane-1,2-diol	74.1 m	16.04 m	1.482 m	374 m	998.7 μ
Propane-1,2-diol	63.37 m	18.39 m	2.345 m	244.6 m	3.945 m
Cyclohexanol	73.51 m	8.41 m	4.26 m	214.2 m	4.77 m
E300	55.31 m	8.296 m	48.73 m	146.3 m	306 m

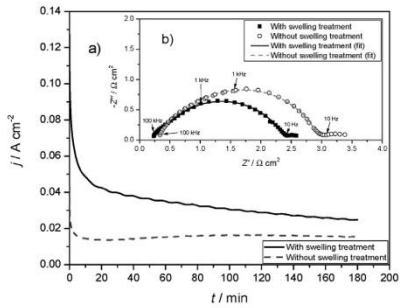


Fig. 2 – a) Chronoamperometries (at 1.7 V and 40 °C) of CCMs with and without swelling treatment. b) Impedance spectra (at 35 mA cm^{-2} and 40 °C) of CCMs with and without swelling treatment.

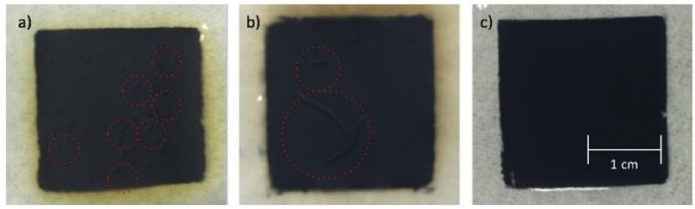


Fig. 1 – Images of the anodes, before hot press, coated using different solvents: a) ethane-1,2-diol; b) propane-1,2-diol; c) cyclohexanol.

electrochemical activity of both CCMs equalizes for longer times. At the end of tests, the swelling treated CCM slightly outperformed the CCM without treatment, indicating that the ionic form modification and posterior reprotonation does not hinder the electrochemical performance of the CCM.

Fig. 2b presents the impedance spectra (at 35 mA cm^{-2}) of CCMs subjected and not subjected to membrane treatment, recorded at the end of tests. The overall impedance of the electrolyzer with treated CCM is smaller than that with the untreated CCM (difference of *ca.* 800 mΩ cm^2) and the largest contribution for the overall impedance is assigned to charge transfer resistances of OER with values of 2.1 Ω cm^2 and 2.5 Ω cm^2, respectively [41–44]. The high frequency resistance (HFR) is 250 mΩ cm^2 for the treated CCM, that is even lower than that of the untreated CCM – 300 mΩ cm^2. This indicates that the swelling treatment has not a negative effect on the ohmic resistance and on the membrane conductivity.

The influence of the solvents used on the surface structure of the anodes is visible in the AFM topography measurements in Fig. 3. In Fig. 3a and c, prepared using cyclohexanol and using propane-1,2-diol, respectively; more pores are present at the surface when compared to Fig. 3b, prepared using ethane-1,2-diol. At this anode, beside a few open pores, regions with a smooth surface are present, and are most-likely Nafion ionomer. The adhesion force and deformation mappings given in Fig. 4 reveal the distribution of catalyst and ionomer. Ionomer can be discerned from the catalyst and support particles by its high adhesion (bright areas in Fig. 4a–c), high deformation values (bright areas in Fig. 4d–f), and low DMT modulus (stiffness) – Figure S2 in Supplementary Information [45–47].

The surface porosity of the three 25 μm^2 topography images of the prepared anodes was evaluated. The porosity of the anode prepared using cyclohexanol solvent was the

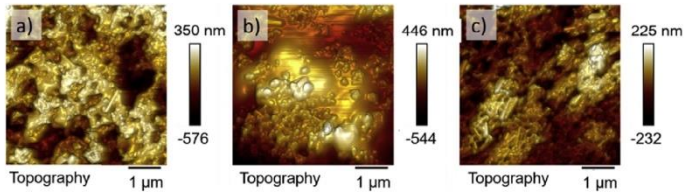


Fig. 3 – AFM topography images of anodes prepared using different solvents: a) cyclohexanol, b) ethane-1,2-diol, c) propane-1,2-diol.

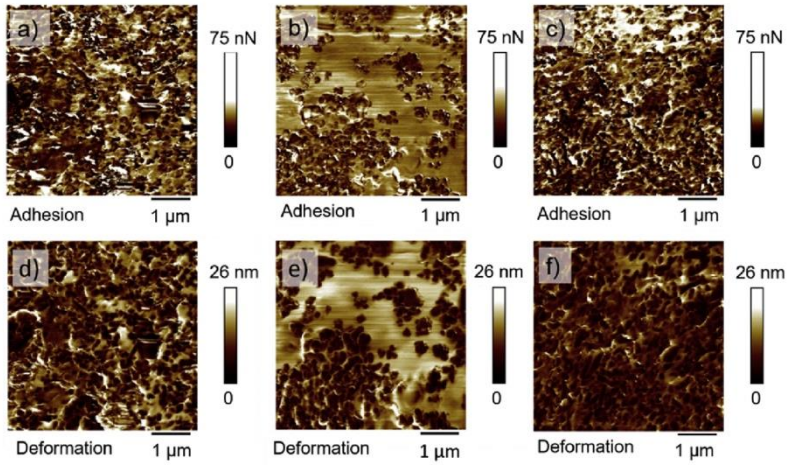


Fig. 4 – AFM adhesion force measurements at the anodes prepared using different solvents. a) cyclohexanol, b) ethane-1,2-diol, c) propane-1,2-diol. Correlated deformation measurements for the anodes prepared using different solvents: d) cyclohexanol, e) ethane-1,2-diol, f) propane-1,2-diol.

highest of the three samples, 26 ± 2%, followed by the sample prepared using propane-1,2-diol with 20 ± 2%. The anode prepared using ethane-1,2-diol had the lowest porosity with 13 ± 2%. Due to the restriction to horizontal geometry, the AFM-determined porosity values are generally lower than those determined by other methods.

The coatings prepared using cyclohexanol and using propane-1,2-diol as solvents presented a comparably good distribution of ionomer and catalyst particles at the surface, as illustrated in Fig. 4. The maximum size of connected ionomer particle area was determined from particle analysis of the adhesion image evaluation. For anodes prepared using cyclohexanol as solvent, the size was the smallest, 1280 ± 170 nm^2; for anodes prepared using propane-1,2-diol, the size was 1900 ± 240 nm^2; and the largest size was displayed by anodes prepared using ethane-1,2-diol, 3420 ± 40 nm^2. In conclusion, the catalyst particle distribution of the anode surface prepared using ethane-1,2-diol was the least homogeneous.

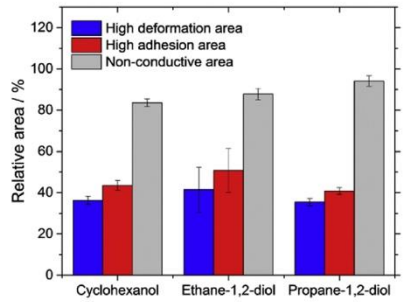


Fig. 5 – Relative area of adhesion, deformation and non-conductive area at the surfaces of the three anodes prepared using different solvents.

Catalyst loading calculation

The manufactured anodes contained Ir-loadings of 0.4 ± 0.02 mg cm^{-2} according to the differences in the weight of the membrane before and after coating the anodes.

TGA (Figure S1 at Supplementary Information) was performed to the anode coated using propane-1,2-diol for validation of the weight difference calculation. The mass-losses at 400 °C correspond to the Nafion membrane and ionomer decomposition. These results are in accordance with the work of Deng and co-workers [48] who noted major decomposition between 355°C and 560 °C corresponding to HF, carbonyl fluorides, and species exhibiting C–F stretching vibrations. In the work by Chen et al. [12], Ti_4O_7 does not show any thermal oxidation below 300 °C. More recently, Senevirathne and co-workers [49] reported that Ti_4O_7 oxidizes to the more stable TiO_2 at 550 °C with a weight gain of 6.2% (higher than the theoretical value of 5.3%). Iridium nanoparticles oxidize to IrO_2 during the TGA measurements under airflow, which additionally increases the total weight gain.

The remaining mass after the TGA measurement was found to be *ca.* 5.3% of the initial mass of 4.90 mg. Since the species present after TGA are not Ir and Ti_4O_7, but instead IrO_2 and TiO_2, different oxygen uptake by the two species was considered to calculate IrO_2 mass content at the end of TGA. The original mass fraction of Ir in the mixture of Ir/Ti_4O_7 was 30 wt%. After the TGA, the theoretical mass fraction of IrO_2 in the mixture of IrO_2/TiO2 would be 32.2 wt% (calculation in Supplementary Information). Finally, from the remaining TGA mass (correspondent to IrO_2 and TiO_2) and the area of the TGA sample, one can obtain the Ir-loading of 0.42 mg cm^{-2}.

The cathode of the CCM was sprayed with 100 μl cm^{-2} of catalyst suspension, and estimated Pt loading was 0.5 mg cm^{-2}, assuming 10% of suspension loss in the gun and borders of the spraying area.

Electrical surface conductivity

In Fig. 5, the fraction of high deformation, high adhesion and non-conductive surface area of the three differently prepared anodes is given. When measuring the ionomer coverage, the highly deformable area fraction is the most significant signal because, by surface deformation values, only regions with approximately more than 30 nm thick ionomer layers at the surface are counted. Due to the high surface sensitivity to the adhesion force, the area measured by adhesion contrast also includes particles covered by a very thin ionomer layer erroneously rated as ionomer. The ionomer area at the surface of the sample prepared using ethane-1,2-diol (42 ± 2%) was larger than that of the two other samples, which had approximately the same ionomer area fraction of 36 ± 2% (propane-1,2-diol) and 35 ± 2% (cyclohexanol). In addition, the non-conductive area derived from the current measurements was much larger in all three cases. The sample prepared using propane-1,2-diol had the largest non-conductive area, followed by the samples prepared using ethane-1,2-diol and cyclohexanol, respectively. This discrepancy can be explained by the different nature of the signals. A conductive surface spot needs to be electrically connected to the back electrode, while the nanomechanical properties reflect the properties of surface and sub-surface. In conclusion, the conductive network was the best for the sample prepared with cyclohexanol, followed by the samples prepared by using ethane-1,2-diol and propane-1,2-diol, respectively.

The AFM-derived conductive area fractions follow the same slope as the current revealed by the polarization measurements of the anodes after a short running period (Fig. 6). Examples of the AFM current measurements are given in Fig. 7; a correlation between electronic conductivity and conductive surface area is apparent. Consequently, a decrease of ionomer content could enhance the electrolyzer performance.

In Fig. 8, the surface topography of 400 μm^2 of the three different surface structures is shown; the roughness was evaluated from the AFM topography images. The highest roughness of 120 ± 30 nm was observed for the anode prepared using ethane-1,2-diol as solvent, followed by the sample prepared using cyclohexanol – 110 ± 10 nm; the lowest roughness was determined for the sample prepared using

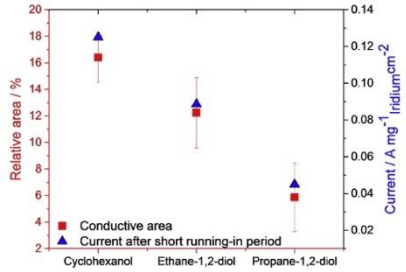


Fig. 6 – Comparison of AFM-derived conductive area and current after short running-in period for the three differently prepared anodes.

propane-1,2-diol, with a roughness of 54 ± 2 nm. The higher roughness of sample prepared using ethane-1,2-diol is likely caused by the large height differences between the ionomer agglomerates and the catalyst-containing phase and does not represent the roughness of the surface film; the large inhomogeneity is also indicated by the large error. The sample prepared using ethane-1,2-diol exhibited the most heterogeneous distribution, with regions of high catalyst density and large ionomer areas without any catalyst.

Electrochemical performance

Chronoamperometries of the CCMs with anodes coated using different solvents are depicted in Fig. 9a. After 180 min of operation, the anode coated using cyclohexanol solvent delivered the highest current density at 1.7 V, followed by the anode coated using propane-1,2-diol. The relative permittivity of the ink solvents impacts on the ionomer conformation and distribution in the catalyst layer. The three solvents used in this work (with $\varepsilon > 10$) make Nafion ionomer remain in solution form [24]. From Fig. 9a, electrochemical activity is higher for solvents with lower relative permittivity. This fact suggests that solvents with ε values closer to the colloidal form frontier ($3 < \varepsilon < 10$) of the ionomer generate a better triple-phase boundary, thus promoting a better catalyst utilization. The single curve with a relatively constant current value at end of tests corresponds to the anode coated using ethane-1,2-diol as ink vehicle. The slow electrochemical activity improvement observed in Fig. 9a can be attributed to CCM activation phenomenon, which is a typical procedure in PEM fuel cells [50]. The origin of this improvement might be related to the accommodation of the microstructure of the catalyst layer and

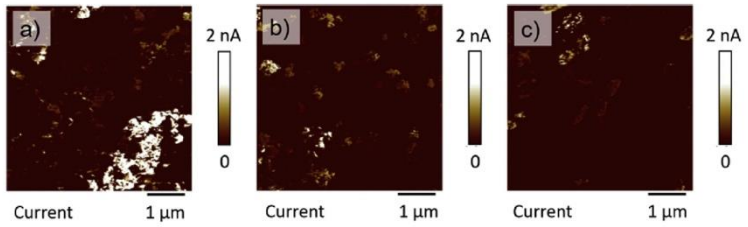


Fig. 7 – AFM measurements of conductive area for the anodes prepared using different solvents: a) cyclohexanol, b) ethane-1,2-diol, c) propane-1,2-diol.

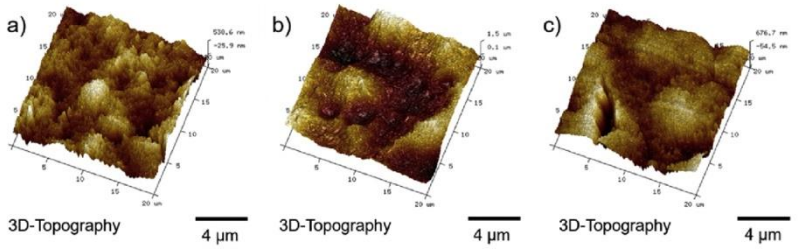


Fig. 8 – AFM 3D-topography measurements of the anodes prepared using different solvents: a) cyclohexanol, b) ethane-1,2-diol, c) propane-1,2-diol.

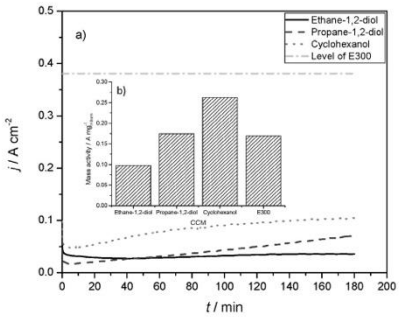


Fig. 9 – a) Chronoamperometries at 1.7 V and 40 °C of CCMs with anodes coated using ethane-1,2-diol propane-1,2-diol, and cyclohexanol as solvents. b) Iridium-mass activity of fabricated CCMs and E300 (Greenerity) at 1.7 V and 40 °C.

membrane/ionomer. Additionally, high potentials typical in water electrolysis (operation above 1.4 V) enable oxidation of Ir to the more OER-active IrO_2 [51]. A commercial CCM (E300 from Greenerity) was also tested under the same conditions (Figure S3 in Supplementary Information). The commercial CCM had been previously activated by the manufacturer. Mass activities of the fabricated CCMs are presented in Fig. 9b. Even though the CCMs coated using propane-1,2-diol and cyclohexanol did not reach steady-state activity at end of tests, they already exceeded the iridium-mass activity of E300 at 1.7 V and 40 °C. The screen-printed CCM using cyclohexanol as ink vehicle delivered the highest Ir-mass activity, that is 0.26 A mg^{-1} at 1.7 V and 40 °C. Compared to the commercial CCM, a higher catalyst utilization was observed for the screen printed CCM using cyclohexanol as a solvent.

Electrochemical impedance spectra (Fig. 10) were recorded in galvanostatic mode (at 35 mA cm^{-2}) at end of tests. The EIS spectra were fitted with the equivalent circuit depicted in Fig. 10 that consisted in (RQ) elements, representing a parallel combination of a resistance with a constant phase element. The high frequency resistances (R_6), associated to the electrolyte, were similar and the highest for the CCMs coated with ethane-1,2-diol and cyclohexanol (~0.29 Ω cm^2), the lowest for the commercial CCM (~0.22 Ω cm^2), followed by the CCM coated with propane-1,2-diol (~0.25 Ω cm^2). R_1 is associated to the HER and the lowest values were obtained for the CCM coated with cyclohexanol and commercial CCM (~33 mΩ cm^2), followed by the CCM coated with ethane-1,2-diol (~64 mΩ cm^2) and the highest for the CCM coated with propane-1,2-diol (~74 mΩ cm^2). Finally, R_2 is associated to the OER and is responsible for the major contribution for the overall impedances. As discussed above and following the trend observed in the chronoamperometries (Fig. 9), the values for R_2 are higher for the anodes coated with the solvents with higher relative permittivity. Among the fabricated CCMs, the highest R_2 value was obtained for the anode coated ethane-1,2-diol (~1.5 Ω cm^2), followed by the anode coated with propane-1,2-diol (~0.98 Ω cm^2) and the lowest for the anode coated with cyclohexanol (~0.86 Ω cm^2). Despite the commercial CCM presented the lowest R_2 among all CCMs (~0.56 Ω cm^2), this difference can be attributed to the higher Ir loading and to several others factors that depend on the materials and methods used in the manufacture.

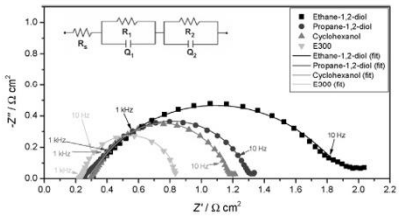


Fig. 10 – Impedance spectra at 35 mA cm^{-2} and 40 °C of E300 (Greenerity) and fabricated CCMs with anodes coated using ethane-1,2-diol; propane-1,2-diol; and cyclohexanol as solvents.

Conclusions

PEM electrolyzer CCMs were successfully fabricated by screen printing technique using three different solvents in the inks and a mixture of Ir-black catalyst and Ti_4O_7 support. As the electronic conductivity is correlated to the conductive surface area derived by AFM, a decrease of ionomer content could lead to a higher electrochemical performance.

This work unveils promising OER activities from inexpensive and easy-scalable screen-printed anodes with reduced iridium loadings of 0.4 ± 0.02 mg cm^{-2}, which is 83% lower than that of the commercial reference. The membrane swelling treatment was found to be effective, minimizing the membrane swelling during the coating process using ethane-1,2-diol as solvent of the paste, without hindering the electrolyzer performance.

Cyclohexanol was found to be a suitable single solvent for coating anodes directly on the membrane. It did not cause any noticeable swelling of the membrane thus enabling to skip the membrane swelling treatment. PEM electrolyzer tests at constant 1.7 V showed that the screen-printed CCM, using cyclohexanol as ink vehicle, delivers the highest current among all the prepared samples. The Ir-mass activity of the CCM with anode coated with cyclohexanol was 1.5 times higher than that of the commercial CCM.

Acknowledgements

The authors acknowledge the EU FP7/2007-2013 for Fuel Cell and Hydrogen Joint Technology Initiative under Grant No. 621237 (INSIDE) and to the Erasmus program of University of

Porto for the financial support. The authors also acknowledge Philip Lettenmeier and Stefan Helmly for sharing their expertise regarding PEM applications; to Jörg Bürkle for the assistance with wet spraying; to Oliver Freitag for the TGA measurements.

Appendix A. Supplementary data

Supplementary data related to this article can be found at https://doi.org/10.1016/j.ijhydene.2018.02.179.

REFERENCES

[1] Carmo M, Fritz DL, Mergel J, Stolten D. A comprehensive review on PEM water electrolysis. Int J Hydrogen Energy 2013;38(12):4901–34.
[2] Friedrich KA. PlanDelyKad: study on large scale water electrolysis and hydrogen storage [in German]. Berlin: German Federal Ministry for Economic Affairs and Energy (BMWi); 2015.
[3] Barbir F. PEM electrolysis for production of hydrogen from renewable energy sources. Sol Energy 2005;78(5):661–9.
[4] Ayers KE, Capuano C, Anderson EB. Recent advances in cell cost and efficiency for PEM-based water electrolysis. ECS Trans May 2012;41(10):15–22.
[5] Ayers KE, Anderson EB, Capuano C, Carter B, Dalton L, Hanlon G, et al. Research advances towards low cost, high efficiency PEM electrolysis. ECS Trans Oct. 2010;33(1):3–15.
[6] Bertuccioli L, Chan A, Hart D, Lehner F, Madden B, Standen E. Study on development of water electrolysis in the EU by E4tech Sàrl with Element Energy Ltd for the fuel cells and hydrogen joint undertaking. Feb. 2014.
[7] Babic U, Suermann M, Büchi FN, Gubler L, Schmidt TJ. Critical review—identifying critical gaps for polymer electrolyte water electrolysis development. J Electrochem Soc Jan. 2017;164(4):F387–99.
[8] Lewinski KA, van der Vliet D, Luopa SM. NSTF advances for PEM electrolysis – the effect of alloying on activity of NSTF electrolyzer catalysts and performance of NSTF based PEM electrolyzers. ECS Trans Sep. 2015;69(17):893–917.
[9] Alia SM, Shulda SM, Ngo C, Pylypenko S, Pivovar BS. Iridium nanowires as highly active, oxygen evolution reaction electrocatalysts. Meet Abstr Sep. 2017;MA2017-02(37):1655.
[10] Lettenmeier P, Wang R, Abouatallah R, Helmly S, Morawietz T, Hiesgen R, et al. Durable membrane electrode assemblies for proton exchange membrane electrolyzer systems operating at high current densities. Electrochim Acta Aug. 2016;210:502–11.
[11] Bladergroen B, Su H, Pasupathi S, Linkov V. Overview of membrane electrode assembly preparation methods for solid polymer electrolyte electrolyzer. In: Janis Kleperis, editor. Electrolysis. InTech.
[12] Chen G, Bare SR, Mallouk TE. Development of supported bifunctional electrocatalysts for unitized regenerative fuel cells. J Electrochem Soc Aug. 2002;149(8):A1092–9.
[13] Siracusano S, Baglio V, D'Urso C, Antonucci V, Aricò AS. Preparation and characterization of titanium suboxides as conductive supports of IrO2 electrocatalysts for application in SPE electrolysers. Electrochim Acta 2009;54(26):6292–9.
[14] Fuentes RE, Farell J, Weidner JW. Multimetallic electrocatalysts of Pt, Ru, and Ir supported on anatase and rutile TiO_2 for oxygen evolution in an acid environment. Electrochem Solid State Lett Mar. 2011;14(3):E5–7.
[15] Mazúr P, Polonský J, Paidar M, Bouzek K. Non-conductive TiO_2 as the anode catalyst support for PEM water electrolysis. Int J Hydrogen Energy 2012;37(17):12081–8.
[16] Stoyanova A, Borisov G, Lefterova E, Slavcheva E. Oxygen evolution on Ebonex-supported Pt-based binary compounds in PEM water electrolysis. Int J Hydrogen Energy 2012;37(21):16515–21.
[17] Slavcheva E, Borisov G, Lefterova E, Petkucheva E, Boshnakova I. Ebonex supported iridium as anode catalyst for PEM water electrolysis. Int J Hydrogen Energy 2015;40(35):11356–61.
[18] Wang L, Lettenmeier P, Golla-Schindler U, Gazdzicki P, Canas NA, Morawietz T, et al. Nanostructured Ir-supported on Ti_4O_7 as cost effective anode for proton exchange membrane (PEM) electrolyzers. Phys Chem Chem Phys Dec. 2016;18(6):4487–95.
[19] Ioroi T, Yasuda K. Iridium nanoparticles supported on magneli phase Ti_4O_7 for PEM water electrolyzers. Meet Abstr Sep. 2016;MA2016-02(38):2419.
[20] Won J-E, Kwak D-H, Han S-B, Park H-S, Park J-Y, Ma K-B, et al. Ptlr/Ti_4O_7 as a bifunctional electrocatalyst for improved oxygen reduction and oxygen evolution reactions. J Catal 2018;358:287–94.
[21] Uchida M, Aoyama Y, Eda N, Ohta A. New preparation method for polymer-electrolyte fuel cells. J Electrochem Soc Feb. 1995;142(2):463–8.
[22] Ngo TT, Yu TL, Lin HL. Influence of the composition of isopropyl alcohol/water mixture solvents in catalyst ink solutions on proton exchange membrane fuel cell performance. J Power Sources 2013;225:293–303.
[23] Yudianti R, Onggo H, Syampurwadi A. Molecular conformation of Nafion ionomer on electrocatalyst layer prepared by screen printing technique. Int J Electrochem Sci 2014;9:3047–59.
[24] Wang W, Chen S, Li J, Wang W. Fabrication of catalyst coated membrane with screen printing method in a proton exchange membrane fuel cell. Int J Hydrogen Energy 2015;40(13):4649–58.
[25] Kim CS, Chun YG, Peck DH, Shin DR, Method for fabricating membrane and electrode assembly for polymer electrolyte membrane fuel cells. Google Patents; 2001.
[26] Antolini E, Giorgi L, Pozio A, Passalacqua E. Influence of Nafion loading in the catalyst layer of gas-diffusion electrodes for PEFC. J Power Sources 1999;77(2):136–42.
[27] Passalacqua E, Lufrano F, Squadrito G, Patti A, Giorgi L. Nafion content in the catalyst layer of polymer electrolyte fuel cells: effects on structure and performance. Electrochim Acta 2001;46(6):799–805.
[28] Springer TE, Wilson MS, Gottesfeld S. Modeling and experimental diagnostics in polymer electrolyte fuel cells. J Electrochem Soc Dec. 1993;140(12):3513–26.
[29] Chan K, Eikerling M. Water balance model for polymer electrolyte fuel cells with ultrathin catalyst layers. Phys Chem Chem Phys 2014;16(5):2106–17.
[30] Agmon N. The Grotthuss mechanism. Chem Phys Lett Oct. 1995;244(5–6):456–62.
[31] Eslamibidgoli MJ, Huang J, Kadyk T, Malek A, Eikerling M. How theory and simulation can drive fuel cell electrocatalysis. Nano Energy 2016;29:334–61.
[32] Kim K-H, Lee K-Y, Kim H-J, Cho E, Lee S-Y, Lim T-H, et al. The effects of Nafion® ionomer content in PEMFC MEAs prepared by a catalyst-coated membrane (CCM) spraying method. Int J Hydrogen Energy 2010;35(5):2119–26.
[33] Siracusano S, Van Dijk N, Payne-Johnson E, Baglio V, Aricò AS. Nanosized IrO_x and $IrRuO_x$ electrocatalysts for the O2 evolution reaction in PEM water electrolysers. Appl Catal B Environ 2015;164:488–95.

[34] Oh H-S, Nong HN, Reier T, Gliech M, Strasser P. Oxide-supported Ir nanodendrites with high activity and durability for the oxygen evolution reaction in acid PEM water electrolyzers. Chem Sci 2015;6(6):3321–8.
[35] Lettenmeier P, Wang L, Golla-Schindler U, Gazdzicki P, Canas NA, Handl M, et al. Nanosized IrOx-Ir catalyst with relevant activity for anodes of proton exchange membrane electrolysis produced by a cost-effective procedure. Angew Chem Jan. 2016;128(2):752–6.
[36] Hou Z, Ming P, Xing D, Song S, Zhang K, Zhang Y. Preparing method for integrated membrane-catalyst coated layer membrane electrode for a fuel cell. Google Patents; 2012.
[37] Lettenmeier P, Kolb S, Sata N, Fallisch A, Zielke L, Thiele S, et al. Comprehensive investigation of novel pore-graded gas diffusion layers for high-performance and cost-effective proton exchange membrane electrolyzers. Energy Environ Sci 2017;10(12):2521–33.
[38] Lettenmeier P, Wang R, Abouatallah R, Saruhan B, Freitag O, Gazdzicki P, et al. Low-cost and durable bipolar plates for proton exchange membrane electrolyzers. Sci Rep Mar. 2017;7:44035.
[39] Lettenmeier P, Wang R, Abouatallah R, Burggraf F, Gago AS, Friedrich KA. Coated stainless steel bipolar plates for proton exchange membrane electrolyzers. J Electrochem Soc Jul. 2016;163(11):F3119–24.
[40] Gago AS, Ansar SA, Saruhan B, Schulz U, Lettenmeier P, Canas NA, et al. Protective coatings on stainless steel bipolar plates for proton exchange membrane (PEM) electrolysers. J Power Sources Mar. 2016;307:815–25.
[41] Siracusano S, Baglio V, Lufrano F, Staiti P, Aricò AS. Electrochemical characterization of a PEM water electrolyzer based on a sulfonated polysulfone membrane. J Membr Sci 2013;448(Supplement C):209–14.
[42] Rozain C, Millet P. Electrochemical characterization of polymer electrolyte membrane water electrolysis cells. Electrochim Acta Jan. 2014;131:160–7.
[43] Dedigama I, Angeli P, Ayers K, Robinson JB, Shearing PR, Tsaoulidis D, et al. In situ diagnostic techniques for characterisation of polymer electrolyte membrane water electrolysers – flow visualisation and electrochemical impedance spectroscopy. Int J Hydrogen Energy Mar. 2014;39(9):4468–82.
[44] Elsøe K, Grahl-Madsen L, Scherer GG, Hjelm J, Mogensen MB. Electrochemical characterization of a PEMEC using impedance spectroscopy. J Electrochem Soc Jan. 2017;164(13):F1419–26.
[45] Helmly S, Hiesgen R, Morawietz T, Yuan X-Z, Wang H, Andreas Friedrich K. Microscopic investigation of platinum deposition in PEMFC cross-sections using AFM and SEM. J Electrochem Soc Jan. 2013;160(6):F687–97.
[46] Hiesgen R, Morawietz T, Handl M, Friedrich KA. Structure and conductivity of fuel cell membranes and catalytic layers investigated by AFM. MRS Proc 2015;1774:19–24.
[47] Morawietz T, Singraber A, Dellago C, Behler J. How van der Waals interactions determine the unique properties of water. Proc Natl Acad Sci Jul. 2016;113(30):8368–73.
[48] Deng Q, Wilkie CA, Moore RB, Mauritz KA. TGA–FTi.r. investigation of the thermal degradation of Nafion® and Nafion®/[silicon oxide]-based nanocomposites. Polymer (Guildf) 1998;39(24):5961–72.
[49] Senevirathne K, Hui R, Campbell S, Ye S, Zhang J. Electrocatalytic activity and durability of Pt/NbO_2 and Pt/Ti_4O_7 nanofibers for PEM fuel cell oxygen reduction reaction. Electrochim Acta 2012;59:538–47.
[50] Qi Z, Kaufman A. Activation of low temperature {PEM} fuel cells. J Power Sources 2002;111(1):181–4.
[51] Siracusano S, Baglio V, Grigoriev SA, Merlo L, Fateev VN, Aricò AS. The influence of iridium chemical oxidation state on the performance and durability of oxygen evolution catalysts in PEM electrolysis. J Power Sources 2017;366(Supplement C):105–14.

Supplementary Information

1- Iridium loading calculation by TGA:

Solution of a system of two equations with two unknown variables.

First equation refers to the iridium weight ratio percentage to total of Ir + Ti_4O_7 in the screen printing paste:

$$\text{Ir wt\%} = \frac{m_{Ir}}{m_{Ir} + m_{Ti_4O_7}}$$

Second equation refers to the remaining mass after TGA that corresponds to the sum of the masses of IrO_2 and TiO_2.

$$\text{TGA final mass} = m_{IrO_2} + m_{TiO_2}$$

$$\begin{cases} \text{Ir wt\%} = \dfrac{m_{Ir}}{m_{Ir} + m_{Ti_4O_7}} \\ \dfrac{\text{TGA final mass}}{\text{Sample area}} = m_{IrO_2} + m_{TiO_2} \end{cases}$$

$$\begin{cases} \text{Ir wt\%} = \dfrac{n_{Ir} * M_{Ir}}{n_{Ir} * M_{Ir} + n_{Ti_4O_7} * M_{Ti_4O_7}} \\ \dfrac{\text{TGA final mass}}{\text{Sample area}} = n_{IrO_2} * M_{IrO_2} + n_{TiO_2} * M_{TiO_2} \end{cases}$$

According to the stoichiometry of the oxidation of both species,

$$\begin{cases} \text{Ir wt\%} = \dfrac{n_{Ir} * M_{Ir}}{n_{Ir} * M_{Ir} + n_{Ti_4O_7} * M_{Ti_4O_7}} \\ \text{Normalized TGA final mass} = n_{Ir} * M_{IrO_2} + 4 * n_{Ti_4O_7} * M_{TiO_2} \end{cases}$$

The variables that will be calculated are n_{Ir} and $n_{Ti_4O_7}$.

Substituting values,

$$\begin{cases} 0.3 = \dfrac{n_{Ir} * 192217}{n_{Ir} * 192217 + n_{Ti_4O_7} * 303461} \\ \dfrac{4.9 * 0.0527380}{0.19635} = n_{Ir} * 224215 + 4 * n_{Ti_4O_7} * 79865 \end{cases}$$

$$\begin{cases} n_{Ir} = 1.88995 * 10^{-6}\ mol\ cm^{-2} \\ n_{Ti_4O_7} = 2.79329 * 10^{-6}\ mol\ cm^{-2} \end{cases}$$

Because $n_{Ir} = n_{IrO_2}$,

$$\mathrm{IrO_2\ weight\ \%} = \frac{m_{IrO_2}}{\text{Normalized TGA final mass}}$$

$$\mathrm{IrO_2\ weight\ \%} = \frac{n_{IrO_2} * M_{IrO_2}}{\text{Normalized TGA final mass}}$$

Substituting values,

$$\mathrm{IrO_2\ weight\ \%} = \frac{1.88995 * 10^{-6} * 224215}{1.3161}$$

$$\mathrm{IrO_2\ weight\ \%} = 0.3219 = 32.2\%$$

Calculating the IrO_2 loading:

$$\mathrm{IrO_2\ loading\ by\ TGA} = \text{Normalized TGA final mass} * \mathrm{IrO_2\ weight\ \%}$$

$$\mathrm{IrO_2\ loading\ by\ TGA} = 1.3161 * 0.3219$$

$$\mathrm{IrO_2\ loading\ by\ TGA} = 0.42\ \mathrm{mg\ cm^{-2}}$$

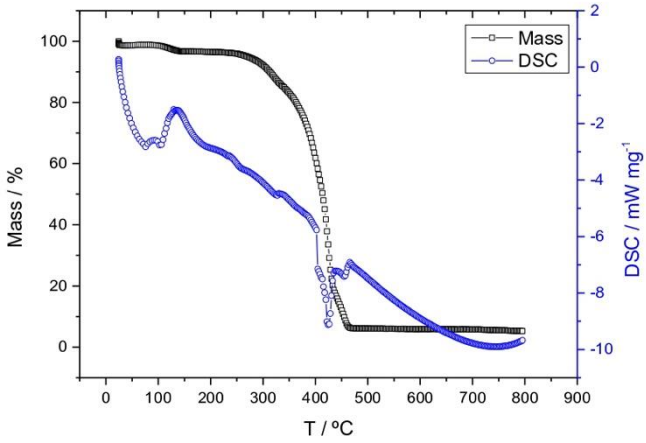


Figure S1: TGA measurement of anode-coated membrane using propane-1,2-diol.

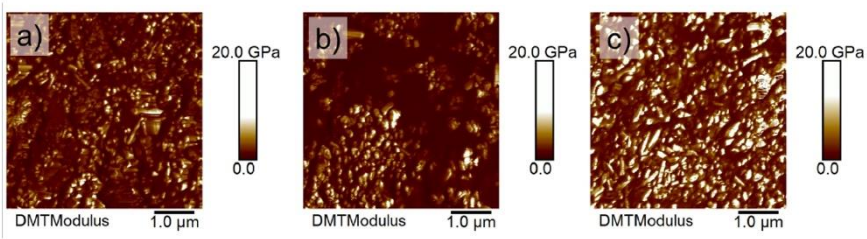


Figure S2: DMT Modulus AFM mappings of the MEAs prepared with: a) cyclohexanol, b) ethane-1,2-diol, and c) propane-1,2-diol.

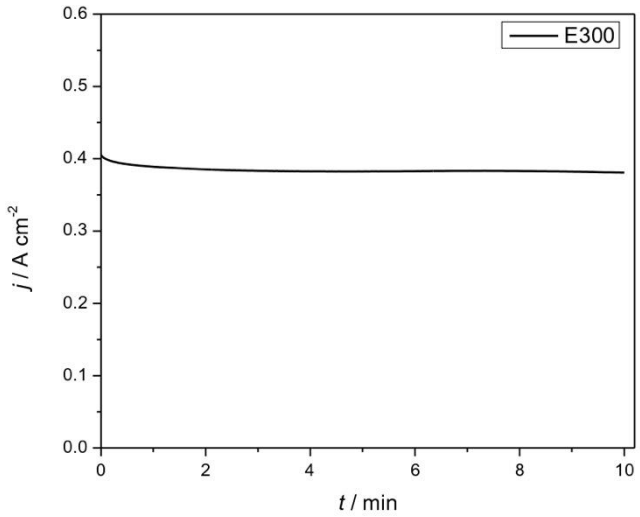


Figure S3: Chronoamperometry at 1.7 V and 40 °C of the commercial CCM (E300).

Int. J. Electrochem. Sci., 15 **(2020)** 613 – 627, doi: 10.20964/2020.01.58

International Journal of
ELECTROCHEMICAL
SCIENCE
www.electrochemsci.org

Air Bleeding Strategies to Increase the Efficiency of Proton Exchange Membrane Fuel Cell Stationary Applications Fuelled with CO ppm-levels

S. Delgado, T. Lagarteira and A. Mendes[*]

Laboratory for Process Engineering, Environmental, Biotechnology and Energy (LEPABE), Faculty of Engineering of University of Porto, Rua Dr. Roberto Frias s/n, 4200-465 Porto, Portugal
[*]E-mail: mendes@fe.up.pt;

Received: 12 August 2019 / *Accepted:* 28 September 2019 / *Published:* 30 November 2019

The use of proton exchange membrane fuel cells (PEMFCs) as efficient electric generators for residential and tertiary sectors to replace conventional internal combustion engines greatly depends on the recent advances in purification technologies. Preferential oxidation and pressure swing adsorption offer reformate hydrogen streams with CO concentrations down to fractional ppm level. However, even small traces of CO cause reversible and irreversible performance losses of the PEMFC stack due to poisoning of the anode Pt catalyst. This work reports the performance loss upon H_2 contamination down to the ppm level and the efficiency gains after applying internal and external air bleeding to the anode of the fuel cell. This work studies both air bleeding strategies under operating conditions typical for stationary applications. By adding solely 1 % of air bleed to a 10 ppm CO contaminated hydrogen stream, it is possible to recover the full performance without compromising the steadiness of the cell. Moreover, a performance loss of < 1 % – DOE target value for reformate streams – can be met using Pt-Ru based anode catalysts allied to a minimal air bleed concentration. Long-term experiments, *ca.* 80 h, were performed to assess the stability of the fuel cells fed with contaminated hydrogen and compare the long-term impacts of both internal and external air bleeding.

Keywords: Proton exchange membrane fuel cell; Membrane electrodes assembly; CO poisoning; Air bleeding.

1. INTRODUCTION

Low-temperature proton exchange membrane fuel cells (PEMFCs) are considered an attractive candidate to power small stationary units including off-grid energy, backup power systems and combined heat and power (CHP) for industry and buildings. CHP systems based on fuel cells are expected to replace natural gas heaters for domestic cogeneration, because of their higher fuel efficiency, modularity, and environmentally friendly operation [1]. However, some challenges still hinder the

widespread commercialization of the technology. The core component of the fuel cell, the membrane-electrodes assembly (MEA), plays a crucial role on the overall cost of fuel stacks due to the need of highly active and durable catalysts and electrodes. In parallel to the high cost of the precious-metal catalysts, the small world-wide production of highly pure hydrogen is a major drawback [2].

Systems for stationary applications usually adopt a fuel processor to produce hydrogen from fossil (natural gas, LPG) or renewable (bio-ethanol, bio-gas) fuels [3]. The reforming of hydrocarbons followed by water-gas shift and purification is the most common production route of hydrogen. Nonetheless, this production route still delivering contaminants (CO_2, H_2S and mainly CO) in the hydrogen stream that poison platinum catalyst activity and durability [4,5]. Therefore, ISO 14687-3 details hydrogen quality requirements for PEM fuel cells for stationary applications. In particular, it defines three categories: two with $H_2 \geq 50$ % and $CO \leq 10$ ppm, and one with $H_2 \geq 99.9$ % and $CO \leq 0.2$ ppm. Hydrogen produced by conventional fuel processors can fulfil the requirements of the first two categories. Japan appears as the world leader on micro-combined heat and power systems based on fuel cells (m-CHP-PEMFC) for buildings with over 140 000 units sold; likewise, Europe is expected to promote the exponential growing of m-CHP-PEMFC [6,7]. The chemisorption of CO on Pt catalyst particles surface reduces the number of active sites for H_2 electro-oxidation [8,9] and hence the fuel cell power output and its useful life. The performance of the fuel cell anode is then highly sensitive to small traces of CO (down to fractional ppm level) and dependent on operating conditions such as temperature, the exposure time to CO, pressure, current density, relative humidity and fuel stoichiometry [10]. Carbon dioxide has a minimal affinity for the Pt catalyst and therefore does not affect the performance of the cell at low current densities (< 300 mA cm^{-2}), behaving as an inert species [11].

In the last two decades, several works have been published focusing on the mitigation of CO poisoning in PEM fuel cells [10,12–14]. The most conventional approach is to use CO-tolerant catalysts at the anode, normally obtained by combining Pt with other metals. Pt-Ru alloy is typically used as CO-tolerant catalyst albeit some impact on the fuel cell durability due to Ru dissolution and migration to the cathode [15,16]. The CO tolerance evidenced by PtRu catalysts is mainly attributed to two mechanisms, the electronic tuning of Pt d-band structure (ligand effect) and/or the acceleration of CO oxidation to CO_2 by providing oxygen species to CO_{ad} on Pt surfaces [17]. The ligand effect consists in the modification of Pt electronic structure that either weakens the Pt-CO bond thus promoting CO oxidation by nearby OH groups; or improves Pt-H_2O activation that leads to direct oxidation of CO on the Pt sites [18].

Another approach to inhibit CO poisoning is to introduce trace concentrations of oxygen in the anode. Oxygen can be supplied to the anode by: i) internal oxygen/air bleeding from the cathode through the membrane; ii) external oxygen/air bleeding; iii) introduction of H_2O_2 in the anode bubbler [10]. Oxygen permeation through the membrane is commonly described in terms of sorption-diffusion mechanisms [19]; specifically, during PEMFC operation oxygen sorbs into the membrane and diffuses from the cathode to the anode side preferably through its hydrated pathways. The membrane permeability to oxygen is proportional to the product of Fick's diffusion coefficient and solubility coefficient [20],[21]. The membrane permeability to oxygen increases with the operating temperature and with the membrane humidification [22–25]. On the other hand, oxygen permeation increases with the partial pressure difference between the two sides of the membrane but decreases with increasing

membrane thickness [26]. The permeated oxygen is partly responsible for the oxidation of CO to CO_2 in the anode catalyst particles surface through heterogeneous catalysis described by the Langmuir-Hinshelwood mechanism [27]. Yet, some negative aspects may arise from the presence of excessive O_2 at the anode such as higher anode overpotential caused by water production from the hydrogen oxidation, catalyst sintering due to the highly exothermic hydrogen oxidation, and membrane degradation from the side-production of H_2O_2 [16]. Therefore, air (oxygen) bleeding must be tuned depending on the CO contamination levels [28].

In this work, the impacts of two different techniques for the mitigation of CO poisoning, internal and external air bleeding, are assessed. For both techniques, oxygen traces at the anode were tuned to determine the minimum amount able to fully recover the efficiency drop caused by CO poisoning. Mid-term operation under CO contamination was compared for both techniques to assess the degradation through potential decay. To the best of the authors' knowledge, these techniques are compared for the first time under PEMFC operating conditions suitable for stationary applications, such as m-CHP-PEMFC.

2. EXPERIMENTAL

The electrochemical measurements were carried out in a 25 cm^2 fuel cell manufactured by Pragma Industries. The graphite flow fields used in both the anode and cathode were single channel type. The cell compression was set to *ca.* 2 MPa, thus guaranteeing the electrical contact between the gas diffusion electrodes (GDE) and the bipolar plates.

MEA#1 was made of a Nafion 212 membrane (N212, 51 µm of thickness) sandwiched by two GDEs, all purchased to Quintech. The anode catalyst layer contained 0.5 mg cm^{-2} of PtRu and the cathode catalyst layer had 0.5 mg cm^{-2} of Pt. The GDEs were hot-pressed to the membrane at 120 °C and 17 bar for 5 minutes. The French Alternative Energies and Atomic Energy Commission (CEA) provided MEA#2 that employs a Nafion reinforced-stabilized HP membrane (NRHP) with 22 µm of thickness. The catalyst layers contained 0.585 mg cm^{-2} of PtRu (66 wt.% of Pt) in the anode and PtCo alloy with 0.468 mg cm^{-2} of Pt in the cathode. The gas diffusion layers of both MEAs (Sigracet 28 BC, SGL Carbon) were 220 µm thick.

The mass flow rates of the reactants, humidification and temperatures of the lines were controlled with a test station. The anode was fed with either high purity H_2 (99.999 %), mixtures of CO/H_2 or synthetic air whilst the cathode was fed with synthetic air. CO was supplied from a cylinder containing a mixture of H_2 balanced with 100 ppm of CO (Linde). Anode and cathode were humidified by bubbling the feed gases into ultra-pure water; the relative humidity was set to 50 % for both the anode and cathode. The stoichiometries of the reactants were set to 1.5/2 for the anode and cathode, respectively. Subsequently, the consumed reactant flow rates were calculated using Faraday's equation, assuming a coulombic efficiency of 100 %.

An electrochemical workstation (Zahner IM6eX) coupled with a PP-240 power potentiostat was used to perform the electrochemical measurements. The MEAs were subjected to break-in at 500 mA cm^{-2}. The conditions for the break-in and experiments of interest are described in Table 1. The break-in

step (conditions of Run# 1) was considered completed when the cell potential variation was less than 5 mV h^{-1} at 500 mA cm^{-2}.

After achieving steady-state performance, a polarization curve was recorded in galvanostatic mode. The cell potential was recorded (Run# 2) as a function of the current density with a dwell time of 3 minutes. Chronopotentiometries were performed at 500 mA cm^{-2} following the conditions of Run #2-Run #10 to evaluate the magnitude of performance loss due to CO exposure and the performance gains after implementing each bleeding technique.

Electrochemical impedance spectroscopy (EIS) was performed in galvanostatic mode at 500 mA cm^{-2}, with a perturbation amplitude of 40 mA cm^{-2} between 10 kHz and 100 mHz.

Figure 1 depicts the equivalent circuit of elements used to fit the electrochemical impedance spectra. The equivalent circuit chosen comprises two simple Randle's circuits, each with a constant phase element ($Q_{a/c}$) and a resistor ($R_{a/c}$) in parallel, along with a resistor connected in series (R_m) [29]. R_m accounts mostly for the resistance associated to protonic conduction through the membrane, R_a and R_c are the charge transfer resistances associated to anode and cathode, respectively. EIS low frequency data, related to mass transfer overpotential, was not included in the fittings since it was not preponderant for this study.

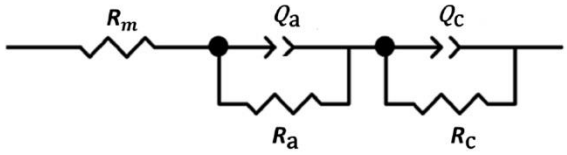


Figure 1. Schematic representation of the equivalent circuit for the PEMFC.

In-situ cyclic voltammetry (CV) was performed to both anode and cathode of the MEAs to estimate the electrochemical surface area (ECSA) at the beginning and end of experiments. The working electrode was purged with N_2 to remove any adsorbed O_2, and the counter electrode was fed with H_2, maintaining the stoichiometry and flow rates calculated for 100 mA cm^{-2} between H_2/O_2. The relative humidity was set to 50 %, the back pressure was set to 1.5 bar for both electrodes, the scan rate was set to 50 mV s^{-1} and the cell temperature was kept at 70 °C.

Table 1. Performed tests and corresponding operating conditions.

#	MEA#	*p* H_2	*p* Air	RH H_2	RH Air	Fuel	Temperature
1 – Break-in	1 / 2	1.5	1.5	80 %	80 %	Pure H_2	80 °C
2 - Reference	1 / 2	1.2	1.2	50 %	50 %	Pure H_2	70 °C

3	1 / 2	1.2	1.2	50 %	50 %	H_2 + 10 ppm CO	70 °C
4	1 / 2	1.1	1.2	50 %	50 %	H_2 + 10 ppm CO	70 °C
5	1 / 2	1.1	1.3	50 %	50 %	H_2 + 10 ppm CO	70 °C
6	2	1.1	1.3	50 %	50 %	H_2 + 20 ppm CO	70 °C
7	2	1.1	1.3	50 %	50 %	H_2 + 30 ppm CO	70 °C
8	1	1.2	1.2	50 %	50 %	H_2 + 10 ppm CO + 0.5 % Air	70 °C
9	1 / 2	1.2	1.2	50 %	50 %	H_2 + 10 ppm CO + 1 % Air	70 °C
10	1	1.2	1.2	50 %	50 %	H_2 + 10 ppm CO + 1.5 % Air	70 °C

3. RESULTS AND DISCUSSION

3.1. Electrochemical performance with pure H_2

The polarization curves (Figure 2a) and EIS spectra at 500 mA cm^{-2} (Figure 2b) of MEA#1 and MEA#2 were obtained for Reference conditions –Table 1. MEA#2 outperformed MEA#1 at current densities higher than 300 mA·cm^{-2}. The greater thickness of membrane N212, inserted in MEA#1, compared with membrane NRHP, inserted in MEA#2, makes its ohmic overpotential higher, limiting the protonic conduction and decreasing the power output [30]. Nafion HP is a sandwich type membrane, similar to its predecessor Nafion XL (*ca*. 28 µm), comprising an inner layer of PTFE-rich reinforcing mesh for mechanical stability, coated with two ultra-thin layers of Nafion in each side (ca. 7 µm thick each). This membrane provides high proton conductivity with better chemical/mechanical durability compared to the benchmark counterparts (*e.g.* Nafion 212 or Nafion 115) [31–33]. Nonetheless, the activation overpotential region (< 100 mA·cm^{-2}) of MEA#2 is higher comparing to MEA#1, thanks to the higher Pt loading of the latter. Nevertheless, ohmic overpotentials are smaller for MEA#2 (Figure 2a). From the EIS spectra (Figure 2b), the difference in the ohmic resistances of MEA#2 and MEA#1 – 107.4 mΩ cm^2 vs 221.4 mΩ cm^2, respectively – was assigned to the membranes thickness where MEA#2 is equipped with a membrane *ca*. 50 % thinner (22 µm) than MEA#1 (51 µm); these results are in line with previous studies [34,35]. Ohmic losses tend to increase linearly with membrane thickness [36]. Additionally, the lower mass transport overpotential of MEA#2 suggests the existence of more gas and liquid diffusion-pathways in the cathode catalyst layer.

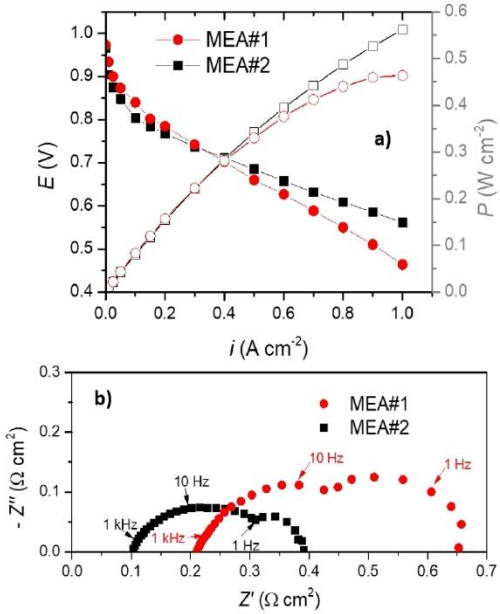


Figure 2. Comparison between the two tested MEAs under the conditions of Run#2 (from Table 1.) by a) a polarization curve; b) EIS at 500 mA·cm^{-2}.

Hereafter both MEA#1 and MEA#2 will assess the defined strategies to mitigate CO contamination – internal and air bleeding – under the operating conditions shown in Table 1. Runs #3 - #13.

3.2. Internal air bleeding

Internal air bleeding was controlled by setting a pressure difference between the two electrodes. The solubility of oxygen in water, which controls the oxygen transport to the anode, is related to its partial pressure. Therefore, the cathode side pressure must be higher to promote oxygen permeation through the membrane [26]. Error! Reference source not found.**a** shows chronopotentiometries of MEA#1, at 500 mA cm^{-2}, for pure hydrogen feed (Run #2) and for hydrogen with 10 ppm of CO feed (Runs #3, #4 and #5). With the introduction of CO at the anode, a linear loss of cell potential was observed until reaching a new steady-state. The effect of the internal air bleeding was not evident up to 0.1 bar of pressure difference. At 0.2 bar of cathode over-pressure, the steady-state cell potential increased *ca.* 20 mV, denoting a partial recovery of catalyst poisoning by CO, *ca.* 51 %.

The impedance spectra obtained at 500 mA cm^{-2}, were fitted to an EC shown in

Figure 1 to better diagnose the effect of the CO poisoning mitigation strategies. From the EIS spectra (Figure 3b), in the high-frequency region the anodic charge transfer resistance increased significantly when CO was fed with no internal bleeding – R_a = 67.8 mΩ cm^2 vs R_a =120 mΩ cm^2. When an internal bleeding is employed, ΔP = 0.2 bar, the anodic charge transfer resistance decreased significantly, R_a = 82.9 mΩ cm^2 (Table 2).

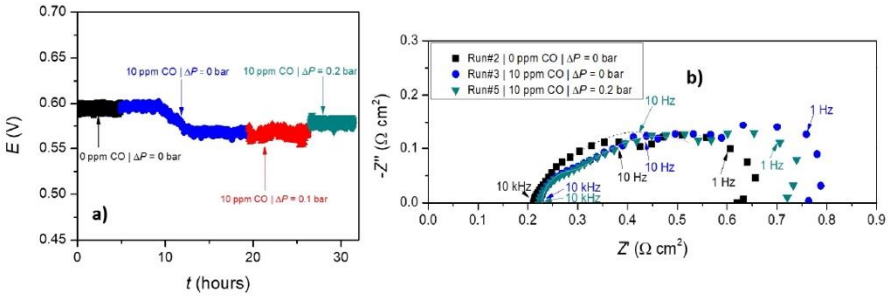


Figure 3. Effect of internal air bleeding on a) chronopotentiometry and b) EIS at 500 mA cm^{-2} of MEA#1.

Table 2. Summary of fitted values from EIS data using the equivalent circuit shown in Figure 1 for MEA#1 and#2; (Frequency range of the EIS fitted data: 2.5 kHz – 10 Hz).

MEA	#	R_m / mΩ cm^2	R_a / mΩ cm^2	Q_a / F cm^2	R_c / mΩ cm^2	Q_c / F cm^2
1	**2** - 0 ppm CO	221.4	67.8	639 m	293.2	789 m
	3 - 10 ppm CO	243	117.7	294 m	347.5	443.8 m
	5 - 10 ppm CO | ΔP =0.2 bar	233.2	82.9	146.9 m	326.5	254.9 m
	10 - 10 ppm CO + 1.5% air bleed	213.1	67.5	681.5 m	278.3	790.5 m
2	**2** - 0 ppm CO	107.4	49.5	16.1	174	23.7
	3 - 10 ppm CO	125.4	237.4	11	315.8	6.3
	5 - 10 ppm CO | ΔP=0.2 bar	122.5	224.3	7.9	252.5	9.4
	9 - 10 ppm CO + 1% air bleed	109.4	44.6	15.6	160.7	22.4

Runs #2, #3, #4 and #5 were repeated with MEA#2. Figure 4**a** displays the chronopotentiometries of MEA#2 at 500 mA cm^{-2}. After CO contamination, the steady-state cell potential increased with the cathode over-pressure (*ca.* 10 ± 2 mV per 0.1 bar). Therefore, internal air bleeding effect is hardly noticeable in EIS (Figure 4**b**), since the spectra of Runs #3 and #5 almost overlap. Moreover, .the effect

of internal air bleeding with an over-pressure of 0.2 bar allows a recovery of 25 % of the pristine performance and a reduction of anode charge transfer resistance of *ca.* 10 mΩ cm^2, comparing with Run #3, according to the EIS fitting - **Table 2**.

Oxygen bleeding on several membranes has been a subject of several studies, which report that CO poisoning mitigation is lower for thicker membranes like Nafion 115 (127 µm) [27]; the work of Wang [37] reported higher oxygen bleeding when the cathode over-pressure increases in ultra-thin membranes (5 µm and 25 µm). These evidences support that performing internal bleeding for CO poisoning mitigation is more effective if thin membranes are used. By promoting back diffusion of water dissolved oxygen through thin membranes (internal bleeding), more CO present at the anode can be oxidized to CO_2, thus reducing the anode overpotential caused by CO poisoning. Increments on the cathode total pressure promotes CO oxidation [37] but only *ca.* 0.25 % of the crossed oxygen molecules oxidize CO to CO_2 [37]. In the present study, a similar performance gain was achieved for both MEA#1 and MEA#2, as seen in Figure 3a and Figure 4b. Nonetheless, no more than 40 % of the initial performance could be re-established; pressure gradients higher than 200 mbar between the electrodes were not employed to avoid high mechanical stress that could lead to form pin-holes in the membrane and consequent gas crossover or internal short-circuits.

There is no agreement whether Nafion-PTFE composite membranes display better gas barrier properties compared with plain Nafion membranes (*e.g.* Nafion 115, Nafion 117 among others); several works [38–40] report greater permeabilities of Nafion/PTFE composite membranes to oxygen and nitrogen. The PTFE mesh in the composite membrane allows to reduce the overall membrane thickness (from typical *ca.* 185 µm -Nafion 117 - to less than 40 µm) while keeping the mechanical stability. These authors observed higher composite membrane permeabilities to gas relatively to thicker non-reinforced membranes [41]. On the other hand, Yu and his co-workers developed a Nafion/PTFE composite with an overall thickness of 20 ± 5 µm and, upon scanning electron microscopy analysis, they confirmed that PTFE pores were completely filled with the Nafion resin. The permeability of the composite membrane to nitrogen was reduced when comparing to non-reinforced Nafion 112, 115 or 117 [39].

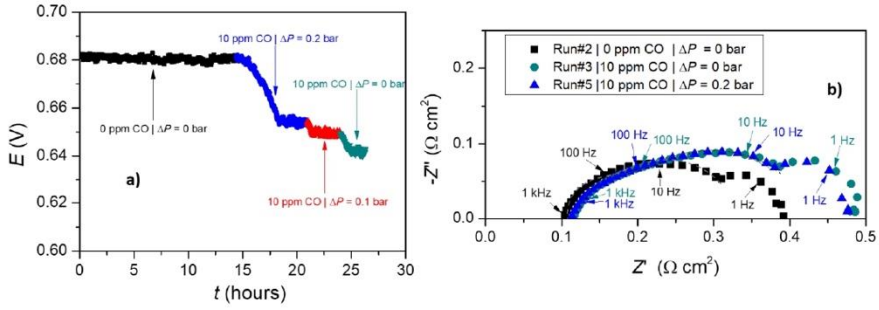


Figure 4. Effect of internal bleeding in MEA#2 at 500 mA·cm^{-2} on a) chronopotentiometry and b) EIS.

In the present study, the use of a thinner membrane (Nafion HP in MEA#2) did not provide better internal bleeding-based performance recovery than thicker Nafion 212 membrane (MEA#1). Nafion HP membranes are reinforced with a backbone that makes them not only mechanically more stable but also less permeable to both hydrogen and oxygen. The lower permeability to oxygen limits internal bleeding and thus CO mitigation is less effective comparing to non-reinforced membranes of similar thickness.

Higher concentrations of CO in the fuel stream were also tested together with internal bleeding. The pressure difference between cathode and anode was set to 200 mbar to enable internal air bleeding under different CO contaminations. Figure 5a shows the chronopotentiometries for four levels of CO contamination (0, 10, 20 and 30 ppm). The efficiency of the cell provided with MEA#1 at 500 mA cm^{-2} and 80 °C fell from the initial value of 45.2 % while feeding neat H_2 to progressively lower efficiencies, *ca.* - 0.55 % with each increase of 10 ppm of CO. In this regard, the steady state potential decreased with the CO concentration, mainly because of increasing anode overpotential.

The impedance spectra (Figure 5b), obtained after each chronopotentiometry, unveils that higher CO concentrations increase the overall impedance. The differences are clear for frequencies lower than 1 Hz, where gradual increments of 10 ppm in the CO concentration originate two-fold higher anode charge transfer resistances, *i.e.,* the resistance increases *ca.* 20 mΩ cm^2 when CO passes from 10 ppm to 20 ppm, and *ca.* 40 mΩ cm^2 when passing from 20 ppm and 30 ppm of CO.

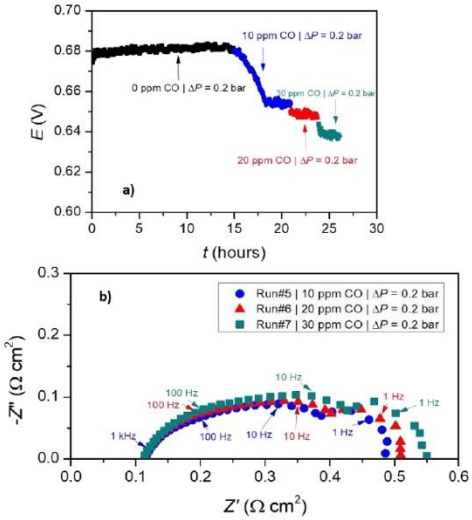


Figure 5. Effect of different CO concentrations at 500 mA cm^{-2} on a) chronopotentiometry and on b) EIS in MEA#1.

The work of Dhar [42] reported that the apparent activation energy for the HOR increases with the CO concentration thus leading to higher anode polarizations. Oetjen [43] studied the effect of different CO concentrations (25 to 250 ppm of CO) on the performance a PEMFC at 80 ºC. These authors concluded that feeding a cell with hydrogen with increasing CO contents causes a more negative slope on the polarization curve compared to that measured with pure hydrogen; this effect was more noticeable for higher current densities (> 300 mA cm^2). Similar results were already reported by other authors. [44,45].

The potential needed to oxidize hydrogen (potential range of 0 to 0.2 V) is inferior to that needed to oxidize CO (a minimum of 350 mV on Pt/Ru) [46,47]; the latter occupies the active sites following a Tempkin adsorption isotherm behaviour. If the temperature is kept constant, the CO coverage increases with its concentration in the feed, progressively blocking the active sites for the HOR resulting in lower performances [42].

3.3. External air bleeding

Figure 6a depicts the cell potential behaviour before and after introducing 10 ppm of CO together with gradually higher concentrations of air (0.5 %, 1 % and 1.5 %) in the fuel stream. 0.5 % of air is enough to cause significant gains in the performance (*ca*. 45 %) while 1.5 % of air in the anode suffices to mitigate the CO poisoning – Run #10. Figure 6b shows the EIS spectra for Runs #2, #3 and #10. Runs #2 and #10 displayed approximately the same anodic charge transfer resistance $R_a \approx 68$ mΩ cm^2 and the same series resistance $R_m \approx 217 \pm 4$ mΩ cm^2; the fuel feed of Run #10 contains 1.5 % of air (*ca*. 0.32 % of oxygen), 10 ppm of CO and the balance of hydrogen, this last from air.

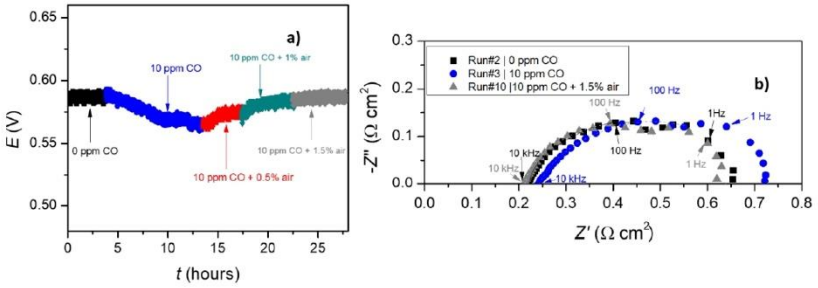


Figure 6. Effect of external bleeding at 500 mA cm^{-2} on a) chronopotentiometry and b) on EIS in MEA#1.

The effect of external air bleeding was also assessed using MEA#2. For this MEA, 1 % of air was enough to fully recover the reference potential, *cf*. Run#2 and #9 in Figure 7a. Impedance spectra for Runs #2, #3 and #9 are depicted in Figure 7b; spectra of Runs #2 and #9 overlap, confirming that the recovery from the CO poisoning was complete, in agreement with the characteristic curve results. Moreover, ohmic resistance increases when CO is added to the feed (Run #3) and returns to the reference

value when external bleeding is provided (Run #9): R_m is *ca.* 125.4 mΩ cm^2 for Run #3 and R_m of 107 ± 2 mΩ cm^2 for Run #2 and #9).

Several works in the literature report that the addition of a fraction of air to a CO contaminated hydrogen stream allows the recovery of the fuel cell performance as if it was operating with pure hydrogen [48–53]. Higher CO concentrations typically require higher levels of air bleeding; for example, anode air bleeding of 15 % (*ca.* 3 % of oxygen) is not enough to fully recover the performance of a cell fed with a 53 ppm CO-contaminated hydrogen stream [54]. However, excessive air bleeding (>15 %) is dangerous and leads to the fast membrane ageing and to the decrease of the output power since a significant amount of fuel oxidizes to water at the anode side. Nevertheless, the work by Wilson and his co-workers [55] is one of the few to report the effect of external air bleeding for mitigating CO poisoning present at low concentrations. These authors reported the use of an external bleeding stream of air (2 %) for fully recover the performance of a PEMFC fed with hydrogen contaminated with 5 ppm and 20 ppm of CO; the anode was loaded with 0.14 mg cm^{-2} of PtRu. A similar work comprehended the use of an external bleeding of 6.7 % (air) for a recovery ratio of 80 % with a 10 ppm CO-contaminated hydrogen stream while using a 0.45mg cm^{-2} Pt-Ru anode [54].

The oxygen reaction with the adsorbed CO on the catalyst surface produces CO_2. As soon as the CO is oxidized and removed, the catalyst sites become available for the HOR. Here, it is reported that 1 – 1.5 % of anode air bleed is sufficient to completely recover the performance of a 10 ppm CO-contaminated fuel stream under typical operating conditions, *i.e.* m-CHP systems. To safely supply oxygen (or air) into the anode, its concentration should be kept always below the limiting oxygen concentration, which for 1 bar and room temperature is *ca.* 5 % of oxygen [56]. Furthermore, such oxygen content at the anode did not impact the open circuit potential of the cell, thus it does not contribute for lowering the PEMFC performance.

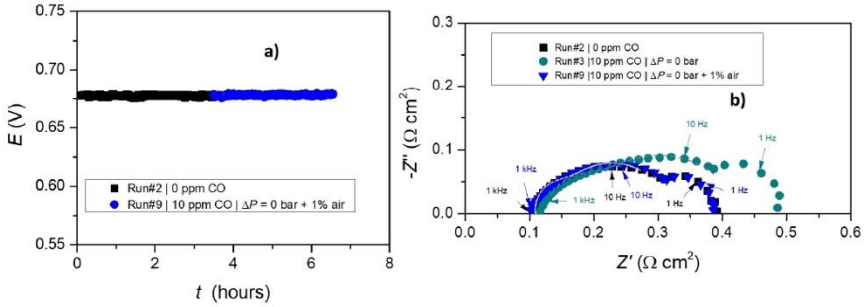


Figure 7. Effect of external air bleeding at 500 mA cm^{-2}on a) chronopotentiometry and on b) EIS in MEA#2.

3.4. Cell electrochemical stability upon implementation of bleeding strategies

Figure 8a and b compare long-term chronopotentiometries of Run #5 and Runs #9 and #10 with internal and external air bleeding, respectively, for MEA#1 and MEA#2. After reaching the steady-state

potential at a current density of 500 mA·cm^{-2}, the potential loss history was recorded for assessing the long-term stability. A potential loss rate of $1.58 \cdot 10^{-4}$ V h^{-1} is observed for an internal bleeding of 200 mbar of cathode over-pressure – Run #5 in MEA#1; on the other hand, after *ca.* 80 h of operation, MEA#2 displays a potential loss rate of $9.45 \cdot 10^{-5}$ V h^{-1} under the same operating conditions. After *ca.* 8 h of operation the performance loss of MEA#1 under external bleeding is negligible (loss rate of *ca.* $4.30 \cdot 10^{-6}$ V h^{-1}) – Run #10, while MEA#2 displays a potential loss rate of $8.04 \cdot 10^{-5}$ V h^{-1} – Run #9. At reference conditions, for a CO free hydrogen feeding, the observed potential loss rate was $9.43 \cdot 10^{-7}$ V h^{-1} for MEA#1 and $9.00 \cdot 10^{-6}$ V h^{-1} for MEA#2. These values are quite similar to the ones obtained for the external bleeding experiments, showing that this method is not only sufficient to recover the performance of the cell but also causes less cell potential decay than internal bleeding; nonetheless, some authors have reported a detrimental effect in long-term performance when using external air bleeding due to H_2O_2 formation [16]. However, the results of demonstrate that MEA#1, that uses a thicker membrane, displays a better long-term stability even at higher air bleed concentrations than MEA#2 – 1.5 % air bleed in MEA#1 vs. 1 % of air in MEA#2.

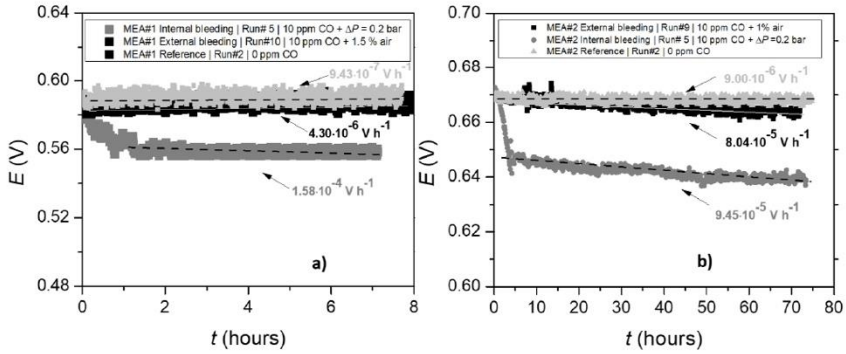


Figure 8. Long-term chronopotentiometry of two types of air bleeding at 500 mA cm^{-2} in a) MEA#1 and b) MEA#2.

Cyclic voltammetry was performed to assess the impact of CO contamination over both anode and cathode ECSA after a complete set of experiments (Runs# 3 to 9) with MEA#2. Figure 9a and b depict the BoL CV, and the end of life (EoL) CV for the anode and cathode of MEA#2, respectively. The CVs present distinct shapes due to the different catalysts used in each electrode. The peak areas reflect the number of Pt active sites to hydrogen adsorption/desorption. The anode CVs display solely one peak typical of Pt-Ru catalysts [57]. On the other hand, the cathode displays two peaks at the anodic currents region ($i > 0$) accounting for the H desorption on Pt (111) at ~ 110 mV and Pt(100) at ~ 215 mV [58]. The reduction process is electrochemically reversible since the difference between the anodic and cathodic peak potentials is less than 59 mV. After performing all tests involving CO coverage, the electrochemically active surface area seems to be kept intact with no signs of loss on catalytic activity,

Figure 9c. This result confirms the great stability of Pt-Ru alloy towards CO contaminated hydrogen streams [59]. Moreover, Wagner and Schulze [60] confirmed by EIS analysis the excellent properties of Pt-Ru/C anodes as CO-tolerant electrocatalysts for the HOR; not only do they provide less anodic charge transfer resistance but also generate less mass transfer resistance compared to Pt/C based anodes. However, there is an evident loss of active surface area of Pt at the cathode, nearly 16 %, due to the typical catalyst layer degradation that comprehends Pt dissolution/sintering, carbon corrosion and ionomer dissolution [61].

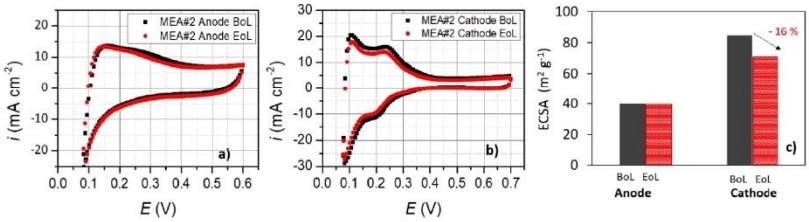


Figure 9. Cyclic voltammograms at beginning of life (BoL) and end of life (EoL) of the **a)** anode and **b)** cathode of MEA#2; scan rate: 50 $mV \cdot s^{-1}$; RH: 50 %; Stoic.: 1.5/2 (H_2/O_2) at 100 $mL \cdot min^{-1}$).

4. CONCLUSIONS

In the present study, the performance of PEMFCs was evaluated while feeding H_2 and CO (10 ppm) to a Pt-Ru based anode and compared with the performance with pure hydrogen at 70 °C. Oxygen concentrations were tuned and applied to the anode – by means of internal air or external air bleeding - to assess the minimum concentration to mitigate CO poisoning. Simultaneously, the long-term stability of the cells was monitored to ascribe the potential decay with each air bleeding strategy.

The potential drop caused by feeding H_2 contaminated with 10 ppm of CO was 3 % at 500 $mA \cdot cm^{-2}$ for the fuel cells equipped with Nafion HP membrane and a Nafion 212 membrane; nonetheless, the dynamic response to the addition of 10 ppm of CO was slow, reaching the new steady state performance after *ca.* 5 h. The air feed over-pressure of 0.2 bar at the cathode allowed the re-activation of the poisoned catalyst and a cell potential recovery of over 30 % in both MEAs. The success of internal bleeding towards CO oxidation along with the stability was found to depend on the mechanical strength of each membrane that equipped the MEAs. Thinner but reinforced and stabilized Nafion HP membrane displayed lower performance recovery but higher stability during mid-term diagnosis, in contrast to the non-reinforced and thicker Nafion 212 membrane.

Performing external air bleeding proved to be the most effective approach. In fact, adding an air bleed of 1 % and 1.5 % in the fuel stream for both MEAs promoted full CO oxidation and thus nearly 100 % recovery of cell performance (comparing to neat hydrogen). Accordingly, up to 1.5 % of air in the anode side showed to be harmless for long-term operation. This strategy is then recommendable for stationary applications, namely for residential power generation, whenever the feeding hydrogen contains up to *ca.* 10 ppm.

ACKNOWLEDGEMENTS
The authors acknowledge the financial support from the project UID/EQU/00511/2019 - Laboratory for Process Engineering, Environment, Biotechnology and Energy – LEPABE funded by national funds through FCT/MCTES (PIDDAC) and PEMFC-SUDOE - nº SOE1/P1/E0293 funded by FEDER funds through COMPETE2020 - Programa Operacional Competitividade e Internacionalização (POCI) and Programa Operacional Regional do Norte (NORTE2020) and by national funds (PIDDAC) through FCT/MCTES.

References

1. J. Tjønnås, F. Zenith, I.J. Halvorsen, M. Klages, J. Scholta, *IFAC-PapersOnLine*, 49 (2016) 302–307.
2. C.A. Rice, P. Urchaga, A.O. Pistono, B.W. McFerrin, B.T. McComb, J. Hu, *J. Electrochem. Soc.*, 162 (2015) F1175–F1180.
3. S. Foresti, G. Manzolini, S. Escribano, *Int. J. Hydrogen Energy*, 42 (2017) 25334–25350.
4. T.J. Park, S.M.; O'Brien, Effects of Several Trace Contaminants on Fuel Cell Performance, (1979).
5. N. Hayter, P R; Mitchell, P; Dams, R A.J.; Dudfield, C; Gladding, The Effect of Contaminants in the Fuel and Air Streams on the Performance of a Solid Polymer Fuel Cell, (1997).
6. P.E. Dodds, I. Staffell, A.D. Hawkes, F. Li, P. Grünewald, W. McDowall, P. Ekins, *Int. J. Hydrogen Energy*, 40 (2015) 2065–2083.
7. I. Staffell, *Appl. Energy*, 147 (2015) 373–385.
8. R.A. Lemons, *J. Power Sources*, 29 (1990) 251–264.
9. H. Igarashi, T. Fujino, M. Watanabe, *J. Electroanal. Chem.*, 391 (1995) 119–123.
10. X. Cheng, Z. Shi, N. Glass, L. Zhang, J. Zhang, D. Song, Z.S. Liu, H. Wang, J. Shen, *J. Power Sources*, 165 (2007) 739–756.
11. Z. Qi, C. He, A. Kaufman, *J. Power Sources*, 111 (2002) 239–247.
12. R.J. Bellows, E.M. Soos, R.P. Reynolds, *Electrochem. Solid-State Lett.*, 1 (1999) 69.
13. L.P.L. Carrette, K.A. Friedrich, M. Huber, U. Stimming, Phys. Chem. Chem. Phys., (2001).
14. C.-C. Chung, C.-H. Chen, D.-Z. Weng, *Appl. Therm. Eng.*, 29 (2009) 2518–2526.
15. R. Bashyam, P. He, S. Wessel, S. Knights, ECS Trans., (2011).
16. S. Knights, R. Bashyam, P. He, M. Lauritzen, C. Startek, V. Colbow, T. Cheng, J. Kolodziej, S. Wessel, *ECS Trans.*, 41 (2011) 39–53.
17. M.J. Lee, J.S. Kang, Y.S. Kang, D.Y. Chung, H. Shin, C.Y. Ahn, S. Park, M.J. Kim, S. Kim, K.S. Lee, Y.E. Sung, *ACS Catal.*, 6 (2016) 2398–2407.
18. S. Alayoglu, A.U. Nilekar, M. Mavrikakis, B. Eichhorn, *Nat. Mater.*, 7 (2008) 333–338.
19. A.H. Thomason, T.R. Lalk, A.J. Appleby, *J. Power Sources* (2004).
20. Y. Kurihara, T. Mabuchi, T. Tokumasu, *J. Electrochem. Soc.* (2017).
21. T. Kawakami, I. Shigemoto, N. Matubayasi, *J. Chem. Phys.* (2012).
22. A.T. Haug, R.E. White, *J. Electrochem. Soc.* (2000).
23. P. Gode, G. Lindbergh, G. Sundholm, *J. Electroanal. Chem.* (2002).
24. K. Lee, A. Ishihara, S. Mitsushima, N. Kamiya, K. Ota, *J. Electrochem. Soc.* (2004).
25. V.A. Sethuraman, S. Khan, J.S. Jur, A.T. Haug, J.W. Weidner, *Electrochim. Acta* (2009).
26. S.S. Kocha, J.D. Yang, J.S. Yi, *AIChE J.*, 52 (2006).
27. J. Zhang, T. Thampan, R. Datta, *J. Electrochem. Soc.* (2002).
28. M. Murthy, M. Esayian, A. Hobson, S. Mackenzie, W. Lee, J.W. Van Zee, M. Murthy,a, J.W. Van Zee, *J. Electrochem. Soc.* (2001).
29. Y. V. Pleskov, Y.E. Evstefeeva, M.D. Krotova, V. V. Elkin, A.M. Baranov, A.P. Dement'Ev, *Diam. Relat. Mater.*, 8 (1999) 64–72.
30. X.-Z. Yuan, S. Zhang, H. Wang, J. Wu, J.C. Sun, R. Hiesgen, K.A. Friedrich, M. Schulze, A.

Haug, *J. Power Sources*, 195 (2010) 7594–7599.
31. L. Yu, F. Lin, L. Xu, J. Xi, *RSC Adv.*, 7 (2017) 31164–31172.
32. DuPont Fuel Cells, DuPont™ Nafion® PFSA Membranes NR-211 and NR-212, (2008).
33. DuPont Fuel Cells, (2010).
34. S. Slade, S.A. Campbell, T.R. Ralph, F.C. Walsh, *J. Electrochem. Soc.*, 149 (2002) A1556.
35. X.-Z. Yuan, S. Zhang, H. Wang, J. Wu, J.C. Sun, R. Hiesgen, K.A. Friedrich, M. Schulze, A. Haug, *J. Power Sources*, 195 (2010) 7594–7599.
36. M.N. Tsampas, A. Pikos, S. Brosda, A. Katsaounis, C.G. Vayenas, *Electrochim. Acta*, 51 (2006) 2743–2755.
37. W. Wang, *J. Power Sources*, 191 (2009) 400–406.
38. K.M. Nouel, P.S. Fedkiw, *Electrochim. Acta*, 43 (1998) 2381–2387.
39. F. Liu, B. Yi, D. Xing, J. Yu, H. Zhang, *J. Memb. Sci.*, 212 (2003) 213–223.
40. J. Shim, H.Y. Ha, S.-A. Hong, I.-H. Oh, *J. Power Sources*, 109 (2002) 412–417.
41. H.-L. Lin, T.L. Yu, L.-N. Huang, L.-C. Chen, K.-S. Shen, G.-B. Jung, *J. Power Sources*, 150 (2005) 11–19.
42. H.P. Dhar, L.G. Christner, A.K. Kush, H.C. Maru, *J. Electrochem. Soc.* , 133 (1986) 1574–1582.
43. U. Oetjen, H.-F., Schmidt, V.M , Stimming, *J. Electrochem. Soc.*, 143 (1996) 3838.
44. V.M. Schmidt, R. Ianniello, H.-F. Oetjen, H. Reger, U. Stinuning, F. Trila, *ECS Proc. Vol.* , 1995–23 (1995) 1–11.
45. Y. Si, R. Jiang, J.-C. Lin, H.R. Kunz, J.M. Fenton, *J. Electrochem. Soc.*, 151 (2004) A1820–A1824.
46. Y. Takasu, T. Kawaguchi, W. Sugimoto, Y. Murakami, *Electrochim. Acta*, 48 (2003) 3861–3868.s
47. T. Gu, W.-K. Lee, J.W. Van Zee, M. Murthy, *J. Electrochem. Soc.*, 151 (2004) A2100–A2105.
48. L.Y. Sung, B.J. Hwang, K.L. Hsueh, F.H. Tsau, *J. Power Sources*, 195 (2010) 1630–1639.
49. T. Tingelöf, L. Hedström, N. Holmström, P. Alvfors, G. Lindbergh, *Int. J. Hydrogen Energy*, 33 (2008) 2064–2072.
50. L.Y. Sung, B.J. Hwang, K.L. Hsueh, W.N. Su, C.C. Yang, *J. Power Sources*, 242 (2013) 264–272.
51. F.A. Uribe, J.A. Valerio, F.H. Garzon, T.A. Zawodzinski, *Electrochem. Solid-State Lett.*, 7 (2004) A376–A379.
52. R.C. Urian, A.F. Gullá, S. Mukerjee, *J. Electroanal. Chem.*, 554–555 (2003) 307–324.
53. T. Morawietz, M. Handl, C. Oldani, K.A. Friedrich, R. Hiesgen, *ACS Appl. Mater. Interfaces*, 40 (2016) 27044–27054.
54. X. Cheng, Z. Shi, N. Glass, L. Zhang, J. Zhang, D. Song, Z.-S. Liu, H. Wang, J. Shen, *J. Power Sources*, 165 (2007) 739–756.
55. S.F.. Wilson, M.S., Derouin, C.R., Valerio, J.A., and Gottesfeld, Conf. 28. Intersoc. Energy Convers. Eng. Conf. Atlanta, GA (United States), 8-13 Aug 1993, (1193).
56. I.A. Zlochower, G.M. Green, *J. Loss Prev. Process Ind.*, 22 (2009) 499–505.
57. S.J. Yoo, T.Y. Jeon, K.S. Kim, T.H. Lim, Y.E. Sung, *Phys. Chem. Chem. Phys.*, 46 (2010) 15240–15246.
58. W. Sheng, Z. Zhuang, M. Gao, J. Zheng, J.G. Chen, Y. Yan, *Nat. Commun.*, 6 (2015) 5848.
59. H.-F. Oetjen, *J. Electrochem. Soc.* (1996).
60. N. Wagner, M. Schulze, *Electrochim. Acta*, 48 (2003) 3899–3907.
61. X. Yu, S. Ye, *J. Power Sources*, 172 (2007) 145–154.

© 2020 The Authors. Published by ESG (www.electrochemsci.org). This article is an open access article distributed under the terms and conditions of the Creative Commons Attribution license (http://creativecommons.org/licenses/by/4.0/).

INTERNATIONAL JOURNAL OF HYDROGEN ENERGY 45 (2020) 20594–20604

Available online at www.sciencedirect.com

ScienceDirect

journal homepage: www.elsevier.com/locate/he

The role of Pt loading on reduced graphene oxide support in the polyol synthesis of catalysts for oxygen reduction reaction

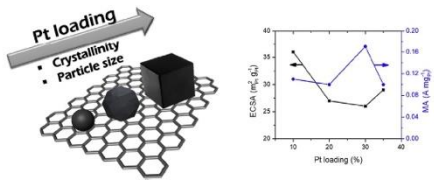
*Tiago Lagarteira, Sofia Delgado, Celina Fernandes, Cátia Azenha, Cecilia Mateos-Pedrero, Adélio Mendes**

Laboratory for Process Engineering, Environmental, Biotechnology and Energy (LEPABE), Faculty of Engineering of University of Porto, Rua Dr. Roberto Frias S/n, 4200-465 Porto, Portugal

HIGHLIGHTS

- 30 wt.% of Pt/rGO presented the best Pt particle dispersion on the support.
- rGO-supported catalysts displayed impressive area-specific ORR activities.
- Increasing Pt loading on rGO led to higher Pt average particle size.

GRAPHICAL ABSTRACT



ARTICLE INFO

Article history:
Received 15 October 2019
Received in revised form
24 December 2019
Accepted 4 February 2020
Available online 27 February 2020

Keywords:
Proton exchange membrane fuel cell
Oxygen reduction reaction
Catalyst durability
Reduced graphene oxide support

ABSTRACT

Common carbon-blacks have shown insufficient stability as cathodic catalyst supports for proton exchange membrane fuel cells (PEMFCs). In this regard, alternative supports have been proposed and, specifically graphene or reduced graphene oxide (rGO), have attracted special attention. Herein, a set of electrocatalysts using reduced graphene oxide (rGO) as support is synthetized by a modified polyol method. The influence of Pt loading on the support is studied and compared with conventional supports, considering Pt particle morphologies and oxygen reduction reaction (ORR) performance in rotating disk electrode (RDE). Despite Pt average particle size typically increases with the Pt loading, 30 wt% of Pt on rGO is the optimal Pt loading, yielding the highest ORR activity among the rGO-supported electrocatalysts. These results show that both Pt loading and type of support greatly impact on the morphology and electrochemical performance of Pt nanoparticles.

© 2020 Hydrogen Energy Publications LLC. Published by Elsevier Ltd. All rights reserved.

* *Corresponding author.*
E-mail addresses: lagarteira@fe.up.pt (T. Lagarteira), sdelgado@fe.up.pt (S. Delgado), celina@fe.up.pt (C. Fernandes), catia@fe.up.pt (C. Azenha), cmpedrero@fe.up.pt (C. Mateos-Pedrero), mendes@fe.up.pt (A. Mendes).
https://doi.org/10.1016/j.ijhydene.2020.02.022
0360-3199/© 2020 Hydrogen Energy Publications LLC. Published by Elsevier Ltd. All rights reserved.

Introduction

Proton exchange membrane fuel cells (PEMFCs) are recognized as a promising power source for both transport and stationary applications owing to the high power density, high efficiency and compact design [1–3]. Moreover, the technology is environmentally friendly since electricity is generated by the direct electrochemical conversion of hydrogen and oxygen into water. Pt-based catalysts, supported on electrically-conductive materials, commonly carbon blacks, are used as electrodes [4]. Particularly, the sluggish kinetics and high overpotential of oxygen reduction reaction (ORR) require high-performance catalysts to achieve high power output with ultra-low Pt loading [5]. The continuous decrease in Pt loading has been a subject of paramount importance among the scientific community; it means a significant reduction in the overall-cost and sustainability of PEMFC stacks, due to the limited world reserves of platinum [6]. Despite some reports [7–11] met the target for ORR mass-specific activity set by the US Department of Energy (0.44 A mg^{-1}_{Pt} @ 0.9 $V_{i\text{-}R\ free}$), stability remains one of the major issues for the widespread commercialization of PEMFCs [12].

Different strategies have been employed to boost ORR activity while reducing the amount of Pt, either by alloying Pt with other metals, dealloying Pt-M alloys to obtain skeleton-like structures or synthetizing core-shell structures. Nevertheless, just the downsizing of Pt particles, by dispersing them on carbon supports, has shown great potential to increase the electrochemical surface area (ECSA) and thus the Pt utilization [5]. Pt nanoparticles smaller than 2–3 nm are thermodynamically unstable [13], displaying a non-defined crystallographic structure and making them less attractive both in terms of stability and activity (particle-size effect) [14–16]. Additionally, the interaction between the support material and the metal catalyst also influences the activity and stability of the supported-catalyst, either from electronic or geometric effects [17,18]. Hence, the main challenge is to support the metallic catalyst in materials with good electrical conductivity, corrosion resistance and suitable porosity to provide reactive sites and enhanced diffusion paths to the reactants and products [19].

Recently, new carbon materials such as ordered mesoporous carbons, carbon aerogels, carbon nanotubes (CNTs) [20,21], carbon nanohorns [22] and carbon nanofibers [23,24] have been tested as supports to meet the above referred criteria. Among those, graphene, a two-dimensional one-atom-thick planar sheet of sp^2-bonded carbon atoms, can be considered as the building block for all fullerene allotropic dimensionalities [25,26]. Graphene, has great potential for many applications, serving from recently discovered anticorrosion additive for solar absorber films to resilient catalyst supports [27–29]. Most studies that report the use of graphene supports, aim to develop not only functional electrocatalysts for ORR but also for anodes of direct methanol fuel cells (DMFCs) due to improved CO tolerance [30–34]. However, there is a huge dispersion of results concerning ECSA values in literature, ranging from ca. 35 to 80 m^2_{Pt} g^{-1}_{Pt}, some of them obtained using very similar preparation methods [30,33,35–39]. This suggests that the electrochemical performance of graphene-supported is highly sensitive not only to the synthesis method (Pt precursor, Pt/carbon ratio, pH, reaction duration, reducing agent, surfactants) but also to post-synthesis treatments and methods used to functionalize the supports.

To the best of authors' knowledge, this work reports for the first time the influence of Pt loading on rGO using the widely-spread polyol electrocatalyst synthesis. The electrochemical performance of the electrocatalysts is correlated with ex-situ analysis carried out to disclose Pt particle size, crystallography and dispersion over rGO. Moreover, other types of carbon materials are used and compared with rGO-supported catalyst with similar Pt loading. The synthetized electrocatalysts and commercial references are analyzed with TEM, TGA, XRD and BET, and characterized electrochemically to measure their ECSA and ORR activity. Finally, the stability of the best-performing electrocatalysts upon accelerated degradation is also assessed.

Materials and methods

Modified polyol synthesis

Electrocatalysts were prepared by chemical reduction of a Pt precursor in ethane-1,2-diol solution. Graphene oxide (Nanoinnova), Vulcan XC-72R (Cabot) and multi-wall carbon nanotubes (Sigma-Aldrich) were used as-received in a typical polyol synthesis. 100 mg of each carbon support was first added to ethane-1,2-diol (VWR, 99%), and the resultant suspension was sonicated for 1 h to obtain a homogenous solution. Following, required amounts of chloroplatinic acid hexahydrate (ACS, $\geq$ 37.5%) and deionized water were added to the above dispersion to obtain 5 vol % of water in ethane-1,2-diol. The synthesis was then carried out for 5 h under reflux at 150 °C with constant stirring. Finally, upon cooling to room temperature, the resulting colloid was filtered and washed extensively with water before being dried in an oven at 120 °C.

Electrocatalysts were named according to their composition, using the following nomenclature, XPtY, where X represents the Pt loading (wt. %) and Y the carbon support (Vulcan – Vulcan XC-72R; CNTs – multi-wall carbon nanotubes; and rGO – reduced graphene oxide). Electrocatalysts that were subjected to accelerated degradation were identified with "AD".

Physicochemical characterization

Thermogravimetric analysis (TGA) was performed using a thermogravimetric analyzer (TG 209 F1 iris, NETZSCH) under 20 cm^3 min^{-1} of air flow, heating from room temperature to 900 °C at 2 °C min^{-1}. In each analysis, ca. 4–7 mg of sample was used.

The synthetized catalysts were examined using a transmission electron microscope (TEM), a Jeol JEM 1400. Samples for TEM analysis were prepared by placing a single drop of ultrasonicated sample suspension onto a copper grid. TEM images were processed with ImageJ software. To calculate the

average particle size, 30 platinum particles were measured in each electrocatalyst sample.

The structure of the catalysts was studied using XRD. The X-ray pattern of the samples was collected using a PANanlytical X'Pert Pro operating in Bragg-Bretano focusing geometry and using Cu Kα radiation at wavelengths Cu Kα1 = 1.5406 Å and Cu Kα2 = 1.54443 Å. The data was collected at 2θ angles (15–95°), with a step size of 0.017°. X-ray scans were compared to those of standard database and the phases were assigned comparing with data available in the literature. The crystallite size of platinum phases was based on X-ray diffraction line broadening and calculated by Williamson-Hall method after peak refining.

Textural properties of the samples were evaluated by N_2 physisorption at −196 °C in a Quantachrome Autosorb-1 Instruments apparatus. The surface area (S_{BET}) was calculated using the Brunauer-Emmett-Teller (BET) equation in the nitrogen partial pressure range (P/P^0) from 0.05 to 0.15. Prior to the analysis, the samples (40 mg) were outgassed in vacuum at 200 °C overnight.

Electrochemical measurements

ORR measurements were performed in a Gamry RDE equipped with an Eurocell Electrochemical Kit. A Zahner IM6-ex was used as potentiostat and impedance spectrometer. The glassy carbon electrode (GCE) was polished with 0.05 μm alumina-particle solution prior to each film deposition. Catalyst inks were prepared by keeping constant the mass of carbon (2 mg), 7.96 ml of ultra-pure water, 2 ml isopropanol (Alfa Aesar) and 40 μl Nafion (5 wt%, Quintech). Catalyst inks were ultrasonicated (50 W, Hielscher UP50H) in an ice-bath for 15 min. Two drops of 10 μl each were deposited on the GCE and dried at 700 rotations per minute (RPM) and room temperature. Immediately after dipping the working electrode (GCE of ca. 0.2 cm^2) into the electrolyte (0.1 M $HClO_{4(aq)}$, 70% conc. Sigma Aldrich), the potential was maintained at 0.4 V to avoid exposure to open circuit potential (OCP). An Ag/AgCl reference electrode was used. The following protocol was chosen considering previous reports [5,40–44]. The electrode was first conditioned in Ar during 100 cycles between 50 mV and 1 V (vs. RHE) at 100 mV s^{-1} and 0 RPM. The electrochemical surface area (ECSA) was then determined by H_{UPD} method at 20 mV s^{-1} and 0 RPM, with charge integration of the hydrogen adsorption/desorption peak from the third negative scan and using **210 μC** cm^{-2} as the charge of a fully H_2-covered Pt monolayer. Electrochemical impedance spectroscopy (EIS) was performed in potentiostatic mode (0.4 V) using a 5 mV perturbation between 1 kHz–0.1 Hz to measure the ohmic resistance of the electrolyte. Linear sweep voltammetry (LSV), between 50 mV–1 V (vs. RHE) at 20 mV s^{-1}, was carried out to measure the background currents (in Ar) and ORR activity (in O_2) both at 1600 RPM. The electrolyte was saturated by bubbling 100 ml min^{-1} of gas during 30 min. Gas blanketing was used to prevent electrolyte contamination from the exterior of the cell. A commercial catalyst was used to compare the performance of the synthesized catalysts: 20% Pt/C ETEK from BASF.

The protocol for studying the catalyst stability comprehends 10 000 cycles, between 20 and 925 mV (vs. RHE), at 500 mV s^{-1} in O_2-saturated electrolyte. The samples were then subjected to a new conditioning in Ar, before measuring the ECSA and ORR activities.

Results and discussion

Suitability of the polyol method

20PtVulcan was prepared using the polyol method and ORR performance is compared with a commercial sample (20PtE-TEK) in Fig. 1. Despite the synthetized 20PtVulcan presents lower ECSA, it displayed higher area and mass specific activities at 0.9 V (vs. RHE), when compared with the commercial sample. After confirming the suitable use of the polyol method for preparing functional electrocatalysts, the rGO and CNTs-supported platinum catalysts were then prepared and characterized.

Influence of the carbon support

The thermal stability and Pt loading of the synthetized electrocatalysts were determined by TGA under air flow. A sample of reduced graphene oxide, submitted to the polyol method but without Pt precursor, was tested to assess if any remaining material, besides platinum, would be present at the end of the analysis. The obtained results indicate a weight loss of almost 100% showing, therefore, that the residual mass of the supported catalysts after TGA corresponds to the Pt content. The influence of type of support employed is depicted in Fig. 2a. Pt/CNTs displays the highest thermal stability followed by Pt/rGO. Chiang et al. observed that the maximum rates of weight loss of their GO and Vulcan XC-72R take place at ca. 715 °C; they also found that Pt/rGO was more thermally stable than Pt/Vulcan [45]. These authors strengthened that when Pt is nucleated in a carbon support, the maximum rate of weight loss decreases significantly.

The influence of Pt content on the thermal stability of the rGO-supported catalysts is depicted in Fig. 2b. The thermograms suggest that Pt increases the thermal stability of the supported catalyst in comparison with the support alone. However, this should be assigned to the reduction of most oxygenated groups during the polyol synthesis, increasing the crystallinity of the support. After the synthesis of 35PtrGO, the filtrate presented a yellow color due to the presence of unreacted precursor, suggesting that all anchoring sites were already occupied [46]. Under the conditions of this synthesis, it seems unfeasible to achieve ratios of Pt/rGO higher than 30–35 wt %. Few works in the literature succeeded to obtain higher Pt loadings on rGO (60–80 wt%) and they achieved them through either support functionalization [47,48] or more complex synthesis methods [34,49].

The synthetized electrocatalysts were analyzed by TEM – Fig. 3 – to evaluate the average size and dispersion of Pt particles. The average Pt particle size is given in Table 1. The catalysts synthetized with 20 wt% of Pt in the three selected supports present an average Pt particle size of 6–7 nm. Regarding the rGO-supported catalysts, the average Pt particle size increases with the Pt loading, ranging from 4 to 9 nm. The polyol synthesis allows to achieve Pt particles of small average sizes, between 2 and 4 nm; however, some cases comprised

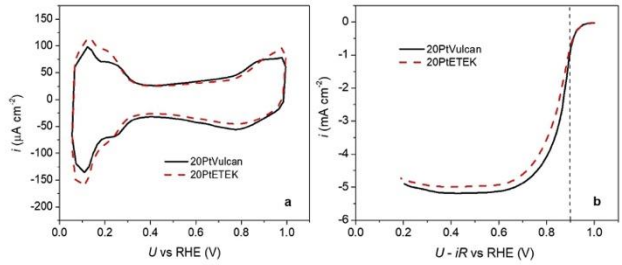


Fig. 1 – ECSA and ORR activity measurements of synthesized 20PtVulcan and commercial sample: a) cyclic voltammograms in Ar at 20 mV s^{-1}; b) linear sweep voltammograms in O_2 at 1600 RPM and 20 mV s^{-1}.

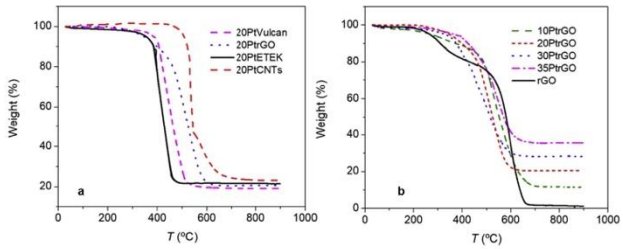


Fig. 2 – Thermal gravimetric analysis (20 ml min^{-1} of air, 2 °C min^{-1}) to assess the influence of a) the carbon support on the thermal stability of carbon-supported Pt catalysts; b) the Pt loading on the thermal stability of Pt/rGO catalysts.

precise pH control throughout the synthesis in contrast to the modified polyol method employed in this study, chosen by its simplicity. The higher Pt particle size obtained in this work can be explained by slightly different pH conditions from those reported by other studies [50,51]. The effect of pH has been a subject of interest but there is not a full agreement in the literate. Some studies report that an acidic pH provided by the glycolate anion can alter the electrostatic forces between the support and the Pt colloid thus increasing the metal particle final size [46,52]. Nonetheless, Liu et al. reports a similar Pt particle mean size distribution, of ca 4.5 nm, also produced by a modified polyol method with no pH control [53].

Despite some agglomeration located especially at the edges of rGO sheets (Fig. 3e), the 30PtrGO sample presents similar dispersion of Pt particles to those supported in Vulcan and CNTs. Nevertheless, the dispersion of Pt particles in the 20PtrGO sample is poor, due to the relatively low BET surface area of the carrier. The intense black zone that is visible in some of the Pt/rGO samples corresponds to the wrinkling of rGO sheets.

For all catalysts, the incorporation of platinum causes a loss of BET specific area (ca. 50–70%), suggesting that the texture of the supports is somehow altered by the Pt particles, Table 2 and Table 3. The low BET surface area measured for 20PtCNTs, of ca. 15 $m^2 g^{-1}$, can again be explained by the low surface area of the carbon nanotubes (28 $m^2 g^{-1}$ is reported by the manufacturer).

X-ray diffractograms of the carbon-supported Pt catalysts are presented in Fig. 4. For the rGO sample, the characteristic (0 0 2) peak assigned to graphitic carbon (JCPDS 75-1621) appears at ca. 26.0° meaning that the functional surface groups of GO (anchoring sites) were partially reduced after the polyol protocol. In the GO sample, the characteristic (1 0 0) peak is dominant over the (0 0 2) [54,55]. One fact that stands out is the high crystallinity evidenced by the sharp peak at ca. 25.0° for the sample 20PtCNTs [56]. The diffraction peaks at 40.0°, 46.0°, 67.5° and 81.4° correspond to the characteristic (1 1 1), (2 0 0), (2 2 0) and (3 1 1) crystalline planes of Pt (JCPDS 04-0802) of a face-centered-cubic structure [30].

The crystallite size of each catalyst was obtained by the Williamson-Hall method and listed in Table 3. As can be observed, the mean Pt crystallite size of the synthesized catalysts was determined to be ca. 5–7 nm, regardless of the carbon support, in good agreement with the TEM results.

This suggests that the carbon support has no major influence in the resulting Pt crystallite sizes. ECSA and ORR activity in RDE of the prepared Vulcan XC-72R, CNTs and rGO-based catalysts are summarized in Table 4. The highest ECSA (64 $m^2 g^{-1}$) was obtained for 20PtVulcan, followed by 20PtCNTs and 20PtrGO, respectively. The geometric activity at 0.4 V typically displays the diffusion-limited activity; the results

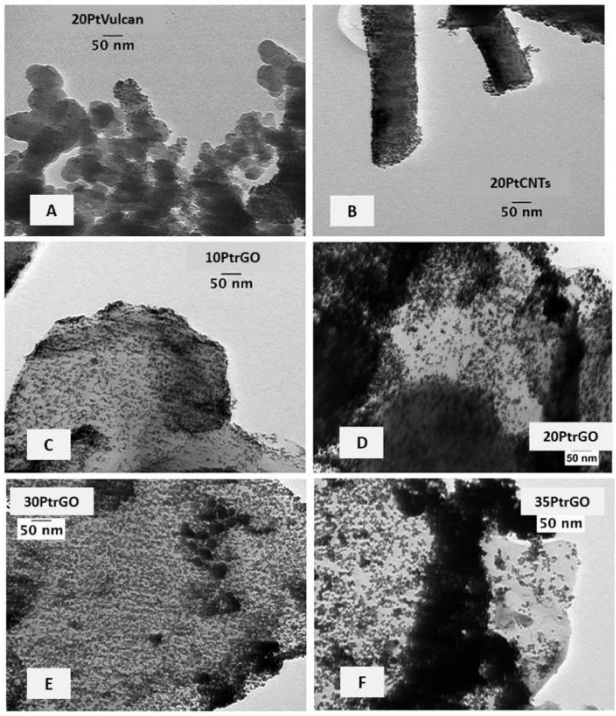


Fig. 3 – TEM images of synthetized catalysts – 200 000x of magnification.

Table 1 – Average Pt particle size of synthetized electrocatalysts measured by TEM.

Catalyst sample	Average Pt particle size (nm)
20PtETEK	2–3[a]
20PtVulcan	5.9
20PtCNTs	6.6
10PtrGO	4.3
20PtrGO	6.3
30PtrGO	8.4
35PtrGO	9.5

[a] Information from the manufacturer.

obtained for 20PtVulcan and 20PtCNTs were similar and lower for 20PtrGO. A performance-microstructure dependence is evident and rGO seems to generate diffusion problems in which O_2 molecules struggle more to reach the active sites [57]. Moreover, the linear scan does not present the plateau that is observed in the other catalysts, which also suggests the existence of increased diffusion overpotentials, Fig. 5b.

30PtrGO displayed the highest area-specific activity (0.66 mA cm^{-2}_{Pt}) outperforming 20PtVulcan (0.33 mA cm^{-2}_{Pt}); on the other hand, the latter presents higher mass-specific activity (0.21 A mg^{-1}_{Pt}) than the former (0.17 A mg^{-1}_{Pt}). The work by Debe [58] provides an interesting explanation about the geometry effects that influence ORR specific activities. The author concluded that polycrystalline single crystal bulk surfaces, possess 5 to 10 times higher oxygen reduction area-specific activity than smaller spheroid metal catalyst particles; this effect balances the lower surface area of the platelet-like metal particles. ORR mechanisms are dependent on the electrode's surface area per unit of volume (cm^2_{Pt}/cm^3_{Pt}) and, in the Knudsen regime, the electrode microstructure influences the number of chemisorption bounds established per unit of time. Pt/rGO seems to possess a microstructure that behaves closer to a platelet-like catalyst owing to its high area-specific activity but low mass-specific activity. Due to the self-similar geometries of dispersed catalysts with respect to surface area and loading, they are more dependent on the catalyst loading than the platelet-like catalyst. A reduction in the

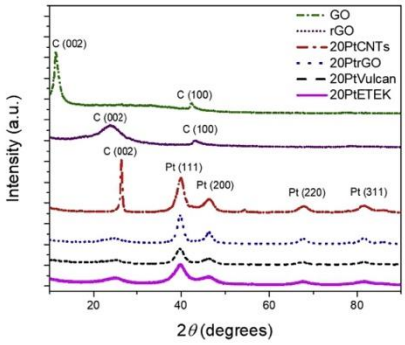


Fig. 4 – X-ray diffraction patterns of the carbon-supported Pt catalysts; graphitic carbon (JCPDS 75-1621), Pt (JCPDS 04-0802).

Table 2 – Results from BET surface area determination.

Sample	Surface area ($m^2\ g^{-1}$)
Vulcan XC72-R	272.2
Graphene oxide	62.3
Reduced graphene oxide	103
CNTs	220
20PtETEK	191.9
20PtVulcan	185.2
20PtrGO	33.4
20PtCNTs	15.1

Table 3 – Pt mean crystallite size determined from XRD.

Catalyst sample	Pt mean crystallite size (nm)
20PtETEK	5.3 ± 0.5
20PtVulcan	5.7 ± 0.5
20PtrGO	6.5 ± 0.5
20PtCNTs	6.9 ± 1

Pt loading will then generate a higher loss of surface area for Pt/Vulcan than for Pt/rGO. Xin et al. reported higher ORR activities for Pt supported on graphene when compared with Pt supported on Vulcan XC-72, both synthetized using $NaBH_4$ as reducing agent [31]. Shao et al. compared the performance of two catalysts synthetized using a modified polyol method, in alkaline conditions, using graphene and CNTs as supports. The catalysts displayed lower ECSA values (of ca. 40 $m^2_{Pt}\ g^{-1}_{Pt}$) than the commercial 20 wt% Pt/C. Nonetheless the Pt/graphene catalyst had the best performance after running the degradation protocol, consisting in 10 000 potential cycles [59]. Jafri et al. used $NaBH_4$ as reducing agent to synthetize Pt/graphene and Pt/CNTs. They measured high ECSA values (in a single-cell) of 95.1 and 77.4 $m^2\ g^{-1}$, respectively [60]. Li et al. reported the synthesis of Pt/rGO and Pt/CNTs by the polyol method and measured lower ECSAs, 36.3 and 33.4 $m^2\ g^{-1}$, respectively [30]. These results indicate that synthesis methods are very sensitive to the operating conditions and to the electrochemical characterization procedure.

Influence of Pt loading on rGO

The Pt loading on carbon supports plays a decisive role in the Pt particle size and dispersion as well as in ECSA and ORR activity of the catalysts. Fig. 6 depicts ECSA and ORR measurements of the prepared catalysts on rGO as a function of the Pt mass fraction. 10PtrGO displays the highest ECSA (36 $m^2\ g^{-1}$), followed by 35PtrGO (29 $m^2\ g^{-1}$), 20PtrGO (27 $m^2\ g^{-1}$) and the lowest for 30PtrGO (26 $m^2\ g^{-1}$); the values of ECSA do not follow the trend of the Pt/rGO mass fraction. Regarding ORR activity at 0.9 V, the 30PtrGO sample displays the highest area and mass-specific activities. The diffusion-limited activity (at 0.4 V) increases with the Pt loading, peaking for 30PtrGO, and decreasing afterwards for 35PtrGO. Increasing Pt loadings allows "processing" more reactant per unit of time but, when Pt particles are too big, they may block the micropores of the electrode thus decreasing the diffusion pathways and consequently the diffusion-limited activity. Additionally, a Koutecky –Levich study was performed to one of the rGO-supported electrocatalyst to estimate the number of electrons transferred during the ORR. Equations S1 and S2 were employed considering a C_0 of 1.18×10^{-6} mol cm^{-3} – bulk concentration of O_2 dissolved in the electrolyte, a D_0 of $1.9 \times 10^{-5}\ cm^2\ s^{-1}$ – O_2 effective diffusion coefficient and a kinematic viscosity of the electrolyte (υ) of $9.87 \times 10^{-3}\ cm^2\ s^{-1}$ at 25 °C for a 0.1 M $HClO_4$(aq) solution [61]. An overall electron-transfer number of 3.94 was estimated, which confirmed a direct 4-electron transfer pathway for the rGO-supported catalysts. Thus, a minimal and despicable portion of the electron-transfer process happens through a 2-electron transfer pathway from O_2 to H_2O_2. Electrochemical measurements are presented in supplementary information (S1).

Speder et al., studied the influence of the mass fraction of Pt on Vulcan and obtained increased ECSA values as Pt/C ratio decreases [62]. The same trend was reported by Choi et al. using surface-modified graphene, instead of Vulcan, as catalyst support [63]. Daş et al. studied the Pt loading on graphene and reported a linear dependence between Pt particle size and Pt/graphene mass fraction; surprisingly, the ECSA values obtained did not follow the same behavior of the two previous works [64]. The results obtained in this work greatly depend on the properties of the GO used in the synthesis and since there are several methods to produce GO with different qualities, a big discrepancy can be expected in terms of electrochemical performances. The rGO sheets used in this work measure ca. 10–20 μm in length whereas the diameter of Vulcan carbon particles is ca. 30 nm. To obtain a homogeneous catalyst layer is much easier using smaller particles, which will also influence the catalytic performance.

Hybrid support to avoid rGO re-stacking

Several works in the literature reported the advantage of mixing catalysts with different supports, namely graphene

Table 4 – Summary of results from RDE measurements.

Catalyst	ECSA ($m^2_{Pt}\ g^{-1}_{Pt}$)	Area-specific activity @ 0.9 V ($mA\ cm^{-2}_{Pt}$)	Mass-specific activity @ 0.9 V ($A\ mg^{-1}_{Pt}$)	Diffusion-limited activity ($mA\ cm^{-2}_{geo}$)	Loading ($\mu g\ cm^{-2}_{geo}$)
20PtVulcan	64	0.33	0.21	5.3	8
20PtVulcanAD	51 (–20%)	0.26	0.13 (–37%)	4.5 (–15%)	8
20PtCNTs	42	0.29	0.12	4.8	8
20PtrGO	27	0.38	0.10	3.8	8
10PtrGO	36	0.30	0.11	2.8	4
30PtrGO	26	0.66	0.17	4.1	12
30PtrGOAD	22 (–15%)	0.25	0.05 (–69%)	3.8 (–7%)	12
35PtrGO	29	0.36	0.10	3.8	14
25|75 PtrGO|PtVulcan	37	0.42	0.16	5	9
50|50 PtrGO|PtVulcan	46	0.39	0.18	4.5	10
50|50 PtrGO|PtVulcanAD	37 (–14%)	0.36	0.13 (–28%)	4.2 (–7%)	10
20PtETEK	81	0.22	0.18	5	8

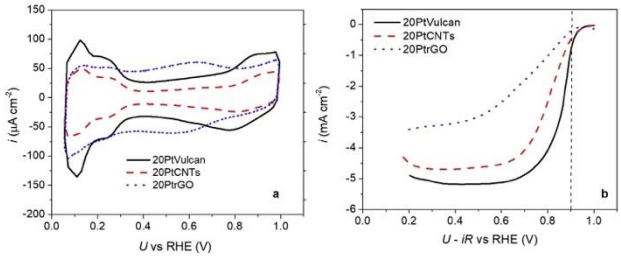


Fig. 5 – ECSA and ORR activity measurement of electrocatalysts synthesized with different supports: a) cyclic voltammograms in Ar at 20 mV s^{-1}; b) linear sweep voltammograms in O_2 at 1600 RPM and 20 mV s^{-1}.

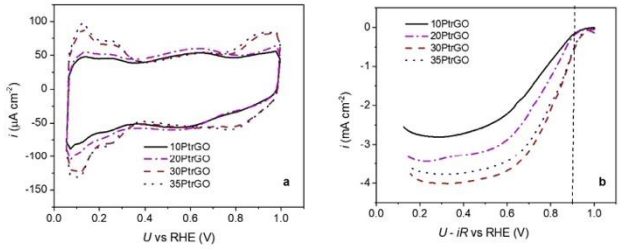


Fig. 6 – ECSA and ORR activity measurement of electrocatalysts synthesized with different Pt loadings on rGO: a) cyclic voltammograms in Ar at 20 mV s^{-1}; b) linear sweep voltammograms in O_2 at 1600 RPM and 20 mV s^{-1}.

with carbon black [35–37,65] or with carbon nanotubes [60]. The idea is to use the second catalyst as a "spacer" for carbon platelets characteristic of graphene-supported platinum catalysts. More interesting is the fact that some of these works measured higher ECSAs using mixed catalysts with different supports than those measured for the individual catalyst types. Şanlı et al. found that rGO:Vulcan mass ratio of 75:25 offers the highest ECSA [65]. The ECSA and ORR activities of different mixed rGO based catalysts with Vulcan-based are shown in Fig. 7.

Both ECSA and ORR activity of the mixtures remain within the values of the catalysts that form the mixture. This is in accordance with the single cell measurements by Jung et al. where the only advantage they found of mixing the two catalysts was to increase the stability upon accelerated degradation [35]. The fact that the use of Vulcan to act as a "spacer" did not generate valuable results may be related to the big length of the rGO sheets. The dimensions of the two types of support are very different and such small spherical particles are not able to prevent re-stacking of rGO sheets.

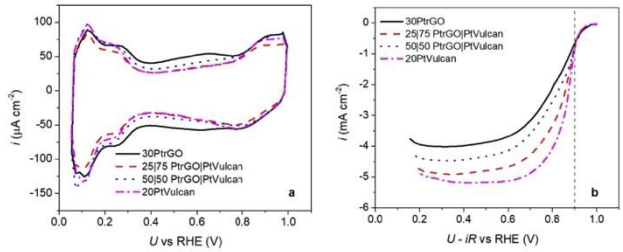


Fig. 7 – ECSA and ORR activities of 30PtrGO, 20PtVulcan and mixtures of rGO and Vulcan-based electrocatalysts: a) cyclic voltammograms in Ar at 20 mV s^{-1}; b) linear sweep voltammograms in O_2 at 1600 RPM and 20 mV s^{-1}.

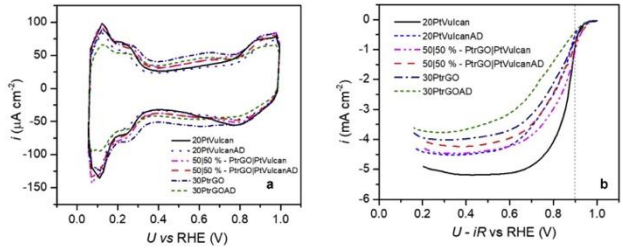


Fig. 8 – Comparison between mixtures of 20PtVulcan and 30PtrGO pristine and upon degradation: a) cyclic voltammograms in Ar at 20 mV s^{-1}; b) linear sweep voltammograms in O_2 at 1600 RPM and 20 mV s^{-1}.

Stability upon accelerated degradation

An accelerated stress test, consisting of 10 000 cycles between 50 mV and 925 mV (vs. RHE) at 500 mV s^{-1} in O_2-saturated electrolyte, was imposed to the best performing catalysts among those that were synthetized - Fig. 8. Catalysts 20PtVulcan, 30PtrGO and 50|50 PtrGO|PtVulcan were characterized. The highest ECSA loss at the end of this test was recorded for 20PtVulcan (−20%), followed by 30PtrGO (−15%) and finally the hybrid support (−14%), the loss of mass activity was significantly higher for the latter (−69%), followed by the former (−37%) and the lowest for the hybrid support (−28%). Nonetheless, the hybrid catalyst displays the least loss rate of ECSA (14%) and mass activity (28%), meaning that it proves valuable to combine these two supports in terms of stability. In the work by Jun et al. it is reported that a Pt/GO catalyst is more stable than Pt/C (losses in ECSA were 45% and 15%, respectively) after imposing a degradation protocol, consisting in cycling between high potentials (0.4–1.2 V), which affects mainly the support [35].

Shao et al. also reported the same trend for both ECSA and ORR activity for Pt/graphene and commercial 20 wt% Pt/C, after imposing a similar degradation protocol [59]. The degradation protocol used in this work consisted in a broader range of potential for ORR but did not include potentials above 925 mV. Carbon corrosion should not be as extent as in the reports mentioned before, meaning that the main degradation should be associated to Pt particles growth by sintering or Ostwald ripening. Despite the small drop in ECSA of the sample 30PtrGO, the loss of specific mass activity was very high; this suggests changes in the metallic structure of platinum, exposing less-reactive planes but with small loss of metal surface area. The smaller loss in diffusion-limited activity compared to 20PtVulcan suggest a lower change in the microstructure after the degradation protocol, keeping most of oxygen diffusion pathways.

Conclusions

Functional ORR catalysts were produced through a simple and easy-scalable synthesis route like the polyol method. Higher Pt loading on rGO led to bigger but more crystalline Pt particles. The area-specific activities of rGO-supported catalysts were the highest, evidencing a behaviour closer to that of a bulk-like catalyst, in which the active sites seem to "work harder" when compared to dispersed particles. 30 wt% on rGO was found to be the optimal Pt loading leading to higher ORR activity and best Pt dispersion in the support.

Upon accelerated degradation, the 30PtrGO sample presented higher loss of ORR mass-specific activity when compared to 20PtVulcan. Still, it possessed much higher area-

specific activity, a promising indicator regarding the use rGO-supported catalysts in increasingly thinner catalyst layers due to their lower performance sensitivity to the reduction of catalyst loading in the fuel cell cathode.

Acknowledgments

This research was supported by the Project "PEMFC-SUDOE" -SOE1/P1/E0293 which is co-financed by the European Regional Development Fund in the framework of the Interreg Sudoe programme. This work was also partially financially supported by project UID/EQU/00511/2019 - Laboratory for Process Engineering, Environment, Biotechnology and Energy – LEPABE funded by national funds through FCT/MCTES (PIDDAC). Azenha, C., is grateful to the Portuguese Foundation for Science and Technology (FCT) for the doctoral grant (reference SFRH/BD/128768/2017).

Appendix A. Supplementary data

Supplementary data to this article can be found online at https://doi.org/10.1016/j.ijhydene.2020.02.022.

REFERENCES

[1] Costamagna P, Srinivasan S. Quantum jumps in the PEMFC science and technology from the 1960s to the year 2000: Part II. Engineering, technology development and application aspects. J Power Sources 2001;102:253–69. https://doi.org/10.1016/S0378-7753(01)00808-4.

[2] Andújar JM, Segura F. Fuel cells: history and updating. A walk along two centuries. Renew Sustain Energy Rev 2009;13:2309–22. https://doi.org/10.1016/J.RSER.2009.03.015.

[3] Wang Y, Chen KS, Mishler J, Cho SC, Adroher XC. A review of polymer electrolyte membrane fuel cells: technology, applications, and needs on fundamental research. Appl Energy 2011;88:981–1007. https://doi.org/10.1016/J.APENERGY.2010.09.030.

[4] Antolini E. Formation of carbon-supported PtM alloys for low temperature fuel cells: a review. Mater Chem Phys 2003;78:563–73. https://doi.org/10.1016/S0254-0584(02)00389-9.

[5] Gasteiger HA, Kocha SS, Sompalli B, Wagner FT. Activity benchmarks and requirements for Pt, Pt-alloy, and non-Pt oxygen reduction catalysts for PEMFCs. Appl Catal B Environ 2005;56:9–35. https://doi.org/10.1016/J.APCATB.2004.06.021.

[6] Holewinski A, Idrobo J-C, Linic S. High-performance Ag–Co alloy catalysts for electrochemical oxygen reduction. Nat Chem 2014;6:828.

[7] Alia SM, Pylypenko S, Dameron A, Neyerlin KC, Kocha SS, Pivovar BS. Oxidation of platinum nickel nanowires to improve durability of oxygen-reducing electrocatalysts. J Electrochem Soc 2016;163:F296–301. https://doi.org/10.1149/2.0081605jes.

[8] Alia SM, Larsen BA, Pylypenko S, Cullen DA, Diercks DR, Neyerlin KC, et al. Platinum-coated nickel nanowires as oxygen-reducing electrocatalysts. ACS Catal 2014;4:1114–9. https://doi.org/10.1021/cs401081w.

[9] Li M, Zhao Z, Cheng T, Fortunelli A, Chen C-Y, Yu R, et al. Ultrafine jagged platinum nanowires enable ultrahigh mass activity for the oxygen reduction reaction. Science 2016. 80.

[10] Zhang C, Hwang SY, Peng Z. Platinum alloy nanocatalyst with manipulated particle composition and morphology for improved ORR property. Meet Abstr 2016;MA2016-01:1698.

[11] Lindahl N, Zamburlini E, Feng L, Grönbeck H, Escudero-Escribano M, Stephens IEL, et al. High specific and mass activity for the oxygen reduction reaction for thin film catalysts of sputtered Pt3Y. Adv Mater Interfaces 2017;4:1700311. https://doi.org/10.1002/admi.201700311.

[12] Borup R, Meyers J, Pivovar B, Kim YS, Mukundan R, Garland N, et al. Scientific aspects of polymer electrolyte fuel cell durability and degradation. Chem Rev 2007;107:3904–51. https://doi.org/10.1021/cr050182l.

[13] Xie J, Wood DL, Wayne DM, Zawodzinski TA, Atanassov P, Borup RL. Durability of PEFCs at high humidity conditions. J Electrochem Soc 2005;152:A104–13. https://doi.org/10.1149/1.1830355.

[14] Kinoshita K. Particle size effects for oxygen reduction on highly dispersed platinum in acid electrolytes. J Electrochem Soc 1990;137:845–8. https://doi.org/10.1149/1.2086566.

[15] Watanabe M, Sei H, Stonehart P. The influence of platinum crystallite size on the electroreduction of oxygen. J Electroanal Chem Interfacial Electrochem 1989;261:375–87. https://doi.org/10.1016/0022-0728(89)85006-5.

[16] Kabbabi A, Gloaguen F, Andolfatto F, Durand R. Particle size effect for oxygen reduction and methanol oxidation on Pt/C inside a proton exchange membrane. J Electroanal Chem 1994;373:251–4. https://doi.org/10.1016/0022-0728(94)03503-2.

[17] Zhang B, Su DS. Probing the metal–support interaction in carbon-supported catalysts by using electron microscopy. ChemCatChem 2015;7:3639–45. https://doi.org/10.1002/cctc.201500666.

[18] Campbell CT. Electronic perturbations. Nat Chem 2012;4:597.

[19] Wang C, Ma L, Liao L, Bai S, Long R, Zuo M, et al. A unique platinum-graphene hybrid structure for high activity and durability in oxygen reduction reaction. Sci Rep 2013;3:2580.

[20] Kaewsai D, Lin H-L, Liu Y-C, Yu TL. Platinum on pyridine-polybenzimidazole wrapped carbon nanotube supports for high temperature proton exchange membrane fuel cells. Int J Hydrogen Energy 2016;41:10430–45. https://doi.org/10.1016/j.ijhydene.2015.09.066.

[21] Vinayan BP, Jafri RI, Nagar R, Rajalakshmi N, Sethupathi K, Ramaprabhu S. Catalytic activity of platinum–cobalt alloy nanoparticles decorated functionalized multiwalled carbon nanotubes for oxygen reduction reaction in PEMFC. Int J Hydrogen Energy 2012;37:412–21. https://doi.org/10.1016/j.ijhydene.2011.09.069.

[22] Boaventura M, Brandão L, Mendes A. Single-wall nanohorns as electrocatalyst support for high temperature PEM fuel cells. J Electrochem Soc 2011;158:B394–401. https://doi.org/10.1149/1.3551495.

[23] Ghasemi M, Shahgaldi S, Ismail M, Kim BH, Yaakob Z, Wan Daud WR. Activated carbon nanofibers as an alternative cathode catalyst to platinum in a two-chamber microbial fuel cell. Int J Hydrogen Energy 2011;36:13746–52. https://doi.org/10.1016/j.ijhydene.2011.07.118.

[24] Zainoodin AM, Kamarudin SK, Masdar MS, Daud WRW, Mohamad AB, Sahari J. High power direct methanol fuel cell with a porous carbon nanofiber anode layer. Appl Energy 2014;113:946–54. https://doi.org/10.1016/j.apenergy.2013.07.066.

[25] Geim AK, Novoselov KS. The rise of graphene. UK: Nanosci. Technol., Co-Published with Macmillan Publishers Ltd; 2009. p. 11–9. https://doi.org/10.1142/9789814287005_0002.

[26] Chen D, Tang L, Li J. Graphene-based materials in electrochemistry. Chem Soc Rev 2010;39:3157–80. https://doi.org/10.1039/B923596E.
[27] Sani E, Vallejo JP, Cabaleiro D, Lugo L. Functionalized graphene nanoplatelet-nanofluids for solar thermal collectors. Sol Energy Mater Sol Cells 2018;185:205–9. https://doi.org/10.1016/J.SOLMAT.2018.05.038.
[28] Šest E, Dražić G, Genorio B, Jerman I. Graphene nanoplatelets as an anticorrosion additive for solar absorber coatings. Sol Energy Mater Sol Cells 2018;176:19–29. https://doi.org/10.1016/J.SOLMAT.2017.11.016.
[29] Vaqueiro-Contreras M, Bartlam C, Bonilla RS, Markevich VP, Halsall MP, Vijayaraghavan A, et al. Graphene oxide films for field effect surface passivation of silicon for solar cells. Sol Energy Mater Sol Cells 2018;187:189–93. https://doi.org/10.1016/J.SOLMAT.2018.08.002.
[30] Li Y, Gao W, Ci L, Wang C, Ajayan PM. Catalytic performance of Pt nanoparticles on reduced graphene oxide for methanol electro-oxidation. Carbon N Y 2010;48:1124–30. https://doi.org/10.1016/J.CARBON.2009.11.034.
[31] Xin Y, Liu J, Zhou Y, Liu W, Gao J, Xie Y, et al. Preparation and characterization of Pt supported on graphene with enhanced electrocatalytic activity in fuel cell. J Power Sources 2011;196:1012–8. https://doi.org/10.1016/J.JPOWSOUR.2010.08.051.
[32] Krishnan D, Kim F, Luo J, Cruz-Silva R, Cote LJ, Jang HD, et al. Energetic graphene oxide: challenges and opportunities. Nano Today 2012;7:137–52. https://doi.org/10.1016/J.NANTOD.2012.02.003.
[33] He D, Cheng K, Li H, Peng T, Xu F, Mu S, et al. Highly active platinum nanoparticles on graphene nanosheets with a significant improvement in stability and CO tolerance. Langmuir 2012;28:3979–86. https://doi.org/10.1021/la2045493.
[34] Hsieh SH, Hsu MC, Liu WL, Chen WJ. Study of Pt catalyst on graphene and its application to fuel cell. Appl Surf Sci 2013;277:223–30. https://doi.org/10.1016/J.APSUSC.2013.04.029.
[35] Jung JH, Park HJ, Kim J, Hur SH. Highly durable Pt/graphene oxide and Pt/C hybrid catalyst for polymer electrolyte membrane fuel cell. J Power Sources 2014;248:1156–62. https://doi.org/10.1016/J.JPOWSOUR.2013.10.055.
[36] Park S, Shao Y, Wan H, Rieke PC, Viswanathan VV, Towne SA, et al. Design of graphene sheets-supported Pt catalyst layer in PEM fuel cells. Electrochem Commun 2011;13:258–61. https://doi.org/10.1016/J.ELECOM.2010.12.028.
[37] He D, Cheng K, Peng T, Pan M, Mu S. Graphene/carbon nanospheres sandwich supported PEM fuel cell metal nanocatalysts with remarkably high activity and stability. J Mater Chem 2013;1:2126–32. https://doi.org/10.1039/C2TA00606E.
[38] Şanlı LI, Bayram V, Yarar B, Ghobadi S, Gürsel SA. Development of graphene supported platinum nanoparticles for polymer electrolyte membrane fuel cells: effect of support type and impregnation–reduction methods. Int J Hydrogen Energy 2016;41:3414–27. https://doi.org/10.1016/J.IJHYDENE.2015.12.166.
[39] Pak Hoe L, Boaventura M, Lagarteira T, Kee Shyuan L, Mendes A. Polyol synthesis of reduced graphene oxide supported platinum electrocatalysts for fuel cells: effect of Pt precursor, support oxidation level and pH. Int J Hydrogen Energy 2018;43(35). https://doi.org/10.1016/J.IJHYDENE.2018.05.147.
[40] Garsany Y, Ge J, St-Pierre J, Rocheleau R, Swider-Lyons KE. Analytical procedure for accurate comparison of rotating disk electrode results for the oxygen reduction activity of Pt/C. J Electrochem Soc 2014;161:F628–40. https://doi.org/10.1149/2.036405jes.
[41] Schmidt TJ, Gasteiger HA, Stäb GD, Urban PM, Kolb DM, Behm RJ. Characterization of high surface area electrocatalysts using a rotating disk electrode configuration. J Electrochem Soc 1998;145:2354–8. https://doi.org/10.1149/1.1838642.
[42] Paulus UA, Schmidt TJ, Gasteiger HA, Behm RJ. Oxygen reduction on a high-surface area Pt/Vulcan carbon catalyst: a thin-film rotating ring-disk electrode study. J Electroanal Chem 2001;495:134–45. https://doi.org/10.1016/S0022-0728(00)00407-1.
[43] Garsany Y, Singer IL, Swider-Lyons KE. Impact of film drying procedures on RDE characterization of Pt/VC electrocatalysts. J Electroanal Chem 2011;662:396–406. https://doi.org/10.1016/j.jelechem.2011.09.016.
[44] Garsany Y, Baturina OA, Swider-Lyons KE, Kocha SS. Experimental methods for quantifying the activity of platinum electrocatalysts for the oxygen reduction reaction. Anal Chem 2010;82:6321–8. https://doi.org/10.1021/ac100306c.
[45] Chiang Y-C, Liang C-C, Chung C-P. Characterization of platinum nanoparticles deposited on functionalized graphene sheets. Materials 2015;8. https://doi.org/10.3390/ma8095318.
[46] Li X, Chen W-X, Zhao J, Xing W, Xu Z-D. Microwave polyol synthesis of Pt/CNTs catalysts: effects of pH on particle size and electrocatalytic activity for methanol electrooxidization. Carbon N Y 2005;43:2168–74. https://doi.org/10.1016/J.CARBON.2005.03.030.
[47] Choi SM, Seo MH, Kim HJ, Kim WB. Synthesis of surface-functionalized graphene nanosheets with high Pt-loadings and their applications to methanol electrooxidation. Carbon N Y 2011;49:904–9. https://doi.org/10.1016/J.CARBON.2010.10.055.
[48] Xin L, Yang F, Rasouli S, Qiu Y, Li Z-F, Uzunoglu A, et al. Understanding Pt nanoparticle anchoring on graphene supports through surface functionalization. ACS Catal 2016;6:2642–53. https://doi.org/10.1021/acscatal.5b02722.
[49] Ha H-W, Kim IY, Hwang S-J, Ruoff RS. One-pot synthesis of platinum nanoparticles embedded on reduced graphene oxide for oxygen reduction in methanol fuel cells. Electrochem Solid State Lett 2011;14:B70–3. https://doi.org/10.1149/1.3584092.
[50] Fievet F, Lagier JP, Blin B, Beaudoin B, Figlarz M. Homogeneous and heterogeneous nucleations in the polyol process for the preparation of micron and submicron size metal particles. Solid State Ionics 1989;32(33):198–205. https://doi.org/10.1016/0167-2738(89)90222-1.
[51] Chen WX, Lee JY, Liu Z. Microwave-assisted synthesis of carbon supported Pt nanoparticles for fuel cell applications. Chem Commun 2002;2588–9. https://doi.org/10.1039/b208600j.
[52] Oh H-S, Oh J-G, Kim H. Modification of polyol process for synthesis of highly platinum loaded platinum–carbon catalysts for fuel cells. J Power Sources 2008;183:600–3. https://doi.org/10.1016/J.JPOWSOUR.2008.05.070.
[53] Liu Z, Ling XY, Su X, Lee JY, Gan LM. Preparation and characterization of Pt/C and PtRu/C electrocatalysts for direct ethanol fuel cells. J Power Sources 2005;149:1–7. https://doi.org/10.1016/J.JPOWSOUR.2005.02.009.
[54] Jeong H-K, Lee YP, Lahaye RJWE, Park M-H, An KH, Kim IJ, et al. Evidence of graphitic AB stacking order of graphite oxides. J Am Chem Soc 2008;130:1362–6. https://doi.org/10.1021/ja076473o.
[55] Chien C-C, Jeng K-T. Effective preparation of carbon nanotube-supported Pt–Ru electrocatalysts. Mater Chem

Phys 2006;99:80–7. https://doi.org/10.1016/j.matchemphys.2005.09.080.
[56] Shanahan PV, Xu L, Liang C, Waje M, Dai S, Yan YS. Graphitic mesoporous carbon as a durable fuel cell catalyst support. J Power Sources 2008;185:423–7. https://doi.org/10.1016/j.jpowsour.2008.06.041.
[57] Kou R, Shao Y, Wang D, Engelhard MH, Kwak JH, Wang J, et al. Enhanced activity and stability of Pt catalysts on functionalized graphene sheets for electrocatalytic oxygen reduction. Electrochem Commun 2009;11:954–7. https://doi.org/10.1016/J.ELECOM.2009.02.033.
[58] Debe MK. Nanostructured thin film electrocatalysts for PEM fuel cells - a tutorial on the fundamental characteristics and practical properties of NSTF catalysts. ECS Trans 2012;45:47–68. https://doi.org/10.1149/1.3701968.
[59] Shao Y, Zhang S, Wang C, Nie Z, Liu J, Wang Y, et al. Highly durable graphene nanoplatelets supported Pt nanocatalysts for oxygen reduction. J Power Sources 2010;195:4600–5. https://doi.org/10.1016/J.JPOWSOUR.2010.02.044.
[60] Jafri RI, Arockiados T, Rajalakshmi N, Ramaprabhu S. Nanostructured Pt dispersed on graphene-multiwalled carbon nanotube hybrid nanomaterials as electrocatalyst for PEMFC. J Electrochem Soc 2010;157:B874–9. https://doi.org/10.1149/1.3374353.
[61] Onoda A, Tanaka Y, Ono T, Takeuchi S, Sakai A, Hayashi T. Myoglobin-based non-precious metal carbon catalysts for an oxygen reduction reaction. J Porphyr Phthalocyanines 2015;19:510–6. https://doi.org/10.1142/S108842461550039X.
[62] Speder J, Zana A, Spanos I, Kirkensgaard JJK, Mortensen K, Hanzlik M, et al. Comparative degradation study of carbon supported proton exchange membrane fuel cell electrocatalysts – the influence of the platinum to carbon ratio on the degradation rate. J Power Sources 2014;261:14–22. https://doi.org/10.1016/J.JPOWSOUR.2014.03.039.
[63] Kim S-H, Jeong GH, Choi D, Yoon S, Jeon HB, Lee S-M, et al. Synthesis of noble metal/graphene nanocomposites without surfactants by one-step reduction of metal salt and graphene oxide. J Colloid Interface Sci 2013;389:85–90. https://doi.org/10.1016/J.JCIS.2012.08.064.
[64] Daş E, Alkan Gürsel S, Işıkel Şanlı L, Bayrakçeken Yurtcan A. Thermodynamically controlled Pt deposition over graphene nanoplatelets: effect of Pt loading on PEM fuel cell performance. Int J Hydrogen Energy 2017;42:19246–56. https://doi.org/10.1016/J.IJHYDENE.2017.06.108.
[65] Işıkel Şanlı L, Bayram V, Ghobadi S, Düzen N, Alkan Gürsel S. Engineered catalyst layer design with graphene-carbon black hybrid supports for enhanced platinum utilization in PEM fuel cell. Int J Hydrogen Energy 2017;42:1085–92. https://doi.org/10.1016/J.IJHYDENE.2016.08.210.

Supplementary information

S.1 - ORR electrochemical performance – Koutecky-Levich analysis

The ORR activity of the catalyst 35PtrGO was also analyzed by hydrodynamic voltammetry under the similar conditions detailed in experimental section 2.3, however at different rotating rates (Figure S1 a) – 100, 400, 900, 1600 and 2500. The results were analyzed using the Koutechy–Levich equation (Equations S1 and S2).

$$I^{-1} = I_K^{-1} + I_L^{-1} \quad \text{(S1)}$$

$$I_L = 0.620\, nFAD_0^{2/3}\, \omega^{1/2}\, \upsilon^{-1/6} C_0 \quad \text{(S2)}$$

where I, I_K, and I_L represent the experimentally measured, kinetically-controlled, and diffusion-limited currents, respectively. ω is the electrode rotation rate, n is the overall number of electrons transferred in the half reaction, F is the Faraday constant (96 485 C mol^{-1}), C_0 is the bulk concentration of O_2 dissolved in the electrolyte (1.18×10^{-6} mol cm^{-3}), A is the electrode surface area (0.196 cm^2), D_0 is the O_2 effective diffusion coefficient (1.9×10^{-5} cm^2 s^{-1}), and υ is the kinematic viscosity of the electrolyte (0.87×10^{-3} cm^2 s^{-1}) at 25 °C for a 0.1 M $HCLO_4$(aq) solution. The plot resulting from the inverse of the measured current *vs.* $\omega^{-1/2}$ yields a straight line in which the interception with yy axis corresponds to I_k and the slopes reflect the I_L at several potentials; the latter were used to determine the number of electrons involved in the ORR (according to equation S2) – Figure S1b.

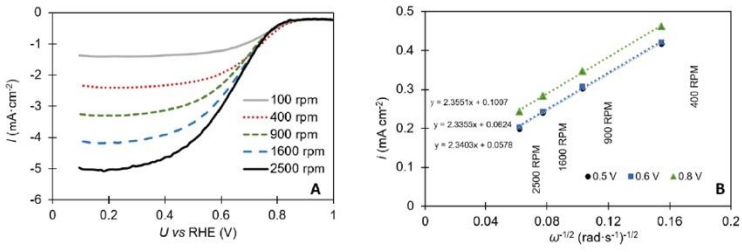


Figure S 1- (a) ORR activity measurement of 35PtrGO at different rotating speeds and using a potential scan rate of 20 mV s^{-1} in O_2-saturated 0.1 M $HClO_4$ aqueous solution; (b) Koutecky-Levich plots at different electrode potentials; The measurements were carried out at 25 °C and 0.21 oxygen pressure.

From S1b), for Koutecky-Levich plots at different electrode potentials, all lines are almost parallel to each other, suggesting that they all have the similar values of 0.620 $nFAD_0^{2/3}$ $\omega^{1/2}$ $\upsilon^{-1/6}C_0$. Thus, through Koutecky–Levich equation it was possible to estimate an electron-transfer number of 3.94.

Oxygen reduction stability of graphene-supported electrocatalyst: electrochemical and morphological evidences

Tiago Lagarteira[1,2,α], Sofia Delgado[1,2,α], Gema P. García[3], Alfredo Ortiz[3], Adélio Mendes[1,2,*]

[1] Laboratory for Process Engineering, Environmental, Biotechnology and Energy (LEPABE), Faculty of Engineering of University of Porto, Rua Roberto Frias s/n, 4200-465 Porto, Portugal

[2] ALiCE - Associate Laboratory in Chemical Engineering, Faculty of Engineering, University of Porto, Rua Dr. Roberto Frias, 4200-465 Porto, Portugal

[3] Chemical and Biomolecular Engineering Department, University of Cantabria, Av. Los Castros 46, 39005, Santander, Spain

* Corresponding author - E-mail: mendes@fe.up.pt; Office.: +351 22041 3612; Mobile: +351 919889237; Fax.: +351 22508 1449.

Accepted and currently under production at the International Journal of Hydrogen Energy.

Keywords: Oxygen reduction reaction, Carbon support, Graphene, Fuel cells; Electrocatalyst.

[α] The first two authors contributed equally in this work.

Abstract

The insufficient Oxygen Reduction Reaction (ORR) stability demonstrated by common carbon supports has been hindering the widespread commercialization of automotive Proton Exchange Membrane Fuel cells (PEMFCs). To meet the stability targets set by the US DoE, other supports are needed with greater corrosion stability, surface area and electronic conductivity.

Graphene has been proposed as support or as co-support for electrocatalysts due to its high electronic conductivity, corrosion stability and high specific surface area compared to common carbon blacks, such as Vulcan. Despite such outstanding properties, comprehensive studies on long-term stability of graphene-supported ORR catalysts are still unavailable or limited.

The stability of graphene as support is now studied and compared with carbon black in terms of electrochemical performance and degradation mechanisms. Catalytic layers with Pt/G were prepared and subjected to a set of three different Accelerated Stress Tests (ASTs) (cycling at high potentials, Open Circuit Potential (OCP) holding and cycling at low potentials) to assess if and why graphene is a better candidate as support. The Pt/G catalyst outperformed the reference

catalyst in all ASTs, delivering both higher electrochemical active surface area (ECSA) and ORR mass-specific activity. Such electrochemical performance was correlated with several degradation mechanisms associated to the support itself and with Pt nanoparticles.

Decision letter

Date: 03-23-2023
To: "Adelio Mendes" mendes@fe.up.pt
cc: abasile2011@yahoo.com
From: "Ibrahim Dincer" ibrahim.dincer@uoit.ca
Subject: Your Submission - HE-D-22-02637R1

Ms. Ref. No.: HE-D-22-02637R1
Title: Oxygen reduction stability of graphene-supported electrocatalyst: electrochemical and morphological evidences
International Journal of Hydrogen Energy

Dear Professor Mendes,

I am pleased to inform you that your paper "Oxygen reduction stability of graphene-supported electrocatalyst: electrochemical and morphological evidences" has been accepted for publication in the International Journal of Hydrogen Energy.

We appreciate and value your contribution to International Journal of Hydrogen Energy. We regularly invite authors of recently published manuscript to participate in the peer review process. If you were not already part of the journal's reviewer pool, you have now been added to it. We look forward to your continued participation in our journal, and we hope you will consider us again for future submissions.

For further assistance, please visit our customer support site at http://help.elsevier.com/app/answers/list/p/7923 Here you can search for solutions on a range of topics, find answers to frequently asked questions and learn more about EM via interactive tutorials. You will also find our 24/7 support contact details should you need any further assistance from one of our customer support representatives.

Yours sincerely,

Ibrahim Dincer, PhD
Associate Editor, IJHE
International Journal of Hydrogen Energy

Reviewer #2: The revision article has been revised in detail in accordance with the revision opinions, which can be accepted and published at present.

#AU_HE#

To ensure this email reaches the intended recipient, please do not delete the above code

In compliance with data protection regulations, you may request that we remove your personal registration details at any time. (Use the following URL: https://www.editorialmanager.com/he/login.asp?a=r). Please contact the publication office if you have any questions.

1. Introduction

Hydrogen has emerged as a promising option for at-scale decarbonization of energy sectors such as transport, industry and buildings [1]. Proton exchange membrane fuel cells (PEMFCs) will play an important role, mainly at the heavy-duty transport sector due to their high-power density, cold-start withstand and ability to operate at low temperature with high efficiency and power output [2]. PEMFCs are especially suited for powering large cars, trucks, buses, ships, trains and even air-planes due to their extended range and quick refueling time. Despite both efficiency and environmental advantages of fuel cells had been already demonstrated, it is still a challenge to meet the cost and durability of competing technologies [2].

Platinum (or its alloys [3]–[6]) is the catalyst of choice for driving both hydrogen oxidation reaction (HOR) and oxygen reduction reaction (ORR), due to its unmatchable activity and stability in acidic medium. For increasing the specific electrochemical surface area (ECSA), state-of-the-art PEMFC electrocatalysts consist in the very small metal nanoparticles supported onto high-surface area and electrically conductive carbon materials (typically Vulcan and Ketjen). Despite the catalyst support has not relevant catalytic activity, it may play a significant role in the stability and activity of the Pt nanoparticles due to geometric and electronic effects. More recently, new materials such as ordered mesoporous carbons, carbon aerogels, carbon nanotubes (CNTs), carbon nanocoils and carbon nanofibers have emerged as promising catalyst supports. The building block of these materials is graphene, a two-dimensional one-atom-thick planar sheet of sp2-bonded carbon atoms.

Some great efforts done in the past decade, especially the alloying of Pt with transition metals, allowed to exceed ORR activity targets set by the EU and US DoE (440 $mA \cdot mg_{Pt}^{-1}$ at 0.9 $V_{iR\text{-free}}$) [7], [8]. However, current PEMFC catalysts cannot withstand the harsh operating conditions, including high potentials, start/stop cycles, low pH, cold starts, low relative humidity and even fuel starvation [9]. The insufficient electrocatalytic stability of the cathode, trigger the irreversible loss of performance throughout the PEMFC lifetime due mainly, to losses of electrochemical surface area (ECSA), increased hydrophilicity, or lower electronic conductivity triggered by the poor interaction between the support, the catalyst and the ionomer. Degradation mechanisms

including the corrosion of the carbon support, Pt migration, Pt detachment and others in a smaller extent, are directly related to the stability of the support [10], [11].

Carbon corrosion rate is significantly accelerated above 1.15 V or during high overvoltage periods that take place at start and stop conditions, even though carbon oxidation is thermodynamically possible at potentials above 0.207 V *vs* SHE. Below 0.9 V *vs* SHE the kinetics of the reaction is extremely slow, still, the presence of Pt promotes oxidation to occur in the potential range of typical PEMFC operation (0.6 V - 0.7 V) [12]. This degradation mechanism may include partial oxidation or multi-step oxidation to CO_2.

Currently, multiple accelerated stress test (AST) protocols are available in the literature [13], including potential cycling below 1.2 V (triangular wave, squared wave and asymmetric wave forms), potential cycling at high potentials (1 V - 1.6 V *vs* RHE) to simulate start-and-stops that sharply accelerate carbon corrosion and potential holding at open circuit potential (OCP). A combination of the three types of ASTs is the most suited comparison to distinguish the ORR stability of PEMFC electrocatalysts. In the search of novel supports to replace carbon blacks, graphene has been widely suggested. Nonetheless, there are insufficient evidences concerning the resulting graphene's morphology influence on the integrity of Pt sites, especially when subjected to sets of different ASTs in ORR conditions. Thereafter, there is a lack of understanding on the degradation mechanisms that govern a Pt/graphene catalyst.

This work compares the stability of a graphene-supported catalyst with a widely used commercial electrocatalyst (Pt/H) under three different types of ASTs. The stability of the electrocatalysts is sequentially unveiled based on electrochemical characterization techniques, such as ECSA, double-layer capacitance and ORR activity. Moreover, through transmission electron microscopy (TEM) and inductively coupled plasma mass spectrometry (ICP-MS), Pt particle growth and Pt dissolution in the electrolyte were quantified. A relationship between electrochemical and physicochemical analyses is proposed aiming at deconvoluting the most relevant degradation mechanisms, as well as their extension, in a graphene supported PEMFC electrocatalyst.

2. Materials and Methods

2.1 Materials

Two electrocatalysts were studied, 40 wt.% Pt/graphene (Pt/G) (Premetek Co.) and 40 wt.% Pt/HiSPEC (Pt/H) (Alfa Aesar). Table 1 details the materials and operating conditions used in this study. Electrochemical measurements were performed in a Gamry RDE coupled with an Eurocell Electrochemical Kit. A Zahner IM6-ex was used as potentiostat and impedance spectrometer. The glassy carbon (GC) electrode was polished with 0.05 µm alumina-particle solution, prior to each film deposition. Immediately after dipping the working electrode (GC of *ca.* 0.2 cm^2) into the electrolyte (0.1 M $HClO_{4(aq)}$), the potential was set to 0.4 V *vs* RHE to avoid exposure to OCP which could generate carbon corrosion after a short time.

Table 1. Materials used for RDE measurements.

Ink composition	**Temperature / °C**
5 mg of electrocatalyst	20
7.96 ml H_2O	**Ar gas purity**
2 ml isopropanol	Linde, 99.999 %
40 µl Nafion (5 wt. %)	**Oxygen gas purity**
Ink application	Linde, 99.995 %
20 µl – 4 μg_{Pt} electrode	**Reference electrode**
700 RPM	Ag/AgCl
Ultrasound equipment	**Counter electrode**
Hielscher UP50H (50 W)	Graphite rod
Ultrasound probe treatment	**Electrolyte**
15 min @ 20 % amplitude in ice bath	70 % conc. $HClO_4$, 99.999 % trace metal bases, Sigma Aldrich

2.2 Electrochemical measurements

The electrode was first conditioned in Ar during 100 cycles between 0.05 V and 1 V (*vs* RHE) at 100 mV s^{-1} and 0 rotations per minute (RPM). Hydrogen underpotential deposition analysis was carried out with cyclic voltammetry (CV) at 20 mV s^{-1} and 0 RPM (from 0.05 - 1 V in Ar) to estimate the ECSA and Pt utilization of each electrocatalyst. The anodic charge attained from 0.05 V to 0.40 V *vs*. RHE refers to desorption of hydrogen from the available Pt active sites. The latter was normalized by 210 µC cm^{-2} which was assumed as the charge generated by a fully covered Polycrystalline Pt (111) monolayer [14].

EIS was performed in potentiostatic mode using a 5 mV perturbation at high frequency range (20 kHz - 3 kHz) to measure the ohmic resistance of the electrolyte. Linear sweep voltammetry (50

mV - 1 V *vs* RHE at 20 mV s^{-1}) was used to measure the background currents (in Ar) and ORR activity (in O_2) both at 1600 RPM. The electrolyte was saturated using 100 ml min^{-1} of each gas, for 30 min. During the measurements, a gas blanketing was set to prevent electrolyte contamination from the exterior of the cell.

2.3 Accelerated stress tests

Figure 1 depicts the three AST protocols employed in this study. AST1 consisted in triangular wave cycling between 1.0 V - 1.6 V *vs* RHE, at 20 °C with a scan rate of 100 mV s^{-1} in O_2; AST2 corresponded to 4 h of OCP holding in O_2. CV and ORR activity were measured in intervals of 2 h. Finally, AST3 comprised triangular wave cycling between 0.6 V - 1 V, at 20 °C at a scan rate of 100 mV s^{-1} in O_2. ASTs 1 and 3 consisted in sets of 2000 potential cycles, including a new break-in step in Ar atmosphere prior to retrieve both the ECSA and ORR back currents activities, followed by saturation of the electrolyte with O_2 to finally retrieve the ORR activity.

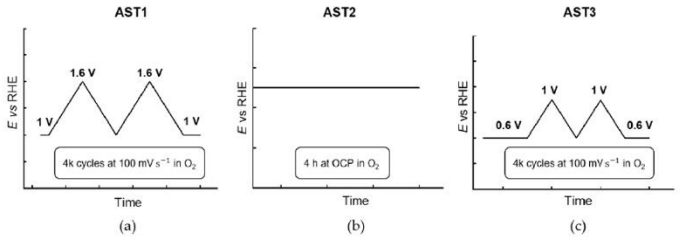


Figure 1. Scheme for the three AST protocols used for the stability study: (a) Triangular wave cycling at high potentials (1.0 V - 1.6 V); (b) Open circuit potential holding; (c) Triangular wave cycling at low potentials (0.6 V - 1.0 V).

2.4 Physical measurements

Pt particle size and dispersion were analyzed for the three electrocatalysts before and after each degradation protocol, using a transmission electron microscope (Jeol JEM 1400). The magnification was set to 600 000 times. To quantify the average particle size distribution, *ca.* 300 Pt nanoparticles were measured from 4 different zones of each TEM image using ImageJ software. The structure of the pristine catalysts was analyzed by X-ray diffraction (XRD). A PANalytical X'Pert Pro device operating in Bragg-Bretano focusing geometry served to collect the X-ray

patterns of the samples. The average crystallite size of Pt was calculated based on the broadening Pt reflection using Scherrer's equation (Equation 1) [14]:

$$d = \frac{K\lambda}{\beta \cos\theta} \quad (1)$$

where d is the average size of the Pt crystallites (nm), K is the crystallite-shape factor while λ stands for the wavelength of the $K\alpha$ radiation of Cu (λ = 1.5418 Å), θ is the Bragg angle, and the broadening of the diffraction line measured at half maximum intensity (FWHM) is represented by β. The average Pt crystallite size was calculated assuming an identical spherical shape and size, so that the K factor was chosen to be 0.9.

The concentration of platinum present in the electrolyte was measured after AST3 using an inductively coupled plasma mass spectrometer (ICP-MS), Agilent 7500 CE.

Raman spectra of the two electrocatalyst samples were obtained using a using a WITec alpha300, excited by a 532 nm laser with an electric current of 0.5 mA.

X-ray photoelectron spectroscopy (XPS) measurements were performed with a hemispherical analyzer-type X-ray photoelectron spectrometer (Kratos Axis Ultra HSA) with monochromatic Al, 90W X-ray source power where 15 kV power and 30 mA were used for all measurements. The spectra were obtained by applying pass energy of 80 eV and 20 eV for survey region and specific peak region respectively. The resultant XPS spectra were analyzed by using CasaXPS software.

3. Results

3.1. Morphological and electrochemical measurements at beginning of life

XRD patterns of 40 wt.% Pt supported on HiSPEC (Pt/H) and 40 wt.% Pt supported on graphene (Pt/G) powders are shown in Figure 2. The diffraction peaks in XRD of both electrocatalysts at 2θ of 39°, 46°, 68°, 81° and 86° correspond to the (111), (200), (220), (311) and (222) lattice planes of the face-centered cubic structures of platinum [15], which is in accordance with the reference card of cubic Pt (JCPDS-04-0802). The broader peak at $2\theta < 30°$ shown in both diffractograms corresponds to carbon (JCPDS 75-1621). For both samples, the broad carbon peak unveils a disordered amorphous structure when compared to the sharp peak typical for graphitic carbon. Although this is expected for spherical nanoparticles (*e.g.* carbon black), in the case of graphene,

it was already reported that exfoliation and re-stacking of graphene sheets decreases the degree of graphitization when compared to original graphite [16].

Using Scherrer's equation, a Pt crystallite size of *ca.* 1.8 nm was calculated for Pt/G. Similarly, calculated Pt crystallite size is twice larger when Pt nanoparticles are supported on HiSPEC (*ca.* 3.7 nm), which is in reasonable agreement with that reported by the manufacturer (maximum of 4.5 nm). Regarding ORR activity, the two most active crystal planes are Pt (111) and (200). For both electrocatalysts, these peaks correspond to *ca.* 70 % of the total sum of Pt crystal planes peaks. These values are summarized in Table 2.

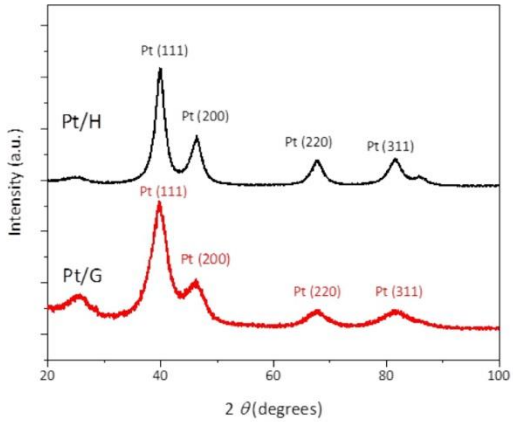


Figure 2. X-ray diffraction patterns of pristine Pt/H and Pt/G; graphitic carbon (JCPDS 75-1621), Pt (JCPDS 04-0802).

Table 2. Summary of X-ray diffraction results: relative peak area and crystallite size.

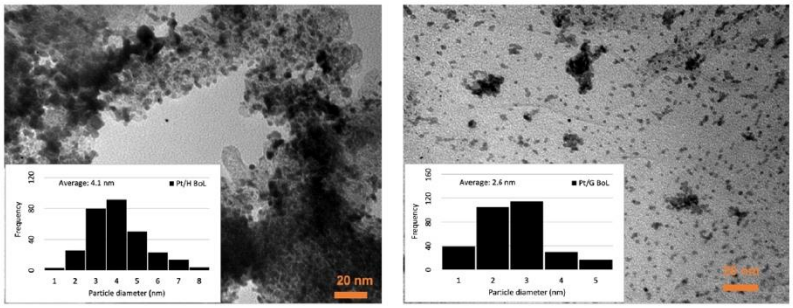
	Pt (111) / %	**Pt (200) / %**	**Pt (220) / %**	**Pt (311) / %**	**Crystallite size / nm**
Pt/H	47	23	13	17	3.7
Pt/G	51	19	13	17	1.8

Pt average particle size was measured from TEM images (Figure 3). The histograms (Figure 3 a-b) show that the particle size distribution fits a Gaussian distribution. The TEM images corresponding to Pt/H depict uniform dispersion of Pt particles despite the presence of some Pt agglomerates, while fewer were observed for Pt/G sample (see Figure S3). The platinum particle size of the two pristine electrocatalysts was different, 4.1 nm for Pt/H and 2.6 nm for Pt/G, which renders higher specific surface area for the latter. Pt/G displays the smallest crystallite size (1.8 nm), compared with Pt/H (3.7 nm). Kinetically, both higher Pt crystallinity and smaller particle sizes generate higher ORR activity; typically, the preferred lattice plane is Pt (111) plane for extended crystallinity [17] and Pt/G demonstrates slightly higher relative amount of such facets compared to than Pt/H.

The support of Pt/H catalyst, Figure 3 (a), consists of spherical-like carbon particles with diameter ranging from 10 to 30 nm. Such carbon particles display high surface area, high hydrophobicity and high electronic conductivity. The existence of pseudo-capacitive groups on the carbon surface caused by the application of pretreatments (in situ electrochemical oxidations, thermal or chemical attacks) may modify the above-mentioned properties [18]. The carbon support of Pt/G, Figure 3 (b), graphene, consists in the ordered arrangement of carbon atoms in two-dimensional structures. Depending on the synthesis or functionalization applied, graphene can contain some functional groups, based on N, O, S, among others. The existence of more capacitive groups in pristine Pt/G is shown in the Raman spectra (Figure S1); the I_D and I_G peaks are much broader than for Pt/H despite the similar peak intensity ratio [19]. For both carbon materials, functional groups are important during the synthesis of Pt/C catalysts. They serve as anchoring sites for nucleating small Pt particles and lead to more uniform Pt dispersion over carbon [20]. After the synthesis, Raman and XPS analyses (Figures S1 and S2) reveal similar graphitization degree and number of oxygenated species present at the near surface of both Pt/H and Pt/G [21] (results are summarized in Table S1).

The Pt particle size distribution for both electrocatalysts reveals a smaller average size for Pt/G (2.6 nm) than on Pt/H (4.1 nm). This hints for the existence of more anchoring sites on graphene that provide better dispersion of Pt particles, which yields smaller Pt average particle size [22]. XPS analysis shows similar C1s spectra, but higher differences are observed in the Pt4f high resolution spectra. The peaks corresponding to Pt valence >+2 are larger for Pt/G which indicates the presence of stronger and more abundant bonds between Pt sites and the support [23]. This is

typically observed for samples with better Pt dispersion with smaller particle sizes (see Figure 3b). Moreover, there is a positive shift in the metallic Pt (Pt^0) peak of 0.2 eV, which is commonly associated to higher ORR activity due to a decrease in the binding strength Pt and the reaction adsorbates [24].



(a) (b)

Figure 3. TEM images and particle size distribution of pristine: (a) Pt/H and (b) Pt/G.

The initial performance of the two electrocatalysts was evaluated using a rotating disk electrode. The Pt loading on the glassy carbon electrode was kept at 42 $\mu g_{Pt} \cdot cm^{-2}$. ORR activities were measured at 0.9 V *vs* RHE. The ECSA at beginning of life (BoL) of both catalysts was calculated from the cyclic voltammograms shown in Figure 4 (a). The capacitance is similar for both catalysts. Yet, the hydrogen desorption/adsorption charge (0.05 V to 0.4 V *vs* RHE) is larger for Pt/G, which is directly related to the existence of more active sites. The higher ECSA obtained for Pt/G (96.2 $m_{Pt}^2 \cdot g_{Pt}^{-1}$) means that Pt is utilized more efficiently in comparison to the Pt/H catalyst (80.2 $m_{Pt}^2 \cdot g_{Pt}^{-1}$). This difference can be explained by many factors but the most important refers to the lower Pt average particle size (Figure 3), which ensure higher Pt utilization due to more electroactive Pt sites exposed and availability to form more triple-phase boundaries [25].

ORR activity was measured in an O_2-saturated electrolyte (0.1 M $HClO_4$) by linear sweep voltammetry (LSV) at 20 $mV \cdot s^{-1}$ and a rotation speed of 1600 RPM; the mass-specific activity (MA), diffusion-limited activity (j_{lim}) and area-specific activity (SA) of each catalyst were calculated. ORR activity is normally presented in two forms: normalized by the catalytic loading

(mA g_{Pt}^{-1}) or by the catalytic surface area (μA cm_{Pt}^{-2}). These allow a direct comparison between electrocatalysts excluding morphological effects (area-specific activity) or catalytic loading (mass-specific activity). The ohmic drop assigned to the liquid electrolyte was measured by EIS and used to correct the *j-V* curves. The latter not only enables a direct comparison with other results in the literature but also excludes the changing of electrolyte properties after long-term experiments [26]. The resulting *jR*-corrected LSVs are shown in Figure 4 (b) – the background currents measured in Ar-purged 0.1 M $HClO_4$ were also subtracted to the curves recorded in O_2-saturated atmosphere. To calculate both mass- and area-specific activities, the net kinetic current (j_k) was determined using Equation (2) [27]:

$$j_k = \frac{j_{\text{lim}} j_{0.9}}{j_{\text{lim}} - j_{0.9}} \qquad (2)$$

where $j_{0.9}$ is the current density at 0.9 V and j_{lim} is the measured diffusion-limited current. The highest mass-specific activity was achieved for Pt/G, 323.4 ± 47.3 mA·g_{Pt}^{-1}, compared to 268.3 ± 35.2 mA·g_{Pt}^{-1} of Pt/H. Though mass-specific activities depend on several factors such as the Pt average particle size, catalyst-support interaction, and Pt crystal structure, it is noticeable that higher ECSA and lower Pt particle size are directly associated to the larger mass-specific activity obtained for Pt/G, which is also supported by the previously mentioned positive shift (see Table S1) of metallic Pt observed in the XPS analysis [28]. In terms of ORR specific-activity, 340.3 ± 29.9 μA·cm_{Pt}^{-2} was achieved for Pt/G and 348.6 ± 18.7 μA·cm_{Pt}^{-2} for Pt/H, since both electrocatalysts display similar contribution from the most active crystalline planes (111 and 200) measured by XRD [29].

Tafel plots were obtained from plotting the electrode potential as function of the logarithm of current density and considering low values of overpotential (up to 330 mV), which excludes the diffusion-limited regime, Figure 4 (c) [30]. The Tafel slope was calculated for both electrocatalysts before subjecting them to accelerated degradation, therefore, the reached values greatly depend on the type of electrocatalyst support. The Tafel slope (b) for Pt/H (54 mV·dec^{-1}) is similar to other electrocatalyst in which Pt particles are supported on carbon nanoparticles [31], [32]. The lower Tafel slope measured for Pt/G (40 mV·dec^{-1}) indicates faster ORR kinetics either due to higher changer-transfer rates or decreased binding energy to reaction adsorbates.

Table 3. Electrochemical active surface area (ECSA), mass-specific activity, area-specific activity and diffusion limited activity of Pt/H and Pt/G catalysts.

	ECSA ($m_{Pt}^2 \cdot g_{Pt}^{-1}$)	Mass-specific activity ($mA \cdot g_{Pt}^{-1}$) @ 0.9 V *vs* RHE	Area-specific activity ($\mu A \cdot cm_{Pt}^{-2}$) @ 0.9 V *vs* RHE	Diffusion-limited activity ($mA \cdot cm_{geo}^{-2}$)
Pt/H	80.2 ± 2.5	268.3 ± 35.2	348.6 ± 18.7	5.41 ± 0.33
Pt/G	96.2 ± 0.8	324.4 ± 47.3	340.3 ± 29.9	4.83 ± 0.33

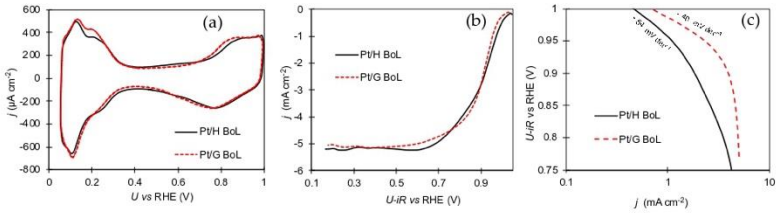


Figure 4. RDE results at beginning of life for Pt/H and Pt/G: (a) cyclic voltammograms at 20 $mV \cdot s^{-1}$ in Ar; (b) Linear sweep voltammograms at 20 $mV \cdot s^{-1}$ and 1600 RPM in O_2; (c) Tafel plots measured using 0.1 M $HClO_4$ at 20 $mV \cdot s^{-1}$ and 1600 rpm in O_2-saturated electrolyte; (Pt loading: 42 $\mu g_{Pt} \cdot cm^{-2}$).

3.2. Triangular wave cycling at high potentials (AST1)

In automotive fuel cells, the cathode is often exposed to high potentials (up to *ca.* 1.5 V) mainly due to a "reverse-current" generated from a sudden potential increase during startups and shutdowns [33]. This is a result of the simultaneous presence of hydrogen and oxygen at the electrode surface takin place in case of membrane failure or when the anode is blown with hydrogen at the start-up and with air during shut-off. This is called as fuel starvation and is typically studied through simulated start-stop cycles through thousands of voltage cycles above 1 V *vs* RHE using a fast scan rate [34]. From the perspective of the carbon support, this AST is aggressive mainly due to the presence of platinum and a highly acidic environment which

accelerate degradation mechanisms. Aged carbon structures typically show massive changes in their morphology, loss of electrical conductivity and increased hydrophilicity. Carbon corrosion has been considered one of the two major degradation mechanisms in PEMFCs together with Pt dissolution.

Apart from degradation mechanisms solely associated to the support, there are others associated to platinum nanoparticles that are also indirectly associated to the support. When exposed to high potentials and low pH, like those found in PEMFC cathodes, Pt nanoparticles are oxidized and may dissolve into the electrolyte (membrane and/or ionomer) or be found in water outlet stream. Wang *et al.* concluded that the equilibrium concentration of dissolved Pt increases monotonically from 0.65 to 1.1 V and then decreases above 1.1 V. Pt dissolution was shown to be highly dependent on Pt particle size under simulated start-stop cycling; Meier *et al.* stated that, under such conditions, smaller Pt particles were more likely to dissolve [35]. Strongly linked to Pt dissolution, Ostwald ripening and particle agglomeration are secondary degradation mechanisms. Dissolved Pt ions can also migrate and nucleate in already existing Pt clusters, leading to particle growth. Particle growth can also take place by the migration and sintering of similar Pt particles [36]. Moreover, carbon corrosion also promotes agglomeration as close Pt particles become in contact upon support shrinking [11].

As mentioned before, graphene is a great candidate for a stable catalyst support since its highly ordered carbon structure not only ensures higher electrical conductivity but also higher resistance to corrosion when compared to amorphous carbon blacks. On the other hand, Pt/G is loaded with smaller Pt particles than Pt/H. Figures 5 (a) and (d) show cyclic voltammograms obtained after subjecting the electrocatalysts to the accelerated stress test (AST1). CVs were recorder before and after 2000 cycles between 1 -1.6 V *vs* RHE at 500 mV s^{-1}. Three different regions are present in the cyclic voltammograms and they provide information about which phenomena have the most important influence on ORR performance: Pt-H adsorption/desorption region (below 0.4 V *vs* RHE), double-layer region (0.4 - 0.6 V *vs* RHE) and Pt-OH interaction region (above 0.6 V *vs* RHE) [37].

Electrochemical surface area (ECSA) is an important parameter since it is directly related the Pt utilization by the quantification of the electrochemically active sites in electrocatalytic films. Almost all degradation mechanisms contribute to a decrease in ECSA. Pt dissolution, agglomeration or Ostwald ripening lead to lower ECSA due to the loss of active Pt or by Pt particle

growth. Support corrosion also reduces the ECSA; Pt particles may simply detach from the support and migrate inside the membrane/ionomer acting there as an electrical insulator. ECSA losses after 2000 cycles are similar but Pt/H presents much lower ECSA (63.7 $m^2 \cdot g_{Pt}^{-1}$) at the end of tests. Remarkably, Pt/G showed minor ECSA loss after 4000 cycles (76.5 $m^2 \cdot g_{Pt}^{-1}$).

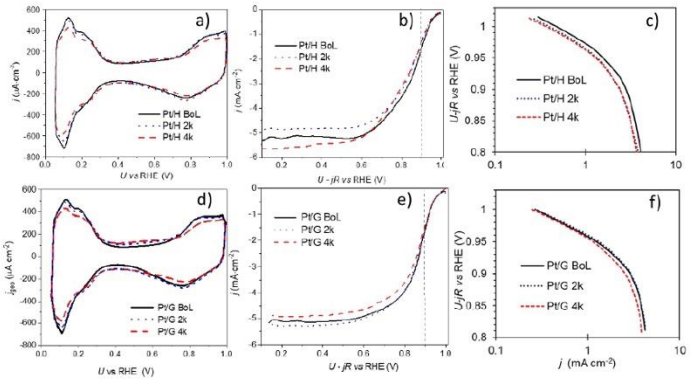
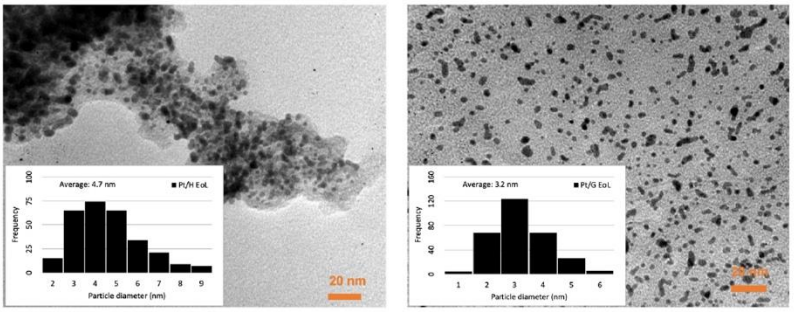


Figure 5. RDE results at beginning of life and upon 2000 cycles and 4000 potential cycles between 1.0 V and 1.6 V in an O_2-saturated electrolyte for Pt/H and Pt/G, respectively - vertical plots: (a,d) cyclic voltammograms at 20 mV s^{-1} in Ar; (b,e,) Linear sweep voltammograms at 20 mV s^{-1} and 1600 RPM in O_2; (c,f,) Tafel plots.

Typically, higher ECSA values account for higher ability to generate larger current densities; a similar conclusion can be taken from the limiting current density in LSVs - Figures 5 (b) and (e), but only the former LSVs corresponding to Pt/H, allow to unveil diffusional losses. At low potentials (below 0.6 V *vs* RHE), the current reaches a plateau which corresponds to the electrode response limited by mass-diffusion for a rotation of 1600 RPM. Unlike Pt/G, that displays similar limiting current density after degradation, Pt/H shows diffusional limitations already after 2000 cycles. The absence of a current plateau is associated to oxygen concentration gradients that are not constant with potential and this is highly associated to changes in the microstructure of the electrocatalyst. The loss of porosity [38] and the formation of excessive oxygen functional groups

328 at the HiSPEC surface increase the hydrophilicity of the support. This enhances flooding effects
329 that limit oxygen diffusion to the active sites [39].
330 The double layer capacitance of an electrode with Pt supported on carbon depends on the surface
331 morphology and type of anchored functional groups in the support. Such functional groups
332 decrease electrical conductivity and increase affinity to water. In particular, the latter may
333 contribute to a more challenging water removal from the fuel cell which actively promotes support
334 corrosion and mostly Pt dissolution. An increase in the double layer capacitance on Pt/G is evident
335 after degradation, and it is three times higher than the increase observed for Pt/H (Table 4).
336 Compared to spherical carbon particles, the planar structure of graphene facilitates the uptake of
337 oxygen functional groups, mainly on the edges of the graphene sheets [40]. The existence of more
338 capacitive groups in pristine Pt/G was already shown in the Raman spectra (Figure S1).
339 Commercial carbon Vulcan XC72 (present in HiSPEC 4000) is also known to possess many
340 defective surfaces (edges and corners of basal planes) with high concentration of oxygenated
341 functional groups at the surface which is evidenced in XPS measurements [41] (see Table S1).
342 Although surface defects had been proven to enhance the ORR activity and to allow better Pt
343 dispersion, long-term observations shown that these properties also led to carbon corrosion due to
344 unsaturated valences and free σ-electrons [42] and to the adverse effect of highly electronegative
345 oxygen functional groups which are prone to partially oxidize the Pt NPs and trigger their sintering
346 and dissolution mechanisms [43].
347 Linear sweep voltammetry was performed to obtain the ORR activity, measured at 0.9 V *vs* RHE.
348 The exchange current density and Tafel slope (Figures 5 (b), (e), (c) and (f)) were used to compare
349 the performance of ORR electrocatalysts. At first glance, it is noticeable that the two
350 electrocatalysts present considerable loss of mass activity at 0.9 V *vs* RHE. Yet, Pt/H not only
351 displays the most pronounced loss of mass activity upon 4000 potential cycles (32 %), but also the
352 highest loss in specific-area activity (32 %), see Figure 6 (a). On the other hand, Pt/G presents an
353 increase in specific-area activity (*ca.* 3.6 %), which suggests particle growth to more acicular-
354 shaped and crystalline Pt particles (Figure 6 (c)) which yield higher specific activity. Previous
355 works report the increase of specific activity with increasing platinum particle sizes for Pt/C
356 catalysts after being subjected to 1500 potential cycles [44]; the same trend is verified in a variety
357 of studies for Pt-alloys supported on carbon subjected to potential cycling (> 1.25 V) [45], [46].
358 Thus, the greater attained specific-area activity of Pt/G was assigned to the increase in the average

359 particle size, from 2.6 nm, at BoL, to 3.2 nm, at EoL (see Table S2). Pt nanoparticles smaller than
360 2-3 nm are thermodynamically unstable. Below the threshold in which Pt utilization would drop
361 considerably, larger Pt particles are typically more stable and display a larger specific area of facets
362 (111) and (200), the most active facets to the ORR [20].
363



(a) (b)

364
365 **Figure 6.** TEM images and particle size distribution of (a) Pt/H and (b) Pt/G at EoL after 4000
366 cycles from 1.0 V to 1.6 V.

367
368 Figure 6 (a) and 6 (b) shows TEM images of Pt/H and Pt/G after being subjected to the first
369 accelerated stress test (AST1). The particle size increased *ca.* 15 % for Pt/H and *ca.* 35 % for Pt/G,
370 relatively to their original size; it is noticeable a broader distribution of nanoparticle sizes (2 - 8
371 nm) for both electrocatalysts, which was assigned to the Ostwald ripening and/or particle
372 coalescence. The presence of Pt dissolved in the electrolyte was measured using ICP-MS. High
373 concentrations of dissolved Pt were detected in the liquid electrolyte (0.4 and 0.8 $\mu g \cdot dm^{-3}$ for Pt/H
374 and Pt/G, respectively). Pt dissolved into the electrolyte can also lead to particle growth following
375 a re-precipitation mechanism [35].
376 Table 4 summarizes the results of the two electrocatalyst during and after subjected to accelerated
377 degradation through potential cycling between 1 V - 1.6 V (*vs* RHE). Pt/G presents lower losses
378 in ECSA, mass-specific (MA) and area-specific (SA) activities. It also reached higher diffusion-
379 limited currents than Pt/H. These are clear signs of graphene's improved stability, showing higher

stability and losing two times less mass-specific activity after 4000 cycles, when compared to Pt/H. Remarkably, the area-specific activity of Pt/G was maintained after 4000 cycles.

Table 4. Summary of results for ECSA, Mass-specific activity (MA), Area-specific activity (SA) and Double-layer (dl) variation of Pt/G and Pt/H, subjected to AST1.

	ECSA variation at 2k cycles (%)	ECSA variation at EoL (%)	MA at 2k cyles (%)	MA at EoL (%)	SA at EoL (%)	DL variation at EoL (%)
Pt/G	-7.6	-21.5	+1.6	-17.2	+3.6	42.0
Pt/H	-8.4	-21.6	-18.2	-32.2	-13.3	12.2

3.3. Open circuit potential holding (AST2)

During the lifetime of a PEMFC system (*ca.* 6000 h), the cathode is exposed to harsh conditions, namely when no power is supplied to the propulsion system and the only power drawn from the cell is that required to withstand the auxiliary systems (*e.g.* cooling pumps). In these periods, the cathode potential reaches *ca.* 0.90 V *vs* RHE [47]. At open circuit potential (OCP), where no current is drawn from the stack, the cathode also reaches high potentials either prior to a fuel cell shutdown or immediately after a start-up. Such realistic situations cause severe degradation thus causing a significant reduction to the lifetime of the electrocatalyst [48]. In this regard, potential holding at OCP was performed to both electrocatalysts.

Figure 7 (a) displays the CVs for Pt/H and Pt/G after 4 h at OCP. The ECSA loss at the end of life was considerably higher for Pt/H (*ca.* 42 %) when compared to Pt/G (*ca.* 22 %). The double layer capacitance of both Pt/G and Pt/H decreased (*ca.* 10 % of their original size), which indicates the removal of anchored surface species or corrosion of carbon material to carbon dioxide [10]. Pt particles supported on HiSPEC display a round shape, suggesting migration and agglomeration as they are *ca.* 1.5-fold larger than their original size (Figure 8 (a) and Table S2). On the other hand, the coalescence of individual Pt particles can be observed in the TEM images of Pt/G at EoL, Figure 8 (b).

Table 5 summarizes the results of the two electrocatalysts exposed to open circuit potential. Pt/G displayed interesting results in terms of ORR mass-specific activity; after 2 h of potential hold, it increased but it then decreased after 4 h. This is likely to occur due to a beneficial increase of the particle size to an optimum size (3 - 4 nm), in which the most active crystal facets allow higher

rates of oxygen reduction. However, with persisting continuous potential cycling, the electrocatalyst lost ORR mass-specific activity but gained ORR area-specific activity. Similar results were previously reported by Kinoshita et al., where the specific activity of ORR was shown to be a function of the particle size and of the surface average distribution of Pt crystal facets. It is also mentioned a maximum ORR mass-specific activity for Pt particle sizes between 3 - 4 nm [49]. During prolonged operation under OCP, the catalyst support is partially or fully oxidized during the startup and shutdown processes. Simultaneously, the Pt particle growth may follow two of the above mentioned mechanisms: agglomeration/growth or dissolution followed by re-deposition [50].

The concentration of dissolved Pt in the electrolyte obtained after 4 h of OCP (*ca.* 0.925 V) in O_2 is similar for the two catalysts (Table S2). This can be attributed to the growth of a protective oxide layer that retrains the dissolution process though it typically is reported to be formed at potentials higher than 1.0 V *vs* RHE [51]. Nevertheless, some studies consider that such Pt oxides play a dual effect of protection against Pt dissolution even being as well, such oxides susceptible to dissolution [52].

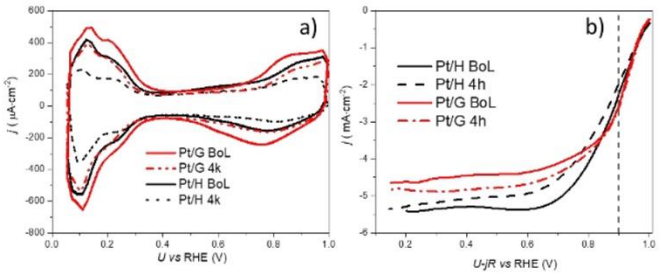
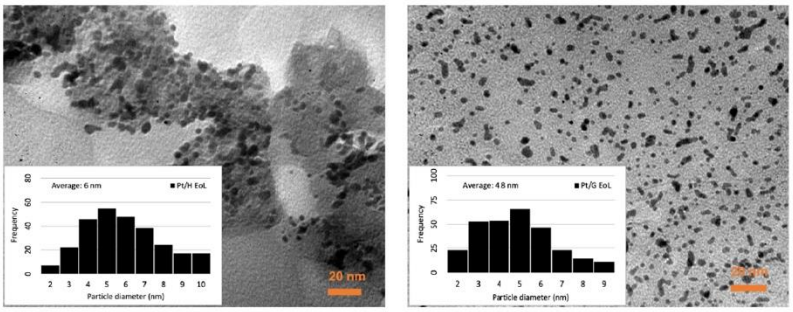


Figure 7. RDE electrochemical results for Pt/H and Pt/G aging (4h at OCP); (a) Cyclic voltammograms at 20 $mV \cdot s^{-1}$; (b) LSVs in O_2-saturated electrolyte at 1600 RPM.



(a) (b)

Figure 8. TEM images and particle size distribution of aged (4 h at OCP): (a) Pt/H; (b) Pt/G.

Table 5. Summary of results for ECSA, Mass-specific activity (MA), Area-specific activity (SA) and Double-layer (dl) variation of Pt/G and Pt/H, subjected to AST2.

Catalyst	ECSA variation after 2h (%)	ECSA variation at EoL (%)	MA after 2h (%)	MA at EoL (%)	SA at EoL (%)	DL variation at EoL (%)
Pt/G	-12.6	-29.7	+13.9	-4.0	+35.8	+11.0
Pt/H	-14.3	-43.0	-19.8	-17.3	+12.1	+10.0

3.4. Triangular wave cycling at low potentials (AST3)

The previous AST protocols were performed to evaluate mainly the carbon corrosion, which also promotes agglomeration/detachment of Pt nanoparticles as well as morphological changes in the electrode's microstructure such as higher hydrophilicity and loss of porosity. The combination of such effects results not only on the loss of Pt utilization but also lead to mass transport limitations. To study degradation as consequence of variations in power demands on the stability of Pt catalysts, potential cycling from 0.6 V to 1.0 V *vs* RHE was performed during 4000 cycles. This protocol is very similar to that defined by the US Drive (US FCTT), in collaboration with the US Department of Energy load-cycling protocol, which uses potential cycling from 0.65 V - 1.0 V *vs* RHE.

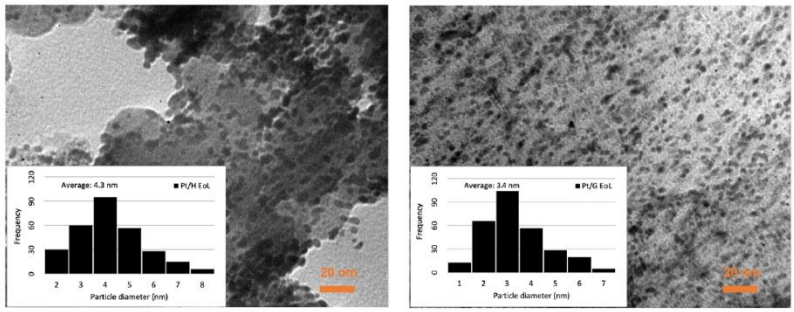
Figure 9 shows TEM images of the two electrocatalysts after subjected to potential cycling between 0.6 - 1 V (*vs* RHE). Pt/G microstructure appears to be kept intact and the average size of the particles identical to BoL conditions (3.4 nm after AST3 vs. 2.6 nm at BoL – see Table S2).

Likewise, the Pt particle size of Pt/H did not increase but more Pt agglomerates are present in Pt/H compared to Pt/G. The concentration of dissolved Pt in the electrolyte is very low (< 0.1 ± 0.05 mg dm^{-3}); see Table S2. Compared to others accelerated stress tests, AST3 appears to be milder in terms support corrosion and loss of Pt surface area. Some works in the literature reported that Pt dissolution occurs both during anodic and cathodic potential scans and especially when the upper potential limit of cycling is ≥ 1.1 V *vs* RHE [36]. On the other hand, other works report that cycling at lower potentials, corresponding to the regions of oxide formation and reduction to metallic particles (0.6 - 1.0 V *vs* RHE), tend to endorse higher dissolution rates instead of holding the potential in the oxide formation region (*ca.* 0.9 V *vs* RHE) or even cycling it at higher potentials [53]. This mechanism consists in the formation and disruption of a place-exchanged oxide film that ultimately leads to mobile platinum species [54].

Figures 10 (a) and (b) show cyclic and linear voltammograms after 4 000 potential cycles from 0.6 V - 1.0 V *vs* RHE. Clearly, Pt/G again presents a remarkable stability with the lowest loss of ECSA and the highest ORR activity at 0.9 V *vs* RHE, after degradation. Compared to the other AST protocols, both Pt/H and Pt/G lost more ECSA (27 % and 12 %, respectively). A similar AST protocol was set by Nissan´s technical lab in which they tested a 40 wt.% Pt supported on a high surface area carbon under load cycle conditions of 0.6 - 0.95 V *vs* RHE, at 80° [55]. They report major ECSA losses (49 % for Pt/H, which was not assigned to platinum dissolution and agglomeration. The authors refer, however, in the framework of cell and stack failure, that the stability of the support is far more important than the stability of the platinum particles that are loaded onto it. Similarly, in the present work, it is clearly shown that electrocatalyst support corrosion triggered during start-up and shutdown (AST1 in this study) is by far more important in terms of degradation than platinum dissolution.

From the results summarized in Table 6, there were no changes in the double layer capacitance on both catalysts. This confirms that by cycling at lower potentials promotes less surface functionalization of the carbon structure, when compared to AST1. On the other hand, the decrease in ORR activity (mass- and area-specific activities) at the end of measurements was the highest, mainly for Pt/H (60 % and 45 %, respectively). In the case of Pt/G, the loss of ORR activities was similar to that of AST1 and much lower than those observed for Pt/H. The low average particle size increase on both electrocatalysts (Figure 9) suggests that the loss of ORR activity was

triggered by electronic effects. These turned the Pt sites (mainly on HiSPEC) less active or unavailable to form triple-phase boundaries, as evidenced by the drop in ECSA.



(a) (b)

Figure 9. TEM images and particle size distribution of aged (4k cycles 0.6 V - 1.0 V): (a) Pt/H; (b) Pt/G.

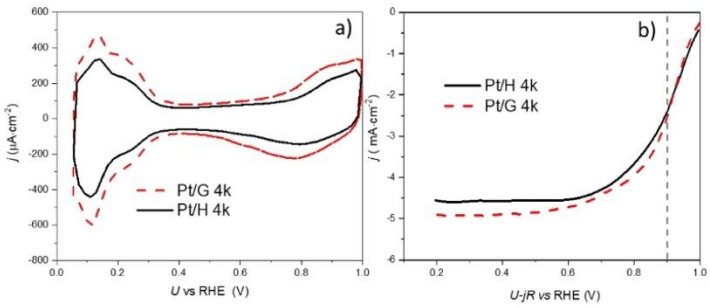


Figure 10. RDE electrochemical results for Pt/H and Pt/G aging (4k cycles between 0.6 V - 1.0 V); (a) Cyclic voltammograms at 20 $mV \cdot s^{-1}$; (b) LSVs in O_2-saturated electrolyte at 1600 RPM.

Table 6. Summary of results for ECSA, Mass-specific activity (MA), Area-specific activity (SA) and Double-layer (DL) variation of Pt/G and Pt/H, subjected to AST3.

Catalyst	ECSA variation at 2k cycles/2h (%)	ECSA variation at EoL (%)	MA at 2k cycles (%)	MA at EoL (%)	SA at EoL (%)	DL variation at EoL (%)
Pt/G	-4.4	-11.9	-10.4	-17.3	-6.1	*ca.* 0
Pt/H	-9.7	-25.7	-30.2	-59.0	-44.9	*ca.* 0

4. Conclusions

The degradation protocols caused clear differences in terms of ORR stability of two catalysts supported on carbon black and graphene. Pt supported on graphene not only outperformed Pt supported on HiSPEC in terms of initial ORR activity and ECSA but also after being subjected to the degradation protocols.

Despite the larger particle growth, Pt/G was able to maintain most of its initial ECSA and mass-specific activity after potential cycling between 1 V - 1.6 V (*vs* RHE). Lowest stability and performance of commercial Pt/H could be attributed to the loss of porosity at the catalyst layer coupled to the generation of O_2 imbalanced concentration gradients arising from the detachment of carbon support into the bulk electrolyte.

When subjected to OCP holding, the double layer capacitance of both catalysts increased because of the introduction of pseudo-capacitive groups on the surface of graphene. Nevertheless, Pt/G presented slightly larger particle growth than Pt/H after 4 h of OCP.

Potential cycling between 0.6 V - 1 V (*vs* RHE), typical PEMFC operation conditions, was more harmful for Pt/H than for Pt/G; three times higher ORR mass- specific activity and seven times higher area-specific activity losses. This degradation protocol caused less average particle growth and ECSA loss similar to AST1.

The superior performance of Pt/G is evident in terms of ECSA and ORR activity and upheld in morphological evidence, shows the benefits of this supported catalyst as alternative to common carbon blacks to be used as cathodic support for automotive PEMFCs.

Acknowledgments

This research was supported by the Project “PEMFC-SUDOE” -SOE1/P1/E0293 which is co-financed by the European Regional Development Fund in the framework of the Interreg Sudoe programme.

This work was partially financially supported by project UID/EQU/00511/2019 - Laboratory for Process Engineering, Environment, Biotechnology and Energy – LEPABE funded by national funds through FCT/MCTES (PIDDAC).

References

[1] International Energy Agency, "No Title," 2015.

[2] B. G. Pollet, S. S. Kocha, and I. Staffell, "Current status of automotive fuel cells for sustainable transport," *Curr. Opin. Electrochem.*, vol. 16, pp. 90–95, Aug. 2019, doi: 10.1016/j.coelec.2019.04.021.

[3] C. Chen *et al.*, "Highly crystalline multimetallic nanoframes with three-dimensional electrocatalytic surfaces," *Science (80-.).*, vol. 343, no. 6177, pp. 1339–1343, 2014, doi: 10.1126/science.1249061.

[4] S. M. Alia *et al.*, "Platinum-Coated Nickel Nanowires as Oxygen-Reducing Electrocatalysts," *ACS Catal.*, vol. 4, no. 4, pp. 1114–1119, Apr. 2014, doi: 10.1021/cs401081w.

[5] X. Huang *et al.*, "High-performance transition metal-doped Pt3Ni octahedra for oxygen reduction reaction," *Science (80-.).*, vol. 348, no. 6240, pp. 1230–1234, Jun. 2015, doi: 10.1126/science.aaa8765.

[6] B. Lim *et al.*, "Pd-Pt Bimetallic Nanodendrites with High Activity for Oxygen Reduction," *Science (80-.).*, vol. 324, no. 5932, pp. 1302 LP – 1305, Jun. 2009, [Online]. Available: http://science.sciencemag.org/content/324/5932/1302.abstract.

[7] DOE, "Technical Targets for Polymer Electrolyte Membrane Fuel Cell Components," 2017.

[8] G. Tsotridis, A. Pilenga, G. De Marco, and T. Malkow, *EU Harmonised Test Protocols for PEMFC MEA Testing in Single Cell Configuration for Automotive Applications; JRC Science for Policy report*. 2015.

[9] D. Schonvogel *et al.*, "Stability of Pt nanoparticles on alternative carbon supports for oxygen reduction reaction," *J. Electrochem. Soc.*, vol. 164, no. 9, pp. F995–F1004, 2017, doi: 10.1149/2.1611709jes.

[10] A. Riese, D. Banham, S. Ye, and X. Sun, "Accelerated Stress Testing by Rotating Disk Electrode for Carbon Corrosion in Fuel Cell Catalyst Supports," *J. Electrochem. Soc.*, vol.

162, no. 7, pp. F783–F788, Apr. 2015, doi: 10.1149/2.0911507jes.

[11] L. Castanheira, W. O. Silva, F. H. B. Lima, A. Crisci, L. Dubau, and F. Maillard, "Carbon Corrosion in Proton-Exchange Membrane Fuel Cells: Effect of the Carbon Structure, the Degradation Protocol, and the Gas Atmosphere," *ACS Catal.*, vol. 5, no. 4, pp. 2184–2194, Apr. 2015, doi: 10.1021/cs501973j.

[12] K. Saikia, B. K. Kakati, B. Boro, and A. Verma, "Current Advances and Applications of Fuel Cell Technologies," in *Recent Advancements in Biofuels and Bioenergy Utilization*, Singapore: Springer Singapore, 2018, pp. 303–337.

[13] S. Stariha *et al.*, "Recent Advances in Catalyst Accelerated Stress Tests for Polymer Electrolyte Membrane Fuel Cells," *J. Electrochem. Soc.*, vol. 165, no. 7, pp. F492–F501, May 2018, doi: 10.1149/2.0881807jes.

[14] S. Trasatti and O. A. Petrii, "Real surface area measurements in electrochemistry," *Pure Appl. Chem.*, vol. 63, no. 5, pp. 711–734, Jan. 1991, doi: 10.1351/pac199163050711.

[15] Y. Li, L. Tang, and J. Li, "Preparation and electrochemical performance for methanol oxidation of pt/graphene nanocomposites," *Electrochem. commun.*, vol. 11, no. 4, pp. 846–849, Apr. 2009, doi: 10.1016/j.elecom.2009.02.009.

[16] B. P. Vinayan and S. Ramaprabhu, "Facile Synthesis of Platinum Decorated Graphene Wrapped Multiwalled Carbon Nanotube and Its Hydrogen Storage Properties," *Nano Commun.*, vol. 1, no. 1, pp. 4–10, Jun. 2014, doi: 10.1166/nano.2014.1003.

[17] H. Sun *et al.*, "Pt nanodendrites with (111) crystalline facet as an efficient, stable and pH-universal catalyst for electrochemical hydrogen production," *Chinese Chem. Lett.*, vol. 31, no. 9, pp. 2478–2482, Sep. 2020, doi: 10.1016/J.CCLET.2020.03.032.

[18] I. Jiménez-Morales *et al.*, "Correlation between the surface characteristics of carbon supports and their electrochemical stability and performance in fuel cell cathodes," *Carbon Energy*, vol. 3, no. 4, pp. 654–665, Aug. 2021, doi: 10.1002/cey2.109.

[19] J.-B. Wu, M.-L. Lin, X. Cong, H.-N. Liu, and P.-H. Tan, "Raman spectroscopy of graphene-based materials and its applications in related devices," *Chem. Soc. Rev.*, vol. 47, no. 5, pp. 1822–1873, 2018, doi: 10.1039/C6CS00915H.

[20] T. Lagarteira, S. Delgado, C. Fernandes, C. Azenha, C. Mateos-Pedrero, and A. Mendes, "The role of Pt loading on reduced graphene oxide support in the polyol synthesis of catalysts for oxygen reduction reaction," *Int. J. Hydrogen Energy*, 2020, doi:

10.1016/j.ijhydene.2020.02.022.

[21] P. Toth, "Nanostructure quantification of turbostratic carbon by HRTEM image analysis: State of the art, biases, sensitivity and best practices," *Carbon N. Y.*, vol. 178, pp. 688–707, Jun. 2021, doi: 10.1016/j.carbon.2021.03.043.

[22] S. M. Choi, M. H. Seo, H. J. Kim, and W. B. Kim, "Synthesis of surface-functionalized graphene nanosheets with high Pt-loadings and their applications to methanol electrooxidation," *Carbon N. Y.*, vol. 49, no. 3, pp. 904–909, Mar. 2011, doi: 10.1016/J.CARBON.2010.10.055.

[23] P. Dhanasekaran, A. Shukla, S. V. Selvaganesh, S. Mohan, and S. D. Bhat, "Silica-decorated carbon-Pt electrocatalyst synthesis via single-step polyol method for superior polymer electrolyte fuel cell performance, durability and stack operation under low relative humidity," *J. Power Sources*, vol. 438, p. 226999, Oct. 2019, doi: 10.1016/j.jpowsour.2019.226999.

[24] Y. Takasu *et al.*, "Size effects of platinum particles on the electroreduction of oxygen," *Electrochim. Acta*, vol. 41, no. 16, pp. 2595–2600, Jan. 1996, doi: 10.1016/0013-4686(96)00081-3.

[25] J. M. Doña Rodríguez, J. A. Herrera Melián, and J. Pérez Peña, "Determination of the Real Surface Area of Pt Electrodes by Hydrogen Adsorption Using Cyclic Voltammetry," *J. Chem. Educ.*, vol. 77, no. 9, p. 1195, Sep. 2000, doi: 10.1021/ed077p1195.

[26] C. Costentin and J.-M. Savéant, "Ohmic drop correction in electrochemical techniques. Multiple potential step chronoamperometry at the test bench," *Energy Storage Mater.*, vol. 24, pp. 1–3, Jan. 2020, doi: 10.1016/j.ensm.2019.07.029.

[27] S. Song, Y. Wang, and P. K. Shen, "Pulse-microwave assisted polyol synthesis of highly dispersed high loading Pt/C electrocatalyst for oxygen reduction reaction," *J. Power Sources*, vol. 170, no. 1, pp. 46–49, Jun. 2007, doi: 10.1016/j.jpowsour.2007.04.012.

[28] A. Holewinski and S. Linic, "Elementary Mechanisms in Electrocatalysis: Revisiting the ORR Tafel Slope," *J. Electrochem. Soc.*, vol. 159, no. 11, pp. H864–H870, Jan. 2012, doi: 10.1149/2.022211jes.

[29] H. A. Gasteiger, S. S. Kocha, B. Sompalli, and F. T. Wagner, "Activity benchmarks and requirements for Pt, Pt-alloy, and non-Pt oxygen reduction catalysts for PEMFCs," *Appl. Catal. B Environ.*, vol. 56, no. 1–2, pp. 9–35, Mar. 2005, doi:

10.1016/J.APCATB.2004.06.021.

[30] Y. Garsany, I. L. Singer, and K. E. Swider-Lyons, "Impact of film drying procedures on RDE characterization of Pt/VC electrocatalysts," *J. Electroanal. Chem.*, vol. 662, no. 2, pp. 396–406, 2011, doi: https://doi.org/10.1016/j.jelechem.2011.09.016.

[31] A. Damjanovic and V. Brusic, "Electrode kinetics of oxygen reduction on oxide-free platinum electrodes," *Electrochim. Acta*, vol. 12, no. 6, pp. 615–628, Jun. 1967, doi: 10.1016/0013-4686(67)85030-8.

[32] M. R. Tarasevich, A. Sadkowski, and E. Yeager, "Oxygen Electrochemistry," in *Comprehensive Treatise of Electrochemistry*, Boston, MA: Springer US, 1983, pp. 301–398.

[33] C. A. Reiser *et al.*, "A Reverse-Current Decay Mechanism for Fuel Cells," *Electrochem. Solid-State Lett.*, vol. 8, no. 6, p. A273, 2005, doi: 10.1149/1.1896466.

[34] W. R. Baumgartner, P. Parz, S. D. Fraser, E. Wallnöfer, and V. Hacker, "Polarization study of a PEMFC with four reference electrodes at hydrogen starvation conditions," *J. Power Sources*, vol. 182, no. 2, pp. 413–421, Aug. 2008, doi: 10.1016/j.jpowsour.2008.01.001.

[35] J. C. Meier *et al.*, "Degradation Mechanisms of Pt/C Fuel Cell Catalysts under Simulated Start–Stop Conditions," *ACS Catal.*, vol. 2, no. 5, pp. 832–843, May 2012, doi: 10.1021/cs300024h.

[36] A. A. Topalov, S. Cherevko, A. R. Zeradjanin, J. C. Meier, I. Katsounaros, and K. J. J. Mayrhofer, "Towards a comprehensive understanding of platinum dissolution in acidic media," *Chem. Sci.*, vol. 5, no. 2, pp. 631–638, 2014, doi: 10.1039/C3SC52411F.

[37] Y. Garsany, O. A. Baturina, K. E. Swider-Lyons, and S. S. Kocha, "Experimental Methods for Quantifying the Activity of Platinum Electrocatalysts for the Oxygen Reduction Reaction," *Anal. Chem.*, vol. 82, no. 15, pp. 6321–6328, Aug. 2010, doi: 10.1021/ac100306c.

[38] H. Schulenburg *et al.*, "3D Imaging of Catalyst Support Corrosion in Polymer Electrolyte Fuel Cells," *J. Phys. Chem. C*, vol. 115, no. 29, pp. 14236–14243, Jul. 2011, doi: 10.1021/jp203016u.

[39] T. N. V. Matthew M. Mench, Emin Caglan Kumbur, *Polymer Electrolyte Fuel Cell Degradation*. 2012.

[40] T. Lagarteira, S. Delgado, C. Fernandes, C. Azenha, C. Mateos-Pedrero, and A. Mendes,

"The role of Pt loading on reduced graphene oxide support in the polyol synthesis of catalysts for oxygen reduction reaction," *Int. J. Hydrogen Energy*, Feb. 2020, doi: 10.1016/j.ijhydene.2020.02.022.

[41] B. Fang, J. H. Kim, M. S. Kim, and J. S. Yu, "Hierarchical nanostructured carbons with meso-macroporosity: Design, characterization, and applications," *Acc. Chem. Res.*, vol. 46, no. 7, pp. 1397–1406, Jul. 2013, doi: 10.1021/ar300253f.

[42] T.-N. Tran *et al.*, "Iron Phosphide Incorporated into Iron-Treated Heteroatoms-Doped Porous Bio-Carbon as Efficient Electrocatalyst for the Oxygen Reduction Reaction," *ChemElectroChem*, vol. 5, no. 14, pp. 1944–1953, Jul. 2018, doi: 10.1002/celc.201800091.

[43] S. Maass, F. Finsterwalder, G. Frank, R. Hartmann, and C. Merten, "Carbon support oxidation in PEM fuel cell cathodes," *J. Power Sources*, vol. 176, no. 2, pp. 444–451, Feb. 2008, doi: 10.1016/j.jpowsour.2007.08.053.

[44] J. H. Kim, J. Y. Cheon, T. J. Shin, J. Y. Park, and S. H. Joo, "Effect of surface oxygen functionalization of carbon support on the activity and durability of Pt/C catalysts for the oxygen reduction reaction," *Carbon N. Y.*, vol. 101, pp. 449–457, May 2016, doi: 10.1016/j.carbon.2016.02.014.

[45] S. Mukerjee, S. Srinivasan, M. P. Soriaga, and J. McBreen, "Effect of preparation conditions of Pt alloys on their electronic, structural, and electrocatalytic activities for oxygen reduction. XRD, XAS, and electrochemical studies," *J. Phys. Chem.*, vol. 99, no. 13, pp. 4577–4589, 1995, doi: 10.1021/j100013a032.

[46] B. C. Beard and P. N. Ross, "The Structure and Activity of Pt-Co Alloys as Oxygen Reduction Electrocatalysts," *J. Electrochem. Soc.*, vol. 137, no. 11, pp. 3368–3374, 1990, doi: 10.1149/1.2086223.

[47] F. N. Büchi, M. Inaba, and T. J. Schmidt, Eds., *Polymer Electrolyte Fuel Cell Durability*. New York, NY: Springer New York, 2009.

[48] X. Cheng *et al.*, "A review of PEM hydrogen fuel cell contamination: Impacts, mechanisms, and mitigation," *J. Power Sources*, vol. 165, no. 2, pp. 739–756, Mar. 2007, doi: 10.1016/j.jpowsour.2006.12.012.

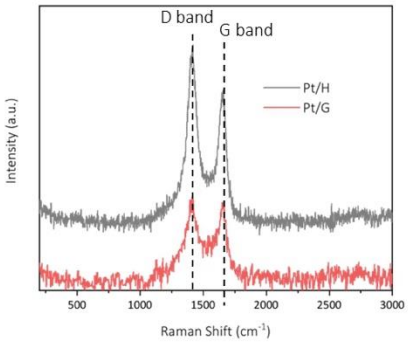
[49] K. Kinoshita, "Particle Size Effects for Oxygen Reduction on Highly Dispersed Platinum in Acid Electrolytes," *J. Electrochem. Soc.* , vol. 137, no. 3, pp. 845–848, Mar. 1990, doi: 10.1149/1.2086566.

659 [50] K. J. J. Mayrhofer *et al.*, "Fuel cell catalyst degradation on the nanoscale," *Electrochem.*
660 *commun.*, vol. 10, no. 8, pp. 1144–1147, Aug. 2008, doi: 10.1016/j.elecom.2008.05.032.
661 [51] S. G. Rinaldo, J. Stumper, and M. Eikerling, "Physical Theory of Platinum Nanoparticle
662 Dissolution in Polymer Electrolyte Fuel Cells," *J. Phys. Chem. C*, vol. 114, no. 13, pp.
663 5773–5785, Apr. 2010, doi: 10.1021/jp9101509.
664 [52] E. F. Holby, Y. Shao-Horn, W. Sheng, and D. Morgan, "Oxide formation and removal on
665 Pt surfaces under potential cycled conditions," in *ECS Transactions*, 2009, vol. 25, no. 1
666 PART 1, pp. 583–592, doi: 10.1149/1.3210609.
667 [53] D. C. Johnson, D. T. Napp, and S. Bruckenstein, "A ring-disk electrode study of the
668 current/potential behaviour of platinum in 1.0 M sulphuric and 0.1 M perchloric acids,"
669 *Electrochim. Acta*, vol. 15, no. 9, pp. 1493–1509, Sep. 1970, doi: 10.1016/0013-
670 4686(70)80070-6.
671 [54] X. Wang, R. Kumar, and D. J. Myers, "Effect of voltage on platinum dissolution relevance
672 to polymer electrolyte fuel cells," *Electrochem. Solid-State Lett.*, vol. 9, no. 5, 2006, doi:
673 10.1149/1.2180536.
674 [55] J. Parrondo *et al.*, "Platinum supported on titanium-ruthenium oxide is a remarkably stable
675 electrocatayst for hydrogen fuel cell vehicles," *Proc. Natl. Acad. Sci. U. S. A.*, vol. 111, no.
676 1, pp. 45–50, 2014, doi: 10.1073/pnas.1319663111.
677
678

Highlights

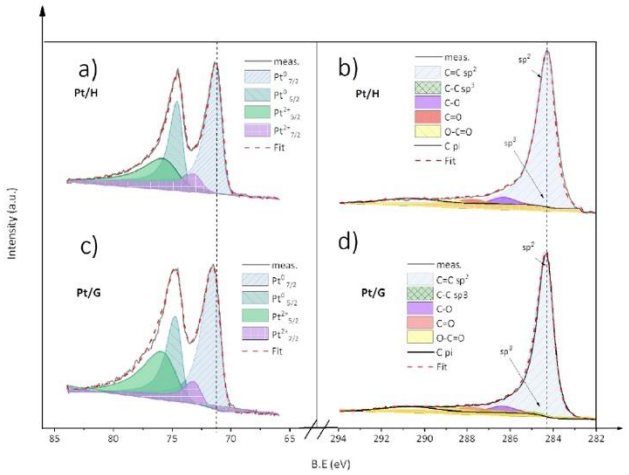
- Stability of Pt/G was studied via three different degradation protocols and compared to Pt/H.
- Potential cycling below 1 V promotes higher ORR mass-specific activity loss, among all ASTs;
- Pt/G maintained higher ECSA and ORR activity than Pt/H upon the different types of ASTs.
- Pt/G is considerably more stable than Pt/H despite observing a higher particle growth.

689 **Supplementary information**



690

691 **Figure S1 –** Raman spectra obtained for pristine Pt/H and Pt/G samples.



692

693 **Figure S2** – High resolution XPS analysis of (a,c) Pt 4f of pristines Pt/H and Pt/G respectively, (b,d) C1s of Pt/H and Pt/G, respectively.

694

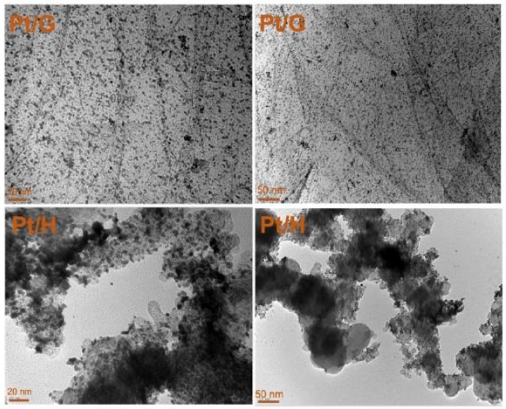


Figure S3 – TEM images with different magnifications for Pt/G and Pt/H.

Table S1 – Fittings for peak binding energy of orbitals 4f and C1s from Pt/H and Pt/G.

Pt/G **Pt 4f orbital**	**Be/ eV**	**FWHM**	**Line Shape**	**At. %**
$Pt^0_{7/2}$	71.1	1.45	LA(1.2,85,70)	43.40
$Pt^0_{5/2}$	74.3	1.3	LA(1.2,85,70)	22.80
$Pt^{2+}_{7/2}$	72.7	1.54	LA(1.2,85,70)	7.23
$P^{2+}_{5/2}$	75.0	2.8	LA(1.2,85,70)	26.57
Pt/H **Pt4f orbital**	**Be/ eV**	**FWHM**	**Line Shape**	**At. %**
$Pt^0_{7/2}$	70.9	1.26	LA(1.2,85,70)	46.8
$Pt^0_{5/2}$	74.2	1.1	LA(1.2,85,70)	26.7
$Pt^{2+}_{7/2}$	72.7	1.5	LA(1.2,85,70)	6.50
$P^{2+}_{5/2}$	74.9	2.8	LA(1.2,85,70)	20.0

Pt/G C1s orbital	Be/ eV	FWHM	Line Shape	At. %
C=C sp^2	284.31	0.75	LA(1.2,2.5,5)	87.2
C-C sp^3	284.81	1.2	GL(30)	0.4
C-O	286.31	1.2	GL(30)	2.8
C=O	287.81	1.2	GL(30)	2.1
O-C=O	288.81	1.2	GL(30)	1.4
C π*	290.72	2.7	GL(30)	6.1
Pt/H **C1s orbital**	**Be/ eV**	**FWHM**	**Line Shape**	**At. %**
C=C sp^2	284.26	0.8	LA(1.2,2.5,5)	86.4
C-C sp^3	284.76	1.2	GL(30)	0.01
C-O	286.26	1.2	GL(30)	3.7
C=O	287.76	1.2	GL(30)	2.39
O-C=O	288.76	1.2	GL(30)	1.52
C π*	290.67	2.7	GL(30)	6.0

700

701 **Table S2 –** Pt average particle sizes and dissolved Pt in the electrolyte for Pt/H and Pt/G.

Pt average size	Pt/H	Pt/G
BoL (nm)	4.1	2.6
AST 1 (nm)	4.7 (+114.6 %)	3.2 (+123.1 %)
AST 2 (nm)	6.0 (+146.3 %)	1.2 (+184.6 %)
AST3 (nm)	4.3 (+104.9 %)	1.2 (+130.8 %)
Pt dissolution	**Pt/H**	**Pt/G**
Initial mass (µg)	4.000	4.000
AST 1 (µg)	0.062 (1.54 %)	0.123 (3.08 %)
AST 2 (µg)	0.0195 (0.49 %)	0.024 (0.60 %)
AST 3 (µg)	0.006 (0.15 %)	0.015 (0.38 %)

702

703

Journal of The Electrochemical Society, **166** (16) A4067-A4072 (2019)
0013-4651/2019/166(16)/A4067/6/$38.00 © The Electrochemical Society

In-Situ Measurement of Vanadium Crossover for the Vanadium Redox Flow Battery

Tiago Lagarteira,[1] Pedro Pacheco,[1] Carlos Almeida,[1] Anders Bentien,[2,*] Ricardo Monteiro,[1] and Adélio Mendes[1,z]

[1]*LEPABE - Laboratory for Process, Environment, Biotechnology and Energy, Faculty of Engineering of the University of Porto, 4200-465 Porto, Portugal*
[2]*Department of Engineering - Biological & Chemical Engineering, Aarhus University, 8200 Aarhus N, Denmark*

A simple in-situ method for the quantification of the crossover in redox flow batteries, adapted from an electrochemical method currently used for quantifying the hydrogen crossover in fuel cells, is proposed and used for characterizing a vanadium redox flow battery. A linear sweep voltammetry (LSV) scan is performed with the pertinent redox species in one side of the electrochemical cell, while in the other side is the supporting electrolyte. The LSV plot should display a plateau where the current is limited by the crossover of the selected species. The crossover results were compared with an external analytical method using MP-AES, showing very good agreement with a maximum relative difference of 6%. This method was used to quantify the crossover of all vanadium species using both cation and anion exchange membranes. The proposed method can be applied for assisting the development and characterization of ion-exchange membranes for redox flow batteries and for in-situ diagnosis of component degradation and failure in RFB systems without disassembling them.
© 2019 The Electrochemical Society. [DOI: 10.1149/2.0331916jes]

Manuscript submitted August 26, 2019; revised manuscript received November 18, 2019. Published December 4, 2019.

The increasing widespread of electricity production from renewable sources led to the critical need of grid-scale energy storage systems to balance the intermittent nature of wind and solar power.[1–3] In this regard, redox flow batteries (RFBs) have emerged due to the advantage of decoupled power and energy scaling, long operation lifetime, easy maintenance, simple manufacture and low cost of storage (LCOS).[4–6] Particularly, all-vanadium redox flow batteries (VRFBs) have the unique feature of using, in both electrodes, redox pairs based in the same chemical element. Also, the used electrolyte is very stable, and, in theory, it can be reused indefinitely.[7,8] This is an important advantage compared to other RFBs since the detrimental crossover of active species through the membrane can be periodically mitigated by remixing the electrolyte.[9] VRFBs have been successfully implemented in stationary applications such as for remote areas, back-up power supply, regulation of grid power quality and frequency control, and in distributed power generation systems.[10] After generating significant commercial interest, VRFBs are now requiring the development of quality control tools, besides the ongoing development of mass production solutions.

Some of the most important causes for performance degradation and system shut-down of VRFBs are the vanadium crossover and existence of internal short-circuits.[11,12] The permeation of unreacted vanadium ions through the membrane (crossover) is problematic since it leads to the (reversible) loss of capacity and self-discharge, thus requiring periodical remixing of the electrolyte. Despite the influence of the operational conditions, such as temperature and flow rate, the membrane type and aging have the biggest impact on vanadium crossover.[13] Different types of membranes used in VRFBs include cationic and anionic exchange membranes; the most commonly reported are perfluorinated cation exchange membranes such as Nafion.[14,15] Regardless of the membrane type, vanadium crossover is inevitable, making it a topic of great interest among the VRFB research community not only to assess but also to mitigate its detrimental effects in the performance and lifespan of the battery.

The crossover in VRFBs is driven by the different electrochemical potentials of each species in the two sides of the membrane, with transport occurring from higher to lower potential. Two contributions are discernible: chemical potential gradients are responsible for diffusive processes, and electric potential gradients cause migration of charged species and solvent molecules (electro-osmotic drag).[16,17] If a porous membrane is employed instead of an ion exchange membrane, bulk convection of the electrolyte can also occur. The most widely reported method for crossover quantification in VRFBs makes use of a diffusion cell,[18,19] where only one of the two chambers, separated by the membrane, contains vanadium ions in the electrolyte. The blank side, initially containing supporting electrolyte, is periodically sampled for posterior analysis to quantify the vanadium concentrations. A simple mass balance to the blank electrolyte yields the following relation:

$$J = \frac{V}{A}\frac{dc}{dt} \quad [1]$$

where J (mol s^{-1}) is molar flux of vanadium species through the membrane, V (m^3) stands for the total volume of blank electrolyte, A is the membrane area (m^2), c (mol m^{-3}) is the concentration of vanadium in the blank electrolyte and t (s) is time. The mass transfer rate of vanadium ions through the membrane remains approximately constant and the concentration increases linearly throughout the experiment, according to Fick's law. Thus, the slope of concentration/time relationship can be used to calculate the molar flux of vanadium through the membrane.

The use of diffusion cells does not allow to account for the contribution of migration driven crossover, since there is no electrical field applied. Other approaches have been proposed to consider migration along with diffusion contributions but none is able to measure vanadium crossover in situ.[20,21] Moreover, all in-situ methods in literature require the use of an external analytic method for the determination of the vanadium concentration of the electrolyte samples, such as UV-Vis spectroscopy,[11,15] potentiometric titration,[1,5,22,23] or inductively coupled plasma atomic emission spectrometry (ICP-AES),[19,24] among others.[23] In real applications, the use of external analytical methods for quality control prove often to be unpractical and time-consuming. Therefore, RFBs are still lacking an in-situ, simple, accurate and reliable methodology for crossover determination.

The PEMFC community makes use of a standard procedure to measure hydrogen crossover through the membrane.[25–27] This procedure consists of performing linear sweep voltammetry (LSV) at low scan rate to a PEMFC fed with hydrogen to the anode and inert N_2 to the cathode. The faradaic response corresponds to the oxidation of hydrogen that permeates through the membrane to the working electrode (WE). After reaching the steady-state, the faradaic current is limited by the flow rate of H_2 through the membrane, despite the linearly increasing potential difference applied on the cell. At this stage, the limiting current is proportional to the rate of hydrogen permeation, as expressed by Faraday's law:

$$J = \frac{j_l}{zF} \quad [2]$$

*Electrochemical Society Member.
zE-mail: mendes@fe.up.pt

where J (mol s^{-1}) is the flow rate of hydrogen through the membrane, j_l (A) is the limiting current, z is the number of electrons exchanged in the electrochemical reaction, and F (96 485 C mol^{-1}) is Faraday's constant.

Inspired in the hydrogen crossover diagnosis for PEMFCs, this work discloses an in-situ method to quantify electrochemically the vanadium crossover in VRFBs. The accuracy and reliability of the proposed method is highlighted with the use of different membranes – cation and anion exchange membranes – and the crossover quantification of all vanadium ion species; this new adaption of the method for RFBs was then validated using an external analytical method. The simplicity of the method, named hereafter electrochemical method, coupled with the fact that it does not require analytical equipment other than an electrochemical workstation, makes it very attractive for the quantification of species crossover in any kind of redox flow batteries. It can be applied to a redox flow cell or stack without disassembly, unlike other methods reported in literature. This method provides not only an effective tool for membrane characterization and development but also for diagnosing failure, enabling the monitoring of active species crossover throughout the lifetime of a redox flow battery.

Experimental

Materials and cell components.—Vanadium electrolyte was sourced from GfE (1.6 M at a 50:50 V^{3+}/V^{4+} ratio). An electrochemical cell was used to charge the two electrolytes to a state of charge (SoC) of ca. 100%, yielding a V^{2+} enriched negalyte and a VO^{2+} enriched posilyte. A 4 M H_2SO_4 aqueous solution was prepared by diluting 95.0 - 97.0 wt% H_2SO_4 (Honeywell International Inc., USA) in deionized water, to be used as blank electrolyte. PAN-based carbon felt (Chemshine Carbon Co., Ltd., China) was employed as the electrode material, with a thickness of 6 mm and 95% porosity when uncompressed. The electrodes were cut to size and treated according to the procedure reported by Monteiro et al.[28] Shortly, the electrodes were thermally treated at 415°C during 12 h under air atmosphere. Cation exchange membranes (Nafion 117, 115 and 212) were purchased from Ion Power (Germany). Anion exchange membrane (Fumasep FAP-450) was purchased from Fumatech BWT GmbH (Germany). Prior to assembly, Nafion membranes were immersed in deionized water during 5 – 10 minutes for mechanical conditioning while FAP 450 was assembled in dry condition. The electrochemical cell used for the crossover measurements had a geometric active area of 16 cm^2. The electrodes were compressed to 60% of their original thickness. Apart from membrane and electrodes, the cell was composed by two steel endplates, two insulating PVC plates, two copper current collectors and graphite bipolar plates machined in a flow-through design, along with EPDM gaskets.

Experimental set-up.—The electrolyte was pumped from the reservoirs to the cell by means of two Watson-Marlow Qdos 120 Universal peristaltic pumps. To prevent oxidation of V^{2+} by oxygen in air, Verdeflex tubing (4.8 mm inner diameter) was used owing to its low oxygen permeability, and nitrogen gas was employed to purge both electrolyte reservoirs. Electrochemical measurements were performed with a Zahner Zennium workstation (Zahner Elektrik, Germany). The cell was connected to the electrochemical workstation in a two-electrode configuration, where the working electrode (WE) was connected to the positive half-cell, and the counter electrode (CE) was connected to the negative half-cell. The reference electrode (RE) lead was connected to the CE. The experimental set-up is schematized in Figure 1.

Crossover measurement.—The negative half-cell was connected to a reservoir of V^{2+} enriched electrolyte, and the positive half-cell was connected to a 100 cm^3 graduated cylinder used as a blank electrolyte reservoir. The positive half-cell was washed thoroughly with blank electrolyte before each experiment. A low flowrate of 0.5 cm^3 min^{-1} was maintained in both sides during the LSV for crossover measurement. The potential was swept from a lower limit corresponding to the open circuit potential (OCP) of the cell to an upper limit of 250 mV. For the scan rate study, scan rates of 50, 75 and 100 $\mu V\ s^{-1}$ were employed. For the study with different membranes, Nafion 212, 115 and 117, and FAP-450 were used. The scan rate in the membrane study was 75 $\mu V\ s^{-1}$. To show the method response in case of internal short-circuit, a scalpel was used to perforate a Nafion 212 membrane in 5 locations (in the center and in the four corners, creating incisions of ca. 2 mm in length). This measurement was also performed at 75 $\mu V\ s^{-1}$.

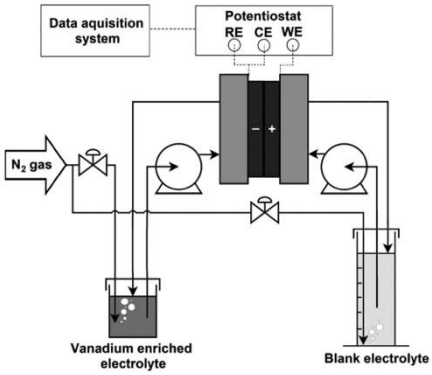


Figure 1. Schematic diagram of the experimental set-up for crossover measurement.

Crossover diagnosis after aging.—The degradation study was performed with Nafion 212 membrane. After the LSV for crossover measurement, as detailed in the previous section, there was a substitution of the electrolytes for fresh ones. The flowrate was set to 50 cm^3 min^{-1}. Fresh electrolytes were charged to ca. 100% SoC, and the cell was then subjected to galvanostatic charge-discharge cycling (CDC) for an extended period to impose degradation to the Nafion 212 membrane. CDC was performed at a current density of 80 mA cm^{-2}, with cutoff voltages of 0.7 V and 1.65 V, for 28 cycles. After CDC, another crossover measurement was performed. Data from CDC allowed for the calculation of charge, voltage and energy efficiencies (CE, VE and EE, respectively), along with discharge capacity loss (DCL) and voltage efficiency loss (VEL) for each cycle:[29]

$$\mathrm{CE}_i = \frac{\int_{t_{\mathrm{d},0}}^{t_{\mathrm{d},\mathrm{f}}} I_{\mathrm{d}}(t)\,dt}{\int_{t_{\mathrm{c},0}}^{t_{\mathrm{c},\mathrm{f}}} I_{\mathrm{c}}(t)\,dt} \quad [3]$$

$$\mathrm{VE}_i = \frac{\int_{t_{\mathrm{d},0}}^{t_{\mathrm{d},\mathrm{f}}} E_{\mathrm{d}}(t)\,dt}{\int_{t_{\mathrm{c},0}}^{t_{\mathrm{c},\mathrm{f}}} E_{\mathrm{c}}(t)\,dt} \cdot \frac{\left(t_{\mathrm{c},\mathrm{f}} - t_{\mathrm{c},0}\right)}{\left(t_{\mathrm{d},\mathrm{f}} - t_{\mathrm{d},0}\right)}. \quad [4]$$

$$\mathrm{EE}_i = \mathrm{CE}_i \cdot \mathrm{VE}_i. \quad [5]$$

$$\mathrm{DCL}_i = \frac{\int_{t_{\mathrm{d},0}}^{t_{\mathrm{d},\mathrm{f}}} I_{\mathrm{d}}(t)\,dt\Big|_{\text{cycle 1}} - \int_{t_{\mathrm{d},0}}^{t_{\mathrm{d},\mathrm{f}}} I_{\mathrm{d}}(t)\,dt\Big|_{\text{cycle } i}}{\int_{t_{\mathrm{d},0}}^{t_{\mathrm{d},0}} I_{\mathrm{d}}(t)\,dt\Big|_{\text{cycle 1}}} \quad [6]$$

$$\mathrm{VEL}_i = \frac{\mathrm{VE}_1 - \mathrm{VE}_i}{\mathrm{VE}_1} \quad [7]$$

where I (A) is the current, E (V) is the cell potential, t (s) stands for time, subscript i stands for cycle number, subscript c for charge, subscript d for discharge, subscript 0 for initial and subscript f for

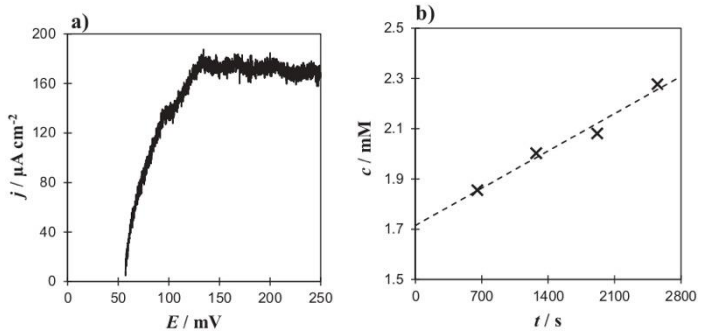


Figure 2. New electrochemical vs sampling chemical analysis crossover methods: a) linear sweep voltammetry data obtained at a scan rate of 75 µV s^{-1} and b) elemental vanadium concentration plotted over elapsed time.

final. DCL and VEL are measures of the percentage loss in charge capacity and voltage efficiency, respectively, for cycle *i*, relative to the initial values (cycle 1). Additionally, after charge-discharge cycling, both membranes submerged in Millipore water for a period of 12 h, and subsequently dried at 60°C during 24h, when their thicknesses were measured. The measurements were performed with a micrometer (Mitutoyo Digimatic Micrometer 293–805), in eight points on both the pristine and aged membranes. These correspond to the four corners of the membranes (ca. 3 mm from the edges of the active area), four points in a cross pattern near the center (ca. 1.5 cm from the edges), and one point in the center.

Determination of vanadium concentration.—During the crossover measurement of the cell assembled with Nafion 115, samples of 1 cm^3 were periodically taken from the blank electrolyte reservoir and diluted by a factor of 10 with Millipore water. The total volume of blank electrolyte contained in the cell and reservoir was 143 $cm.^3$ Elemental vanadium concentration was determined by Microwave Plasma coupled with Atomic Emission Spectroscopy (MP-AES, Agilent 4200), at a wavelength of 437.9 nm.

Results and Discussion

Optimization of parameters.—The WE was washed carefully to remove any traces of vanadium which directly impact the starting point of the LSV. The supporting electrolyte used in washing was stored for further recycling and use. After washing the WE with blank electrolyte, the OCP of the cell sat typically within the range of 0 – 100 mV, slowly decreasing due to traces V^{2+} from immediate crossover. The difference in potential across the two half-cells is assigned to the differing concentrations of V^{2+} and V^{3+}, as the cell effectively behaves as a concentration cell. After starting the LSV, the redox reactions occurring in the cell, as the potential in the WE is swept, are:

$$\text{Counter electrode (vanadium electrolyte)}: V^{3+} + e^- \rightarrow V^{2+} \quad [8]$$

$$\text{Working electrode (blank electrolyte)}: V^{2+} \rightarrow V^{3+} + e^- \quad [9]$$

Preliminary tests were performed with wider potentials to determine the most suitable potential range for running the LSV. Considering that the standard oxidation potentials of V^{2+} to V^{3+} and V^{3+} to V^{4+} are separated by 600 mV, an upper potential of 250 mV was found to be adequate, since, in one hand, this potential the reaction is not electrochemically limited, and in the other it does not enable the further oxidation of V^{3+} to V^{4+}. To investigate whether the blank electrolyte was indeed electrochemically inert or if hydrogen evolution would not take place within the LSV potential range, as initially hypothesized, a blank test was performed. The resulting voltammogram displayed a nearly negligible constant current of ca. 6 µA cm^{-2}, as shown in Figure S1.

Following, for optimizing the scan rate value, several LSVs were performed at different scan rates. In Figure S2, are shown voltammograms obtained with scan rates of 50, 75 and 100 µV s^{-1}. A scan rate of 75 µV s^{-1} was found to be adequate as it generated a well-defined current plateau and was adopted for all subsequent crossover measurements. Higher scan rates result in a pronounced peak current leading to a less well-defined current plateau due to fast oxidation of accumulated V^{2+} in the blank electrolyte while shorter scan rates result in longer test durations for the same potential range. No variation in the volume of blank electrolyte was observed during the LSV measurements, which typically lasted from 30 to 50 minutes.

Electrochemical method vs ex-situ vanadium quantification.—The validation of the method for VRFBs was accomplished comparing the results obtained electrochemically over time with those obtained directly from the determination of the elemental vanadium concentration in the blank electrolyte by MP-AES. A stable plateau is evident in Figure 2a with an average limiting current density of 171 µA cm^{-2}. Throughout the electrochemical measurement, the blank electrolyte was periodically sampled and later analyzed by MP-AES. Using the concentration and collecting time of each sample, the vanadium concentration (at the initially blank electrolyte) over time can be found in Figure 2b, along with the linear model that fits the data; the slope of this line is directly related to the crossover rate by Equation 1, which is 6.8 µmol h^{-1} cm^{-2}.

Similarly, based on the limiting current density obtained by LSV (Equation 2), a crossover flux of 6.4 µmol h^{-1} cm^{-2} was obtained. These values differ for just 6% (relative difference), which was considered to be within the experimental error. As for hydrogen crossover measurement for PEMFCs, the vanadium permeate flux is compensated by an electrochemical reaction at the electrode containing higher vanadium concentration to maintain steady-state conditions and the required current is measured. Moreover, the conditions (low scan rate and low flow rate) were set to ensure that the dominant factor influencing the current response is the step of vanadium ion diffusing through

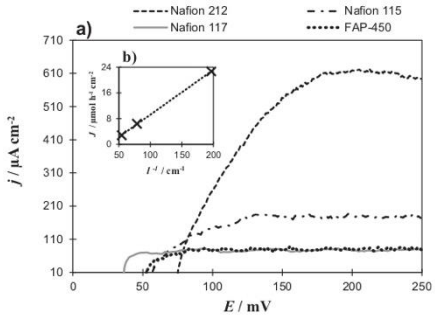


Figure 3. a) LSV voltammograms performed at 75 µV s^{-1} with cells assembled with Nafion membranes with different thicknesses and FAP-450 from fumatech. b) V^{2+} crossover flux for Nafion 212, 115 and 117, plotted against the inverse of membrane thickness.

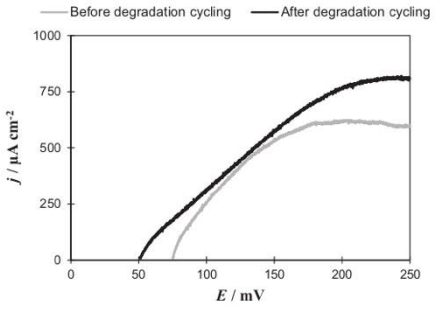


Figure 4. LSV voltammograms performed at 75 µV s^{-1}, before and after charge-discharge aging.

the membrane, similarly as reported for H_2 crossover quantification in PEMFCs.[30,31]

Vanadium crossover on different membranes.—The adapted method was used for comparing the crossover through membranes with different thicknesses, Nafion 212, 115 and 117, and different chemical structures, Fumasep FAP-450. Voltammograms resulting from the crossover measurements can be found in Figure 3a. The V^{2+} crossover rate through each membrane is displayed along with the dry membrane thickness in Table I. Membranes with the same chemical structure, Nafion 212, 115 and 117, displayed V^{2+} crossover inversely proportional to their thickness (Figure 3b), which in turn also validates the accuracy of the method. This is in agreement with the Nernst-Planck equation of mass conservation, which dictates that the diffusion and migration components of mass transfer are proportional to the inverse of the diffusion path length.[32] Despite having a similar thickness to Nafion 212, Fumasep FAP-450 has a nine-fold lower crossover. FAP-450 is an anion exchange membrane, with a high selectivity for anions, diminishing the transport of vanadium cations.[33] Moreover, it has a sterically hindered aromatic polyamine chemical structure that contains a backbone that is aromatic-based, leading to lower porosity comparing to the cation-exchange counterpart.[34] Figure S3 illustrates the LSV response in the case of internal short-circuit caused by membrane perforation. Unlike for pristine membranes, the current response increased continuously without reaching a plateau, as it happens for PEMFC with a perforated membrane.

Vanadium crossover after battery cycling.—The electrochemical cell assembled with the Nafion 212 membrane in the membrane comparison study was chosen due to its smaller thickness. The use of a thinner membrane promotes a greater impact of charge-discharge cycling on increasing vanadium crossover. The charge-discharge history can be found in the supplementary material, Figure S4. Before and after battery cycling, crossover measurements were obtained as illustrated in Figure 4. After battery cycling, an increase of 25% in vanadium crossover was observed. The membrane, after dissembled, displayed no perforations or pinholes. To evaluate any membrane thinning caused by battery operation, the thickness of the used Nafion 212 membrane was measured at nine points before and after charge and discharge cycles. The average measured thickness for the cycled membrane was 50.4 ± 0.9 µm, while for the pristine membrane, a value of 55 ± 0.5 µm was obtained. This represents a relative reduction of ca. 8% in membrane thickness upon charge-discharge cycling that may be the reason for higher crossover after battery cycling.

Table I. Comparison of crossover rates for different ion exchange membranes.

Membrane model	Dry thickness/µm	V^{2+} crossover rate/µmol h^{-1} cm^{-2}
Nafion 117	183	2.9
Nafion 115	127	6.4
Nafion 212	51	29.7
Fumasep FAP-450	50	3.3

Figure 5a plots the coulombic, voltaic and energy efficiencies (CE, VE and EE, respectively), while Figure 5b showcases discharge capacity loss (DCL) and voltage efficiency loss (VEL), as functions of the cycle number. These metrics were computed according to Equations 3–7. An increase in DCL can be observed starting from cycle 10 and accelerating steeply from cycle 23 onwards. DCL can result from an actual reduction in the charge capacity of the electrolytes, which can be caused by side-reactions due to crossover, gas evolution, or electrolyte oxidation by air; however, when CDC is performed galvanostatically, DCL can result from the progressive decrease of VE. This is explained by the fact that lower VE implies higher overpotential for the same cell current. Then, the cutoff voltages for the discharge and charge processes are reached at lower SoC. Consequently, the range of SoC available during CDC is smaller, and the available charge capacity is lower. In Figure 5b, a strong correlation between DCL and VEL can be observed (note that VEL is scaled to have a similar magnitude to that of DCL for easier comparison), meaning that the decrease in VE is the predominating cause of the increase in DCL, not crossover. In this case, the CDC curve does not contain information regarding crossover. To isolate this phenomenon from other causes for efficiency loss, the LSV for crossover measurement is of paramount importance.

Vanadium crossover of all ionic vanadium species.—Crossover measurements were also performed for the remaining vanadium species using two membranes with different chemical structure (Nafion 115 and FAP 450) – Figure 6. The linear voltammetry plots are shown in supplementary material, Figures S5 (Nafion 115) and S6 (FAP 450), for species V^{2+}, V^{3+}, VO^{2+} and VO_2^+. The potential values were normalized and the current signal of VO_2^+ (reduced to VO^{2+} at the WE) inverted to facilitate comparing the actual crossover with each other. The crossover through FAP 450 membrane was higher for $V^{2+} > VO^{2+} > VO_2^+ > V^{3+}$. Such trend was also reported by Tang and co-workers[35] who studied a redox flow cell assembled using

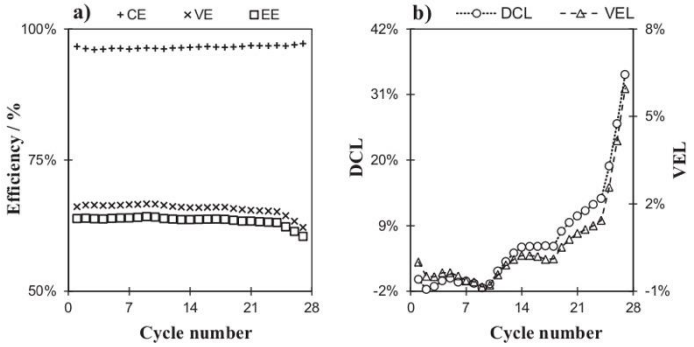


Figure 5. a) Coulombic, voltaic and energy efficiency (CE, VE, EE, respectively) for each cycle. b) Discharge capacity loss and voltage efficiency loss (DCL and VEL respectively) for each cycle. CDC was performed at 80 mA cm^{-2}, with upper and lower potential limits of 1.65 and 0.7 V respectively, for 28 cycles.

a Selemion AMV membrane. Membrane FAP 450 displayed three-fold less crossover than Nafion 115 for V^{2+}, V^{3+} and VO^{2+}; VO_2^+ crossover was also slightly lower for FAP 450. This behavior has been assigned to anion exchange nature of membrane FAP 450, which hinders the permeation of the positively charged vanadium cation ions.[19,35,36]

The crossover through Nafion 115 membrane was $V^{2+} > VO^{2+} > VO_2^+ \approx V^{3+}$, a slightly different trend as for FAP 450 membrane. This behavior was also observed in many experimental and modelling studies using Nafion membranes.[9,13,19,32] However, when vanadium crossover was experimentally studied during battery operation, authors do not agree on the crossover trend. Darling and co-workers[10] reported higher crossover for VO^{2+} and VO_2^+ than for V^{2+} and V^{3+}, respectively. On the other hand, Agar and co-workers[9] reported a similar sequence as the one obtained in this work. Such deviations may be explained by the test conditions, namely: a) larger pressure drop between the inlet and outlet of the cell, which imposes large pressure differences through the membrane,[37] b) gas evolution reactions during charge and c) air oxidation of V^{2+}.[36] The electrochemical method here reported uses very low electrolyte flowrates, minimal overpotentials and nitrogen purging when needed, such as for V^{2+}; this makes this method reliable and accurate.

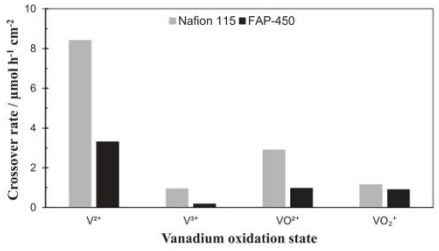


Figure 6. Crossover quantification for V^{2+}, V^{3+}, VO^{2+} and VO_2^+ using a cation exchange membrane (Nafion 115) and an anion exchange membrane (FAP-450).

Conclusions

An in-situ electrochemical method for determining the crossover of the redox species in redox flow batteries was successfully adapted from the widely used hydrogen crossover determination in PEMFCs and experimentally validated. The optimized potential range for the LSV applied to the V^{2+} crossover is between OCP and 250 mV and the scanning rate is 75 μV s^{-1}. The V^{2+} crossover increases with the potential until reaching a plateau which can then be calculated based on the Faraday's law from the diffusion-limiting current.

The new electrochemical method for RFBs was validated by MP-AES analysis and crossover results were compared for four different membranes: Nafion 212, 115 and 117 and Fumasep FAP-450, this last an anion exchange membrane. It was concluded that the two methods produce the same results within the experimental error. It was also concluded that the V^{2+} crossover varies inversely with the membrane thickness, which is in agreement with the Nernst-Planck equation of mass conservation. For perforated membranes the current response increases with the applied potential (internal short) without reaching a plateau.

Problems such as electrolyte imbalance, gas evolution, and V^{2+} air oxidation are avoided using the developed method. As concluded in other works that used external analytical methods, the anion exchange membrane displays lower vanadium crossover than the cation exchange counterpart due to electrostatic repulsion of positively-charged membrane groups and vanadium cations. For Fumasep FAP-450, the crossover of the vanadium species was $V^{2+} > VO_2^+ > VO^{2+} > V^{3+}$, while for Nafion 115 it was $V^{2+} > VO^{2+} > VO_2^+ \approx V^{3+}$.

The developed in-situ crossover determination method is then a powerful tool for assisting the development of ion-exchange membranes for RFB, characterization of ion-exchange membranes for new redox systems and for diagnosing in situ redox systems without opening them.

Acknowledgments

This work was financially supported by: research unit UID/EQU/00511/2019 - Laboratory for Process Engineering, Environment, Biotechnology and Energy – LEPABE funded by national funds through FCT/MCTES (PIDDAC); LEPABE-2-ECO-INNOVATION, POCI-01-0247-FEDER-003405 - POWERFLOW – POCI-01-0145-FEDER-016387 – SUNSTORAGE – POCI-01-0145-FEDER-030510 – SUNFLOW - and POCI-01-0145-FEDER-030223

– POLYSOL – funded by FEDER funds through COMPETE2020 – Programa Operacional Competitividade e Internacionalização (POCI) and Programa Operacional Regional do Norte (NORTE2020) and by national funds (PIDDAC) through FCT/MCTES.

This research was partially supported by the Project "PEMFC-SUDOE" – SOE1/P1/E0293 which is co-financed by the European Regional Development Fund in the framework of the Interreg Sudoe programme.

C. Almeida is grateful to the Portuguese Foundation for Science and Technology (FCT) for the doctoral grant (reference SFRH/BD/131230/2017).

ORCID

Tiago Lagarteira https://orcid.org/0000-0003-2549-2091
Pedro Pacheco https://orcid.org/0000-0002-4592-3058
Anders Bentien https://orcid.org/0000-0002-7204-9167
Adélio Mendes https://orcid.org/0000-0003-2472-3265

References

1. M. Skyllas-Kazacos, M. Rychcik, R. G. Robins, A. G. Fane, and M. A. Green, *J. Electrochem. Soc.*, **133**, 1057 (1986).
2. C. Ponce de León, A. Frías-Ferrer, J. González-García, D. A. Szánto, and F. C. Walsh, *J. Power Sources*, **160**, 716 (2006).
3. T. Monai, H. Suzaki, and K. Yano, *FUJI Electr. Rev.*, **63**, (2017).
4. B. Schwenzer et al., *ChemSusChem*, **4**, 1388 (2011).
5. R. A. Potash, J. R. McKone, S. Conte, and H. D. Abruña, *J. Electrochem. Soc.*, **163**, A338 (2016).
6. M. Skyllas-Kazacos, M. H. Chakrabarti, S. A. Hajimolana, F. S. Mjalli, and M. Saleem, *J. Electrochem. Soc.*, **158**, R55 (2011).
7. S. C. Chieng, 230–301 (1993).
8. D. N. Buckley et al., *J. Electrochem. Soc.*, **165**, A3263 (2018).
9. K. W. Knehr, E. Agar, C. R. Dennison, A. R. Kalidindi, and E. C. Kumbur, *J. Electrochem. Soc.*, **159**, A1446 (2012).
10. R. M. Darling, A. Z. Weber, M. C. Tucker, and M. L. Perry, *J. Electrochem. Soc.*, **163**, A5014 (2016).
11. F. Grossmith, P. Llewellyn, A. Fane, and M. Kazacos, in *Proceedings of Electrochemical Society Symposium*, p. 363 (1988).
12. D. Schulte, J. Drillkens, B. Schulte, and D. U. Sauer, *J. Electrochem. Soc.*, **157**, A989 (2010).
13. X. Teng et al., *J. Power Sources*, **189**, 1240 (2009).
14. E. Wiedemann, A. Heintz, and R. N. Lichtenthaler, *J. Memb. Sci.*, **141**, 215 (1998).
15. C. Sun, J. Chen, H. Zhang, X. Han, and Q. Luo, *J. Power Sources*, **195**, 890 (2010).
16. E. Agar, K. W. Knehr, D. Chen, M. A. Hickner, and E. C. Kumbur, *Electrochim. Acta*, **98**, 66 (2013).
17. L. Hao, Y. Wang, and Y. He, *J. Electrochem. Soc.*, **166**, A1310 (2019).
18. J. Xi et al., *J. Mater. Chem.*, **18**, 1232 (2008).
19. P. K. Leung, Q. Xu, T. S. Zhao, L. Zeng, and C. Zhang, *Electrochim. Acta*, **105**, 584 (2013).
20. Q. Luo et al., *J. Power Sources*, **218**, 15 (2012).
21. D. C. Sing and J. P. Meyers, *ECS Trans.*, **50**, 61 (2013).
22. J. Chen, B. Wang, and J. Yang, *Solvent Extr. Ion Exch.*, **27**, 312 (2009).
23. J. S. Lawton, A. Jones, and T. Zawodzinski, *J. Electrochem. Soc.*, **160**, A697 (2013).
24. X. Luo et al., *J. Phys. Chem. B*, **109**, 20310 (2005).
25. Florida Solar Energy Center, *Work Performed Under DOE Contract # DE-FC36-06GO16028*, 11 (2009).
26. K. R. Cooper, *Fuel Cell Mag.*, **8**, 34 (2008).
27. M. Inaba et al., *Electrochim. Acta*, **51**, 5746 (2006).
28. R. Monteiro, J. Leirós, M. Boaventura, and A. Mendes, *Electrochim. Acta*, **267**, 80 (2018).
29. H. A.-Z. Al-Fetlawi, *ECS Trans.*, **58**, 33 (2014).
30. B. Bensmann, R. Hanke-Rauschenbach, and K. Sundmacher, *Int. J. Hydrogen Energy*, **39**, 49 (2014).
31. X. Cheng et al., *J. Power Sources*, **167**, 25 (2007).
32. P. A. Boettcher, E. Agar, C. R. Dennison, and E. C. Kumbur, *J. Electrochem. Soc.*, **163**, A5244 (2016).
33. F. G. Donnan and E. A. Guggenheim, *Zeitschrift für Phys. Chemie*, **162**, 346 (1932).
34. B. Bauer, *"Anion-Exchange Membr. with Improv. Stab. Energy Appl. Present. "Anion-Exchange Membr. Energy Gener. Technol. Work. IAS - Univ. Surrey.*, 12 (2013).
35. A. Tang, J. Bao, and M. Skyllas-Kazacos, *J. Power Sources*, **196**, 10737 (2011).
36. M. Skyllas-Kazacos and L. Goh, *J. Memb. Sci.*, **399–400**, 43 (2012).
37. T. Mohammadi, S. C. Chieng, and M. Skyllas Kazacos, *J. Memb. Sci.*, **133**, 151 (1997).

Supplementary Material

In-situ measurement of vanadium crossover for the vanadium redox flow battery

Tiago Lagarteira[1], Pedro Pacheco[1], Carlos Almeida[1], Anders Bentien[2], Ricardo Monteiro[1], Adélio Mendes[1,z]

[1] LEPABE - Laboratory for Process, Environment, Biotechnology and Energy, Faculty of Engineering of the University of Porto, Rua Dr. Roberto Frias s/n, 4200-465 Porto, Portugal

[2] Department of Engineering – Biological & Chemical Engineering, Aarhus University, Hangøvej 2, 8200 Aarhus N, Denmark

[z] Corresponding Author: mendes@fe.up.pt

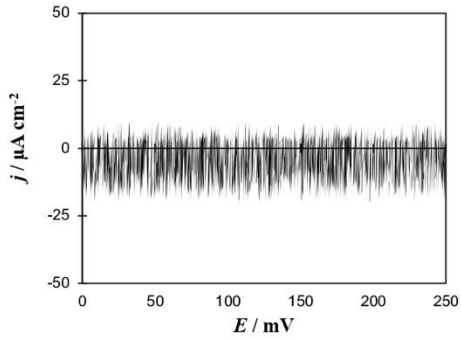


Figure S1. Effect of blank electrolyte on current during LSV measurements. The voltammogram was obtained at 75 μV s^{-1} and the potential was swept from the OCP to 250 mV.

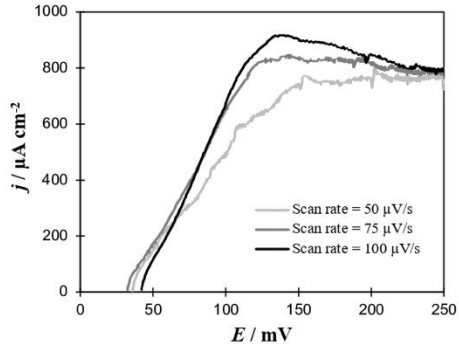


Figure S2. Effect of scan rate on voltammogram response. The voltammograms were obtained at different scan rates (see legend) and the potential was swept from the OCP to 250 mV.

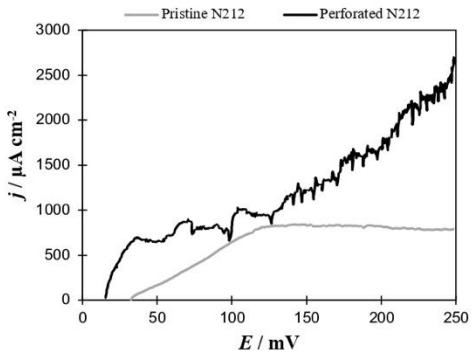


Figure S3. Comparison between the current response of pristine and perforated Nafion 212 membranes. The voltammograms were obtained at 75 µV s^{-1} and the potential was swept from the OCP to 250 mV.

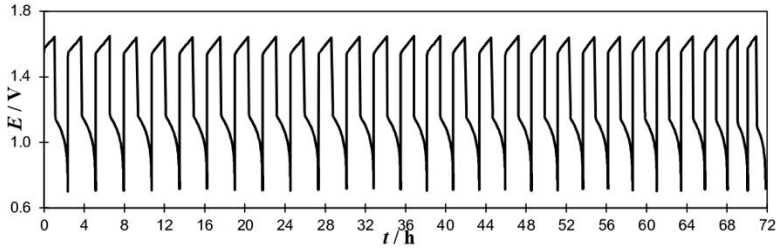


Figure S4. Charge-discharge cycling for membrane degradation, performed at 80 mA cm^{-2}, with the upper and lower potential limits set to 1.65 and 0.7 V, respectively. The cell was subjected to 28 charge-discharge cycles.

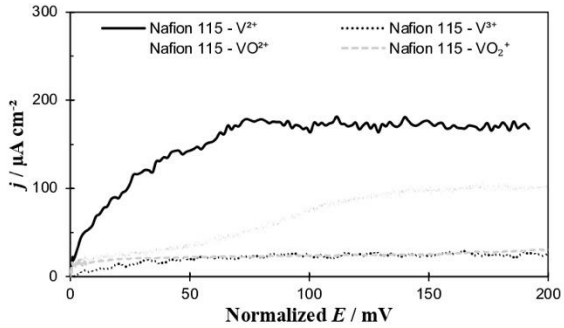


Figure S5. Comparison between the current response of all oxidation states of vanadium for Nafion 115 membrane. The voltammograms were obtained at 75 µV s^{-1} and the potential was swept from the OCP to 250 mV.

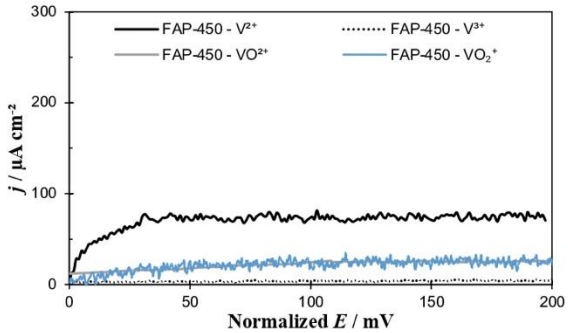


Figure S6. Comparison between the current response of all oxidation states of vanadium for FAP 450 membrane. The voltammograms were obtained at 75 µV s^{-1} and the potential was swept from the OCP to 250 mV.

ANNEX 3

DECLARATION STATING THE NATURE OF ALL COLLABORATIONS WITH CO-AUTHORS



To Whom it May Concern

The PhD candidate Tiago Lagarteira hereby states that his doctoral Thesis entitled "Electrochemical Technologies for Renewable Energy Storage" does not include a formal supervisor. All published articles included in this Thesis are listed below with the description of all collaborations and work done by all co-authors. The author also declares that none of these works was or will be included in other Theses.

Highly active screen-printed Ir/Ti_4O_7 anodes for proton exchange membrane electrolyzers, International Journal of Hydrogen Energy, Volume 43, Issue 35, 2018, Pages 16824-16833, ISSN 0360-3199, https://doi.org/10.1016/j.ijhydene.2018.02.179.

Tiago Lagarteira: Conceptualization, Experimental work; Writing – original draft.
Feng Han: Conceptualization; Supervision; Writing – review and editing.
Tobias Morawietz: AFM measurements; Writing – review and editing.
Renate Hiesgen: Writing – review and editing.
Daniel Garcia Sanchez: Writing – review and editing.
Adélio Mendes: Supervision; Writing – review and editing.
Aldo Gago: Conceptualization; Resources; Supervision; Writing – review and editing.
Rémi Costa: Conceptualization; Resources; Funding; Supervision; Writing – review and editing.

Air Bleeding Strategies to Increase the Efficiency of Proton Exchange Membrane Fuel Cell Stationary Applications Fuelled with CO ppm-levels, International Journal of Electrochemical Science, Volume 15, 2020, Pages 613-627, doi: 10.20964/2020.01.58.

Sofia Delgado: Writing – original draft;
Tiago Lagarteira: Conceptualization, Experimental work; Writing – original draft.
Adélio Mendes: Conceptualization; Resources; Funding; Supervision; Writing – review and editing.

The role of Pt loading on reduced graphene oxide support in the polyol synthesis of catalysts for oxygen reduction reaction, International Journal of Hydrogen Energy, Volume 45, Issue 40, 2020, Pages 20594-20604, ISSN 0360-3199, https://doi.org/10.1016/j.ijhydene.2020.02.022.

Tiago Lagarteira: Conceptualization, Experimental work; Writing – original draft.
Sofia Delgado: Writing – review and editing.
Celina Fernandes: Writing – review and editing.
Cátia Azenha: Analysis of morphological measurements; Writing – review and editing.
Cecilia Mateos-Pedrero: Analysis of morphological measurements; Writing – review and editing.
Adélio Mendes: Conceptualization; Resources; Funding; Supervision; Writing – review and editing.

Oxygen reduction stability of graphene-supported electrocatalyst: electrochemical and morphological evidences, accepted and currently under production at the International Journal of Hydrogen Energy.

Tiago Lagarteira: Conceptualization, Experimental work; Writing – original draft.
Sofia Delgado: Experimental work; Writing – original draft.
Gema Garcia: ICP-MS measurements; Writing – review and editing.
Alfredo Ortiz: Writing – review and editing.
Adélio Mendes: Resources; Funding; Supervision; Writing – review and editing.

In-Situ Measurement of Vanadium Crossover for the Vanadium Redox Flow Battery, Journal of The Electrochemical Society, Volume 166, Issue 16, 2019, https://dx.doi.org/10.1149/2.0331916jes.

Tiago Lagarteira: Conceptualization, Experimental work; Writing – original draft.

Pedro Pacheco: Experimental work; Writing – review and editing.

Carlos Almeida: Experimental work.

Anders Bentien: Writing – review and editing.

Ricardo Monteiro: Writing – review and editing.

Adélio Mendes: Resources; Funding; Supervision; Writing – review and editing.



(Tiago Lagarteira)